

# **Exchange bias in magnetic thin films and nanoparticles.**

*Study of spin glass, spin dynamics and anisotropy.*

Von der Fakultät für Mathematik, Informatik und Naturwissenschaften der Rheinisch-Westfälischen Technischen Hochschule (RWTH) Aachen zur Erlangung des akademischen Grades eines Doktors der Naturwissenschaften genehmigte Dissertation

vorgelegt von  
Master of Philosophy in Physics

**Muhammad Bilal Janjua**

aus Rawalpindi, Pakistan

Berichter:      Universitätsprofessor Dr. Gernot Güntherodt  
                    Universitätsprofessor Dr. Markus Morgenstern  
                    Universitätsprofessor Dr. Wolfgang Kuch

Tag der mündlichen Prüfung: 29.04.2016

Diese Dissertation ist auf den Internetseiten der Universitätsbibliothek online verfügbar.



---

## Abstract

The spin valve structure has important applications in the hard disk drives, magnetic sensors, magnetoresistive random-access memory and consequently is actively researched. The materials having perpendicular magnetic anisotropies are in high demand for perpendicular magnetic recording and heat-assisted magnetic recording. Other than the magnetic thin films, the magnetic nanoparticles have strong contribution in the emerging technologies, such as, drug delivery, tagging or labeling of the desired biological entity and magnetic resonance imaging.

The goal of this thesis is to explore the different magnetic behaviours, i.e., exchange bias (EB), perpendicular magnetic anisotropy (PMA), spin glass (SG) phases, spin dynamics, interparticle interactions in the magnetic thin films and nanoparticles. Moreover, this thesis includes some new magnetic behaviours which have not been reported yet after the careful literature survey. The PMA is studied in the thin films of CoPd alloy. Perpendicular EB is developed by using IrMn as an antiferromagnet. A transition in the EB is observed at low temperatures, where the in-plane (IP) EB field becomes larger than the out-of-plane (OP) EB field. It is found that with decreasing temperature there is a spin structure transition in the IrMn (111) layer related to a 3Q (favors OP spins component) to 2Q transition (favors IP spins component) in the bulk. This transition is responsible for the increase in the IP EB at low temperatures and has not been reported before. A spin reorientation transition from OP to IP (at higher temperatures) is also observed in the CoPd alloy, but is too weak to perturb the spin structure transition of IrMn. The most interesting result is an increase in PMA of CoPd/IrMn with decreasing the thickness of CoPd layer, which is contrary to bare CoPd alloy. The bulk 3Q spin structure of IrMn and the angle difference between the CoPd and IrMn moments at the interface are the reasons of this discrepancy.

Memory effect, aging, Morin transition and EB effect are studied in the agglomerated hematite nanoparticles of different shapes from spherical to spindle. The super spin glass (SSG) and surface SG phases are found in these nanoparticles generating EB field. The interesting behaviour is the sign change in the EB field along with Morin transition, where the rotation of Fe ions in the core changes the exchange coupling at interface resulting in positive EB field. Morin transition is diminished with increasing the aspect ratio of nanoparticles due to the enhanced lattice strain and surface defects. In order to eliminate agglomeration, silica coating is used around the

---

nanoparticles. The silica coating enhances the surface disorder, decreases magnetization and depletes Morin transition. The sign of the EB field is changed to negative as compared to uncoated ones.  $Co_{1-x}Mg_xFe_2O_4$  nanoparticles are studied in quasi-free state and semi-compressed form. Spontaneous exchange bias (SEB) is observed along with conventional exchange bias (CEB) in the both states of nanoparticles. In the quasi-free state of nanoparticles, SEB is larger than CEB, while SEB becomes weak in semi-compressed form. The initial magnetic state has strong influence on SEB, where strong randomness contributes to the volume fraction of SG phase. The frustration and smooth movement of nanoparticles enhance SEB in quasi-free state of nanoparticles. The metastable domain states are developed in the system due to strain and dilution which perturbed by the rotation of the ferrimagnetic core moments with increasing temperature.

The temperature driven sign reversal in Fe/Cr bilayer is studied and explained by the formation of interface alloying. The FeCr alloy at the interface transforms into SG phase during cooling. At low temperatures, the ferromagnetic interactions between frozen Fe clusters in alloy and adjacent Fe layer, results into enhanced negative EB field. The Cr rich alloy favours re-entrant SG to antiferromagnetic phase transition in alloy with increase in temperature. This phase transition changes the ferromagnetic coupling to antiferromagnetic between uncompensated Cr moments and Fe layer at interface resulting into positive EB.

The novel results in the EB in different magnetic systems certainly encourage further probe into it by changing the thickness of IrMn layer for CoPd/IrMn system and the interparticle interactions.

---

## Zusammenfassung

Die Spin-Ventil-Struktur wird in Anwendungen wie Festplattenlaufwerken, Magnetsensoren sowie magnetoresistiven Arbeitsspeichern genutzt, und ist somit Bestandteil der aktuellen Forschung. Materialien, mit senkrechter magnetischer Anisotropie sind für senkrechte magnetische Aufzeichnung sowie wärmeunterstützter Magnetaufzeichnung (heat-assisted magnetic recording) von großer Interesse. Im Gegensatz zu magnetischen dünnen Schichten, liefern magnetische Nanopartikel einen großen Beitrag zu neu aufkommenden Technologien, wie zum Beispiel, Drug Delivery, Tagging und Magnetresonanztomografie.

Das Ziel dieser Arbeit ist, das magnetische Verhalten von magnetischen dünnen Schichten sowie Nanopartikel zu erforschen. Hierbei werden Exchange Bias (EB), senkrechte magnetische Anisotropie (perpendicular magnetic anisotropy: PMA), Spin-Glas (SG) Phasen, Spin Dynamik sowie magnetische Wechselwirkungen in den magnetischen dünnen Schichten und Nanopartikel untersucht. Darüber hinaus beinhaltet diese Arbeit einige neue magnetische Verhaltensweisen, von der sich, auch nach sorgfältiger Literaturstudie, keine Befunde finden ließen. Die PMA wird in Dünnschichten von CoPd-Legierungen untersucht. Senkrechter EB wird durch die Verwendung von IrMn als Antiferromagnet erzeugt. Ein Übergang in den EB wird bei niedrigen Temperaturen beobachtet. Hierbei wird das ebene (In-plane: IP) EB-Feld größer als das EB-Feld, das aus der Ebene herausragt (out-of-plane: OP). Es wurde festgestellt, dass mit abnehmender Temperatur es einen Übergang in der Spin Struktur der IrMn (111) Schicht gibt, der mit dem Übergang von 3Q (begünstigt OP Spin-Komponente) hin zu 2Q (begünstigt IP Spin-Komponente) des Bulk-Materials verbunden ist. Dieser Übergang ist für die Erhöhung der IP EB bei niedrigen Temperaturen verantwortlich und wurde bisher in der Literatur nicht berichtet. Ein Spin Reorientierungsübergang von OP zu IP (bei höheren Temperaturen) wird auch in der CoPd-Legierung beobachtet, welcher jedoch zu schwach ist, um den Spin-Struktur Übergang von IrMn zu stören, der die Temperaturabhängigkeit des EB dominiert. Das interessanteste Ergebnis ist ein Anstieg der PMA von CoPd / IrMn mit Abnahme der Dicke der CoPd-Schicht, welches im Gegensatz zur reinen CoPd-Legierung steht. Die Bulk 3Q Spin Struktur von IrMn und der Winkel zwischen den magnetischen Momenten von CoPd und IrMn an der Grenzschicht sind die Gründe für diese Diskrepanz.

Memory-Effekte, Alterungs-Efekte, Morin Übergänge sowie EB-Effekt werden an

---

agglomerierten Hämatit-Nanopartikel unterschiedlicher Formen von kugelförmigen zu spindelförmig untersucht. Die Superspinglas (SSG)- und oberflächen SG-Phasen werden in diesen EB-Feld erzeugenden Nanopartikel gefunden. Hierbei zeigt sich das interessante Verhältnis des Vorzeichenwechsels im EB-Feld zusammen mit einem Morin-Übergang. Die Drehung der Fe-Ionen im Kern ändert die Austauschwechselwirkung an der Grenzfläche zu positiven EB-Feldern. Der Morin-Übergang ist verringert mit Erhöhung des Seitenverhältnisses von Nanopartikeln, was zu gesteigerten Gitterspannung und Oberflächenfehlern führt. Um eine Agglomeration zu vermeiden, werden die Nanopartikel mit einer Siliciumdioxid-Beschichtung versehen. Die Silica-Beschichtung erhöht die Oberflächenunordnung, verringert die Magnetisierung und verringert den Morin Übergang. Im Vergleich zu den unbeschichteten Nanopartikeln ändert sich das Vorzeichen des EB-Feldes zum negativen hin.  $Co_{1-x}Mg_xFe_2O_4$  Nanopartikel werden im quasi-freien Zustand und semi-komprimierter Form untersucht. In beide Zustandsformen weisen die Nanopartikel sowohl spontane Exchange Bias (SEB) sowie herkömmlichen Exchange Bias (conventional EB: CEB) auf. Im quasi-freien Zustand ist der SEB größer als der CEB, während der SEB bei der semi-komprimierter Form schwächer als der CEB ist. Der anfängliche Magnetisierungszustand hat starken Einfluss auf das SEB, wenn starke Zufälligkeit zu dem Volumenanteil der SG-Phase beiträgt. Die Frustration und reibungslose Bewegung von Nanopartikeln fördert SEB in quasi-freien Zustand von Nanopartikeln. Die metastabile Domänenzustände werden im System aufgrund von Spannung und Verdünnung entwickelt, welche durch die Drehung des ferromagnetischen Kernmomente mit zunehmender Temperatur gestört werden.

Die temperaturangetriebene Vorzeichenumkehr in Fe/Cr-Doppelschichten werden untersucht und durch die Bildung von Grenzschichtvermischungen erläutert. Die FeCr-Legierung an der Grenzschicht wandelt sich beim Abkühlen in die SG-Phase. Bei niedrigen Temperaturen führt die ferromagnetischen Wechselwirkungen zwischen gefrorenen Fe-Cluster in der Legierung und benachbarten Fe-Schicht zu gesteigerten negativen EB Feld. Die Cr-reichen Legierung, begünstigt reentrant SG vor einem antiferromagnetischen Phasenübergang in Legierung mit Erhöhung der Temperatur. Dieser Phasenübergang ändert die ferromagnetische Kopplung hin zu antiferromagnetischer Kopplung zwischen unkompenzierten magnetischem Momenten in Cr und Fe-Schichten an der Grenzfläche und führt zu positiven EB.

Die neuen Ergebnisse in den EB in verschiedene Magnetsystemen fördert sicherlich weitere Untersuchungen an Proben mit geänderter Schichtdicke von IrMn in

---

CoPd/IrMn Systeme sowie geänderte Wechselwirkungen zwischen den Partikeln.



# Contents

<b>1</b>	<b>Introduction</b>	<b>1</b>
<b>2</b>	<b>Background physics</b>	<b>5</b>
2.1	Exchange bias . . . . .	5
2.1.1	Phenomenology of exchange bias . . . . .	7
2.1.2	Applications . . . . .	8
2.2	Exchange bias models . . . . .	9
2.2.1	Meiklejohn and Bean model . . . . .	9
2.2.1.1	Rigid Antiferromagnet model . . . . .	10
2.2.1.2	$K_{AFM}t_{AFM} \ll J_{EB}$ . . . . .	12
2.2.2	Néel: Domain wall - Weak coupling . . . . .	13
2.2.3	Malozemoff: Random field model . . . . .	13
2.2.4	Mauri: Parallel domain wall . . . . .	15
2.2.5	Koon: Spin-flop coupling model . . . . .	15
2.2.6	Domain state model . . . . .	17
2.3	Spin glass . . . . .	19
2.3.1	Introduction . . . . .	19
2.3.2	Exchange bias using spin glass . . . . .	21
<b>3</b>	<b>Experimental techniques</b>	<b>23</b>
3.1	Molecular beam epitaxy . . . . .	23

3.1.1	MBE chamber	24
3.1.2	Metal MBE chamber	25
3.1.3	Analysis chamber	29
3.1.4	Load lock chamber	30
3.1.5	Transfer chamber	30
3.2	Other experimental techniques	31
<b>4</b>	<b>The study of exchange bias, spin structure , spin re-orientation transitions and anomalous anisotropy in CoPd/IrMn system</b>	<b>33</b>
4.1	Introduction	33
4.2	Sample preparation and structural characterization	34
4.3	Measurement procedure	36
4.4	Perpendicular anisotropy in CoPd alloy	38
4.4.1	Magnetic measurements of CoPd samples	39
4.4.2	Reasons of the perpendicular anisotropy	41
4.4.3	Discussion	42
4.5	Study of exchange bias in CoPd-IrMn bilayers	46
4.5.1	Hysteresis measurements	46
4.5.2	Temperature dependence of in-plane and out-of-plane exchange bias	48
4.5.3	Spin structure of IrMn	49
4.5.4	Literature survey	52
4.5.4.1	Q- spin structure and exchange bias	52
4.5.4.2	In-plane and out-of-plane exchange bias	54
4.5.4.3	Exchange bias in CoPd system	55
4.5.5	Discussion of the experimental results of exchange bias	56
4.5.6	Magnetization versus temperature measurements: 2Q-3Q spin structure transition	60
4.5.6.1	Exchange biased and FM only samples	60

4.5.6.2	Sole IrMn sample . . . . .	63
4.5.7	Effect of the thickness of CoPd layer on 2Q-3Q transition of IrMn . . . . .	66
4.5.8	Effect of annealing . . . . .	67
4.6	Spin re-orientation transition in sole CoPd and CoPd/IrMn samples	68
4.7	Anomalous change in the anisotropy of CoPd/IrMn system . . . . .	71
4.7.1	Interpretation . . . . .	76
4.8	Summary of the chapter . . . . .	77
<b>5</b>	<b>The study of spin dynamics, Morin transition, shape anisotropy, exchange bias and silica coating in hematite nanoparticles</b>	<b>81</b>
5.1	Introduction . . . . .	81
5.2	Sample preparation and structural analysis . . . . .	82
5.2.1	Synthesis . . . . .	82
5.2.2	Structural characterizations . . . . .	83
5.3	Magnetic characterization of hematite nanoparticles . . . . .	85
5.3.1	Study of exchange bias . . . . .	85
5.3.2	Study of spin dynamics and spin glass behaviour . . . . .	88
5.3.2.1	Magnetization versus temperature measurements and AT-line . . . . .	89
5.3.2.2	Aging and memory effects . . . . .	94
5.3.3	Cooling field dependence of exchange bias . . . . .	98
5.4	Morin transition . . . . .	99
5.4.1	Presence of exchange bias below Morin transition . . . . .	103
5.4.2	Shape dependence Morin transition . . . . .	109
5.4.3	Summary of study of the un-coated hematite nanoparticles .	111
5.5	Silica coated hematite nanoparticles . . . . .	112
5.5.1	Silica coating on hematite nanoparticles . . . . .	112
5.5.2	Study of exchange bias in silica coated hematite nanoparticles	113

5.6	Effect of silica coating	122
5.7	Summary of chapter	126
<b>6</b>	<b>Study of zero-field cooled exchange bias in <math>Co_{1-x}Mg_xFe_2O_4</math> nanoparticles</b>	<b>127</b>
6.1	Introduction	127
6.2	Synthesis	128
6.3	Magnetic characterization of nanoparticles in quasi-free state	131
6.3.1	Spontaneous exchange bias	131
6.3.2	Spin dynamics	138
6.4	Exchange bias in semi-compressed form	140
6.5	Explanation	141
6.6	Summary	144
<b>7</b>	<b>Effect of interface alloying on exchange bias in Fe/Cr bilayers</b>	<b>147</b>
7.1	Introduction	147
7.2	Study of exchange bias in Fe/Cr samples	148
7.3	Effect of reversed interface: Cr/Fe interface	150
7.4	Oxide barrier: Verification of interdiffusion	151
7.5	Effect of Fe dilution in Cr on exchange bias	152
7.6	Explanation	154
7.7	Summary	156
<b>8</b>	<b>Summary and future work</b>	<b>157</b>
<b>Bibliography</b>		<b>160</b>
<b>A Appendices</b>		<b>181</b>
A.1	Appendix 1	181
A.2	Appendix 2	182

<b>List of publications</b>	<b>183</b>
<b>Acknowledgments</b>	<b>185</b>
<b>Curriculum Vitae</b>	<b>187</b>

# Chapter 1

## Introduction

Magnetism has attracted large interest and research focus due to its various technological applications. The reduced dimensions in the magnetic systems, provide building blocks for the data storage technology, magnetic sensors and spintronics applications. Since the discovery of giant magnetoresistance (GMR) effect<sup>1</sup>, new magnetic materials are heavily studied to be used in the magnetic field sensors. The magnetic field sensors have vast applications in hard disk drives, biosensors, micro-electro-mechanical systems (MEMS) and magnetoresistive random-access memory (MRAM). MRAM, a non-volatile memory, is a new technology which will become universal memory<sup>2</sup>. It is much faster and requires much lower power as compared to other memories. Spintronics is a rapidly emerging field of technology, that has a significant impact on the future of electronics.

The spin valves, comprising of two ferromagnetic layers that are separated by a non magnetic layer, are the common magnetic sensors which are widely used in different devices. A spin valve is considered as a unit cell of MRAM. They are based on either of the two magnetoresistance effects, i.e., GMR or tunnel magnetoresistance (TMR). The ferromagnetic layer in the spin valve is pinned through the exchange bias (EB) phenomenon, which is still important toady, ever since it was discovered by Meiklejohn and Bean<sup>3</sup>. The need for spintronics devices has accelerated the research on hetrostructures like ferromagnet (FM)/antiferromagnet (AFM), FM/semiconductors and diluted magnetic semiconductors. Furthermore, the high density magnetic storage technology has raised immense interest in the materials having perpendicular magnetic anisotropies (e.g., FePt, CoPt, CoPd), which are in high demand for perpendicular magnetic recording and heat-assisted magnetic recording (HAMR). Besides the magnetic thin films, magnetic nanoparticles have

strong contribution in the emerging technology. Apart from electrical, mechanical, and optical applications, the biocompatible nanoparticles also offer attractive possibilities in the field of biomedicine, such as, drug delivery, tagging or labeling of the desired biological entity and magnetic resonance imaging (MRI)<sup>4</sup>.

The aim of this thesis is to explore different magnetic behaviours, i.e., EB, perpendicular magnetic anisotropy, spin glass (SG) phases, spin dynamics, interparticle interactions in magnetic thin films and nanoparticles. Since several decades, the phenomenon of EB has been studied and observed in many systems (thin films and nanoparticles) under different conditions, however, new aspects are still observed, which need to be investigated in order to resolve the hidden mechanisms.

An introductory overview of the research work is given in chapter 1. Chapter 2 focuses on the background physics of the phenomena discussed in the proceeding chapters of this thesis. The chapter mainly discusses different models of EB phenomenon. Various SG systems and Stoner-Wohlfarth model for superparamagnetism are also discussed.

The experimental techniques used in the preparation, structural and magnetic characterization of the samples are discussed in chapter 3. The multi-chamber molecular beam epitaxy (MBE) system is also described, that was used for the deposition of the thin films.

Chapter 4 presents the magnetic studies in sole CoPd alloy and CoPd/IrMn bilayers. The perpendicular anisotropy in the CoPd alloy and the factors controlling it, are studied. IrMn is used as an AFM, in order to get perpendicular EB in the CoPd/IrMn bilayers. The effect of CoPd thickness on the perpendicular anisotropy in the sole CoPd layers and exchange biased layers are investigated, where its behaviour is opposite in CoPd/IrMn bilayers as compared to the sole CoPd layers. The spin re-orientation transition that occurred in CoPd does not affect EB, while the spin structure transition in IrMn strongly affects the EB field ( $H_{EB}$ ). The 3Q spin structure of IrMn also explains the enhanced perpendicular anisotropy.

Morin transition, memory effects, aging and EB phenomena are studied in hematite nanoparticles of different aspect ratios, in chapter 5. Super spin glass (SSG) and surface SG phases are observed, which generate the EB phenomenon. Morin transition is suppressed, with increasing aspect ratio. In the spherical shaped nanoparticles, Morin transition is related to sign reversal in  $H_{EB}$ . In order to avoid agglomeration, hematite nanoparticles are coated with silica. The effect of silica coating on EB, surface disorder and Morin transition is clearly observed. The surface disorder

---

increases, while Morin transition vanishes due to silica coating. The remarkable behaviours in these nanoparticles are the presence of  $H_{EB}$  below Morin transition in uncoated nanoparticles and the enhanced negative  $H_{EB}$  in coated nanoparticles.

In chapter 6, magnetic properties of  $Co_{1-x}Mg_xFe_2O_4$  nanoparticles with different Mg substitutions are investigated. Spontaneous EB (SEB) is observed after zero field cooling, which depends on the Mg substitution and the initial magnetic state of the system. The spin frustration inside the system is also related to the substitution of Mg ions. The interparticle interactions and the easy rotation of nanoparticles are controlled by pressing them inside the capsule. This results in reduced SEB. The interesting part is the sign reversal in SEB field, that relates to the metastable domains at the interface of core and surface SG.

The magnetic study of Fe/Cr bilayers is done in chapter 7, where the sign reversal in the  $H_{EB}$  and the enhanced negative  $H_{EB}$  at low temperatures, are observed. These phenomena originate due to the competing interfacial exchange interactions of different signs, depending on the temperature. These competing interactions occur in FeCr SG alloy, formed due to intermixing at Fe/Cr interface.



# Chapter 2

## Background physics

### 2.1 Exchange bias

The phenomenon of exchange bias (EB) is an interesting topic that has been observed and investigated several times, since its discovery in 1956 during the study of Co particles embedded in their native antiferromagnetic oxide, CoO<sup>3</sup>. The implications for basic research and device applications, make the EB effect still important for the scientific research. The EB effect is the result of exchange interactions at the interface between two different magnetic phases and has been observed in many systems<sup>5</sup>. In general, the system consists of ferromagnet (FM)/antiferromagnet (AFM)<sup>6</sup>, but this effect is also observed at the interface of different systems like, ferrimagnet (FI)/AFM<sup>7</sup>, FM/spin glass (SG)<sup>8</sup>, FI/SG<sup>9</sup> and FM/FI<sup>10</sup>. The magnetic systems exhibiting EB effect are, nanoparticles<sup>4;11</sup>, thin films<sup>5;12</sup>, nanostructures<sup>13</sup> and bulk alloys<sup>14;15</sup>.

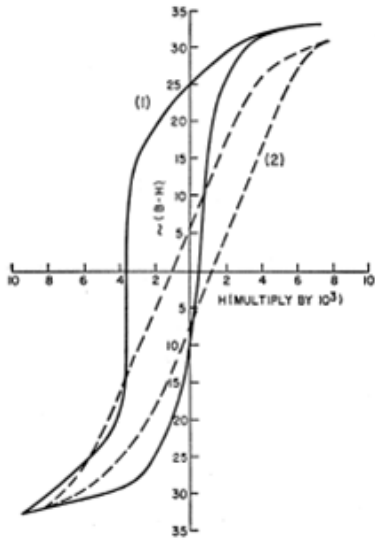


Figure 2.1.1: Hysteresis loops at 77 K of oxide coated Co particles. Curve (1) shows the resulting loop after cooling the particles in 10 kOe field and curve (2) shows the loop when cooled in zero field. From Ref.<sup>3;16</sup>.

In order to generate EB in a system containing FM/AFM bilayer, the field cooling is done and the EB effect is depicted by the shift in the hysteresis loop opposite to the cooling field direction, generally. Meiklejohn and Bean discovered the unidirectional anisotropy in oxide coated Co particles due to the exchange interaction between ferromagnetic and antiferromagnetic materials. They measured the hysteresis loop of Co/CoO particles after cooling in the magnetic field of 10 kOe from 300 K to 77 K through Néel temperature ( $T_N$ ) of CoO (293 K) and also in zero field<sup>3;16</sup>. The resultant field cooled (FC) and zero-field cooled (ZFC) hysteresis loops are exhibited in Fig. 2.1.1. The FC hysteresis loop (loop 1) is shifted as indicated by the solid line and the dashed curve (loop 2) which was obtained after cooling in zero field, is symmetric and centered at  $H = 0$ , as shown in Fig. 2.1.1. The loop is shifted to the opposite direction of the cooling field, the reason is the development of “new magnetic anisotropy”, described as the exchange anisotropy between Co and CoO at the interface. The shift in the loop after field cooling is 1.6 kOe and is called as EB field ( $H_{EB}$ ). In addition to the loop shift, Meiklejohn and Bean also noticed the rotational hysteresis in the torque magnetometry measurement of Co/CoO nanoparticles after field cooling<sup>16</sup>.

### 2.1.1 Phenomenology of exchange bias

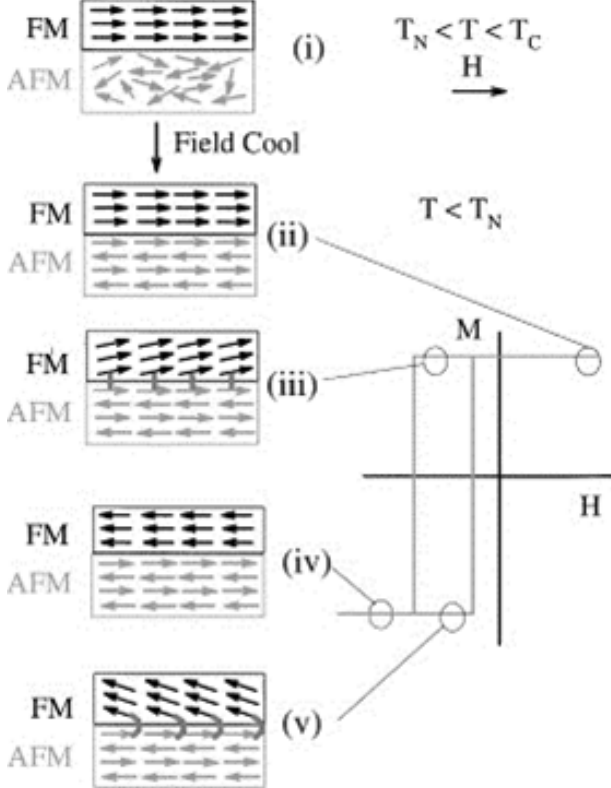


Figure 2.1.2: Schematic diagram of the spin configuration of an FM/AFM bilayer at different stages (i)-(v) of an exchange biased hysteresis loop. It is important to note that the spin configurations illustrate the effect of the coupling and they are not necessarily accurate portraits of the actual rotation of the FM or AFM magnetic moments. From Ref.<sup>5</sup>.

Usually, the EB effect is observed and measured by the shift in the hysteresis loop after cooling through  $T_N$  in the presence of magnetic field. The simple interpretation of EB effect is the presence of unidirectional anisotropy, which arises due to the interfacial exchange coupling between FM and AFM. Although the microscopic explanation of EB phenomenon is still under consideration, here, a simple model with FM/AFM, is used to understand this effect. The origin of EB effect is phenomenologically described in Fig. 2.1.2<sup>5</sup>. The Curie temperature ( $T_C$ ) of FM should be higher than  $T_N$  of an AFM, in order to retain the magnetic order in the FM through the cooling process. The magnetic field is applied in the positive direction at a temperature  $T$ , where  $T_N < T < T_C$ . At this temperature, the spins in the FM align along the field direction, while spins in the AFM are randomly oriented

because of paramagnetic state, and the applied field is strong enough to saturate the FM (see Fig. 2.1.2(i)). During field cooling, as temperature passes through  $T_N$ , the antiferromagnetic spins next to the FM, align ferromagnetically or parallel (assuming ferromagnetic interaction). The alignment in the antiferromagnetic spins adjacent to FM, occurs due to exchange interaction between FM and AFM at the interface. The next layer of AFM is arranged in antiparallel order to the previous one, to retain antiferromagnetic order and so on (see Fig. 2.1.2(ii)). It should be noted that, the spins of AFM at interface are uncompensated, providing a net magnetization to this layer of AFM. When the field is reversed, the spins in FM try to rotate in-plane towards opposite direction, to follow the field. The spins in AFM do not rotate, because of large anisotropy. Therefore, the exchange interaction present between the both spins at the interface, try to align the ferromagnetic spins in the direction of cooling field. In other words, the spins of antiferromagnetic layer at interface, exert a microscopic torque on the spins in FM, to align them ferromagnetically. This gives the only single stable configuration to the ferromagnetic spins, i.e., the unidirectional anisotropy (see Fig. 2.1.2(iii)). In order to reverse the ferromagnetic spins, an extra large field is required to overcome the exchange coupling with AFM. On the way back from negative saturation to positive field, the spins in FM require smaller field to rotate back to original position. The reason is the interaction with the antiferromagnetic spins, which now exert a torque in the same direction as the applied field (see Fig. 2.1.2(v)). As a result, the coercive field in the descending branch is larger than the ascending one, thus, the hysteresis loop shifts in negative direction (opposite to cooling field direction). This displacement of the center of hysteresis loop is  $H_{EB}$ , which is negative due to the shift in opposite direction compared to the cooling field direction.

This is the simple model to explain EB effect in the FM/AFM system with uncompensated AFM at interface. There are other different factors such as, anisotropy, surface roughness, compensated AFM and spin configuration etc., which strongly affect EB phenomenon, but can not explain through this model<sup>5;12</sup>.

### 2.1.2 Applications

Since the discovery of EB effect, it has been studied in both nanoparticles and thin films of various magnetic materials under different conditions. The presence of EB effect in the nanoparticles make their use as permanent magnetic materials and

magnetic recording media. Although, the study of EB in nanoparticles does not have much technological applications as compared to thin films, but it helps in the deep understanding of the phenomenon in various materials like different phases of SGs<sup>5;13</sup>.

The most important industrial applications of EB effect are applicable in the form of thin film. The spin valve structure is the most common technological device, where the EB effect is used to fix the ferromagnetic layer as a reference. The spin valve structure consists of two ferromagnetic layers, which are separated by either a non magnetic metallic spacer or a tunnel barrier layer for the use in giant magnetoresistance (GMR) or tunnel magnetoresistance (TMR) devices, respectively. Spin valves are extensively used in magnetic sensors, read-heads for hard disk and as a building unit of magnetoresistive random-access memory (MRAM)<sup>17-19</sup>.

## 2.2 Exchange bias models

### 2.2.1 Meiklejohn and Bean model

The intuitive but idealized model of EB mechanism, as proposed by Meiklejohn and Bean, is described in section 2.1.1. In this model, the energy per unit area of the EB system, assuming coherent rotation of magnetization, can be written as<sup>16;20</sup>,

$$E = -HM_F t_{FM} \cos(\theta - \beta) + K_F t_{FM} \sin^2 \beta + K_A t_{AFM} \sin^2 \alpha - J_{EB} \cos(\beta - \alpha) \quad (2.2.1)$$

where  $K_F$  and  $K_A$  are the anisotropy constants of FM and AFM, respectively and both anisotropy axes are considered in same direction (i.e., collinear).  $H$  is the applied field making an angle  $\theta$  with FM anisotropy axis,  $M_F$  is the saturation magnetization,  $t_{FM}$  and  $t_{AFM}$  are the thicknesses of the FM and AFM layers, respectively.  $\alpha$  and  $\beta$  are the angles between FM and AFM sublattice magnetization with respect to their respective anisotropy axes, the graphic presentation is shown in Fig. 2.2.1.  $J_{EB}$  is the interfacial exchange energy per unit area.

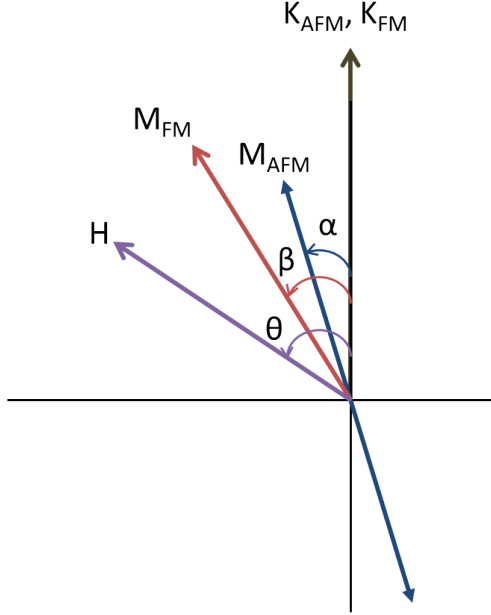


Figure 2.2.1: Schematic diagram of angles and vectors used in Meiklejohn and Bean Model<sup>16</sup>. Where,  $M_{FM}$  is the magnetization of ferromagnet (FM),  $M_{AFM}$  is the net magnetization of antiferromagnet (AFM) and  $H$  is applied field. The vectors  $H$ ,  $M_{FM}$  and  $M_{AFM}$  are at angles  $\theta$ ,  $\beta$  and  $\alpha$  with respect to easy axis of FM and AFM represented by their respective anisotropy constants  $K_{FM}$  and  $K_{AFM}$ .

The first term in the equation (2.2.1) is related to the effect of the applied field on the FM layer, where the second and third terms account for the effect of the anisotropies of FM and AFM layers, respectively. The last term in the equation, takes into consideration the interface exchange coupling between FM and AFM. The following assumptions are considered; the layer of FM rotates as a whole, both FM and AFM are single domain, the spins of AFM at interface are fully uncompensated, the interface is smooth and ferromagnetically coupled. The applied field is also assumed to be parallel to the FM easy axis ( $K_{FM}$ ), it implies that  $\theta = 0$ . This condition refers to the direction along which the hysteresis loops are measured, i.e., parallel to cooling field. For the torque measurements or azimuthal dependence of the EB field,  $\theta \neq 0$ .

### 2.2.1.1 Rigid Antiferromagnet model

It is the case where  $K_{AFM}t_{AFM} \gg K_{FM}t_{FM}$ , i.e., the anisotropy of AFM is strong enough such that spins in AFM layer do not rotate with the applied field. This means

that spins in AFM align along the AFM easy axis ( $K_{AFM}$  direction), making  $\alpha \approx 0$ . In this case Eq. 2.2.1 becomes,

$$E = -HM_{FM}t_{FM}\cos(\beta) + K_{FM}t_{FM}\sin^2\beta - J_{EB}\cos(\beta) \quad (2.2.2)$$

Now minimizing the energy with respect to  $\beta$ ,

$$\partial E / \partial \beta = 0 \quad (2.2.3)$$

gives,

$$\beta = \cos^{-1} [(-J_{EB} - HM_{FM}t_{FM}) / (2K_{FM}t_{FM})] \quad (2.2.4)$$

The energy has extrema corresponding to the positive and the negative saturation at  $\beta = 0$  and  $\beta = \pi$ , respectively. The stability of  $\beta = 0$  configuration is possible if  $J_{EB} + HM_{FM}t_{FM} + 2K_{FM}t_{FM} > 0$ , and if  $-J_{EB} - HM_{FM}t_{FM} + 2K_{FM}t_{FM} > 0$ , the stability of  $\beta = \pi$  configuration is possible<sup>21</sup>. This corresponds to the coercive fields  $H_{C1}$  for  $\beta = 0$  and  $H_{C2}$  for  $\beta = \pi$ , which are given as,

$$H_{C1} = -(2K_{FM}t_{FM} + J_{EB}) / M_{FM}t_{FM} \quad (2.2.5)$$

$$H_{C2} = (2K_{FM}t_{FM} - J_{EB}) / M_{FM}t_{FM} \quad (2.2.6)$$

The coercive field  $H_C$  and EB field  $H_{EB}$  can be calculated according to,

$$H_C = (-H_{C1} + H_{C2}) / 2 \quad \text{and} \quad H_{EB} = (H_{C1} + H_{C2}) / 2 \quad (2.2.7)$$

by putting values of  $H_{C1}$  and  $H_{C2}$ ,

$$H_C = 2K_{FM} / M_{FM} \quad (2.2.8)$$

$$H_{EB} = -J_{EB} / M_{FM}t_{FM} \quad (2.2.9)$$

Eq. 2.2.9 gives Meiklejohn and Bean's expression for EB field under ideal conditions. The negative sign shows that hysteresis loop shifts in negative direction. It is clear

that  $H_{EB}$  is inversely proportional to the thickness and magnetization of FM. Another important result is also obtained from this minimization that the condition  $K_{AFM}t_{AFM} \geq J_{EB}$ , is required for the observation of EB anisotropy.

### 2.2.1.2 $K_{AFM}t_{AFM} \ll J_{EB}$

In this case:  $K_{AFM}t_{AFM} \ll J_{EB}$ , where the AFM has weak anisotropy. Under this condition, it is energetically more favourable that moment of AFM rotates as whole freely, with ferromagnetic moment under the applied field. Since AFM has been rotated out of its easy direction defined by  $K_{AFM}$ , there is no shift in the loop but coercivity is increased. Therefore,  $\alpha \neq 0$  in this case. Under this assumption, Eq. 2.2.1 becomes,

$$E = -H M_{FM} t_{FM} \cos(\beta) + K_{FM} t_{FM} \sin^2 \beta + K_{AFM} t_{AFM} \sin^2 \alpha - J_{EB} \cos(\beta - \alpha) \quad (2.2.10)$$

By minimizing the Eq. 2.2.10 with respect to  $\beta$  and  $\alpha$ , the results are,

$$\frac{H}{\frac{-J_{EB}}{M_{FM} t_{FM}}} \sin \beta + \sin(\beta - \alpha) \quad (2.2.11)$$

$$\frac{K_{AFM} t_{AFM}}{J_{EB}} \sin 2\alpha - \sin(\beta - \alpha) \quad (2.2.12)$$

In order to simplify the above two expressions, the parameters involved in the equations can be written as,  $H_{EB} = -J_{EB}/M_{FM} t_{FM}$  and  $R = K_{AFM} t_{AFM}/J_{EB}$ .  $H_{EB}$  is EB field when anisotropy of AFM is infinity large and  $R$  is the ratio which defines the strength of AFM layer with respect to the interfacial exchange energy. In Eq. 2.2.11, the anisotropy of FM is neglected ( $K_{FM}=0$ ) to simplify the discussion, therefore, the coercivity relates only to AFM<sup>12</sup>. From this numerical evaluation, it seems that  $\beta$  angle defines fully the hysteresis loop which delivers the values of  $H_{C1}$  and  $H_{C2}$  and defines loop shift and coercivity depend on  $\beta$ , while  $\alpha$  influences the shape of the hysteresis loop for small values of ratio  $R$ . For high values of  $R$ , the rotation angle of AFM moment is nearly zero, which results into maximum  $H_{EB}$ .

In Ref<sup>12</sup>, three different values of  $R$  are discussed. When  $R \geq 1$ , the antiferromagnetic spins are rigid, they do not rotate, which results into maximum  $H_{EB}$  and

zero coercivity. The second case is,  $0.5 \leq R < 1$ . In this region, spins in AFM are not rigid, rotate irreversible with FM, causing coercivity at expense of EB field. However, the rotation is not coherent but in jumps depending on the interplay of anisotropy and coupling. The third case is  $R < 0.5$ ; in this case the AFM's spins rotate reversibly with FM 's spins. EB field is zero and coercivity is finite.

### 2.2.2 Néel: Domain wall - Weak coupling

After Meiklejohn and Bean, Néel was first to propose an alternative model for EB<sup>22</sup>, by considering the formation of partial domain wall. A continuum approach is used to split FM and AFM layers in small slices parallel to interface, when the field is reversed, a partial domain wall is formed either in FM or AFM, but parallel to interface. The formation of partial domain wall significantly lowers the shift of the hysteresis loop since it stores a large amount of the exchange energy. Néel's model predicts that a minimum thickness of AFM is required to produce EB field.

### 2.2.3 Malozemoff: Random field model

Malozemoff suggested another model to explain the EB effect, due to random exchange field which is generated by interface roughness<sup>23</sup>. The chemical roughness or alloying at the interface, which is present for any realistic bilayer system, causes lateral variations of the exchange field acting on the FM and AFM layers. The resultant random field causes the AFM to break up into magnetic domains due to the energy minimization. The effect of random impurities or disorder on ordering phenomena, such as ferromagnetism and antiferromagnetism has been discussed by Imry and Ma<sup>24</sup>. Where for large ordered systems, the small random fields, caused by impurities or lattice distortion lead to a breakup of the whole sample into domains.

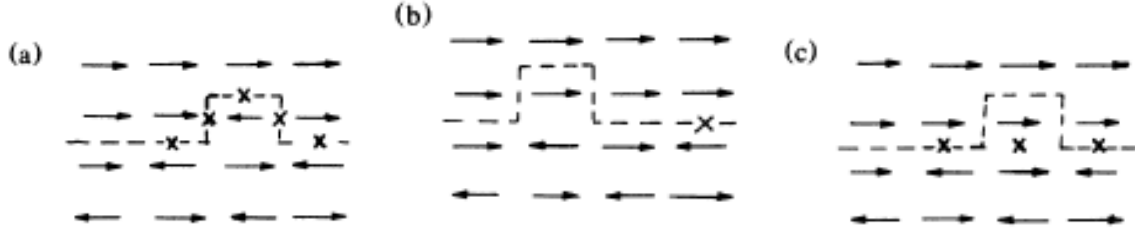


Figure 2.2.2: Schematic side view of possible atomic moment configurations for nonplanar interface. The bumps should be visualized on two-dimensional interface. Configuration (c) represents the lower energy state of (a). Configuration (b) is energetically equivalent to flipping the ferromagnetic spins of (a). The “x” signs represents frustrated bonds. From Ref.<sup>23</sup>.

To illustrate the origin of the random field in the framework of the Malozemoff model, a single mono-atomic defect in the form of a bump at the compensated interface is considered in Fig. 2.2.2(a). One ferromagnetically oriented nearest neighbour pair across the interface is now replaced by five antiferromagnetic pairs. A bump sifted by one lattice spacing (see Fig. 2.2.2(b)), which is equivalent to reversing the ferromagnetic spins. It means that, due to the bump, several frustrated magnetic couplings occur in the system. A coupling between two of the atoms is considered frustrated when two neighbouring atoms are forced to an orientation of their magnetic moments which does not fit to their exchange interaction. This frustrated exchange interaction is not energetically favourable, the system will try to minimize the energy. Each interface irregularity gives a local energy difference, which can be described by an intrinsic local field. Due to the random distribution of defects, this field is of random character and similar to those introduced by Imry and Ma<sup>24</sup>. The presence of such random field leads to domain formation either in the FM or in AFM. Restricting the description to a region with single domain FM, the AFM has to break into domains in order to minimize the free energy from the random field. It is energetically favorable to form domains walls perpendicular to the interface.

The mathematical expression of  $H_{EB}$  calculated by Malozemoff is<sup>23</sup>,

$$H_{EB} = \frac{2z\sqrt{A_{AFM}K_{AFM}}}{\pi^2 M_{FM} t_{FM}} \quad (2.2.13)$$

Where  $A_{AFM}$  and  $K_{AFM}$  are the exchange stiffness and uniaxial anisotropy energy of AFM, respectively.  $z$  is the number of order unity, which characterizes the frustrated states at the interface.  $M_{FM}$  and  $t_{FM}$  are the saturation magnetization and

thickness of ferromagnetic layer, respectively. Within the Malozemoff model, the relevant parameters of an antiferromagnetic domain are the characteristic length L, (where  $L=\pi\sqrt{\frac{A_{AFM}}{K_{AFM}}}$ ) and height h, ( $h=L/2$ ). It is important to mention that the stability of the AFM domains was never tested in the Malozemoff model as it does not consider the effect of thermal relaxation on AFM spins, which is the main merit of Domain State Model (DSM).

#### 2.2.4 Mauri: Parallel domain wall

The model proposed by Mauri et al.<sup>25</sup>, is based on the assumption that a parallel domain wall forms in the AFM directly below the interface. It is also assumed that, the FM is thinner than its domain size thus it is single domain, the interface is atomically flat, ferromagnetic layer rotates rigidly and AFM is uncompensated. The width of the domain wall depends on the exchange stiffness of the antiferromagnetic spin lattice ( $A_{AFM}$ ) and the anisotropy constant ( $K_{AFM}$ ). Exchange interaction ( $J_{EB}$ ) is assumed to depend on the exchange stiffness of the antiferromagnetic moments and their distance  $\xi$  to the neighbouring ferromagnet thus being  $J_{EB}=A_{12}/\xi$ .  $A_{12}$  is the exchange stiffness at interface. The mathematical expression for EB field is,

$$H_{EB}=-J_{EB}/M_{FM}t_{FM} \quad \text{for } \lambda \ll 1 \quad (2.2.14)$$

and

$$H_{EB}=-2(\sqrt{A_{AFM}K_{AFM}})/(M_{FM}t_{FM}) \quad \text{for } \lambda \gg 1 \quad (2.2.15)$$

where  $\lambda=A_{12}/\xi 2\sqrt{A_{AFM}K_{AFM}}$ , is the interface exchange and can be  $< 0$  or  $> 0$ , depending on whether parallel or antiparallel coupling of the spins is favored<sup>25</sup>.

#### 2.2.5 Koon: Spin-flop coupling model

Koon presented the microscopic explanation of EB in thin films having compensated antiferromagnetic-ferromagnetic interface<sup>26</sup>. Heisenberg model was used to show that due to frustration of the moments at interface, ferromagnetic moments minimizes the energy when it aligns perpendicular to antiferromagnetic easy axis, as

shown in Fig. 2.2.3. The term, spin-flop coupling in bulk AFMs, is used to describe this type of exchange coupling between AFM and FM at interface. In this model EB effect is observed through a mechanism similar to Mauri<sup>25</sup>, where the domain wall is formed in AFM during the reversal of ferromagnetic moment. The only restriction is, the motion of the spins during field reversal to the plane parallel to interface. The magnetic moments in the AF interface layer exhibit canting but there is no symmetry breaking along cooling field direction. In fact, the minimum energy is achieved with the antiferromagnetic spins adopting a relatively small canting angle relative to the AFM bulk easy axis, with a component opposite to the cooling field direction.

Later, Schulthess and Butler<sup>27</sup> has shown that for perfectly flat interfaces, spin-flop coupling does not lead to EB, but rather introduces a uniaxial anisotropy. This is responsible for large coercivity observed in exchange biased films. Therefore, spin-flop coupling is not sufficient to generate EB, the introduction of interfacial defects causing uncompensated spins, explain EB in FM/AFM bilayer. This suggests Koon model is now outdated to explain EB in various systems.

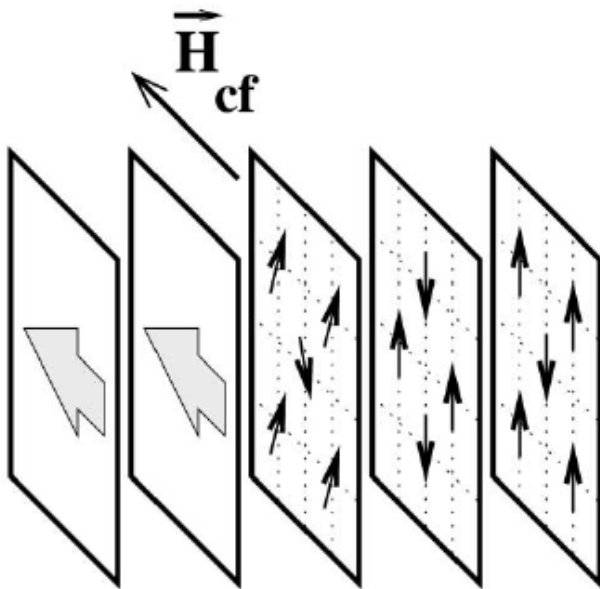


Figure 2.2.3: Illustration of the perpendicular FM and AFM interface configuration, with spin canting in the first AF layer. From Ref.<sup>28</sup>.

### 2.2.6 Domain state model

Domain state (DS) model is a microscopic model developed by Nowak and coworkers<sup>29–31</sup>, in which disorders are introduced via magnetic dilution not only at the interface but also in the bulk of the antiferromagnetic layer. The main idea is that AFM has non zero magnetization due to defects through dilution. The dilution may either be related to nonmagnetic impurities or structural defects(point defects or vacancies). The AFM is considered as diluted Ising antiferromagnet in an external field (DAFF) which exhibits a phase diagram, presented in Fig. 2.2.4. In zero field, the system undergoes a Néel transition from a disordered, paramagnetic state to a long-range-ordered antiferromagnetic phase at the dilution dependent  $T_N$ . In the low temperature region, for small fields, the long-range interaction phase is stable in three dimensions. When the field is increased at low temperatures, the diluted AFM develops a domain state phase with a SG like behaviour<sup>32</sup>. The formation of the antiferromagnetic domains in the DS phase originates from the statistical imbalance of the number of impurities of the two antiferromagnetic sublattices within any finite region of the DAFF. This imbalance leads to a net magnetization which couples to the external field. A reversal of the staggered magnetization, i. e., the creation of a domain, increases the energy of the system. The necessary energy increase due to formation of a domain wall can be minimized if the domain wall passes through nonmagnetic defects at a minimum cost of exchange energy<sup>30</sup>.

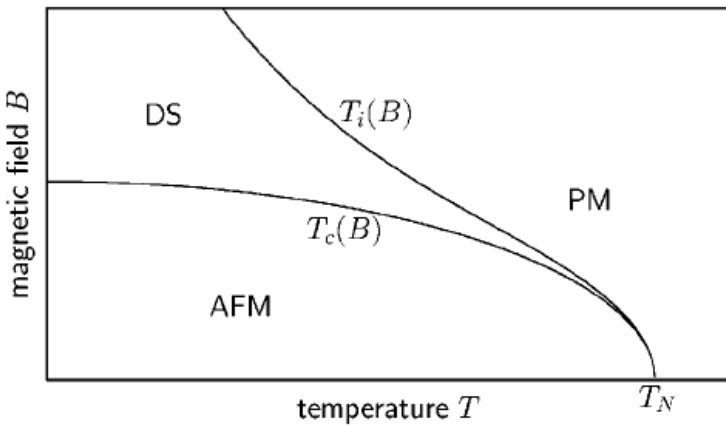


Figure 2.2.4: Schematic phase diagram of a three-dimensional DAFF (Ref.<sup>30</sup>)

The Monte Carlo simulations were performed on a model consisting of a ferromagnetic mono-layer exchange coupled to a diluted AFM. The sketch of the system

used in the simulation is shown in Fig. 2.2.5. AFM is modeled as magnetically diluted Ising system with an easy axis parallel to FM. FM is described by classical Heisenberg model with the nearest neighbour exchange constant,  $J_{FM}$ . The z-axis is considered as the easy axis of FM. The dipolar interaction is approximated by an additional anisotropy term which includes the shape anisotropy (along the x-axis). As a result of these two anisotropy directions, the magnetization is preferentially in the y-z plane. The Hamiltonian of the FM/AFM system, used in the simulations is<sup>30</sup>,

$$\begin{aligned}
 H = & -J_{FM} \sum_{\langle i,j \rangle \in FM} S_i \cdot S_j - \sum_{i \in FM} (d_z S_{iz}^2 + d_x S_{ix}^2 + \mu B \cdot S_i) - \\
 & J_{AFM} \sum_{\langle i,j \rangle \in AFM} \varepsilon_i \varepsilon_j \sigma_i \sigma_j - \sum_{i \in AFM} \mu B_z \varepsilon_i \sigma_i \\
 & -J_{INT} \sum_{\langle i \in AFM, j \in FM \rangle} \varepsilon_i \sigma_i S_{jz}
 \end{aligned} \tag{2.2.16}$$

where  $S_i$  and  $\sigma_i$  represent the spin vectors at the  $i^{th}$  site of the FM and AFM, respectively. In Eq. 2.2.16, the first two terms are related to energy contribution of the FM. Third and fourth terms describe the diluted AFM and the last term includes the exchange coupling across the interface between FM and AFM, under the assumption that the Ising spins in the top most layer of the AFM interact with the z component of the Heisenberg spins of the FM. The nearest-neighbor exchange constant  $J_{AFM}$  of the AFM is chosen to be  $J_{AFM} = -J_{FM}/2$ . The same absolute value for the coupling constant  $J_{INT}$  as for the AFM ( $J_{INT} = |J_{AFM}|$ ) are considered in the model. Assuming that all spins in the FM remain parallel during the field reversal and that some net magnetization of the interface layer of the AFM remains constant during the reversal of the FM, the estimated EB field is given by<sup>30</sup>,

$$l\mu H_{EB} = J_{INT} m_{INT} \tag{2.2.17}$$

where  $l$  is the number of ferromagnetic layers,  $m_{INT}$  is the interface magnetization of the AFM per spin. For an ideal uncompensated interface one would expect  $m_{INT}=1$ , which leads unrealistically high bias field, while for an ideal compensated interface, on the other hand, one would expect  $m_{INT}=0$  and, hence,  $H_{EB}=0$ .

However, in experiments there is often no big difference between compensated and uncompensated interfaces and on the other hand it is found that  $H_{EB}$  is much smaller than  $J_{INT}/l\mu$ . The solution of this puzzle is that  $m_{INT}$  is neither constant during field reversal nor is it a simple known quantity<sup>30</sup>. Moreover, DS model has been proved experimentally in many systems like, Co/CoO<sup>31</sup> and CoFe/IrMn<sup>33</sup>.

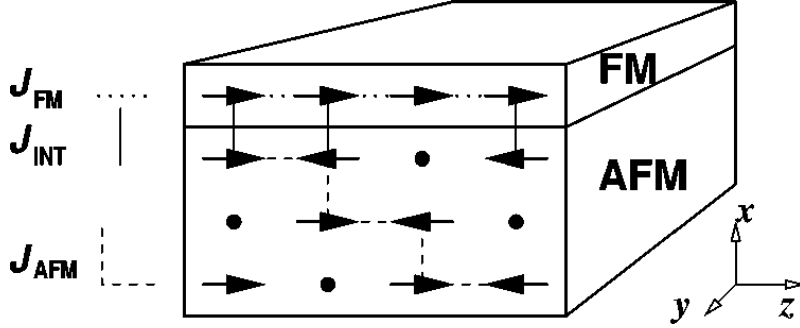


Figure 2.2.5: Sketch of the model with one FM layer and three diluted AFM layers. The dots present defects. From Ref.<sup>30</sup>.

## 2.3 Spin glass

### 2.3.1 Introduction

Spin glass (SG) is defined as a magnetic system with frustrated interactions, in which two nearby localized magnetic moments have a roughly equal probability of interacting either through a ferromagnetic interaction (in which energy is lowered by the parallel aligning of moments) or an antiferromagnetic one (energy lowered by antiparallel alignment)<sup>34</sup>. The mixture of aligned and misaligned spins create distortions or frustrated interactions, opposite to a conventional long range ordered system. The frustrated spins become frozen at a certain temperature, called the freezing temperature  $T_f$ , or denoted as  $T_{SG}$ , below which the SG phase is established. Above  $T_{SG}$ , the system is in the paramagnetic state. The SG transition is characterized by a random freezing of the moments in such a way that the long range order is absent in frozen state. The SG state is irreversible and metastable, as the magnetic spins experience random interactions with other magnetic spins. In general, the SG phase is characterized by cusp in the low field ac-susceptibility measurements at temperature  $T_{SG}$ , also it is determined by FC magnetization versus temperature,  $M(T)$  measurements<sup>35</sup>.

The SG phases are achieved in several ways. The most common way is substitution at random locations, by a very small concentration of a magnetic element, often Fe or Mn, inside a nonmagnetic metallic host, such as one of the noble metals (Cu, Ag, Au). In these diluted magnetic alloys, spins localized on the impurity atoms polarize the surrounding conduction electron gas in concentric spheres of alternating spin polarization. This leads to an indirect exchange interaction, called Ruderman-Kittel-Kasuya-Yosida (RKKY) interaction. Depending on the placement of two nearby magnetic impurities, the conduction mediated magnetic interaction can therefore be either ferromagnetic or antiferromagnetic<sup>35</sup>. CuMn, AuMn, AgMn, AuFe etc., are examples of canonical SGs, where the long range RKKY interactions are present. As the concentration of magnetic impurity increases, the probability for a magnetic impurity being the first or second nearest neighbour to another impurity also increases, resulting into a short range RKKY interaction. This situation refers to the magnetic clustering, where the magnetic behaviour is dominated by the presence of magnetic clusters, called cluster SG<sup>34</sup>. In cluster SG, the degree of randomness, the chemical inhomogeneity and solubility problems of the given alloys are critical. The magnetic properties are sensitive to the local distribution of magnetic clusters in the host matrix. The crystalline alloys like  $Cr_{1-x}Fe_x$ ,  $(Fe_{1-x})_3Al_x$  etc. and amorphous alloys such as  $(Fe_xMn_{1-x})_{75}P_{16}B_6Al_3$ ,  $(Fe_xNi_{1-x})$ -P-B-Al, are examples of cluster SGs<sup>34</sup>. The other forms of SGs, e.g., re-entrant SG (RSG), super SG (SSG) and surface SG are discussed with detail in different magnetic systems, in the next chapters.

The modern theory of SG began with the work of Edwards and Anderson<sup>36</sup>, who proposed that the essential physics of SG is not in the details of their microscopic interactions, but rather in the competition between the quenched ferromagnetic and antiferromagnetic interactions. They described the cusp in the susceptibility measurements due to SG phase. In the diluted magnetic alloy, the interaction between the spins oscillates in sign according to the distance. Rather than mean ferromagnetic or antiferromagnetic state, there will be a ground state with spins aligned in definite directions, which could be random at the critical temperature, the existence of these preferred directions affects the orientation of spins, leading to a cusp in the susceptibility. In Edwards-Anderson model, the spins arranged on a d-dimensional lattice with only nearest neighbour interactions similar to the Ising model. The Hamiltonian  $H$ , for this spin system is given by<sup>36</sup>,

$$H = -\sum_{\langle i,j \rangle} J_{ij} S_i S_j \quad (2.3.1)$$

where  $S_i$  refers to the spin at site  $i$ , the couplings  $J_{ij}$  are independent random variables chosen from a common distribution (such as Gaussian with mean zero and variance one). A negative value of  $J_{ij}$  denotes an antiferromagnetic type interaction between spins at points  $i$  and  $j$ .

### 2.3.2 Exchange bias using spin glass

According to DS model, it is clear that for diluted AFM, EB is strongly effected by the concentration of non magnetic dilution<sup>31</sup>, not at the interface, but in the volume part of AFM. At high cooling fields, DAFF develops a DS with behaves like SG<sup>32</sup>. SG is an interesting material to study because of its various dynamics. The effect of EB is observed in many SG systems, where SG phase acts as AFM. It is observed in both nanoparticles and thin films. The different forms of SGs are observed in different systems. In nanoparticles, usually the surface SG phase is the reason to generate EB field<sup>37</sup>. In diluted magnetic alloys, the most prominent SG systems exhibiting EB phenomenon are Mn based alloys, like CuMn, AgMn, NiMn<sup>8</sup>.

The EB model for spin glass, introduced by Radu and Zabel<sup>12</sup> is interesting because it uses a very simple approach to account for the interfacial frustrated spins in an AFM. The AFM layer contains two states at the ferromagnetic/antiferromagnetic interface after field cooling, i.e., frozen-in and rotatable antiferromagnetic spins. It is important to note that a SG system is characterized by its unique dynamic behaviour: A spin glass which is field cooled from above its glass transition temperature shows a remanent magnetization which is decaying on a very long time scale<sup>35</sup>. This behaviour is in contrast to other magnetic phases which show very fast dynamics when going to an equilibrium but then remain constant in this state. If the AFM in EB systems really has a kind of spin glass like interface with the ferromagnet, the spins affected should show a similar long timescale decay of their remanence. It would be very interesting to investigate the dynamics of the uncompensated rotatable moments.



# Chapter 3

## Experimental techniques

The different experimental techniques were used for the fabrication and characterization of samples. This chapter is focused on the description of the molecular beam epitaxy (MBE) system, present at the Institute of Physics II A, RWTH Aachen University. All other techniques used for the preparation and characterization of the samples discussed in this thesis are briefly mentioned at the end of the chapter.

### 3.1 Molecular beam epitaxy

MBE is a process for growing thin, epitaxial films of a wide variety of materials, such as oxides, metals and semiconductors. These films are unique due to precise control on their thickness, composition, morphology etc. In this process, beams of atoms or molecules are incident upon a substrate (crystal) that has previously been processed to produce a nearly atomically clean and smooth surface. The whole evaporation process is done in ultra high vacuum (UHV - less than  $10^{-9}$ mbar), where the beam of atoms or molecules moves in nearly collision free path. The arriving constituent atoms form a crystalline layer in registry with the substrate. The beams of atoms or molecules are formed by evaporating the material in UHV using techniques such as electron beam evaporation or effusion (Knudsen) cells. Because of the cleanliness of the growth environment and the precise control over composition, MBE structures closely approximate the idealized models used in solid state theory. The detailed information concerning the physics and the technology of MBE can be found in the comprehensive reviews of Arthur<sup>38</sup> and Finnie et al.<sup>39</sup>.

### 3.1.1 MBE chamber

The samples of magnetic thin films that have been studied in the chapters 4 and 7 of this thesis were prepared using the MBE system available at the 2nd Institute of Physics of RWTH Aachen University. The schematic drawing of the complete MBE system is shown in Fig. 3.1.1. The system is divided into 6 autonomous vacuum chambers, each equipped with vacuum pumps and pressure gauges. Two chambers namely the metal MBE chamber and HTSL (high temperature superconductor)

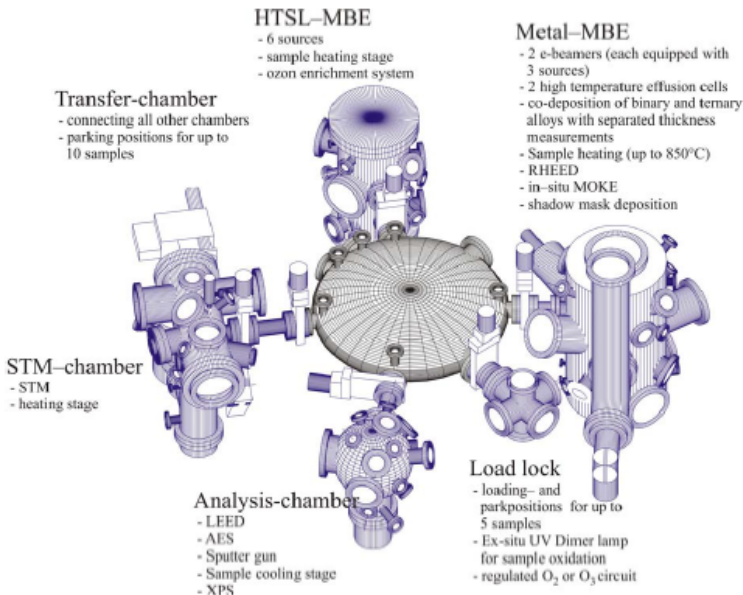


Figure 3.1.1: Schematic drawing of the multi-chamber molecular beam epitaxy (MBE) system. The chambers are marked with the respective facilities.

MBE chamber is conceived for sample preparation. For structural analysis of samples and substrates an STM (scanning tunneling microscopy) chamber and an analysis chamber are available. For sample transfer into UHV, a load-lock is attached to the system, which can serve also as an oxidation chamber. The central unit of the system is a transfer chamber, which allows in-situ transfer of samples through the entire system. In the following a description of the individual modules of the system is given. The description is focused only on some experimental details concerning the MBE system. The HTSL-MBE chamber was not used for sample preparation and therefore would not be discussed in the following.

### 3.1.2 Metal MBE chamber

The metal MBE chamber was the most important chamber of the MBE system for the purpose of sample preparation containing metallic thin films. All the exchange biased thin film samples studied in this thesis (see chapters 4 and 7) were deposited in this chamber. In addition to the deposition of metals, the MBE system is also used for the evaporation of oxides. The metal MBE chamber can be divided in two chambers, the source chamber (lower part) and the substrate chamber (upper part). The actual MBE chamber has been redesigned. A shielding plate separating the beams of constituent atoms of different materials is placed in front of the valve. Therefore, the valve which separates the two parts of the chamber must be always open. This is shown later in Fig. 3.1.4. The schematic top-view of source chamber is shown in Fig. 3.1.2. The evacuation of this chamber is performed by different types of pumps containing a turbomolecular pump, an ion getter pump, a Titanium sublimation pump, a helium cryopump and two liquid nitrogen cryopumps. The source chamber is divided into five partial segments separated by shields in order to achieve thermal isolation of the individual source installed in these segments. The largest partial segment is equipped with a dual electron beam evaporator from Thermionics company (Model: 100-1030).

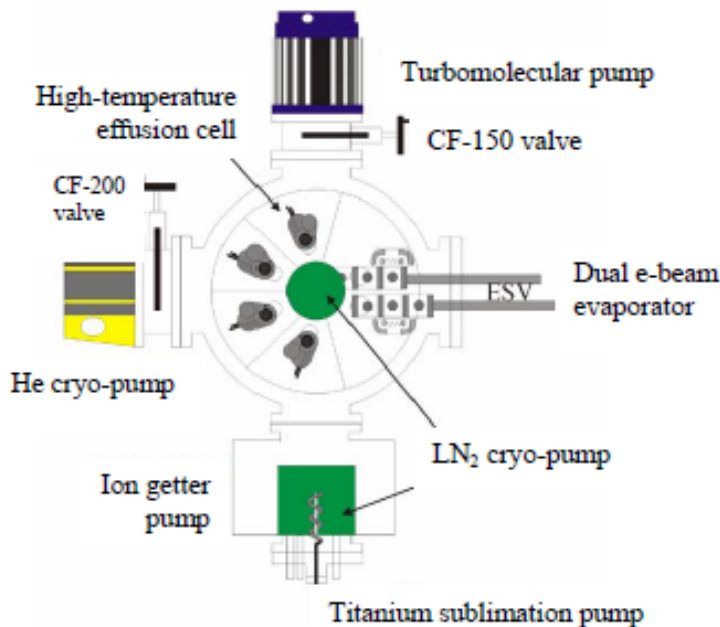


Figure 3.1.2: Schematic-top view of the source chamber.

A picture of the dual electron beam evaporator is shown in Fig. 3.1.3. The metals for evaporation are placed inside of crucibles. Each crucible can contain approximately 2.5 cc of the source material. The dual electron beam evaporator has one filament for each half containing three sources. Hence, it allows simultaneous evaporation of two metals. In total, six materials can be accommodated in the dual electron beam evaporator. The electron beam is emitted from tungsten filament under high voltage (max. 10 kV, 6 A), which is accelerated by a positive voltage and focused by magnetic fields to heat the material placed in front of the filament. The beam strikes the evaporant material with a spot of 1/8 th cm of diameter and an intensity of 25 kW/cm<sup>2</sup>. As a result, the metal is heated locally at temperatures up to 3000 °C. These temperatures allow evaporation of most metals. The beam deflection and effective shielding keeps the filament hidden from the evaporant vapor. During the evaporation, the system is cooled through a continuous flux of water through the cooling pipes. The rate of evaporation depends upon many factors such as power input, charge size and charge shape. However, the thermal conductivity and evaporation temperature of the material for evaporation are also important factors which influence the deposition parameter.

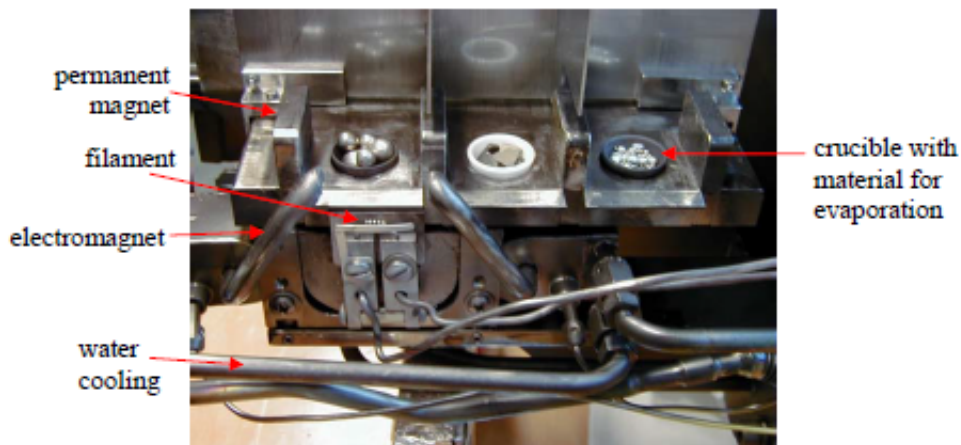


Figure 3.1.3: Photograph of the electron beam evaporator showing a sole electron gun.

The other four segments of the source chamber can accommodate four Knudsen cells. They are used for evaporation of metals and enable very stable evaporation rates. In principle an effusion cell has a crucible which contains the metal for evaporation and a filament surrounding the crucible. The electrons emitted by the filament heat

homogeneously the crucible and the material. A precise feedback loop between the temperature controller and the power supply of the filament can regulate very stable temperatures and therefore very stable evaporation rates. The two standard high temperature effusion cells (Model EPI-95-2455) are installed in our MBE system. The maximum temperature which can be reached with the Knudsen cells installed in the metal MBE chamber is about 2000 °C, allowing evaporation of a whole range of metals such as Cu, Au, Fe, Co, Ni, etc. The oxides are also deposited through the electron beam evaporator, such as MgO was deposited to use as tunnel barrier between graphene and ferromagnet layer.

Some time the samples containing ternary alloys, are deposited. For their preparation a Knudsen cell and the dual electron beam evaporator were simultaneously used. In order to control the deposition rate of each material individually during the deposition of the ternary alloys a LABVIEW program was used, which controls the whole deposition process. The substrate chamber is the upper part of the metal MBE chamber. A schematic front view of the substrate chamber is shown in Fig. 3.1.4. The evacuation of this chamber is performed by a turbomolecular pump, an ion getter pump and a  $LN_2$  cryopump. The substrate chamber contains three quartz sensors for measuring the deposition rates of three different materials, a sample manipulator and the poles of an electromagnet. The substrate is mounted on especially designed sample holder made of molybdenum material. The sample manipulator contains a filament which allows heating of substrates at temperatures up to 850 °C in order to degas water and other impurities (elements such as C) from their surface. The sample manipulator allows horizontal and vertical rotation of samples, as for instance from the loading position (position 1 in Fig. 3.1.4) to the deposition position (position 2 in Fig. 3.1.4). During deposition, the sample can be placed between the poles of an electromagnet (see Fig. 3.1.5) to deposit the magnetic material on substrate in the presence of a magnetic field. This favours the appearance of an uniaxial anisotropy in the magnetic thin films during deposition. When the sample is in the deposition position, an automatically controlled shutter can be placed in front of the sample (see Fig. 3.1.5). In this way one can avoid deposition on the substrate until the evaporation rates for binary or ternary alloys become constant. The dual sensor box containing two quartz sensors and the third quartz sensor for the thickness measurements of the deposited thin films, are shown in Fig. 3.1.5.

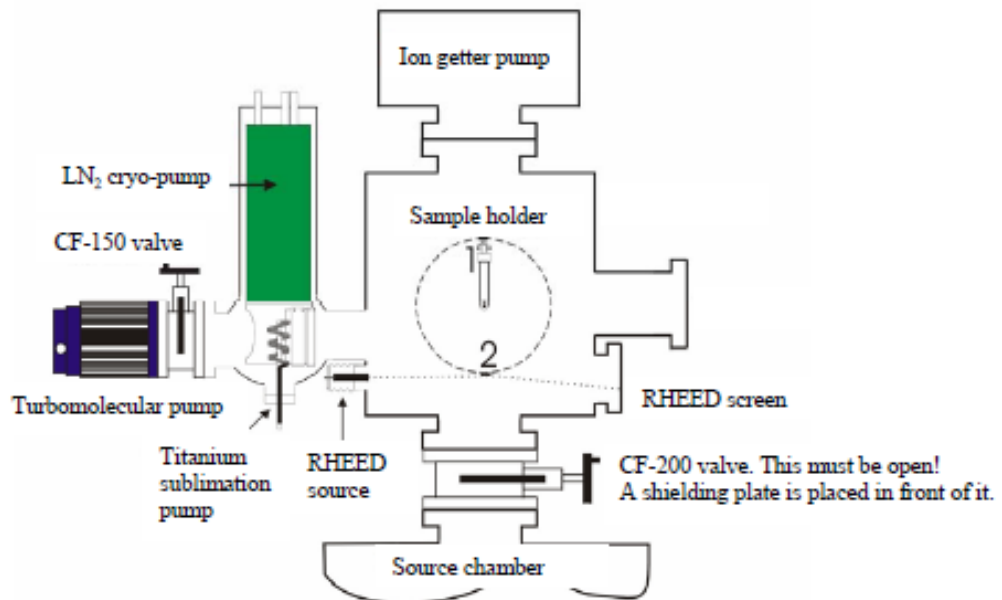


Figure 3.1.4: The schematic front-view of the substrate chamber of MBE system.

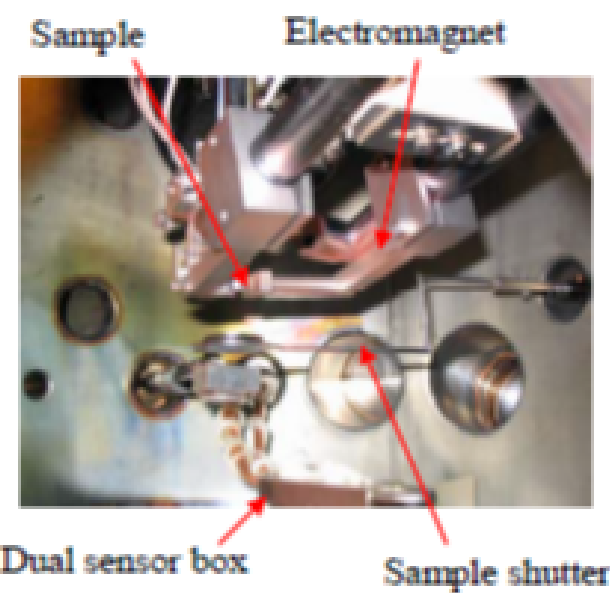


Figure 3.1.5: Internal view of the substrate chamber, showing quartz sensors and electromagnet. The sample is aligned between the magnetic poles.

### 3.1.3 Analysis chamber

The analysis chamber is used to in-situ investigate the surface characterization of the samples and the substrates. It contains the following experimental techniques: LEED (Low Energy Electron Diffraction), AES (Auger Electron Spectroscopy) and XPS (X-ray Photoelectron Spectroscopy). These techniques are essential for the MBE system. Additionally, a sputter gun, an electron gun, a scintillator and a spherical energy analyzer are connected to the analysis chamber. Fig. 3.1.6 shows the picture of the analysis chamber.

LEED enables investigation of the surface crystallographic structure of the samples. The surface of a sample is bombarded with low energy electrons (approx. 20-200 eV). The diffracted electrons are observed as spots on a phosphorescent screen. The relative position of the spots on the screen is correlated with the crystallographic structure of the surface. The diffracted spots will move as the energy of the incident electrons changes and the intensity of the spots as a function of incident electron energy reveals information about surface reconstructions.

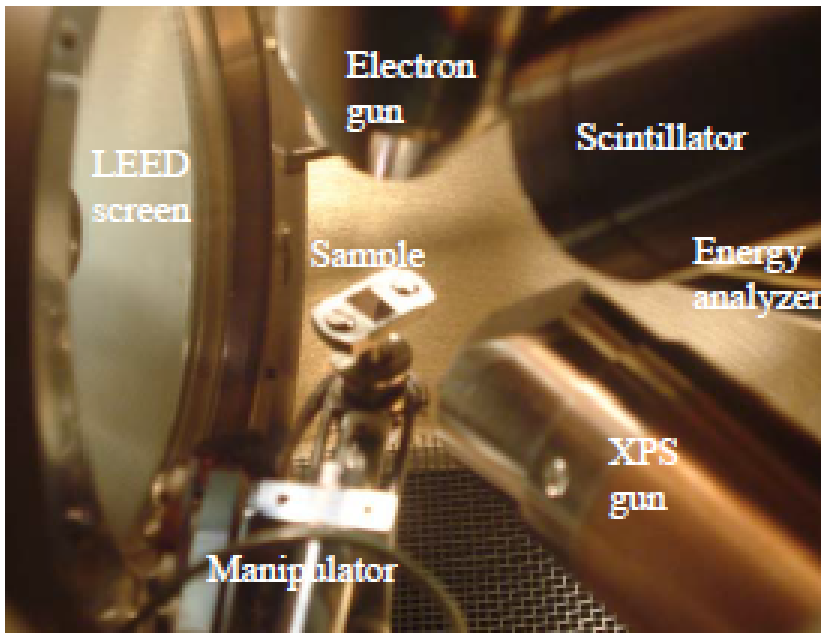


Figure 3.1.6: Photograph showing internal view of analysis chamber.

AES is a surface specific technique which uses the emission of low energy electrons in an Auger process. It is one of the most commonly employed surface analytical techniques for determining the chemical composition of the surface layers of a sample.

When an electron is ejected from an inner shell of an atom, the resultant vacancy can be filled by a radiative (x-ray) or non-radiative (Auger) process. The electron gun emits focused electrons which are incident on the sample. The emitted (Auger) electrons are deflected into the energy analyzer (see Fig. 3.1.6). An element specific kinetic energy distribution of the Auger electrons is then recorded.

The XPS technique is based on the photoelectric effect. It gives information about the composition and electronic state of the surface region of a sample. Within the photoelectric effect, a photon is absorbed by an atom in a solid, leading to ionization and the emission of a core (inner shell) electron. The kinetic energy distribution of the emitted photoelectrons can be measured using an energy analyzer and a photo-electron spectrum can thus be recorded. Each element has a characteristic binding energy associated with each core atomic orbital. In other words, each element will give rise to a characteristic set of peaks in the photoelectron spectrum at kinetic energies determined by the photon energy and the respective binding energies. For XPS, Al K $\alpha$  (1486.6 eV) or Mg K $\alpha$  (1253.6 eV) are the photon energies of choice.

The sputter gun can be used for ionizing Ar gas which is then sputtered on different substrates with the purpose of cleaning.

### 3.1.4 Load lock chamber

The load lock chamber is attached to the system for loading and unloading samples into MBE system. The load lock chamber is equipped with only one turbomolecular pump and it therefore operates at high vacuum ( $10^{-7}$ mbar). However, the relatively small volume of this chamber allows quick purging of prior to open the valve to transfer chamber for sample transport. The load lock chamber does not require bake-out due to the fact that the chamber is vented each time when loading or unloading the samples. The load lock chamber can also serve as an oxidation chamber for thin films.

### 3.1.5 Transfer chamber

The transfer chamber is the central part of the MBE system that connects all other chambers. The transferring of the sample from one chamber to other is done through this chamber. The transfer chamber contains a telescope arm which can be rotated

360° with stopping positions in the front of each chamber of the system. Additionally, the telescope arm can be elongated into each chamber while fixed in one of the stopping positions. The transfer chamber is equipped only with an ion getter pump. Therefore, it is the only chamber, which cannot be independently evacuated. In order to vent the transfer chamber, one needs to vent another chamber simultaneously. For the purging of the transfer chamber one can use the turbomolecular pump of the load lock chamber while pumping down both chambers simultaneously. This chamber also contains parking positions to store the samples in UHV.

## 3.2 Other experimental techniques

Various other experimental techniques have been used for preparation, structural and magnetic characterization of the samples. These techniques are,

- Sputtering technique for the deposition of thin films.
- Superconducting Quantum Interference Device (SQUID) magnetometer.
- Optical lithography and clean room facilities for preparing nanostructures.
- Transmission electron microscopy (TEM).
- Focused ion beam (FIB) milling, to fabricate nano-holes.
- X-ray diffractometer.
- Polar-magneto-optical Kerr-effect (p-MOKE).
- Atomic force microscopy (AFM).
- Scanning electron microscopy (SEM).



# Chapter 4

## The study of exchange bias, spin structure , spin re-orientation transitions and anomalous anisotropy in CoPd/IrMn system

This chapter describes the detailed study of perpendicular anisotropy in CoPd alloy and exchange bias (EB) in CoPd/IrMn bilayer. It relates the perpendicular anisotropy of CoPd alloy with the observed perpendicular EB as a function of thickness of the CoPd alloy. The strong effect of spin structure of IrMn on EB is observed during the study of EB along in-plane and out-of-plane directions. Spin re-orientation transition is depicted in CoPd alloy, that does not affect the EB phenomenon in the bilayer. The most exciting part is the anomalous behaviour of perpendicular anisotropy of CoPd/IrMn as function of thickness of CoPd alloy. Moreover, according to the careful literature survey, it is the first time that the EB is reported in pure CoPd alloy and the effect of spin structure transition of IrMn is observed through the behaviour of in-plane and out-of-plane EB field.

### 4.1 Introduction

The investigation of perpendicular magnetic anisotropy is highly demanded due to its application in the higher density, higher speed and extremely low-dimensional based spintronics devices. The perpendicular anisotropy is observed and studied in

both the multilayers and the alloys of the different systems like CoPd, CoPt, FePt, FePd. Among them, ferromagnetic CoPd alloy films attract wide attentions for the application of high density magnetic and magneto-optical recording media, due to their ease of fabrication and having strong perpendicular magnetic anisotropy without requiring annealing.

## 4.2 Sample preparation and structural characterization

The different series of CoPd alloy and CoPd/IrMn exchange biased samples were grown by molecular beam epitaxy technique on the Si(100) substrate with 300 nm thermal oxide layer of  $\text{SiO}_2$ . In order to remove the water vapours and the other contamination, the substrates were degassed in ultra high vacuum (UHV) at 150°C for half an hour before deposition. The thin film materials were deposited at room temperature without applying any magnetic field. The base pressure before deposition was below  $5 \times 10^{-10}$  mbar. The series of the samples containing sole ferromagnet (FM), has the sequence Si/ $\text{SiO}_2$ /Pd(10 nm)/Co<sub>27</sub>Pd<sub>73</sub>(x nm)/Pd(4 nm), where x=8 nm, 16 nm, 30 nm. The exchange biased samples were grown using different thicknesses of CoPd alloy as FM with fixed thickness of IrMn alloy as an antiferromagnet (AFM). Si/ $\text{SiO}_2$ /Pd(10 nm)/Co<sub>27</sub>Pd<sub>73</sub>(x nm)/Ir<sub>23</sub>Mn<sub>77</sub>(15 nm)/Pd(4 nm) is the layer sequence of the exchange biased samples, where x= 8 nm, 12 nm, 16 nm, 30 nm. The top Pd(4 nm) layer is used as capping layer to avoid oxidation, while the bottom Pd(10 nm) is used as buffer layer to prevent Co from intermixing with oxygen due to the presence of  $\text{SiO}_2$  on the substrate. The Pd(10 nm) under layer also acts as a seed layer to induce the (111) texture in CoPd. The concentration of Co is 27% in CoPd alloy and Ir is 23% in IrMn alloy in all samples. The CoPd alloy has the strongest perpendicular anisotropy at around 30% Co concentration<sup>40</sup> and IrMn<sub>3</sub> has highest Néel temperature ( $T_N$ ) and giant magnetic anisotropy as compared to other concentrations<sup>41;42</sup>. The selected percentage composition of Co and Ir in the samples is very close to these values. The schematic representation of the layer sequence of the ferromagnetic samples and the exchange biased samples are shown in Fig. 4.2.1.

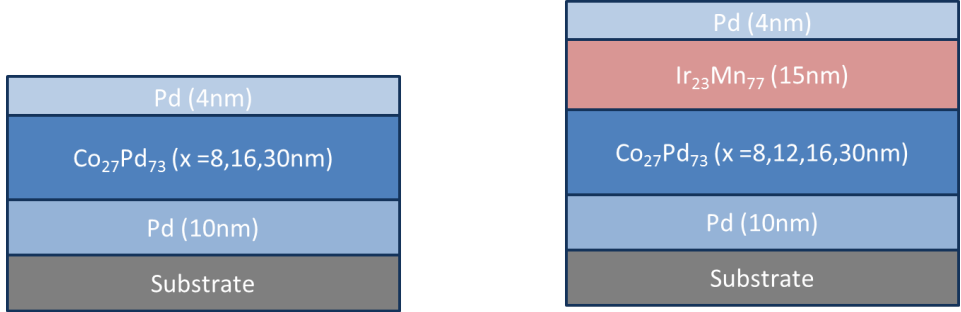
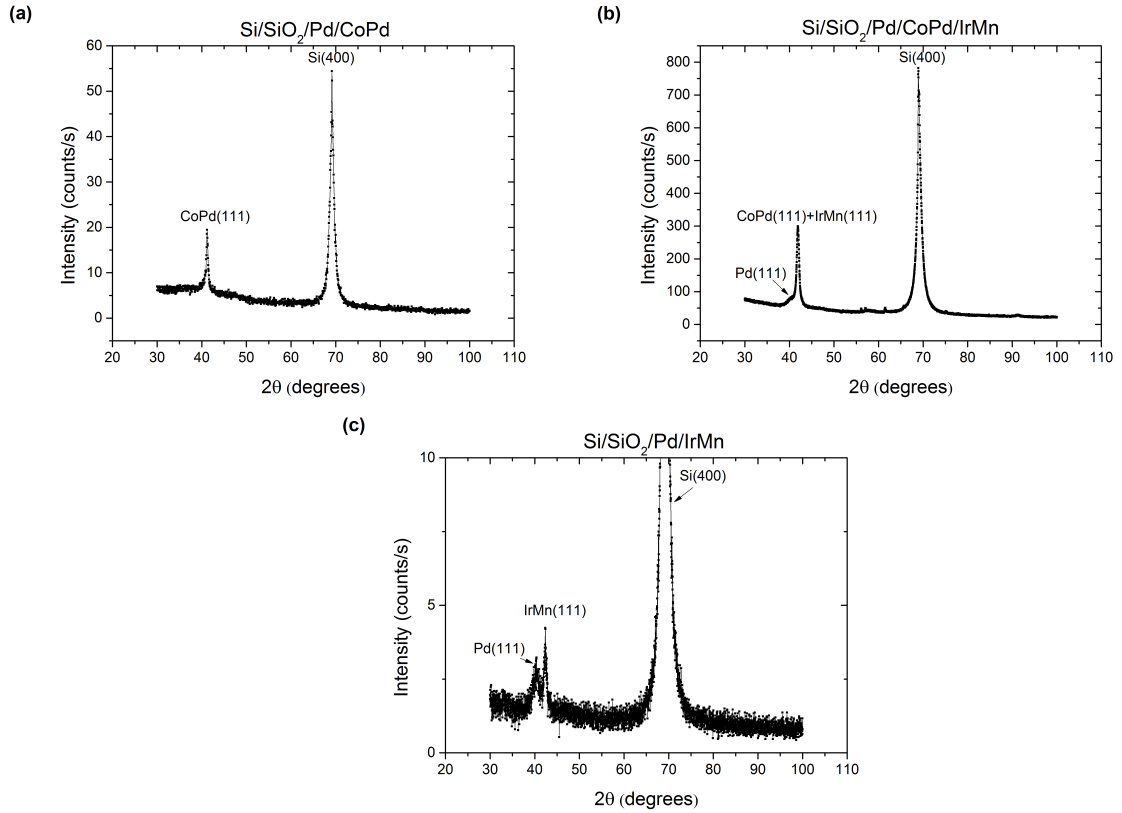


Figure 4.2.1: Schematic representation of sole CoPd and exchange biased samples.

The x-ray diffraction measurement of the sole CoPd sample with layer sequence  $\text{Si}/\text{SiO}_2/\text{Pd}(10 \text{ nm})/\text{Co}_{27}\text{Pd}_{73}(40 \text{ nm})$  is shown in the Fig. 4.2.2(a), which clearly indicate the presence of the (111) texture in CoPd alloy<sup>43</sup>.


 Figure 4.2.2: X-ray diffraction,  $\theta - 2\theta$  scans of (a)  $\text{Si}/\text{SiO}_2/\text{Pd}/\text{CoPd}$ , (b)  $\text{Si}/\text{SiO}_2/\text{Pd}/\text{CoPd}/\text{IrMn}$  and (c)  $\text{Si}/\text{SiO}_2/\text{Pd}/\text{IrMn}$  samples.

The x-ray diffraction pattern of the exchange biased sample having layer sequence of  $\text{Si}/\text{SiO}_2/\text{Pd}(10 \text{ nm})/\text{Co}_{27}\text{Pd}_{73}(30 \text{ nm})/\text{Ir}_{23}\text{Mn}_{77}(15 \text{ nm})$  is presented in Fig. 4.2.2(b).

This indicates (111) texture in both IrMn<sup>44</sup> and CoPd layers of the sample. In the x-ray diffraction pattern, the peaks of IrMn and CoPd layers are not distant since the  $2\theta$  values of both of these samples for (111) texture have very small difference. The presence of Pd(111) is also indicated at  $2\theta = 40.4$ , verifying that the Pd seed layer helps to induce (111) texture in the above deposited layers. The x-ray diffraction measurement was also done for the sole IrMn sample with layer sequence Si/SiO<sub>2</sub>/Pd(10 nm)/Ir<sub>23</sub>Mn<sub>77</sub>(30 nm) where the Pd and IrMn layers have (111) texture, as evident from the measurement in Fig. 4.2.2(c).

### 4.3 Measurement procedure

The magnetic measurements of all these samples were performed in a Superconducting Quantum Interference Device (SQUID) magnetometer called as Magnetic Property Measurement System (MPMS) XL7 from Quantum Design. As mentioned in section 4.2, all samples were deposited in the absence of a magnetic field. The  $T_N$  of IrMn is very high, i.e., around 730 K for  $\gamma$ -phase IrMn<sub>3</sub> bulk alloy<sup>41</sup>. Therefore, to initialize the exchange bias (EB) of the samples where the AFM has a blocking temperature ( $T_B$ ) above the room temperature, annealing was done in the presence of external magnetic field. The bilayers, i.e., FM/AFM were annealed at 475 K in an external magnetic field of 10 kOe for 1 hour and then the temperature was decreased from 475 K to 300 K in the presence of an applied field. The external magnetic field was applied along the perpendicular direction of the samples in order to enhance the perpendicular EB. In order to avoid any oxidation, the annealing and field cooling were done in vacuum. The sole CoPd and the exchange biased samples, were measured in SQUID magnetometer along the in-plane (IP) and out-of-plane (OP) directions. It should be noted that there is no preferential direction for magnetic field along IP direction. In order to study the EB effect, the samples containing FM/AFM bilayers were further field cooled (FC) along the IP and OP directions from 350 K to 5 K before the measurements in SQUID. The measurements of magnetization versus field loops (MH-loops) were initialized from 5 K temperature, and then was increased in steps to the required temperature subsequently. Prior to the measurements, an additional hysteresis loop was obtained at 5 K, in order to reduce the training effect. The exchange bias field ( $H_{EB}$ ) and coercive field ( $H_C$ ) are determined from the left and right coercive fields ( $H_C^{Left}$ ,  $H_C^{Right}$ ) of hysteresis loop, where  $H_{EB}=(H_C^{Left}+H_C^{Right})/2$  and  $H_C=-(H_C^{Left}-H_C^{Right})/2$ .  $H_{EB}$  gives

difference, while  $H_C$  is the average of  $H_C^{Left}$  and  $H_C^{Right}$ .

The SQUID magnetometer (MPMS - XL7) is highly sensitive to measure the small magnetic moment (m), its sensitivity is around  $1 \times 10^{-8}$  emu (for 0 to 250 mT field) and  $6 \times 10^{-7}$  emu (for field up to 7T). To maintain the high performance of the SQUID magnetometer, the system was calibrated according to instructions provided, using given palladium as reference sample. The field uniformity is 0.01% over 4 cm size which is quite stable in the present samples having maximum size of 0.5 x 1 cm. The typical residual or remnant field ranges from 2 Oe to 6 Oe depending on the applied field. In order to reduce the noise and background signal, different steps were used during measurements. The “Magnet Reset” option was used prior to each measurement to remove the trapped magnetic flux from superconducting magnet. At each data point, at least 3 scans were done during measurement in magnetometer to increase the accuracy. In order to remove the background signal, the empty substrate measurement was subtracted to get the magnetic response of the samples.

Fig. 4.3.1 shows the diamagnetic behaviour of Si/SiO<sub>2</sub> substrate and magnetic moment of sole CoPd (30 nm) sample. Error bars are applied to highlight the uncertainty in the data. It is found that the measured magnetic moment of CoPd/IrMn samples are in the the order of  $10^{-5}$  emu and  $10^{-4}$  emu for remnant (IP - loops) and saturated state (or at higher fields), respectively. The measured magnetic moment is 100 to 1000 times higher than the sensitivity of the MPMS, decreasing the background moment. Therefore, the remnant field, distribution of data points and strength of signal are more important factors for determining error bars. In CoPd/IrMn samples, the MH-loops along IP direction have small distribution of data points as compared to OP measurements causing decrease in the uncertainty. The typical remnant field of 4 Oe is used in most cases, as  $H_{EB}$  is determined from the subtraction of coercive fields including same remnant (residual) field from magnetometer so the effect is cancelled as compared to  $H_C$ , which is determined from the averaging of fields. The error in  $H_{EB}$  for CoPd/IrMn samples ranges from  $\pm 10$  to  $\pm 4$  Oe (usually  $\pm 6$  to  $\pm 4$  Oe in most cases) in Fig. 4.5.2 and Fig. 4.5.10. The uncertainty in the  $H_{EB}$  is calculated by adding errors due to differences in distribution of data points (having error ranges from  $\pm 6$  to  $\pm 2.5$  Oe) and background signal of substrate (having error ranges from  $\pm 4$  to  $\pm 1.5$  Oe) at  $H_C^{Left}$  and  $H_C^{Right}$ . The background signal from substrate produces an offset in the values of  $H_C^{Left}$  and  $H_C^{Right}$  in the range of 4 to 1.5 Oe for CoPd/IrMn samples.

It is noteworthy that due to different scales in the graph, the size of error bars

change. It is also found that the measured nanoparticles have strong magnetic moment, better distribution of data points and weak background moment than thin films. The magnetic moment of hematite nanoparticles (discussed in chapter 5) is in the range of  $10^{-3}$ emu to  $10^{-2}$ emu and  $Co_{1-x}Mg_xFe_2O_4$  nanoparticles (discussed in chapter 6) have magnetic moment of the order of  $10^{-1}$  emu. The strong and stable magnetic signal of nanoparticles reduces the effect of uncertainty as maximum background moment from teflon capsule of the order of  $1\times 10^{-4}$ emu has very weak effect (see Fig. 5.3.1(a)). In nanoparticles, the error ranges from  $\pm 1.5$  to  $\pm 5$  Oe for  $H_{EB}$ (error due to distribution of data points+offset due to background signal of capsule/sample holder) and  $\pm 4$  to  $\pm 9$  Oe for  $H_C$ (error due to distribution of data points+offset due to background signal+residual field). The increase in the error of  $H_C$  is due to the addition of remnant (residual) field of 3 to 4 Oe. The measurements of  $H_{EB}$  and  $H_C$  are shown in Figs. 5.3.2, 5.3.8, 5.4.6, 5.5.3 and 5.6.2 (for hematite nanoparticles), while in Figs. 6.3.1, 6.3.3, 6.3.4 and 6.4.1 for  $Co_{1-x}Mg_xFe_2O_4$  nanoparticles. The uncertainty in  $H_{EB}$  and  $H_C$  of Fe/Cr system (discussed in chapter 7) ranges from  $\pm 1.5$  to  $\pm 3.5$  Oe.

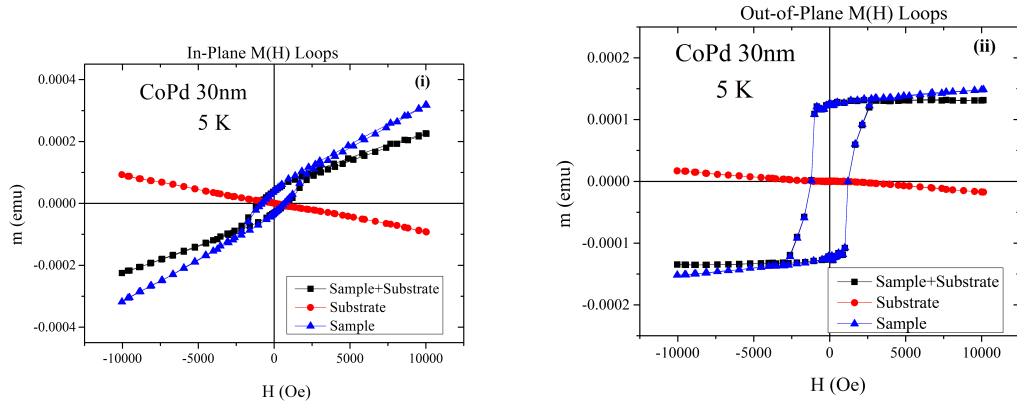


Figure 4.3.1: Hysteresis loops of  $Si/SiO_2$  substrate and CoPd sample of 30 nm thickness at 5 K along in-plane (IP) (i) and out-of-plane (OP) (ii) directions.

## 4.4 Perpendicular anisotropy in CoPd alloy

The perpendicular magnetic anisotropy (PMA) is found and studied in both multilayers and alloys of different systems. Co/Pt, Co/Pd multilayers are some of the common systems which are extensively used to produce perpendicular anisotropy<sup>45</sup>. It has been found that the process conditions effect PMA, it is shown that perpendic-

ular anisotropy of Co/Pt multilayers is less than  $2.5 \times 10^{-6}$  erg/cm<sup>3</sup>, while for Co/Pd it is increased to  $3.5 \times 10^{-6}$  erg/cm<sup>3</sup> by changing sputtering gas (argon) pressure during deposition<sup>45</sup>. The CoPt and CoPd alloys also exhibit PMA, where magnetic anisotropy of CoPt alloy is around  $4 \times 10^{-6}$  erg/cm<sup>3</sup> at elevated temperature and CoPd has above  $3.5 \times 10^{-6}$  erg/cm<sup>3</sup><sup>46</sup>. In another study<sup>47</sup>, it is reported that the magnetostriction constant  $\lambda_{111}$  of CoPd alloy is larger as compared to CoPt alloy, Co/Pd and Co/Pt multilayers indicating higher magnetic anisotropy in CoPd alloy. The PMA in both multilayers and alloys, has been studied as a function of thickness, preparation conditions, microstructures and alloy composition. The alloys are preferred to use because they are easy to fabricate and they exhibit strong PMA as compared to multilayers. It is reported in CoPt and CoPd alloys that they have a stronger PMA, high remanence and coercivity as compared to their multilayer systems<sup>46;48-51</sup>. For the CoPt alloy, the elevated substrate temperature is required during the film growth to get large PMA<sup>48;52</sup>, while the CoPd alloy evaporated at room temperature has large PMA<sup>40;49</sup>. Consequently, growth temperature and annealing are not required conditions to get large PMA. Therefore, the CoPd alloy is a strong candidate for the perpendicular magnetic data storage device, as it has a large perpendicular anisotropy that is easy to establish.

There are two main types of ordered alloys of CoPd,  $L1_0$  and  $L1_2$ , depending upon the ratio of the Co and Pd concentrations. The  $L1_0$  is CuAu(I) type tetragonal structure, while  $L1_2$  is Cu<sub>3</sub>Au type and has fcc structure, which is found in  $A_3B$ -type binary alloys<sup>53</sup>.

#### 4.4.1 Magnetic measurements of CoPd samples

The magnetic characterizations of sole CoPd samples are carried out under different conditions of temperatures and fields. The samples were cooled down to 5 K and the measurements were taken during heating.

For sole CoPd samples, Si/SiO<sub>2</sub>/Pd(10 nm)/Co<sub>27</sub>Pd<sub>73</sub>(x nm)/Pd(4 nm) is the layer sequence, where x=8 nm, 16 nm and 30 nm. Fig. 4.4.1 presents the IP and OP MH-loops of the CoPd samples at different temperatures showing that it is easy for the magnetization of CoPd alloy of the given Co concentration to orient along the OP instead of the IP direction.

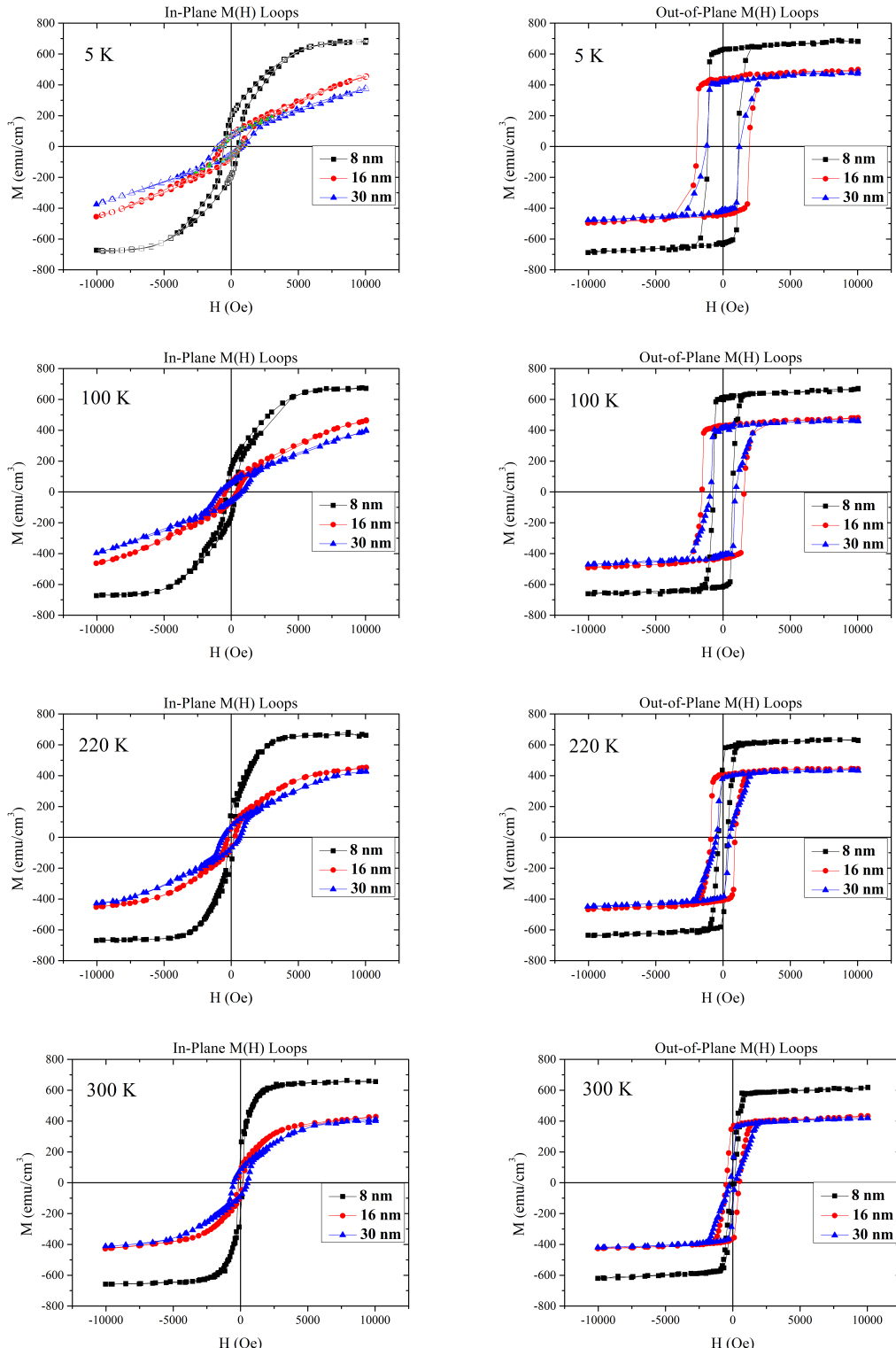


Figure 4.4.1: Hysteresis loops of CoPd sample of 8 nm, 16 nm and 30 nm thickness at different temperatures along in-plane (IP) and out-of-plane (OP) directions.

For the MH-loops along the IP direction, it is observed that the spins do not align easily along the IP direction, especially at low temperatures and the shape of the loops show hard axis behaviour. The OP MH-loops show that the spins of CoPd alloy are easily aligned along the perpendicular direction indicating clear easy axis loops. Therefore these samples of CoPd alloy have perpendicular anisotropy for the given thicknesses. From the study of MH-loops, it is also observed that the perpendicular anisotropy in CoPd alloy is not only dependent upon the temperature but also depends on the thickness of the CoPd alloy. The quantitative study of perpendicular anisotropy of CoPd alloy is done in section 4.4.4, where it is cleared that perpendicular anisotropy increases with increasing the thickness of CoPd alloy and decreases with increase in the temperature.

#### 4.4.2 Reasons of the perpendicular anisotropy

The reason of perpendicular anisotropy in the CoPd alloy is not well understood because of the limited direct structural information and the lack of experimental/theoretical studies. In the Co/Pd multilayers, the multiple reasons of the perpendicular anisotropy are the broken symmetry of Co atoms at the Co/Pd interface<sup>54</sup>, stress at the interface and partial atomic ordering<sup>55</sup>. However there are two main phenomena explaining the perpendicular anisotropy in the CoPd alloy.

##### a) Magnetostriiction

CoPd alloy is known to have large magnetostriiction coefficient. S. Hashimoto et al.<sup>40</sup> related the perpendicular anisotropy in sputtered CoPd alloy thin films to the magnetostriuctive effect. The CoPd alloy has large negative magnetostriiction constant  $\lambda$ , of the order of  $10^{-4}$ , in a Pd-rich composition. It is found that the value of a negative  $\lambda$  and the perpendicular magnetic anisotropy energy  $K_u$ , both increase with increase in the Pd concentration and attain a peak around 70% Pd, showing the correlation between the perpendicular anisotropy and magnetostriiction. Also the stress-induced anisotropy  $K_u^{\lambda\sigma} = (3/2)\lambda\sigma$ , which is obtained from the measured  $\lambda$  and film stress  $\sigma$ , behaves similar to the experimentally measured  $K_u$  as a function of Pd concentration and Ar gas pressure during deposition. Therefore, the

perpendicular anisotropy in the CoPd alloy is due to the stress-induced anisotropy which is caused by the coupling of magnetostriction and film stress.

H. Takahashi et al.<sup>47</sup> measured magnetostriction constants  $\lambda_{100}$  and  $\lambda_{111}$  in the (111) oriented polycrystalline CoPd alloy and multilayered films. The magnetostriction constants are estimated from the magnetic anisotropy induced by the application of in-plane uniaxial strain. In CoPd alloy, the estimated magnetostriction constants agree well with those of CoPd single-crystal alloys. It is observed that  $\lambda_{111}$  is negative over the entire range of composition and of the order of  $10^{-4}$ , having maximum value around 70% Pd, so it follows the same behaviour which is also reported by Hashimoto et al.<sup>40</sup>. On the other hand  $\lambda_{100}$  is negative in Pd-rich region and becomes positive in Co-rich region<sup>56</sup>.

In more detail, Kim et al.<sup>49</sup> did polarized extended x-ray absorption fine structure (EXAFS) study of the (111)-textured polycrystalline CoPd alloy. The different Co-Co correlations along parallel and perpendicular orientations w.r.t. the film plane and the enhancement in the strain anisotropy due to the Pd underlayer are the reasons of the perpendicular anisotropy in CoPd alloy.

### b) LS-Coupling

Spin-orbit coupling is an important source to induce anisotropy. The enhanced orbital moment in Co/Pd multilayers is experimentally proved as compared to bulk Co, that is a reason of perpendicular anisotropy<sup>57</sup>. C. Boeglin et al.<sup>58</sup> discussed the role of spin-orbit coupling in the CoPd thin films.

#### 4.4.3 Discussion

In the magnetic measurements, the magnetic moment of the thin films is divided by the volume of the CoPd alloy only, so the volume contains the contribution of Pd contents in the CoPd alloy, as depicted in the hysteresis loops of sole CoPd alloy in Fig. 4.4.1. If the magnetic moment is only normalized by the Co volume, the magnetization is greater than the bulk magnetization of Co, e.g., the saturation magnetization of CoPd (30 nm) per unit volume of Co only, is 1820 emu/cm<sup>3</sup>, which is even greater than the bulk Co value (1422 emu/cm<sup>3</sup>)<sup>59</sup>. On the other hand, Pd is paramagnetic and its magnetization is very small as compared to Co (around 0.619 emu/cm<sup>3</sup> measured from Pd reference sample used for SQUID). The reason of

this increase in the magnetization of CoPd alloy per unit volume of Co as compared to bulk Co value is related to the polarization of Pd atoms present near the Co atoms. The reason for the polarization of Pd atoms is the exchange interaction between the 3d-4d electrons of Co and Pd atoms, respectively<sup>60;61</sup>.

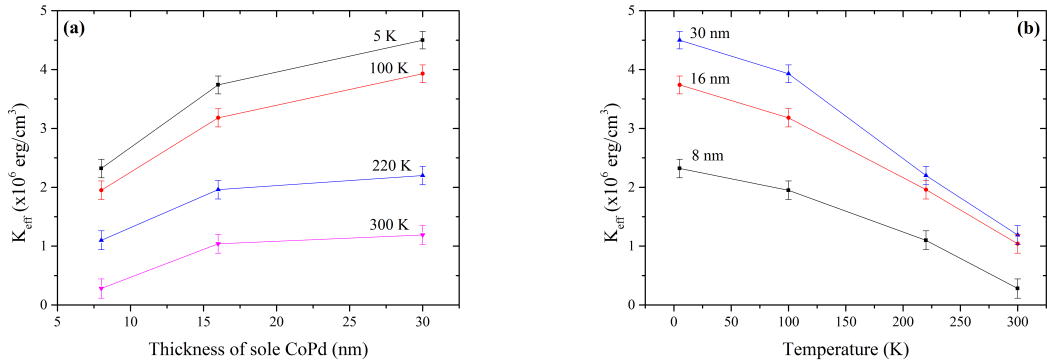


Figure 4.4.2: (a) Effective magnetic anisotropy,  $K_{eff}$  as a function of film thickness of CoPd layer at different temperatures. (b) Temperature dependence of  $K_{eff}$  for different thicknesses of CoPd layer.

The effective magnetic anisotropy energy  $K_{eff}$  depends upon volume anisotropy ( $K_V$ ) and interface anisotropy ( $K_S$ ) and can be defined as<sup>62</sup>,

$$K_{eff} = K_V + 2K_S/t \quad (4.4.1)$$

where “t” is the thickness of the magnetic layer.  $K_{eff}$  of the CoPd alloy is determined from the area enclosed between the IP and OP hysteresis loops<sup>62;63</sup> and is presented in Fig. 4.4.2. The M(H) loops are measured in 3T field, that is high enough for the saturation of IP hysteresis loops. The positive value of  $K_{eff}$  indicates that the direction of the magnetization is oriented perpendicular to the plane<sup>62;64</sup>.

The behaviour of  $K_{eff}$  as a function of the thickness of CoPd alloy at different temperatures is presented in Fig. 4.4.2(a), which shows that the  $K_{eff}$  increases with the thickness of CoPd alloy. The perpendicular anisotropy as a function of the thickness of the CoPd layer is reported in Ref.<sup>40;65</sup>, where it is increased with thickness up to some extent and then decreases with increasing the thickness of CoPd layer. This is related to the tensile stress of CoPd alloy which shows the same behaviour as that of perpendicular anisotropy as a function of the thickness of CoPd layer<sup>66</sup>. The increase in the perpendicular magnetic anisotropy with the thickness of FM is also

observed in different alloy systems like CoPt and FePt<sup>67;68</sup>. In the case of multilayers like Co/Pd or Co/Pt, decrease in the  $K_{eff}$  is observed for the large thicknesses of Co layer which is due to the decrease in the contribution of surface anisotropy and increase in volume and shape anisotropies<sup>69</sup>. The perpendicular anisotropy is enhanced with increasing the repetition number of Co/Pd multilayers<sup>70</sup>.

From the measured magnetic hysteresis curves of CoPd alloy of different thicknesses, as shown in Fig. 4.4.1, it is observed that the saturation magnetization ( $M_s$ ) of the CoPd alloy decreases with increasing thickness of the CoPd layer which is an unusual behaviour. In general, the saturation magnetization increases with increase in the thickness of the FM layer, reasons are the larger domains, grain size and the decrease in the ratio of surface disorders as compared to the bulk of FM layer<sup>59</sup>.

In order to understand this unusual behavior of saturation magnetization as a function of thickness of CoPd, the angle of remanent magnetization w.r.t. the horizontal plane and the effective magnetic anisotropy energy ( $K_{eff}$ ) of the CoPd samples with different thicknesses are measured. In the Fig. 4.4.3(a), it is shown that the remanent magnetization( $M_r$ ) is making an angle  $\theta$  w.r.t. the horizontal plane.  $\theta$  is calculated by the formula  $\theta = \tan^{-1}(M_rOP/M_rIP)$ , where  $M_rIP$  and  $M_rOP$  are remanent magnetization along the IP and OP directions, respectively, and are determined from the hysteresis loops along IP and OP directions. Fig. 4.4.3(b) shows the values of  $\theta$  as a function of CoPd thickness at different temperatures. It is observed that the value of  $\theta$  increases with increase in the thickness. There is no big difference between the values of  $\theta$  of CoPd samples of different thicknesses from 5 K to 220 K, this shows that in the vast range of temperature, the spins of CoPd remain perpendicular. At 300 K, the value of  $\theta$  of CoPd(8 nm) is reduced from 72° to 30°, i.e., the spins become more IP as temperature increases, this drastic change in  $\theta$  corresponds to spin re-orientation transition which will be discussed later.

If we look at the hysteresis loops of CoPd(x nm) samples as shown in Fig. 4.4.1 than it is cleared that the value of saturation magnetization ( $M_s$ ) of CoPd(8 nm) thick sample is larger than that of the CoPd(16 nm) and CoPd(30 nm) samples in both IP and OP directions. This observation shows that the magnetic moments of CoPd(8 nm) sample can easily follow the applied external field and more moments are aligned along the direction of the applied field, as it has larger  $M_s$  values in both IP and OP directions as compared to the thicker ones. This movement of spins of CoPd(8 nm) sample with external field can also be understood by considering the magnetic anisotropy, CoPd(8 nm) sample has a weak magnetic anisotropy as

compared to the CoPd(16 nm) and CoPd(30 nm) samples, which allows the spins to follow the applied external field more easily. Secondly, CoPd(8 nm) is easily saturated along the IP direction, and has larger  $M_r$ IP value as compared to the thicker samples, which shows that the perpendicular magnetic anisotropy in CoPd(8 nm) is not strong as compared to the thicker ones. The magnetic anisotropy of different thicknesses is shown in the Fig. 4.4.2, where CoPd(8 nm) has the smaller effective magnetic anisotropy value.

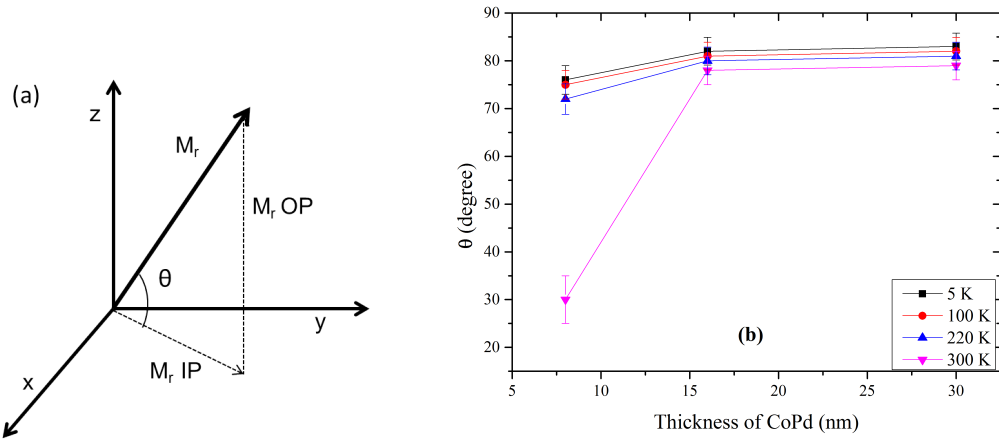


Figure 4.4.3: (a) Schematic representation of remanent magnetization,  $M_r$ , at an angle  $\theta$  with horizontal plane. (b)  $\theta$  (angle of  $M_r$  w.r.t. horizontal plane) as a function of thickness of sole CoPd samples at different temperatures.

By analyzing the results of hysteresis measurements (Fig. 4.4.1),  $K_{eff}$  measurements (Fig. 4.4.2) and the angle of remanent magnetization ( $M_r$ ) at different temperatures (Fig. 4.4.3(b)) for different thicknesses of CoPd samples, it is clear that in the absence of external field the spins of CoPd alloy are not lying exactly along the OP direction, but rather they are tilted and making a certain angle w.r.t. the horizontal plane. When an external field is applied to the samples along the IP or OP directions, the moments follow the applied field accordingly. The number of spins which follow the external applied magnetic field depends upon the magnitude of magnetic anisotropy of the sample. In the thin CoPd samples, the spins are more tilted toward IP, have weak effective magnetic anisotropy and can easily follow the applied field. With increasing the thickness of the CoPd alloy, the spins are tilted toward OP, the effective magnetic anisotropy increases and it becomes difficult for the spins to follow the applied field. As a result  $M_s$  decreases with increasing the thickness of CoPd layer.

## 4.5 Study of exchange bias in CoPd-IrMn bilayers

### 4.5.1 Hysteresis measurements

$\text{Si}/\text{SiO}_2/\text{Pd}(10 \text{ nm})/\text{Co}_{27}\text{Pd}_{73}(x \text{ nm})/\text{Ir}_{23}\text{Mn}_{77}(15 \text{ nm})/\text{Pd}(4 \text{ nm})$  is the layer sequence of exchange biased samples, where  $x=8 \text{ nm}, 16 \text{ nm}, 30 \text{ nm}$ . The FC hysteresis loops of these samples at different temperatures are shown in Fig. 4.5.1. As described earlier that in order to establish EB in the bilayers, these samples were annealed at 475 K in an external magnetic field of 10 kOe along OP direction for 1 hour and then the temperature was decreased from 475 K to 300 K in the presence of applied field. To study IP and OP exchange bias at low temperatures, these samples were measured in SQUID magnetometer. During the present measurements, the further field cooling was under taken from 350 K to 5 K along IP and OP directions for the IP and OP measurements, respectively. The measurements of MH-loops were taken at different temperatures during heating from 5 K to 350 K. The cooling and measuring field is 10 kOe which is enough for the IP measurements, as from IP measurements at 5 K, the MH-loops are closed and the saturation seems to be reached. These samples exhibit exchange bias along both IP and OP directions. From the shape of the MH-loops, it is clear that the perpendicular direction is considered as the easy axis, because of the large remanence and complete saturation in OP hysteresis loops. On the other hand, it is difficult to saturate along IP direction especially at low temperatures as indicated from MH-loops along IP direction. From the hysteresis measurements of exchange biased samples, the thickness dependence of saturation and remanence indicates the change in the PMA of the system. It is observed that the PMA increases with decreasing the thickness of CoPd layer in these CoPd/IrMn samples. The change in the magnetic anisotropy of these exchange biased layers with increasing the thickness of CoPd layer will be discussed in section 4.7.

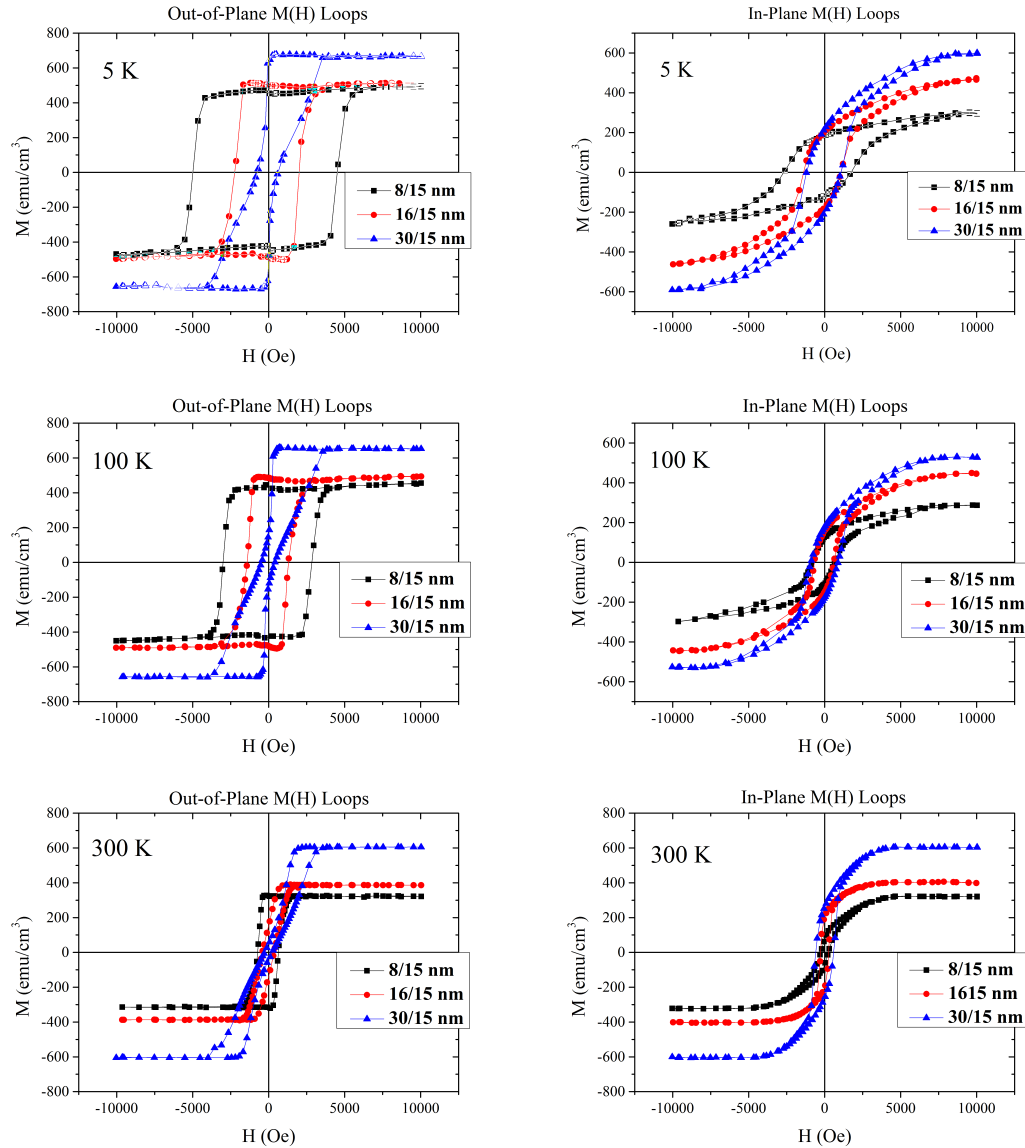


Figure 4.5.1: Hysteresis loops of CoPd( $x$  nm)/IrMn(15 nm) samples, where  $x = 8$  nm, 16 nm and 30 nm at different temperatures along out-of-plane (OP) and in-plane (IP) directions.

#### 4.5.2 Temperature dependence of in-plane and out-of-plane exchange bias

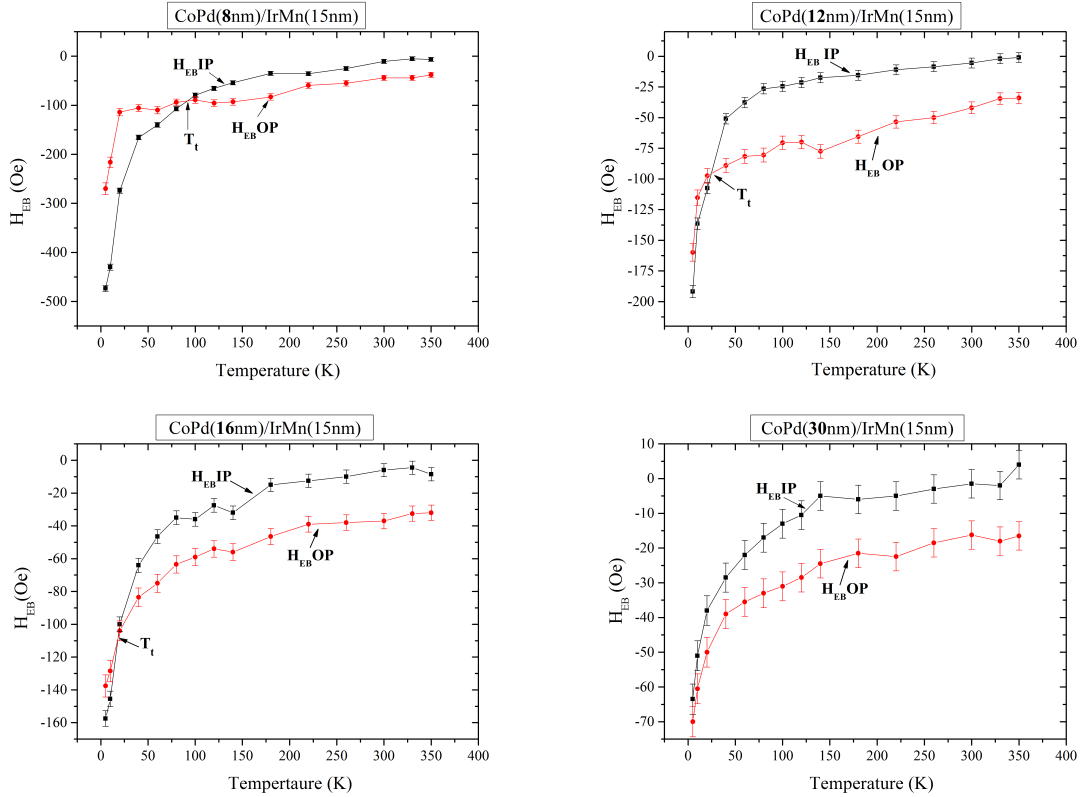


Figure 4.5.2: Temperature dependence of IP and OP exchange bias field ( $H_{EB}$ ) of CoPd/IrMn samples with different thickness of CoPd layer.

The exchange bias field ( $H_{EB}$ ) as a function of temperature is studied along both IP and OP directions in the CoPd/IrMn samples with different thicknesses of CoPd layer (8 nm, 12 nm, 16 nm, 30 nm) and having the same thickness of IrMn layer (15 nm). The temperature dependence of in-plane exchange bias field ( $H_{EB}IP$ ) and out-of-plane exchange bias field ( $H_{EB}OP$ ) of these samples is shown in Fig. 4.5.2. It should be noted that on y-axis of the graphs, values of  $H_{EB}$  are with negative sign (due to loop shift in direction opposite to applied field). It is observed that the magnitude of  $H_{EB}IP$  and  $H_{EB}OP$  decreases with increasing the temperature and the thickness of CoPd layer, which is very common and a well known behaviour of the exchange bias. If we look at the graph of exchange bias behaviour of CoPd(8 nm)/IrMn(15 nm) sample, it is clearly observed that the curves of  $H_{EB}IP$  and  $H_{EB}OP$  intersect each other at the certain temperature called transition tem-

perature ( $T_t$ ). Below  $T_t$ , the  $H_{EB}$ IP is greater than the  $H_{EB}$ OP while above  $T_t$ ,  $H_{EB}$ OP becomes larger than the  $H_{EB}$ IP. This transition of  $H_{EB}$ IP and  $H_{EB}$ OP is also observed in other samples containing 12 nm and 16 nm CoPd layer. With increasing the thickness of the CoPd layer,  $T_t$  moves to lower temperatures. This behaviour of  $H_{EB}$ IP and  $H_{EB}$ OP at lower and higher temperatures, is the most important and exciting part of the study of exchange bias in the CoPd/IrMn system which has not been yet reported. In order to understand the increase and decrease of  $H_{EB}$ IP versus  $H_{EB}$ OP at lower and higher temperatures, it is important to study the spin structure of IrMn alloy.

#### 4.5.3 Spin structure of IrMn

IrMn alloy has two kinds of crystal structures, ordered and disordered.

##### a) Ordered IrMn alloy

IrMn has also two types of ordered alloys, i.e.,  $L1_0$  and  $L1_2$ , depending upon the ratio of Ir and Mn<sup>71</sup>.  $L1_0$  is CuAu(I) type tetragonal structure. It is found in ordered AB binary alloys, where A atoms order on alternate (001) planes and B atoms on the others. This ordering gives a two layered structure modulated along the c-axis normal to the (001) planes.  $L1_2$  structure is of Cu<sub>3</sub>Au type. It has fcc structure, which is found in  $A_3B$ - binary alloys, where B atoms lie at the corners of a cube and A atoms are at the center of six faces of a cube.

##### b) Disordered IrMn alloy

Yamaoka<sup>41</sup> has studied the crystallographic and magnetic properties of disordered  $\gamma$ -phase  $Ir_xMn_{1-x}$  bulk alloys with different concentrations. The  $Ir_xMn_{1-x}$  alloys with composition range  $0.14 < x < 0.31$  have disordered face-centered cubic (fcc) structure and the alloys having composition range  $0.08 < x < 0.13$ , the structure is disordered face-centered tetragonal(fct) with axial ratio  $c/a > 1$ . The two anomalies were observed in the magnetic susceptibility versus temperature measurements with  $x < 0.14$ , the highest temperature (around 700 K) anomaly corresponds to magnetic transition and the low temperature (500 K – 200 K) range is related to the crystal transformation from fct to fcc.  $T_N$  of the disordered fcc  $Ir_xMn_{1-x}$  alloy increases with alloying Ir up to 730 K at  $x=0.25$  and it is extrapolated to  $500 \pm 20$  K for fcc

Mn. The reason of increase in the  $T_N$  is the perturbation of band structure due to alloying, leading to the stronger magnetic interaction.

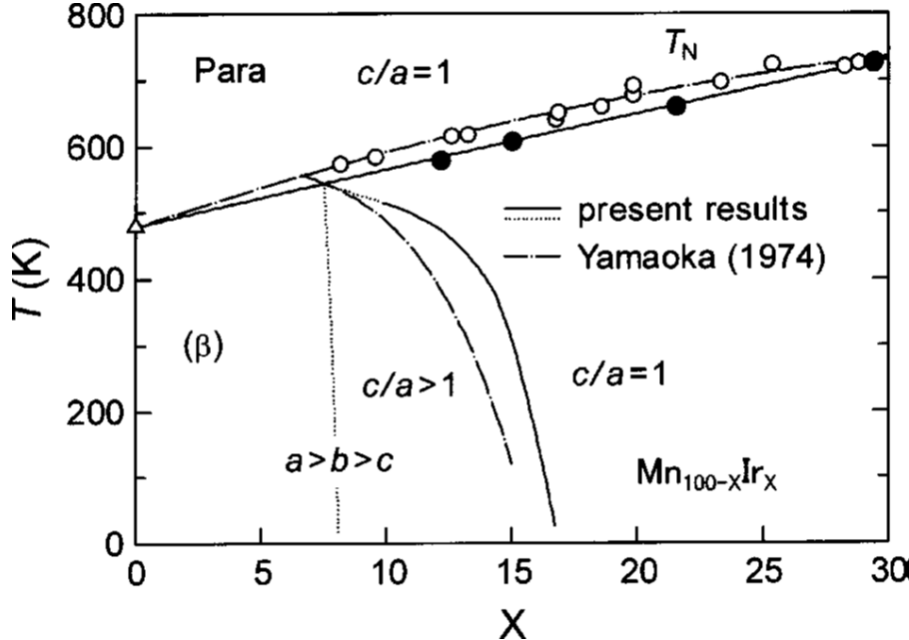


Figure 4.5.3: The phase diagram of Néel temperature ( $T_N$ ) as composition of Ir in Mn-Ir alloy, proposed by Sakuma<sup>71</sup>.

The disordered  $\gamma$ -Mn based alloys has multiple-Q spin density wave (SDW) structures, i.e., 1Q, 2Q and 3Q, where the 1Q is collinear while the 2Q and 3Q are noncollinear spin structures<sup>72</sup>. In general, neutron scattering is used to identify the different phases of SDW structures which is an easy tool in the case of 1Q spin structure, but neutron diffraction can not distinguish the different SDW phases due to the contribution of different domains, therefore, Mössbauer transmission and  $\gamma$ -ray emission techniques are used<sup>73;74</sup>. The magnetic structures of  $\text{Ir}_x\text{Mn}_{100-x}$  bulk alloys are also studied by A. Sakuma et al.<sup>71</sup> in more details.  $\gamma$ -phase disordered IrMn bulk alloy has also multiple-Q spin density wave structures like other Mn based alloys. The spin structure of 1Q, 2Q and 3Q phases of  $\gamma$ -phase disordered IrMn bulk alloy are illustrated in Fig. 4.5.4 for a primitive cell consisting of four atoms in the fcc structure. The 1Q structure is collinear where spins are parallel to the c axis with tetragonal lattice distortion and  $c < a$ . In the 2Q structure, spins are lying on the ab-plane making an angle of  $45^\circ$  to the crystal axis. The 2Q structure is also having a tetragonal distortion with  $c > a$ . In the 3Q structure, the spins are directed to the center of tetrahedron, making an angle ( $\theta$ ) of  $54.7^\circ$  along c axis, having  $c = a$  (for the angle calculation see appendix 1)<sup>71;72</sup>.

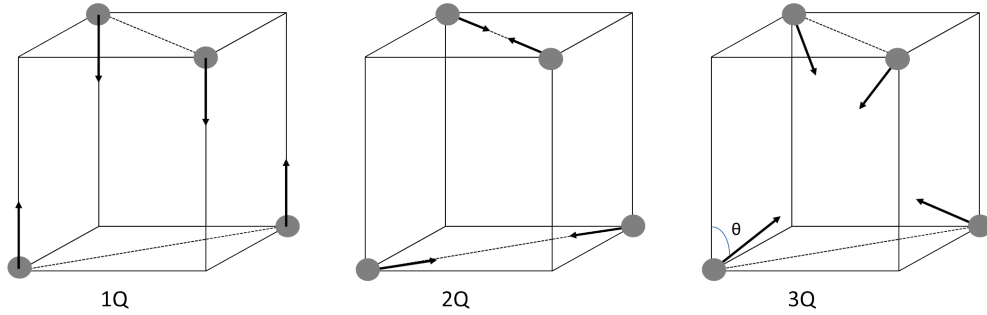


Figure 4.5.4: The unit cell of 1Q, 2Q and 3Q spin structure of  $\gamma$ -phase disordered IrMn alloy.

It is observed theoretically and experimentally that in general, the 3Q is most stable state in the  $\gamma$ -phase disordered IrMn alloy as compared to the pure  $\gamma$ -Mn where 2Q is the stable state. From theoretical determination of electronic total energy for different concentrations of  $\gamma$ -disordered  $\text{Ir}_x\text{Mn}_{100-x}$  alloy as a function of angle of spins w.r.t. c-axis, it is observed that the energies of 2Q and 3Q are lower than that of 1Q structure, hence 1Q structure is not energetically favourable for IrMn alloy. The spin structure is strongly dependent upon the concentration of Ir in the  $\text{Ir}_x\text{Mn}_{100-x}$  alloy, the 2Q structure is stable for  $x \leq 13$  and the 3Q structure is stable for  $x > 13$  under the conditions of  $c/a=1$  and  $a=3.785 \text{ \AA}$ <sup>71</sup>. The magnetic transition from 2Q to 3Q as a function of Ir concentration takes place at 13%, which is quite close to the concentration where the axial ratio changes from  $c/a > 1$  to  $c/a=1$  as observed by Yamaoka<sup>41</sup>. It is found that the lattice distortion of  $c/a > 1$  further lowers the total energy of 2Q structure. For the same concentration, the stable state depends upon the  $c/a$  ratio. From calculations<sup>71</sup>, it is found that for  $\text{Ir}_{15}\text{Mn}_{85}$  alloy, the total energy of 2Q structure becomes lower than 3Q structure when  $c/a=1.05$  (3Q is the stable state of  $\text{Ir}_{15}\text{Mn}_{85}$  for  $c/a=1$ ), whereas the 3Q structure is still stable in  $\text{Ir}_{20}\text{Mn}_{80}$  under the same condition of  $c/a=1.05$ . The critical concentration for the magnetic transition  $x_m$  does not necessarily coincide with the concentration for the lattice distortion  $x_t$ , as the 3Q structure of  $\gamma$ -phase disordered  $\text{Ir}_{20}\text{Mn}_{80}$  is found to prefer  $c/a > 1$  energetically rather than  $c/a=1$ , while for the  $\text{Ir}_{25}\text{Mn}_{75}$  alloy the lattice keeps  $c/a=1$  with 3Q structure. Therefore one can conclude that the concentration of magnetic structure transition is lower than that of the lattice distortion, i.e.,  $x_m < x_t$ . The x-ray diffraction of  $\gamma$ -phase disordered  $\text{Ir}_{15}\text{Mn}_{85}$  at 80, 200 and 300 K revealed that fct structure with  $c/a > 1$  is observed at 80 K and 200 K, whereas fcc structure is observed at 300 K<sup>71</sup>. Sakuma et al.<sup>71</sup> also observed two anomalies in

the magnetic susceptibility versus temperature measurements of  $\gamma$ -phase disordered Ir<sub>15</sub>Mn<sub>85</sub>, first one is around 125 K which is related to 2Q to 3Q transition and the second one is around 600 K which is related to T<sub>N</sub>. No anomaly is observed in the magnetic susceptibility at the transition temperature from fct to fcc, which was shown by x-ray diffraction measurements. At the transition from high-temperature phase 3Q to low-temperature 2Q, the magnetic susceptibility is reduced by few percent which is related to the change of spin structure. Fishman and Liu<sup>72</sup> calculated the magnetic susceptibility of  $\gamma$ -Mn alloys and showed that the average susceptibilities are different for different magnetic SDW structures. Therefore the transition between different SDW structures would be identified as the sudden change in the magnetic susceptibility as a function of temperature or concentration.

#### 4.5.4 Literature survey

##### 4.5.4.1 Q- spin structure and exchange bias

C. H. Marrows studied the exchange bias (EB) in *Co/Pd<sub>N</sub>-FeMn* polycrystalline system having (111) texture, where FeMn was deposited on the top of final Co layer<sup>75</sup>. At the room temperature, no exchange bias is observed along the IP and OP directions for the as deposited condition, but after field cooling along the z-direction (OP),  $H_{EB,OP}$  becomes 94 Oe and  $H_{EB,IP}$  is zero. For field cooling along the x-direction (IP)  $H_{EB,OP}$  is zero and  $H_{EB,IP}$  is 134 Oe. He concluded that the three dimensional nature of exchange bias confirms that the AFM spins are not confined to the sample plane and  $H_{EB}$  is not same in all directions (as might to be expected from high-symmetry 3Q spin structure), which shows that the spin structure at interface deviates from usual 3Q spin structure of FeMn.

Lin et al.<sup>76</sup> established a physical model of perpendicular exchange bias (PEB), which is based on an energy competition between anisotropy energy of interfacial exchange coupling energy ( $J_{ex}$ ), AFM ( $K_{AFM,xt_{AFM}}$ ) and FM ( $K_{FM,eff,xt_{FM}}$ ).  $J_{ex}$  is directly relevant to the net magnetization of FM and AFM spins along the perpendicular direction rather than the magnetization angle difference observed in an in-plane system. The anisotropy energy of FM is found to be significant to enhance the PEB, which is completely different to the IP exchange bias system. The effect of EB is studied experimentally in different [Pd/Co]<sub>5</sub>/FeMn systems in order to confirm the physical validity of the proposed model.  $H_{EB}$  is zero for the bottom configuration (where FeMn layer is underneath the Co/Pd multilayers) and

non zero for the top configuration because of the presence of strong (111) texture of fcc  $\gamma$ -phase FeMn in top configuration which results in a strong crystalline anisotropy of FeMn. In order to confirm the assumption that increase in  $K_{FM,eff}xt_{FM}$  and  $J_{ex}$  by decreasing the angle of magnetization of FM and AFM along the OP direction can increase the  $H_{EB}$ , annealing is done in different conditions. The annealing along the perpendicular direction in the presence of magnetic field, does not effect the  $H_{EB,OP}$  value as compared to as deposited condition, but  $H_C$  of the annealed samples is increased. IP annealing also does not affect the  $H_{EB,OP}$  value but induces  $H_{EB}$  also along the IP direction. EB along OP and IP is also explained on the basis of 3Q spin structure of FeMn at the interface of FeMn and  $[Pd/Co]_N$ .

C. Mitsumata et al. investigated the EB phenomena in in-plane FM and Mn-based AFM bilayers by means of Monte Carlo simulations within the frame work of classical Heisenberg model<sup>77;78</sup>. The bilayers are (111) oriented and the interface between FM and AFM is without any roughness. The magnetization loops are obtained using Landau-Lifshitz equation, EB is only observed in 3Q structure which has noncollinear spin structure and the magnetization loops of 1Q, 2Q and L1<sub>0</sub> structures (collinear spin structures) of Mn-based AFM alloys show no loop shift. The reason of EB in 3Q structure is that the noncollinear 3Q spin structure induces the in-plane magnetization reversal (2D reversal) which is related to the domain wall formation in AFM layer parallel to interface. The EB would disappear during phase transition from 3Q to 2Q or 1Q. However, EB is obtained by introducing the frustrated spins into the ordered L1<sub>0</sub> phase of AFM. By the introduction of the multi-domains in L1<sub>0</sub> structure, frustrated spins arise at the AFM domain boundaries which causes exchange bias in L1<sub>0</sub> structure. They showed that the spin structure at the interface is important for the shift of MH- loop and also concluded that the prerequisites of EB are the frustrated spins and the formation of magnetic domain wall in the AFM, which is parallel to the interface. Also the L1<sub>2</sub>-type ordered phase of AFM has EB because of its noncollinear spin structure<sup>79</sup>. C. Mitsumata et al. also reported that in bilayers having AFM with 3Q spin structure, the uncompensated spin element appears in AFM layer under the influence of EB. As the exchange coupling between FM and AFM layers influences the relaxation of the direction of spins therefore the direction of the AFM spins near the interface is different from that of bulk ground state, as a result uncompensated spin element is generated due to the frustration of spins<sup>80</sup>.

M. Tsunoda et al.<sup>81</sup> studied EB in FM/IrMn system, where the FM has IP anisotropy,

by means of XMCD and also support their work by micromagnetic simulation within the framework of classical Heisenberg model considering 3Q structure of IrMn. The XMCD study shows that the resonant absorption magnitude of Mn L edge increases with increase in the thickness of IrMn but XMCD signal does not change so much, it implies that the uncompensated spins are not homogeneously in the whole AFM layer and are localized at interface. When the FM layer is modified, XMCD signal of Mn L edge drastically changes not only its magnitude but also in the sign. In the absence of FM, the XMCD signal is not observed which means that uncompensated Mn components are induced at the interface through the exchange interaction between the FM and AFM layers. The theoretical study also supports the experimental result. In these calculations by considering atomic flat interface, it is observed that the AFM spin structure is modified by bending of spin component along the x-direction near the interface which indicates the presence of uncompensated spins (UCS). Furthermore, the XMCD studies in exchange biased bilayers containing IrMn as AFM show that the magnitude and the sign of uncompensated Mn moment strongly depend upon the composition of FM alloy, therefore by changing the composition of FM (or also the crystal structure) the exchange bias strength changes because of change of exchange coupling energy at the heterointerface<sup>82;83</sup>.

The phenomenon of EB related to the Q structure of Mn based AFMs by other groups is described above in detail. The reason is to highlight the commonality and differences of existing work with ours. Contrary to Mitsumata et al.<sup>77;78</sup>, EB is observed in 2Q (collinear) spin structure of IrMn. It is reported that in IrMn, exchange interaction causes the uncompensated Mn component<sup>81</sup>. But the magnetization measurements of sole IrMn sample reported here (see Fig 4.5.8), shows the presence of UCS spins which may be related to disorders in the system.

#### 4.5.4.2 In-plane and out-of-plane exchange bias

In Cu(30 nm)/FeMn(8 nm)/[FeNi(2 nm)/FeMn(8 nm)]<sub>15</sub>/Cu(30 nm) system, L. Sun et al.<sup>84</sup> studied the exchange bias along longitudinal (along IP) and perpendicular (along OP) directions, where the FM FeNi has intrinsic IP anisotropy. It is observed that in the field cooling along longitudinal direction,  $H_{EB}$  is non zero along IP measurement and it is zero along OP measurement, while in the case of perpendicular field cooling,  $H_{EB,OP}$  is non zero and  $H_{EB}$  is zero for IP measurement. This means that exchange bias is established only in the field cooling direction and perpendicular field cooling established out-of-plane EB in the system having IP

anisotropy. During the field cooling and measuring the sample in the same direction at different temperatures, it is observed that the longitudinal EB is always greater than the perpendicular EB with the constant difference over the whole temperature range from 5 K to 300 K. In another work<sup>85</sup>, where the  $H_{EB}$  and  $H_C$  along the perpendicular direction resembles longitudinal measurements for the above sequence as function of layer thicknesses of FM, AFM and temperature, it results that the same mechanism is responsible for inducing uniaxial anisotropy at FM/AFM interface along the perpendicular and longitudinal cooling field directions. The reason of smaller perpendicular  $H_{EB}$  as compared to longitudinal is attributed to the IP-shape anisotropy existing in FeMn layer.

The IP and OP exchange bias is also investigated in [FePt(x nm)-FeMn(y nm)]<sub>N</sub> multilayers deposited on MgO substrate<sup>86</sup>. For thin FePt layers, the IP and OP hysteresis loops are almost identical and with increasing the thickness of FePt the OP loops become more slanted, this shows the IP anisotropy becomes stronger with increasing the thickness of FePt alloy in the multilayers. They did not discuss the  $H_{EBIP}$  and  $H_{EBOP}$  as a function of temperature quantitatively, but from the graphs it is observed that at low temperatures  $H_{EBIP}$  is little bit larger than  $H_{EBOP}$  and then they become nearly same with increase in temperature. They also showed that the blocking temperature ( $T_B$ ) along IP is higher than OP, the reason is the tilted spins at the interface. At the interface there is the competition between surface anisotropy (which tries the spins to align in perpendicular direction) and shape anisotropy (which tries the spins to lie in the plane of film), therefore the spins are tilted at the interface. As the shape anisotropy is stronger than the surface anisotropy, the easy axis is closer to parallel direction as compared to normal direction. Therefore, the ordering of the antiferromagnetic spins at interface along IP direction is larger than in the perpendicular direction, so the  $T_B$  is higher along IP direction<sup>86-90</sup>.

Above results show the  $H_{EB}$  as function of temperature along IP and OP directions. They did not observe any crossing over in the  $H_{EB}$  related to 2Q-3Q transition in FeMn which has also the similar spin structure as IrMn, may be the reason is that they used FMs having IP anisotropy.

#### 4.5.4.3 Exchange bias in CoPd system

According to the careful literature survey, exchange bias is only studied in Co/Pd multilayers, no publication is found on exchange bias in CoPd alloy as FM. Above

discussed references<sup>75</sup> and<sup>76</sup> explained the exchange bias phenomenon in Co/Pd multilayers. Chesnel et al. has shown the possibility of creating magnetic domain memory in thin FM by inducing spatially varying exchange coupling interactions in [Co/Pd]IrMn multilayers<sup>91</sup>.

#### 4.5.5 Discussion of the experimental results of exchange bias

The important observations related to the experimental study of  $H_{EB}IP$  and  $H_{EB}OP$  as a function of temperature in  $Co_{27}Pd_{73}(x \text{ nm})/Ir_{23}Mn_{77}(15 \text{ nm})$  samples are,

- 1). At low temperatures, for  $T < T_t$ :  $H_{EB}IP > H_{EB}OP$
- 2). At high temperatures, for  $T > T_t$ :  $H_{EB}OP > H_{EB}IP$
- 3). The transition temperature ( $T_t$ ) decreases with increasing the thickness of CoPd layer.

For  $H_{EB}$  as a function of temperature of CoPd(8 nm)/IrMn(15 nm) sample as shown in Fig. 4.5.2, we find  $T_t=92$  K. In order to describe this behaviour of EB in this system, the spin structure of IrMn is considered, which is the AFM in our system. As discussed above the  $\gamma$ -phase disordered  $Ir_xMn_{1-x}$  bulk alloy has 1Q, 2Q and 3Q spin structure, depending upon the temperature and concentration of the alloy<sup>71</sup>.

From the discussion of spin structure of IrMn bulk alloy in section 4.5.3, it is known that 1Q structure of IrMn is not energetically favourable. At low temperatures IrMn has 2Q structure and at higher temperatures the spin structure of IrMn is 3Q. Also for the EB, it is well known that the uncompensated spins of AFM play an important role, therefore there should be some uncompensated spins or projections of uncompensated spins of IrMn along the IP and OP directions for  $H_{EB}IP$  and  $H_{EB}OP$ , respectively. In the 3Q structure (in Fig. 4.5.4), there are four nearest atoms in the fcc structure located at the corners of a tetrahedron and the spins are tilted and directed toward the center of tetrahedron.

According to the XRD measurements, IrMn has the (111) texture, therefore, the (111) plane is considered which is marked by the red lines as shown in Fig. 4.5.5. This (111) plane is parallel to the interface of CoPd/IrMn bilayers, where CoPd has also (111) texture from XRD measurements. In 3Q structure, the spins of three atoms are canted at a certain angle w.r.t. (111) plane while the spin of fourth atom makes an angle of  $-90^\circ$  with (111) plane. The canting angle between the spins of three atoms and (111) plane is calculated and found as  $19.5^\circ$  (see appendix 2) which

is also in accordance to the findings by Lin et al.<sup>76</sup>. For these three atoms, whose spins are canted at 19.5°, the spin moment is divided into two components, i.e., parallel and perpendicular to (111) plane. The spin components parallel to (111) plane of these three atoms are concentric at the center of the triangle with same magnitude having an angle of 120° between each other, therefore, the sum is zero. The sum of perpendicular components of these three atoms compensate with the spin of the fourth atom which is perpendicular to (111) plane, as  $\text{Sin}(19.5^\circ)=1/3$ .

In 3Q structure, along (111) plane, which is parallel to interface, the spin of one atom is completely perpendicular and the remaining three atoms also have spin components along perpendicular direction. Therefore, the UCS which are developed in the AFM because of the disorder are most probably along the perpendicular direction or have strong perpendicular components. This stronger perpendicular component of uncompensated spins couples to the spins of CoPd, which has also perpendicular anisotropy and results in the stronger EB in OP direction at high temperatures ( $T>T_t$ ). While the parallel component of uncompensated spins of IrMn in 3Q is responsible for the weaker EB along IP direction at high temperatures. The increase in the  $H_{EB}$  along the IP direction at low temperatures ( $T<T_t$ ), shows that the parallel components of the uncompensated spins of IrMn become stronger. With decrease in temperature, the bulk IrMn has magnetic structural transition from 3Q to 2Q (see section 4.5.4), where the spins lie along the (001) plane of the fct crystal structure.

If the (111) plane is considered in 2Q structure (Fig. 4.5.5), the spins of two atoms lie on the (111) plane in opposite directions, the orthogonal spins of remaining two atoms are canted at a certain angle w.r.t. the (111) plane in the opposite directions. Therefore, in 2Q structure, the spins of two atoms lie completely parallel to the (111) plane and the spins of other two atoms have perpendicular and parallel components along (111) plane. The spin arrangements of 2Q structure along (111) plane shows the strong indication that the parallel component of uncompensated spins of IrMn is much stronger than the perpendicular component. This strong parallel component of 2Q structure of IrMn causes the increase of  $H_{EB}$  along the IP direction at low temperatures. The 2Q structure has partial perpendicular component of spins which may partially support OP exchange bias. This explanation shows that IP and OP  $H_{EB}$  depend upon the orientation of spin structure in IrMn, which changes from 3Q to 2Q with decreasing temperature.

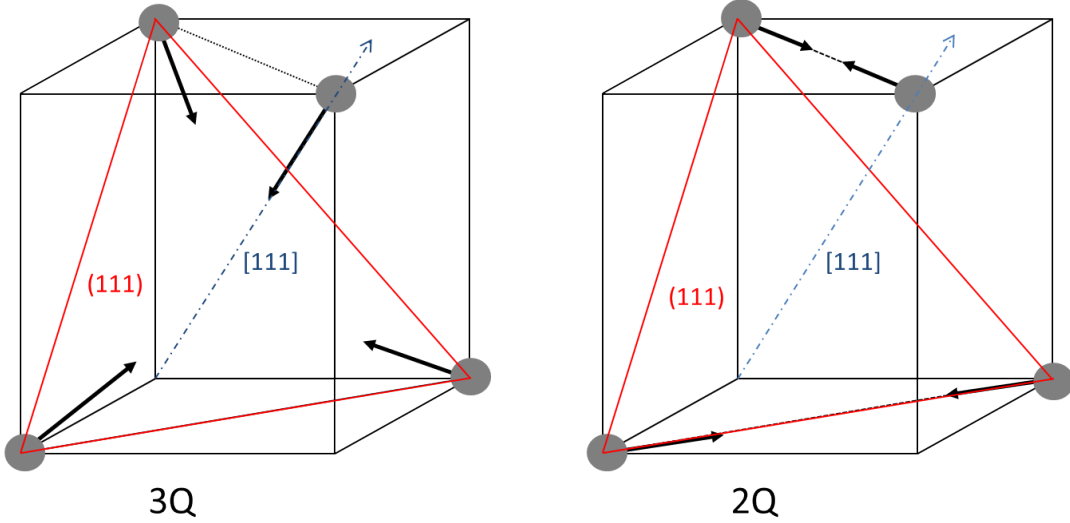


Figure 4.5.5: The unit cell of 3Q and 2Q spin structure of  $\gamma$ -phase disordered IrMn alloy, where (111) plane is represented by the red coloured triangle.

The effect of spin structure of AFM on the EB behavior was also observed by Maat et al. in polycrystalline (111) textured Co/Pt multilayers biased with CoO<sup>92</sup>. They showed that the  $H_{EB}$  along the IP direction is always larger (factor of 2) than the OP direction. This behavior is related to the bulk spin structure of highly anisotropic CoO, where the spins are aligned in ferromagnetic (111) sheets and point in [117] directions. In the case of field cooling, the CoO spins freeze into a direction which is close to cooling field direction. In (111) textured CoO samples, for OP field cooling the spins of CoO lie along the directions which is different to the IP field cooling, this difference in the projection of CoO spins along the IP and OP, causes the increase in EB along the IP direction as compared to the OP direction. Later, Marrows discussed the dependence of EB on the structure of FeMn in  $Co/Pd_N$ -FeMn samples<sup>75</sup>. The spin structure of bulk FeMn alloy is similar to IrMn alloy as both are Mn-based alloys, with  $\gamma$ -phase FeMn having also 1Q, 2Q and 3Q spin structure<sup>72;93</sup>. Marrows did measurements at room temperature, it is observed that OP field cooling only generates EB in OP direction and similarly IP EB occurs only due to IP field cooling, the  $H_{EB}IP$  is zero for OP field cooling and vice versa . He also observed that  $H_{EB}IP$  is larger than  $H_{EB}OP$  and concluded that the reason for these results is because the spin structure at the interface deviates from the usual 3Q structure of FeMn. The behavior of EB, studied by Marrows is opposite to the results reported here for CoPd/IrMn, as in our system  $H_{EB}IP$  and

$H_{EB}$ OP always co-exist either for IP field cooling or OP field cooling, the presence of 3Q structure in IrMn of our samples is the explanation of this discrepancy. Lin et al. observed the presence of OP EB for the annealing along IP direction in polycrystalline  $[Pd/Co]_5/FeMn$  (111) textured samples<sup>76</sup>. The presence of  $H_{EB}$ IP and  $H_{EB}$ OP for IP annealing is related to the 3Q spin structure of FeMn.

Here, I want to comment on Marrows result as he showed that the spin structure of FeMn (having weak (111) texture) is deviated from usual 3Q structure which is based on the experimental result that  $H_{EB}$  is not same along IP and OP ( $H_{EB}$ IP  $>$   $H_{EB}$ OP), it should be equal as expected from high-symmetry 3Q structure. But in my opinion, for a system having 3Q spin structure even with (111) texture too, have projections of spins along IP and OP directions. But, it's not necessary that the spin components would be same along IP and OP directions, therefore, EB could not be equal along IP and OP directions. Also, IP and OP EB would be present irrespective of field cooling direction either in IP or OP direction. As from our results, both IP and OP EB occur after annealing the samples along OP direction and  $H_{EB}$  is larger along OP direction because 3Q spin structure favours OP direction. These results are similar to Lin work<sup>76</sup>, where he showed both IP and OP EB after IP annealing, he did not compare the magnitude of EB along IP and OP direction just show the MH-loop along IP direction but if we closely look at the MH-loop along IP direction then it is clear that EB along IP direction is smaller than OP direction. In the above discussed articles<sup>75;76</sup>,  $H_{EB}$  is explained in FeMn (with 3Q spin structure) with FM having perpendicular anisotropy and was measured at room temperature, not studied as a function of temperature.

In FeMn with FM having IP anisotropy, IP and OP EB as a function of temperature is also discussed, where EB along IP direction is always larger than OP over the whole temperature range<sup>84;86</sup>. Therefore, with the careful literature survey, the crossing in the IP  $H_{EB}$  and OP  $H_{EB}$  as a function of temperature is not observed yet in  $\gamma$ -Mn based system, which reveals the transition from 3Q to 2Q spin structure at low temperatures. From our experimental results, 2Q-3Q transition is easily observed by  $H_{EB}$  as a function of temperature along IP and OP directions.

#### 4.5.6 Magnetization versus temperature measurements: 2Q-3Q spin structure transition

In order to further investigate and understand the magnetic behaviour of the samples and to identify spin structure transition in IrMn, magnetization measurements of CoPd, IrMn and exchange biased samples are done as a function of temperature under different conditions of field cooling and zero field cooling.

##### 4.5.6.1 Exchange biased and FM only samples

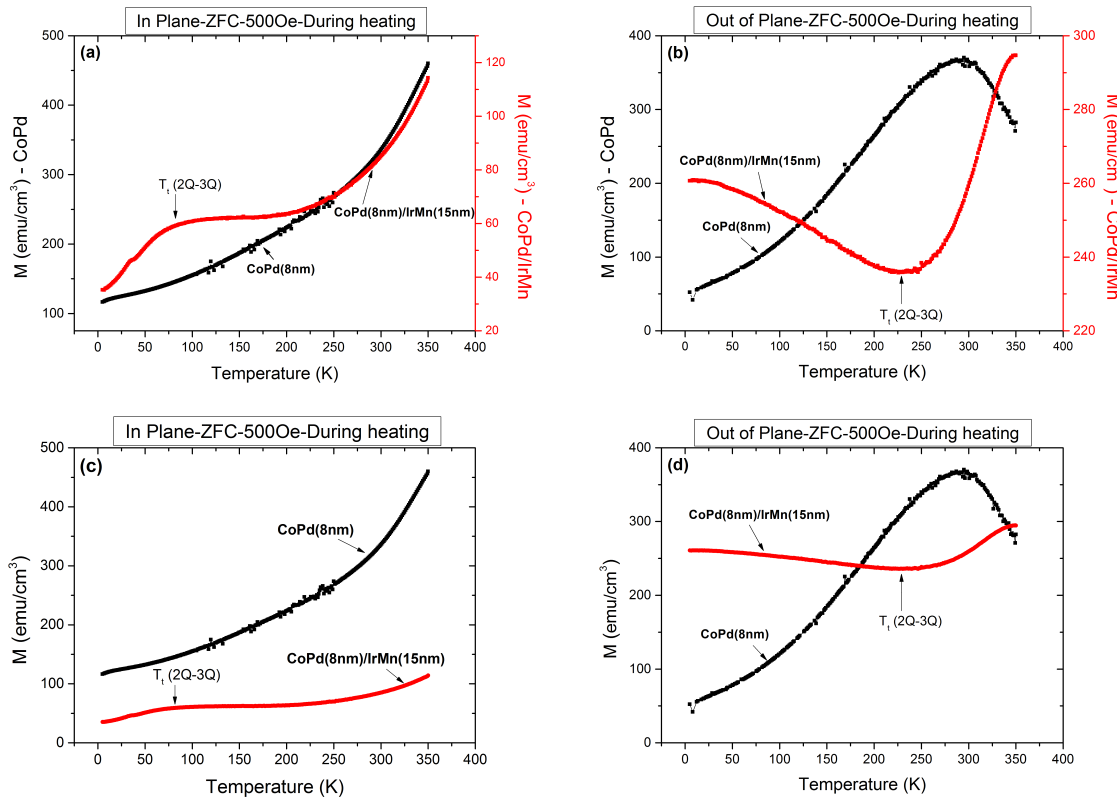


Figure 4.5.6: Magnetization versus temperature,  $M(T)$  measurements of CoPd (8 nm) and CoPd(8 nm)/IrMn(15 nm) after zero field cooling and then heating in the presence of 500 Oe magnetic field. (a), (c) along IP direction, in (c) on same scale; (b), (d) along OP direction, in (d) on same scale.

Fig. 4.5.6 shows the magnetization versus temperature( $M(T)$ ) measurements of exchange biased sample CoPd(8 nm)/IrMn(15 nm) and sole CoPd sample having thickness 8 nm, after zero field cooling and then heating in the presence of 500 Oe field

from 5 K to 350 K. Fig. 4.5.6(a) exhibits the IP measurements of magnetization as a function of temperature. The zero field cooled (ZFC) magnetization curve of CoPd(8 nm)/IrMn(15 nm) sample started from 5 K, first it increases abruptly up to 80 K, then becomes constant and then again increases. This increase in the magnetization curve of exchange biased sample at low temperatures is due to the 2Q structure of IrMn. As in 2Q structure, spins of IrMn favour IP direction, therefore, the spins can easily align along the IP direction with the applied IP external field of 500 Oe. After 80 K, instead of further increase in the magnetization due to the presence of external magnetic field and increase in thermal energy, it becomes constant. This behaviour of magnetization indicates that now the spin structure is no more 2Q and it becomes 3Q, as in 3Q structure the spins are more OP so it does not favour IP direction. Therefore, the curve should decrease but due to the presence of CoPd layer, the strong decrease in the magnetization does not occur. At higher temperatures, the increase in the magnetization curve of exchange biased sample is due the response of CoPd spins to the external field as they have higher thermal energy. The magnetization curve of sole CoPd with 8 nm thickness increases monotonically, which shows that the change in the magnetization curve of exchange biased sample below 250 K is due to IrMn which undergoes a 2Q-3Q transition of IrMn near 80 K.

The OP  $M(T)$  measurements of CoPd(8 nm)/IrMn(15 nm) and sole CoPd (8 nm) are shown in Fig. 4.5.6(b). At low temperatures, the decrease in the OP magnetization curve of CoPd/IrMn sample is due to the presence of 2Q structure of IrMn because it favours IP direction, while the increase in the magnetization curve above 228 K is due to the 3Q structure of IrMn, as in 3Q structure the spins of IrMn are more in OP direction, along with they align more easily in the presence of external field. The OP magnetization of CoPd sample is increased with temperature, because of its perpendicular anisotropy. The decrease in the magnetization of sole CoPd at higher temperature is due to spin re-orientation which will be discussed later.

The same magnetization measurements are also done for the thicker CoPd samples, Fig. 4.5.7 shows the  $M(T)$  measurements of CoPd(16 nm)/IrMn(15 nm) and sole CoPd (16 nm) samples along IP and OP directions under the same conditions. The IP magnetization measurement of CoPd(16 nm)/IrMn(15 nm) increases with temperature, but there is an anomaly around 29 K (see inset of Fig. 4.5.7(a)). Below 29 K the magnetization increases more rapidly as compared to the increase in magnetization above 29 K. This change in slope around 29 K is related to 2Q-

3Q transition, where because of 2Q structure the IP magnetization increases fast as compared to the magnetization behaviour above 29 K. In the OP magnetization measurement of the CoPd(16 nm)/IrMn(15 nm), this anomaly occurs at 39 K, as shown in inset of Fig. 4.5.7(b). Above 39 K, the slope of the magnetization curve of the exchange biased sample increases due to the 3Q structure of the IrMn, favouring OP direction. The decrease in the OP magnetization curve of exchange biased sample above 300 K is due to spin re-orientation. No such anomaly occurs in the magnetization curves of sole CoPd(16 nm) sample along IP and OP directions.

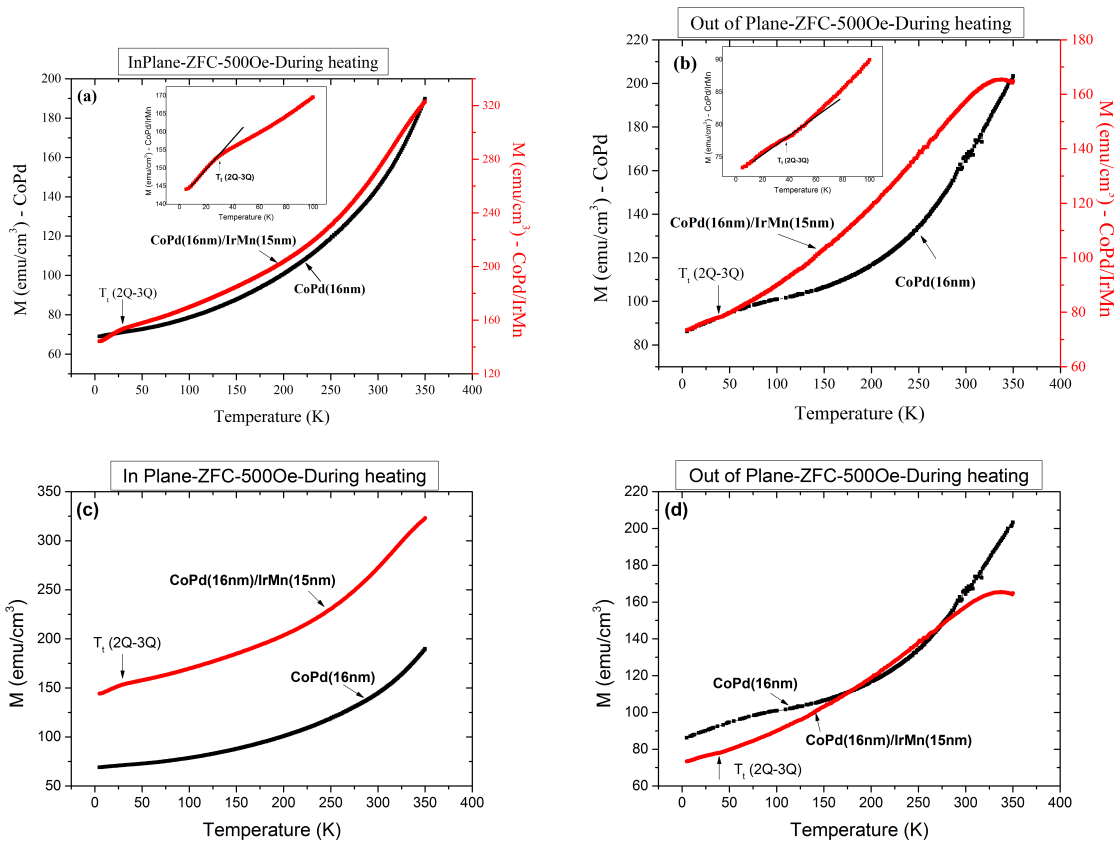


Figure 4.5.7:  $M(T)$  measurements of CoPd (16 nm) and CoPd(16 nm)/IrMn(15 nm) after zero field cooling and then heating in the presence of 500 Oe magnetic field. (a), (c) along IP direction, in (c) on same scale; (b), (d) along OP direction, in (d) on same scale.

From the magnetization measurements of exchange biased and sole CoPd samples along IP and OP directions, it is clearly seen that 2Q-3Q spin structure transition occurs in exchange biased samples w.r.t the change in temperature because of the presence of IrMn, as such kind of transition is not observed in sole CoPd samples.

Therefore, it is clear that the behaviour of  $H_{EB}IP$  and  $H_{EB}OP$  as a function of temperature is due to IrMn. The 2Q and 3Q spin structure transition is clearly observed in the magnetization measurements, because of IrMn in exchange biased samples.

#### 4.5.6.2 Sole IrMn sample

The previous M(T) measurements indicate that exchange biased samples behave differently as compared to CoPd samples due to the change in the spin structure of IrMn. In order to observe 2Q-3Q transition in sole IrMn samples, the IrMn samples having sequence Si/SiO<sub>2</sub>/Pd(10 nm)/Ir<sub>23</sub>Mn<sub>77</sub>(30 nm)/Pd(4 nm) were grown under the same conditions as the other samples. It's not easy to get magnetic moment signal from sole AFM as compared to FM. Therefore, the double thickness of IrMn as compared to that used in exchange biased samples is used to get reasonable signal. In previous M(T) measurements of exchange biased samples, the magnetic field of 500 Oe is used during the heating in order to avoid the strong response from CoPd in exchange biased samples to identify 2Q-3Q transition. While in the M(T) measurements of sole IrMn sample, 10 kOe magnetic field is used during the measurements to get large magnetic signal from uncompensated magnetic moments. In bulk Ir<sub>15</sub>Mn<sub>85</sub> alloy, 2Q-3Q transition temperature is around 130 K<sup>71</sup>.

Fig. 4.5.8(a) presents the ZFC magnetization measurement of IrMn(30 nm) sample along the IP direction during heating in the presence of 10 kOe field from 5 K to 350 K. The measurement is very sensitive and has high uncertainty due to background diamagnetic behaviour of the substrate, the magnetic moments of IrMn sample and substrate are of the same order ( $10^{-5}$  emu). Therefore, it does not show the clear transition but one can get an idea about the trend of magnetization of sole IrMn along IP direction. At low temperatures around 58 K, there is the trend in the magnetization of IrMn to decrease. Although the change in the slope of 2Q state of IrMn is not pronounced, one can still see the tendency of magnetization as a function of temperature due to distribution of measured data points. Above 58 K, the magnetization decreases because now the spin structure of IrMn is changed from 2Q to 3Q where the spins have OP component, therefore, the IP magnetization should decrease. One can also get an idea that around 246 K the slope of the magnetization through measured data points changes. The decrease in the magnetization gives an indication of the spins becoming more OP so the IP magnetization decreases. .

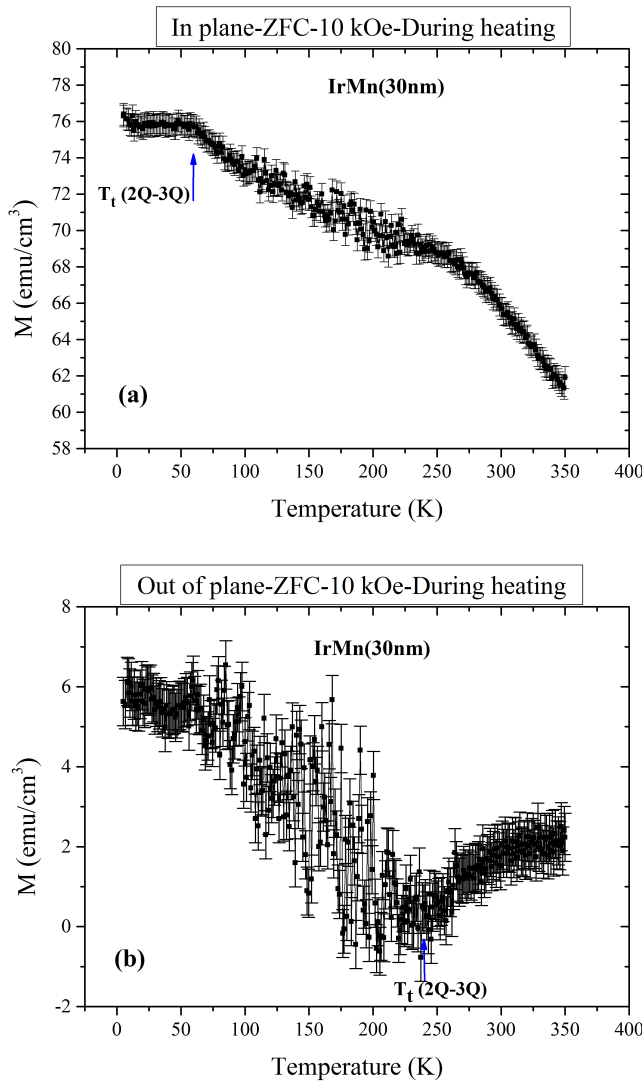


Figure 4.5.8:  $M(T)$  measurements of sole IrMn(30 nm) sample after zero field cooling and then heating in 10 kOe field. (a) along in-plane direction, (b) along out-of-plane direction.

In the OP  $M(T)$  measurement of IrMn as illustrated in Fig. 4.5.8(b), there is a clear but noisy decrease in the magnetization till 240 K. This decrease in the magnetization is due to the 2Q structure and above 240 K, the increase in the magnetization indicates the 3Q structure of IrMn favouring OP direction. In the OP measurement, one can get an idea of the small peak around 60 K which can be related to the starting of transition of IrMn structure from 2Q to 3Q phase and then the curve becomes noisy. This noise in magnetization is due to the transformation of spin structure from 2Q to 3Q, as the spins are changing their orientation. The clear transition to

3Q phase is visible above 240 K, where the curve becomes relatively smooth, indicates that all spins are in 3Q phase. From this behaviour of magnetization of IrMn sample along IP and OP direction, it is inferred that at low temperatures IrMn has 2Q structure, in the temperature range from 58 K (60 K from OP measurement) to 246 K (240 K from OP measurement) the spins are in the transition phase and then they transform into 3Q spin structure.

It is also observed that for IP measurement of magnetization, the visible indication of 2Q-3Q transition is at lower temperature as compared to OP measurements. In exchange biased sample CoPd(8 nm)/IrMn(15 nm), the IP measurement shows 2Q-3Q transition at 80 K while OP measurement shows transition around 228 K, also the magnetization measurements of sole IrMn shows that the 2Q-3Q transition started at 58 K and 240 K for IP and OP measurements respectively, therefore, it is clear that this difference in transition temperature is because of the IrMn which behaves differently along OP and IP direction. This difference has its origin in anisotropy of IrMn, which is different along IP and OP directions. Maat et al. reported that CoO behaves differently along IP and OP directions because of anisotropy induced by the (111) textured growth of the film<sup>92</sup>. In our case, the IrMn used in all samples has also (111) texture, which could be the reason of this difference. He also proposed that upon field cooling the AFM spins are frozen-in to the spin anisotropy axes that are closest to the applied field

The effect of external magnetic field on the alignment of the spins of IrMn is opposite here. As IP and OP magnetic field did not enhance the range of the 2Q (as 2Q favours IP) and 3Q (as 3Q favours OP) structure, respectively. From IP magnetization measurements 3Q phase is strongly visible earlier and the same case is with OP measurements, where 2Q phase is prominent in the long temperature range.

#### 4.5.7 Effect of the thickness of CoPd layer on 2Q-3Q transition of IrMn

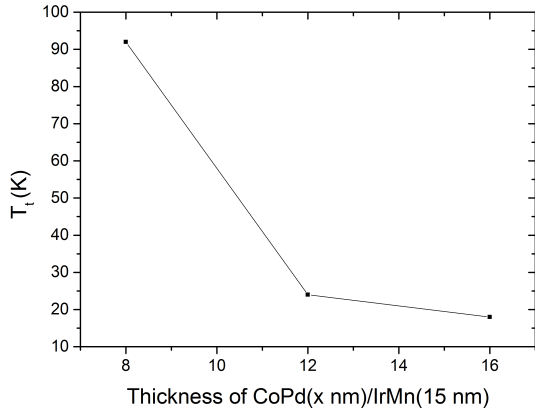


Figure 4.5.9: Dependence of 2Q-3Q transition temperature ( $T_t$ ) on the thickness of CoPd layer in CoPd(x nm)/IrMn(15 nm) system.

From the  $H_{EB}$  versus temperature measurements of CoPd( $x=8, 12, 16, 30$  nm)/IrMn(15 nm) samples along IP and OP directions as shown in Fig. 4.5.2,  $T_t$  is determined through the intersection of  $H_{EB}IP$  and  $H_{EB}OP$  curves. As it is discussed above that below  $T_t$ , samples show 2Q spin structure of IrMn while the 3Q spin structure is present above  $T_t$ . The behaviour of 2Q-3Q transition temperature ( $T_t$ ) of IrMn in CoPd( $x=8, 12, 16$  nm)/IrMn(15 nm) samples as a function of thickness of CoPd layer ( $t_{CoPd}$ ) is shown in Fig. 4.5.9. It is observed that  $T_t$  decreases with increasing  $t_{CoPd}$  and in CoPd(30 nm)/IrMn(15 nm) sample, no transition is observed up to 5 K temperature. It is reported that 2Q-3Q  $T_t$  strongly depends upon the concentration of Ir in IrMn alloy<sup>71</sup>. In the present data, thickness of Ir<sub>23</sub>Mn<sub>77</sub> layer in exchange biased samples is same. Therefore, one should assume that 2Q-3Q transition in exchange biased samples should be occur at same temperature but  $t_{CoPd}$  strongly influenced the  $T_t$ . The effect of spin structure of IrMn on CoPd is decreased with increasing the  $t_{CoPd}$ . The effect of spin structure of IrMn is diminished in exchange biased samples with increasing the thickness of CoPd layer. This also observed in the M(T) measurements. The M(T) measurements of CoPd(8 nm)/IrMn(15 nm) sample along IP and OP directions as shown in Fig. 4.5.6, clearly show the pronounced change in the magnetization because of 2Q - 3Q spin transition of IrMn. This indicates the stronger role of spin structure of IrMn in the case of thin CoPd layer. In the M(T) measurements of CoPd(16 nm)/IrMn(15 nm) sample (Fig. 4.5.7),

the change in magnetization due to 2Q-3Q transition is diminished, which depicts the weak effect of IrMn spin structure on the thicker CoPd layer.

#### 4.5.8 Effect of annealing

In order to establish exchange bias in CoPd/IrMn system, annealing is done at 475 K in an external magnetic field of 10 kOe along OP direction for 1 hour and then the temperature decreases from 475 K to 300 K in the presence of applied field. Fig. 4.5.10 shows the behavior of exchange bias before and after annealing. It is observed that annealing did not effect the 2Q-3Q spin structure transition as the  $T_t$  is nearly same in both cases. It is also observed that after annealing, the magnitude of IP and OP exchange bias is reduced at low temperatures which is due to the intermixing at interface. While the  $H_{EB}OP$  increased at higher temperatures which can be related to the annealing along OP direction.

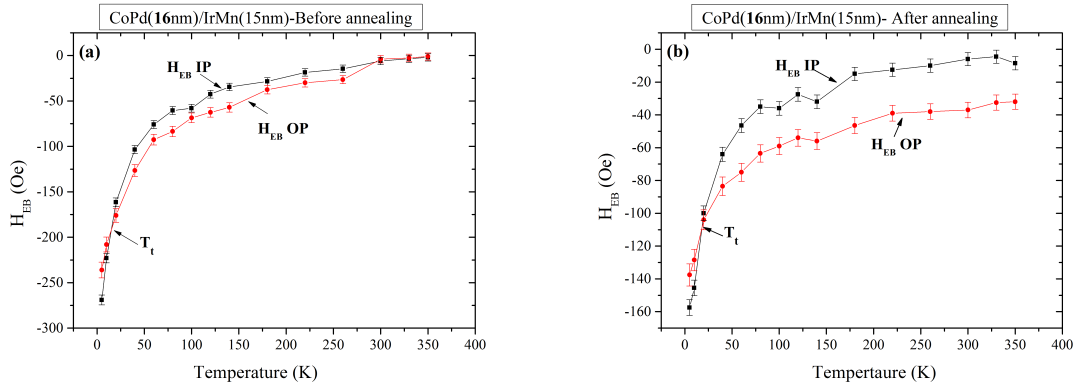


Figure 4.5.10: Temperature dependence of IP and OP  $H_{EB}$  of CoPd(16 nm)/IrMn(15 nm) sample. (a) before annealing, (b) after annealing.

## 4.6 Spin re-orientation transition in sole CoPd and CoPd/IrMn samples

The spin-reorientation transition (SRT) is the change in the direction of magnetization from out-of-plane (OP) to in-plane (IP) direction as a function of temperature, film thickness or the change in the composition of the FM. The magnetization can also change its direction from IP to OP which is called as “reverse SRT”<sup>94</sup>.

Here the SRT in the sole CoPd and exchange biased samples is reported. The samples are field cooled from 350 K to 5 K in the presence of 15 kOe, and then measured during heating from 5 K to 350 K in zero field. The orientation of the applied field depends upon the direction of measurements along IP and OP directions for IP and OP thermoremanent magnetization ( $M_{TRM}$ ) measurements, respectively. Fig. 4.6.1 presents the  $M_{TRM}$  measurements of sole CoPd(8 nm) and CoPd(16 nm) samples along OP and IP directions. From OP  $M_{TRM}$  curves, it is observed that with increasing the temperature the magnetization decreases as spins deviate from perpendicular direction because of the thermal activity. This decrease in magnetization is very small because of the stronger perpendicular anisotropy in the system. At higher temperatures, the OP  $M_{TRM}$  is dropped suddenly which shows that the perpendicular anisotropy of the system does not remain strong any more. This behaviour of magnetization is due to SRT as the spins of CoPd alloy now turn along IP which causes the sudden decrease in the magnetization along the OP direction. According to the OP  $M_{TRM}$  measurements, the SRT occurs in CoPd(8 nm) and CoPd (16 nm) around 200 K and 257 K, respectively.

The IP  $M_{TRM}$  measurements of CoPd(8 nm) and CoPd(16 nm) also show the SRT behaviour. At low temperatures, the IP magnetization decreases with increase in temperature because of the strong perpendicular anisotropy of the system. As the temperature increases further, the IP  $M_{TRM}$  increases. This increase in the  $M_{TRM}$  along IP direction shows the rotation of spins of CoPd alloy from OP to IP direction. In Fig. 4.6.1, the IP and OP measurements are shown in the same graph, from which one can easily seen the behaviour of the  $M_{TRM}$  of CoPd sample along IP and OP directions.

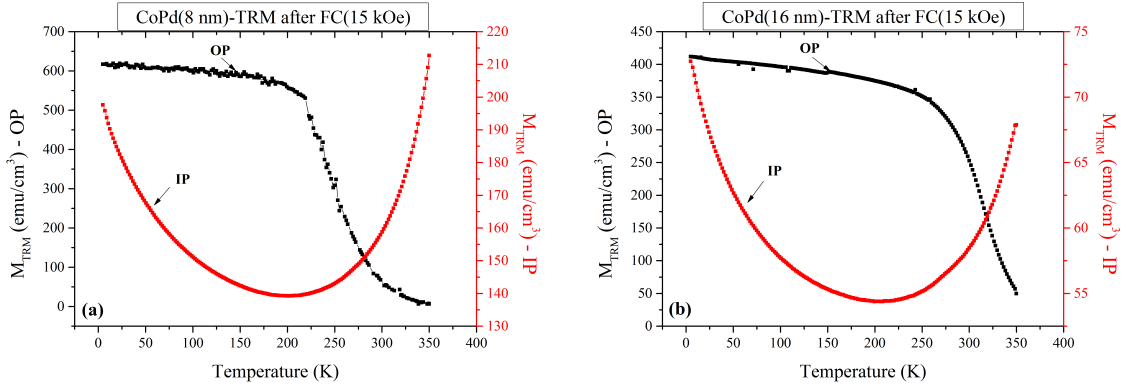


Figure 4.6.1: Thermoremanent magnetization ( $M_{TRM}$ ) versus temperature measurements after field cooling in 15 kOe, then heating in zero field from 5 K to 350 K along OP (black curve, left scale) and IP (red curve, right scale) directions; (a) CoPd(8 nm) sample, (b) CoPd(16 nm) sample.

Fig. 4.6.2 exhibits the  $M_{TRM}$  along OP and IP directions of sole CoPd samples having thickness of 8 nm, 16 nm and 30 nm. The  $M_{TRM}$  measurements along both OP and IP directions of the sole CoPd samples reveal that the SRT from OP to IP direction moves to higher temperatures with increasing the thickness of CoPd alloy. This behavior shows the presence of stronger OP component in thicker CoPd samples. As for reorientation from OP to IP direction, the spins of thicker CoPd need more thermal energy. This resembles the behavior of perpendicular anisotropy of sole CoPd alloy as a function of thickness of CoPd layer in Fig. 4.4.2(a), where the  $K_{eff}$  increases with the thickness of CoPd alloy. It is observed that the magnitude of  $M_{TRM}$  decreases with increasing the thickness of the CoPd layer. This is also indicated from the  $M(H)$  loops of these CoPd samples (see Fig. 4.4.1), where the saturation magnetization ( $M_S$ ) decreases with increasing the thickness of the CoPd layer. The only difference is that in  $M(H)$  loops of sole CoPd samples, the  $M_S$  of the thin sample remains larger over the whole temperature range, i.e., at higher temperatures too. As for  $M(H)$  loops, the magnetic field was present during the whole measurement process which aligned the spins of thin CoPd alloy more easily along its direction (as discussed in section 4.4.4). While in the  $M_{TRM}$  measurements, SRT is easily visible as there is no external magnetic field which could effect the direction of the spins of CoPd alloy, especially for the thin sample. Furthermore, the  $M_{TRM}$  measurements of CoPd samples also confirmed the previous discussion related to the magnetic anisotropy of the CoPd alloy in section 4.4.4.

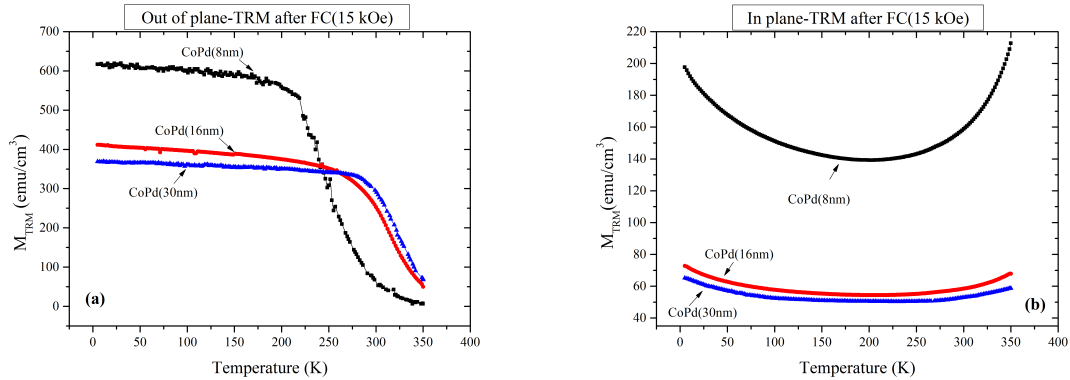


Figure 4.6.2: Temperature dependence  $M_{TRM}$  of sole CoPd samples with 8 nm, 16 nm and 30 nm thickness. (a) along OP direction, (b) along IP direction.

The SRT is also observed in the exchange biased samples. The  $M_{TRM}$  measurements of the CoPd/IrMn samples under the same condition as for sole CoPd samples are presented in Fig. 4.6.3. The  $M_{TRM}$  measurement of CoPd(8 nm)/IrMn(15 nm) along OP direction shows that SRT starts at very high temperature, the IP curve does not show the SRT up to 350 K. This is the evidence of the strong perpendicular anisotropy in this sample. CoPd(16 nm)/IrMn(15 nm) also depicts SRT around 205 K, with the sudden decrease in the OP  $M_{TRM}$  curve and increase in the IP  $M_{TRM}$  curve.

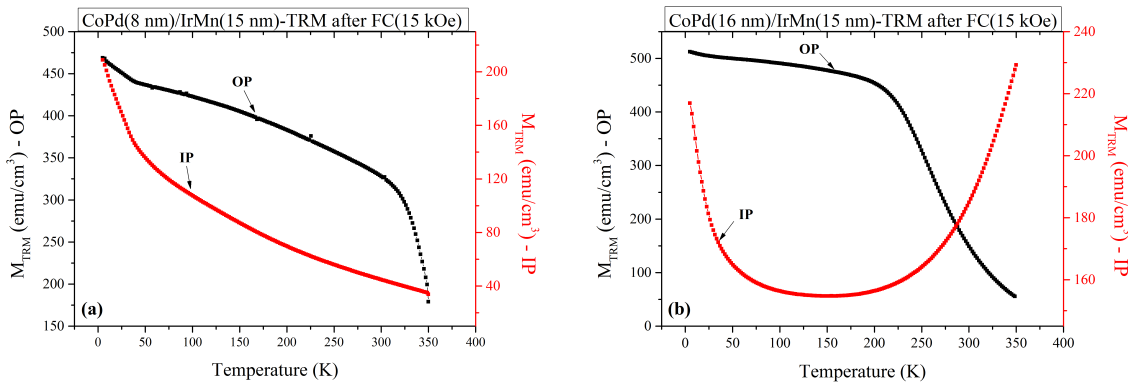


Figure 4.6.3:  $M_{TRM}$  versus temperature measurements after field cooling in 15 kOe, then heating in zero field from 5 K to 350 K along OP (black curve, left scale) and IP (red curve, right scale) directions; (a) CoPd(8 nm)/IrMn(15 nm) sample, (b) CoPd(16 nm)/IrMn(30 nm) sample.

Fig. 4.6.4 illustrates the  $M_{TRM}$  measurements of exchange biased sample of different thicknesses of CoPd layer along IP and OP directions after field cooling in 15 kOe

and then measuring during heating in the absence of magnetic field as done with sole CoPd samples. With increase in the thickness of CoPd layer, SRT moves to lower temperatures. It indicates that the direction of the magnetization of exchange biased samples containing thicker CoPd alloy can easily transform to IP which results into decrease in perpendicular anisotropy of the system with increasing the thickness of CoPd layer. By comparing the SRT behaviour with sole CoPd samples, it is observed that as a function of CoPd layer thickness, SRT behaves oppositely in CoPd/IrMn samples as compared to sole CoPd.

From the SRT measurements, it is clear that in the exchange biased samples, the perpendicular anisotropy decreases with increasing the thickness of CoPd layer contrary to behaviour in sole CoPd samples. This opposite dependence of perpendicular anisotropy on CoPd layer in sole CoPd and exchange biased samples is explained in the next section 4.7.

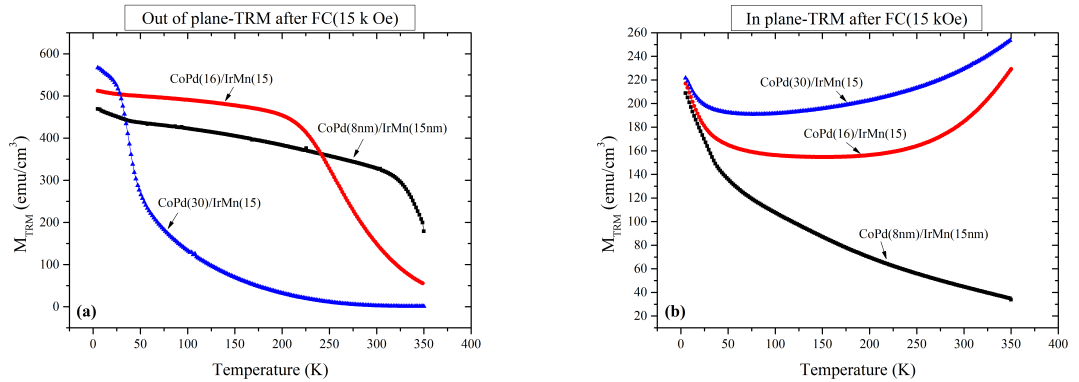


Figure 4.6.4: Temperature dependence  $M_{TRM}$  of CoPd(x nm)/IrMn(15 nm) samples where x=8 nm, 16 nm and 30 nm. (a) along OP direction, (b) along IP direction.

## 4.7 Anomalous change in the anisotropy of CoPd/IrMn system

Before explaining this section, some previous experimental results of sole CoPd samples are again shown here in order to compare these results with the exchange biased samples, related to the observation of the anomalous change in the anisotropy of the system.

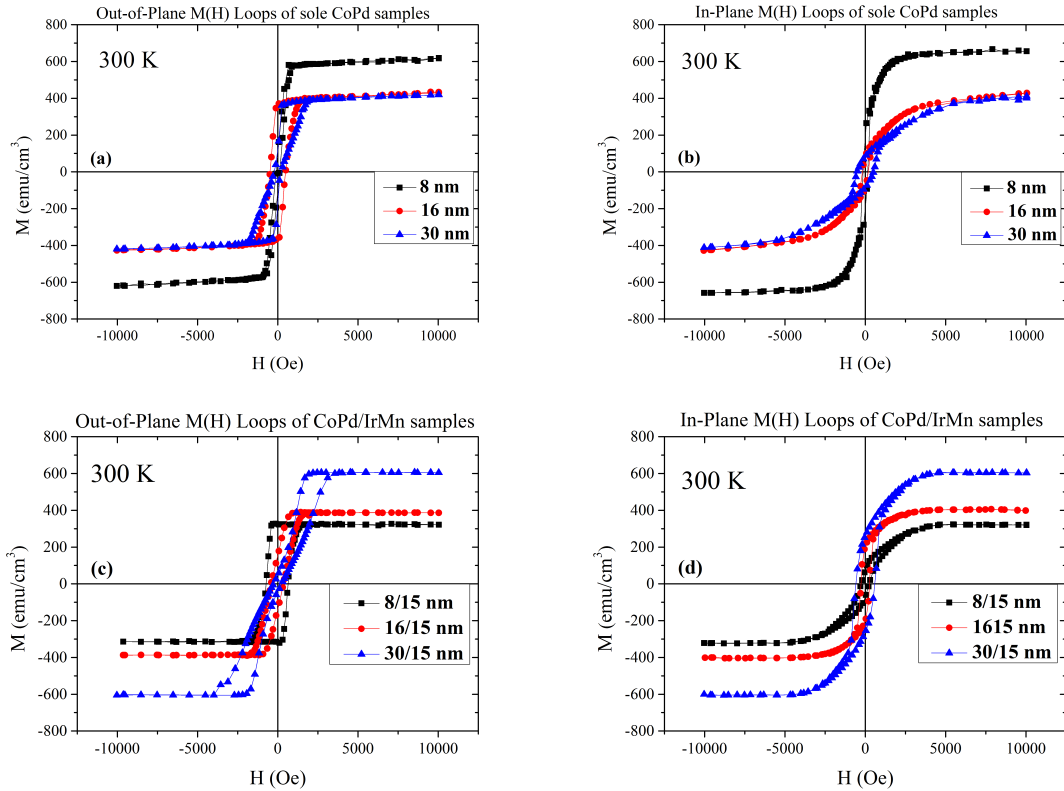


Figure 4.7.1: Hysteresis loops at 300 K of CoPd samples (along OP direction (a), along IP direction (b)) and CoPd/IrMn samples (along OP direction (c) and along IP direction (d)) with different thicknesses of CoPd.

The study of sole CoPd samples in section 4.4.4 resulted that the perpendicular anisotropy becomes stronger with increasing the thickness of the CoPd layer. In order to get exchange bias, IrMn is deposited on the top of CoPd layer. For the exchange biased samples, the magnetic anisotropy as a function of the thickness of CoPd layer now behaves oppositely as compared to the sole CoPd samples . The CoPd(x nm)/IrMn(15 nm) samples in Fig. 4.7.1(c) and (d), containing thinner CoPd have stronger anisotropy along perpendicular direction compared to the IP-direction. Also the  $M_S$  increases with increasing the thickness of the CoPd layer in CoPd/IrMn samples, while M(H) loops of sole CoPd samples show opposite behaviour (see Fig. 4.7.1(a) and (b)). The angle of the remanent magnetization w.r.t. the horizontal plane of CoPd/IrMn samples is shown in Fig. 4.7.2(b). With increasing the thickness of CoPd layer in exchange biased samples, the CoPd spins move toward IP, which shows the decrease in the perpendicular anisotropy. The spins of CoPd/IrMn system are directed toward OP direction at low temper-

atures. With increase in the temperature, the spins of CoPd(8 nm)/IrMn(15 nm) stayed remain along OP direction but the angle of thermoremanent magnetization of CoPd(30 nm)/IrMn(15 nm) sample is drastically reduced because of SRT or weak perpendicular anisotropy. This shows that change in the temperature has strong effect on the exchange biased samples containing thicker CoPd layer. On the other hand, the angle of thermoremanent magnetization of sole CoPd samples increases with the thickness of CoPd layer and the effect of temperature is strongest in CoPd(8 nm) sample.

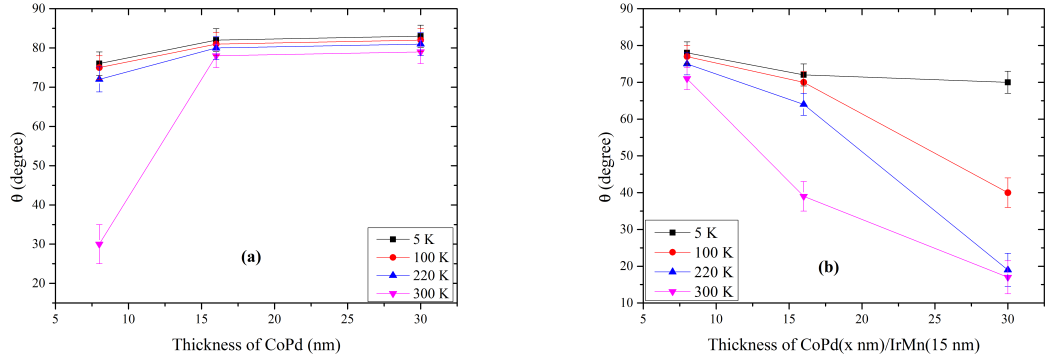


Figure 4.7.2: Angle of  $M_r$  with horizontal plane  $\theta$ , as a function of CoPd film's thickness in (a) sole CoPd(x nm) samples and (b) CoPd(x nm)/IrMn(15 nm) samples.

Fig. 4.7.3 shows the effective magnetic anisotropy ( $K_{eff}$ ) calculations of sole CoPd and exchange biased samples as a function of the thickness of CoPd ( $t_{CoPd}$ ) layer in these samples. The  $K_{eff}$  of the exchange biased samples is also determined from the area enclosed between the IP and OP hysteresis loops, where these loops are measured in the field of 30 kOe. The effective anisotropy of sole CoPd samples and CoPd/IrMn samples behaves totally opposite. In sole CoPd samples from all measurements which are discussed so far (like hysteresis loops, angle of remanent magnetization, SRT and effective anisotropy), it is found that with increasing the thickness of CoPd the perpendicular anisotropy becomes stronger. In the exchange biased samples the perpendicular anisotropy becomes weak when the thickness of CoPd layer increases. This is the anomalous behaviour where the anisotropy of FM as a function of thickness behaves in reverse order as when an AFM is deposited on the top of FM. Therefore, IrMn is the reason of changing the anisotropy behavior of CoPd alloy.

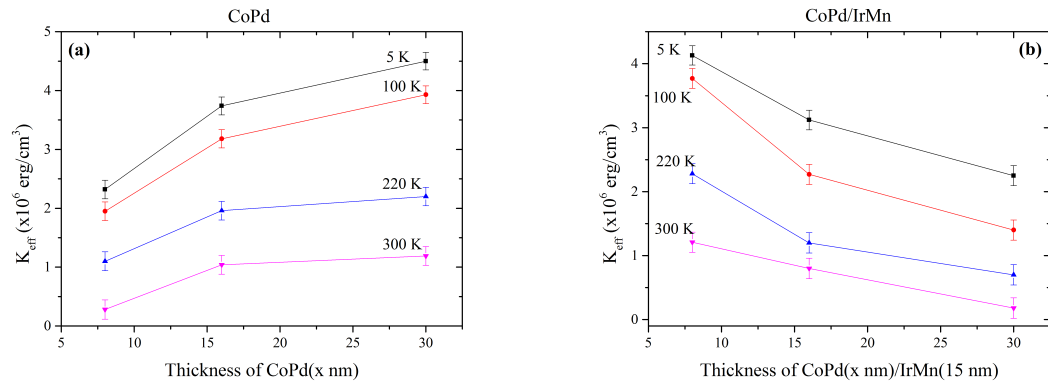


Figure 4.7.3: CoPd thickness dependence of  $K_{eff}$  for (a) sole CoPd(x nm) samples and (b) CoPd(x nm)/IrMn(15 nm) samples.

From the study of magnetic anisotropy in both CoPd and CoPd/IrMn systems, beside the simple observation that magnetic anisotropy behaves oppositely as a function of thickness of CoPd layer, there are other important observations that

1. The perpendicular magnetic anisotropy of CoPd(8 nm)/IrMn(15 nm) sample becomes stronger than CoPd(8 nm) sample.
2. The perpendicular magnetic anisotropy of CoPd(16 nm)/IrMn(15 nm) and CoPd(30 nm)/IrMn(15 nm) samples is weak as compared to CoPd(16 nm) and CoPd(30 nm) samples, respectively.

These observation are also easily deduced from the  $M_{TRM}$  measurements of sole CoPd and exchange biased samples along the OP direction as shown in Fig. 4.7.4. The SRT temperature value of CoPd(8 nm)/IrMn(15 nm) is higher than CoPd(8 nm) sample while the SRT in CoPd(16 nm)/IrMn(15 nm) and CoPd(30 nm)/IrMn(15 nm) samples occurs at low temperatures as compared to CoPd(16 nm) and CoPd(30 nm) samples, respectively.

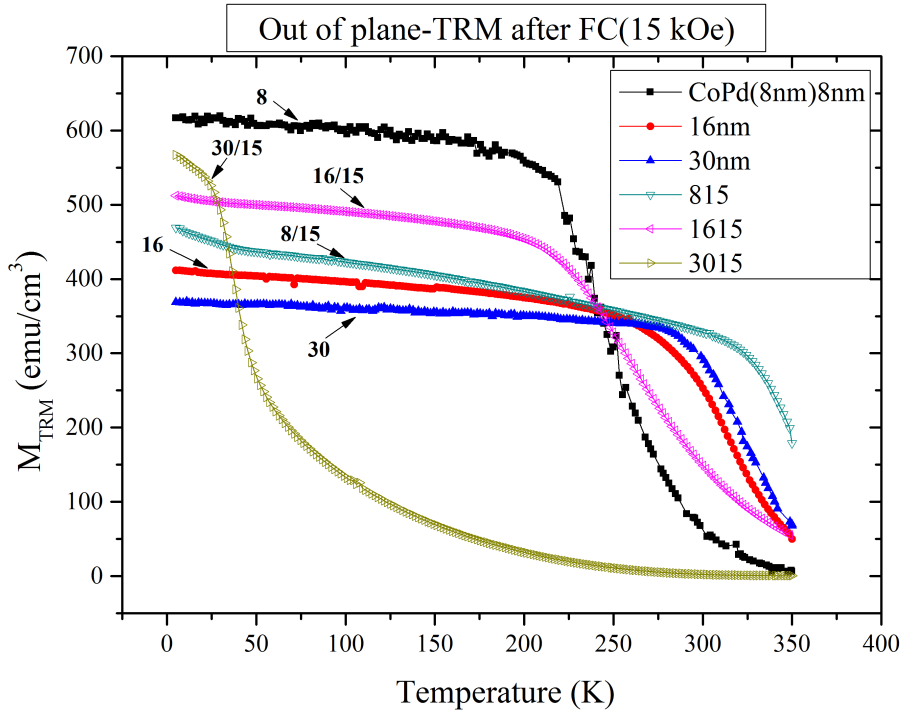


Figure 4.7.4: Temperature dependence  $M_{TRM}$  of CoPd( $x$  nm) and CoPd( $x$  nm)/IrMn(15 nm) samples where  $x=8$  nm, 16 nm and 30 nm along OP direction. Filled symbols represent CoPd samples and empty symbols are for CoPd/IrMn samples.

The increase in the perpendicular anisotropy of CoPd(8 nm) sample after the deposition of IrMn is understood by the 3Q spin structure of IrMn. The spin structure of IrMn is discussed earlier, having strong effect on the behaviour of exchange bias. The 3Q spin structure of IrMn favours OP direction, therefore, it enhances the perpendicular anisotropy of the CoPd(8 nm) and extends the temperature range in which CoPd preserves the perpendicular orientation. One can also expect the same effect of 3Q spin structure of IrMn on the thicker CoPd films, but it is contrary to the thin CoPd sample. In the thicker CoPd exchange biased samples, instead of increase in the perpendicular anisotropy due to 3Q spin structure of IrMn, the perpendicular anisotropy is decreased, especially there is a drastic decrease in the perpendicular anisotropy of CoPd(30 nm)/IrMn(15 nm) sample. In order to investigate the reason of this decrease in perpendicular anisotropy, factors other than spin structure of IrMn should be considered.

#### 4.7.1 Interpretation

The increase in the perpendicular anisotropy of FM (Pt/Co-multilayers) because of AFM (IrMn and FeMn) is also observed by Sort et al.<sup>95</sup>. This is not explained on the basis of spin structure of AFM, just related to the additional anisotropy induced to the FM by AFM. The thickness of FM and AFMs are fixed so there is no information in case of thicker FM. For CoPd(8 nm)/IrMn(15 nm) sample, it is clear that the increase in the magnetic anisotropy of CoPd is related to 3Q spin structure of IrMn which induces an additional perpendicular anisotropy to CoPd layer.

In the EB systems, the interface between coupled FM and AFM plays a crucial role besides this, the bulk structure of AFM also plays a significant role in the pinning of uncompensated spins (UCS) at the interface<sup>96</sup>. From the experimental results, it is cleared that the sole CoPd(8 nm) sample has smaller  $K_{eff}$  and the spins can easily affect by the external force like external magnetic field as compared to the thicker ones. Moreover, the spins of sole CoPd(8 nm) sample are tilted toward more IP, i.e., at an angle of 30° at room temperature. Also in 3Q structure, the IrMn spins are canted at an angle of 19.5°. Therefore, when IrMn is deposited on the top of CoPd(8 nm) layer at room temperature, the angle between the spins of CoPd and IrMn is smaller as compared to the angle between the spins of IrMn and thicker CoPd layers. As the interfacial exchange interaction depends upon the cosine of the angle between the FM and AFM magnetic moments<sup>76</sup>. It implies that in CoPd(8 nm)/IrMn(15 nm), the exchange interaction between the spins of IrMn and CoPd is stronger which results in the strong control of thinner CoPd alloy by spin structure of IrMn. This is also evident from the experimental results of  $H_{EB}$  and magnetization measurements versus temperature, where the effect of spin structure of IrMn is clearly visible for CoPd(8 nm)/IrMn(15 nm) sample as compared to the thicker ones. The 3Q spin structure is not related to any interface phenomenon, it is related to the bulk spin structure of IrMn. Therefore, in CoPd(8 nm)/IrMn(15 nm) sample, the bulk spin structure of IrMn is retained at the interface and plays an important role in order to control the anisotropy of the system.

Now CoPd(16 nm)/IrMn(15 nm) and CoPd(30 nm)/IrMn(15 nm) samples are considered. The spins of sole CoPd(16 nm) and CoPd(30 nm) samples are canted more OP and have stronger  $K_{eff}$  (see Fig 4.7.2(a) and Fig. 4.7.3(a)). Therefore, during the deposition of IrMn on the top of these CoPd layers, the angle between CoPd and IrMn spins becomes larger and also the CoPd spins do not respond strongly to IrMn layer having weak proximity effect. This results in weak exchange interaction

between the spins of IrMn and CoPd at interface. This weakens the effective control of bulk spin structure of IrMn on CoPd spins, producing spin frustration and disturbing the 3Q spin structure of IrMn at the interface. The interface UCS, roughness because of the defects and disorders at interface cause the spins of AFM to move from OP to IP direction<sup>97,98</sup>. The effect of AFM on the FM's anisotropy is also observed in FeMn/Ni/Cu(001) epitaxial sample, it is observed that the FeMn layer changes the Ni spin direction from OP to IP direction, which is related to the formation of additional anisotropy because of OP spin frustration at FeMn-Ni interface<sup>99</sup>. The spin frustration at the interface may cause the new additional anisotropy which favours IP orientation. This makes the role of interface more stronger as compared to the bulk IrMn structure where 3Q spin structure is destroyed at the interface because of spin frustration.

The decrease of perpendicular anisotropy is more pronounced with increasing the thickness of CoPd in exchange biased samples. The reasons are the increased angle difference between CoPd and IrMn spins and increased  $K_{eff}$  of CoPd underlayer with thickness. The result is decreased exchange interaction between both spins at interface. This increases spin frustration at the interface which damaged the 3Q spin structure of IrMn more and makes the additional anisotropy more stronger to favour enhanced IP orientation.

In conclusion, the two phenomena, i.e., increase and decrease in the perpendicular anisotropy of FM due to AFM, occur in the same FM and AFM system but depends upon the thickness of FM. In thin CoPd exchange biased sample, bulk spin structure of IrMn plays more stronger role. The 3Q spin structure is retained at interface and enhances the perpendicular anisotropy. While in the thicker CoPd exchange biased samples, the 3Q spin structure is destroyed at interface due to spin frustration, diminishing its effect and causing the IP anisotropy in these samples. This is also observed from the  $H_{EB}$  versus temperature measurements (see Fig. 4.5.2) and M(T) measurements (see Fig. 4.5.6 and Fig. 4.5.7), where 2Q-3Q transition is more pronounced in CoPd(8 nm)/IrMn(15 nm) sample and  $T_f$  is higher than other samples.

## 4.8 Summary of the chapter

In this chapter, the perpendicular anisotropy of sole  $Co_{27}Pd_{73}$  alloy and the perpendicular exchange bias in  $Co_{27}Pd_{73}/Ir_{23}Mn_{77}$  system are discussed with various

thicknesses of CoPd. The perpendicular anisotropy is found in CoPd alloy and strongly depends upon the thickness of CoPd alloy film. It is found that the spins of CoPd alloy are not exactly directed along OP direction, rather they are tilted at a certain angle depending upon the thickness of CoPd alloy. With increasing the thickness of sole CoPd film, the  $K_{eff}$  increases and the perpendicular anisotropy becomes stronger. The  $M_S$  increases with decreasing the thickness of the CoPd alloy. This is because of the weak  $K_{eff}$  of thin sole CoPd sample, where the tilted spins easily follow the external field resulting large  $M_S$ .

The perpendicular exchange bias is observed in  $Co_{27}Pd_{73}/Ir_{23}Mn_{77}$  system. The exchange bias is strongly affected by the spin structure of IrMn. The 2Q spin structure of IrMn favours IP while the 3Q structure favours OP direction. The spin structure transition of IrMn from 2Q to 3Q is also observed in the exchange bias and magnetization versus temperature measurements, which is more pronounced in CoPd/IrMn samples containing thin CoPd layer. The sole IrMn sample is also measured along IP and OP directions, revealing 2Q-3Q spin structure transition. The SRT is observed in the exchange biased samples due to CoPd layer and has no effect on the EB. In the sole CoPd samples, the SRT occurred at high temperatures with increasing the thickness, while in the exchange biased samples containing thicker CoPd layer, SRT is observed at low temperatures.

The behaviour of  $K_{eff}$  as a function of thickness of CoPd( $t_{CoPd}$ ) layer is opposite in sole CoPd samples as compared to CoPd/IrMn samples. The perpendicular anisotropy increases with increasing  $t_{CoPd}$  in unbiased samples while it decreases with increasing  $t_{CoPd}$  in exchange biased samples. This anomalous behaviour of  $K_{eff}$  as a function of  $t_{CoPd}$  in exchange biased samples, is related to the importance of bulk spin structure of IrMn and the different anisotropy at the interface for the thinner and thicker CoPd layers in CoPd/IrMn system, respectively. The 3Q spin structure (which favours OP direction) of IrMn enhances the perpendicular anisotropy of CoPd(8 nm)/IrMn(15 nm) sample, where the bulk of IrMn plays more important role as compared to interface. On the other hand, in CoPd(16 nm)/IrMn(15 nm) and CoPd(30 nm)/IrMn(15 nm) samples, the spin frustration at the interface due to the larger angle difference between CoPd and IrMn spins, causes an additional anisotropy which favours IP direction of the spins. During the deposition of IrMn on the top of CoPd layer, the angle difference between the CoPd and IrMn spins at the interface becomes larger for thicker CoPd layers, so the spin frustration enhances at interface in the case of thicker CoPd layer, which in-

duces stronger IP anisotropy. Consequently, the exchange biased samples containing thicker CoPd layer, have weaker perpendicular anisotropy.



# Chapter 5

## The study of spin dynamics, Morin transition, shape anisotropy, exchange bias and silica coating in hematite nanoparticles

### 5.1 Introduction

Iron (III) oxide or ferric oxide has following phases, alpha phase ( $\alpha\text{-Fe}_2\text{O}_3$ ), beta phase ( $\beta\text{-Fe}_2\text{O}_3$ ), gamma phase ( $\gamma\text{-Fe}_2\text{O}_3$ ) and epsilon phase ( $\varepsilon\text{-Fe}_2\text{O}_3$ ). Among iron oxides, hematite ( $\alpha\text{-Fe}_2\text{O}_3$ ) is the most stable phase under ambient conditions and is the most commonly found iron oxide in nature. A lot of attention has been given to synthesize and characterize the hematite nanoparticles due to their applications in different fields of technologies, such as solar cells, antcorrosive agents, sensor devices, batteries and catalysis. This vast range of applications motivate us to understand the fundamental properties of hematite nanoparticles<sup>100</sup>.

Bulk hematite has corundum crystal structure, it is refined either in rhombohedral or hexagonal space group. The oxygen (O) anions lie in hexagonal close-packed layers and iron (Fe) cations occupy two thirds of octahedral sites<sup>101</sup>. The primitive cell is rhombohedral that contains two molecules of  $\text{Fe}_2\text{O}_3$ . Bulk hematite orders antiferromagnetically below the Néel temperature ( $T_N=955$  K). Additionally, it shows another magnetic phase transition that is related to the spin re-orientation of Fe ions called Morin transition around 263 K, denoted as Morin temperature

( $T_M$ ). The rhombohedral (111) planes (c-planes in the hexagonal setting) form the layers of Fe ions which are separated by the layers of O ions. The spins of Fe ions in any (111) plane remain parallel with each other but antiparallel with the adjacent planes. Above  $T_M$ , Fe spins lie along the (111) planes but are slightly canted which produces uncompensated magnetic moment. This is the reason of weak ferromagnetism in hematite above Morin transition. When the temperature decreases below  $T_M$ , the spins of Fe ions change theirs directions from in plane to out of plane w.r.t. (111) plane. The spins are then completely perpendicular to (111) plane and there is no spin canting. In any (111) plane, Fe ions are directed upward, however, they are directed downward in the adjacent planes. In the given (111) plane Fe ions are parallel with each other. This re-orientation of Fe spins below  $T_M$  presents perfect antiferromagnetic order in hematite<sup>102-104</sup>.

## 5.2 Sample preparation and structural analysis

### 5.2.1 Synthesis

The magnetic study of hematite nanoparticles reported here were synthesized in collaboration with Karla Doermbach and Prof. Dr. Andrij Pich at DWI institute, RWTH Aachen University<sup>105</sup> and I am thankful for providing the samples. To synthesize dispersions of uniform hematite nanoparticles a precipitation method following approach of Matijevic and co-workers was used<sup>106</sup>. In a general procedure, 1000 mL of a 0.02 M  $\text{FeCl}_3$  solution containing  $\text{NaH}_2\text{PO}_4$  in concentration ranging between 0 M to  $4.5 \times 10^{-4}$  M was heated to boiling point under reflux conditions. If  $\text{NaH}_2\text{PO}_4$  was added, ellipsoidal particles were obtained, otherwise spherical particles were synthesized. The solution was kept at boiling point for the next 48 hrs. Afterward, the dispersion was cooled down to room temperature and the solvent was removed partially by vacuum evaporation. The particles were collected from the concentrated dispersion with an Eppendorf Centrifuge 5810 by centrifuging at about 12,900 rcf for 10 min. The precipitates obtained by this method were repeatedly centrifuged and washed with deionized water to remove excess ions from the dispersion.

The size and the shape of different hematite nanoparticles undertaken depend upon their aspect ratios (the ratio between major and minor axes) which vary from 1 (for spherical shape) to 6 (for spindle shape). The four samples of hematite nanoparticles

having different aspect ratios have been studied. These samples are named as sample A, sample B, sample C and sample D containing nanoparticles of aspect ratio of 1, 1.5, 4.4 and 6, respectively, as shown in Table 5.1.

Sample Name	Major Axis (nm)	Minor Axis (nm)	Aspect Ratio
Sample A	73	73	1
Sample B	98	67	1.5
Sample C	223	51	4.4
Sample D	246	41	6

Table 5.2.1: Size of the hematite nanoparticles of different samples undertaken for experimentation.

### 5.2.2 Structural characterizations

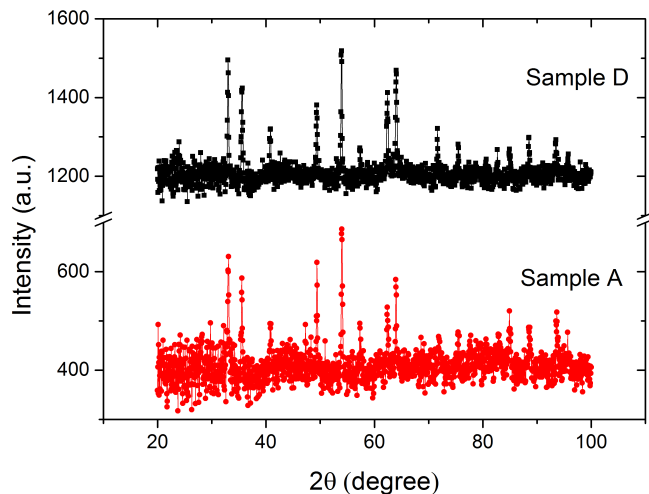


Figure 5.2.1: X-ray diffraction of hematite nanoparticles of sample A and sample D.

The x-ray measurements of hematite nanoparticles were carried out at room temperature using Cu  $K\alpha$  radiation ( $\lambda = 1.5406$  Å). Fig. 5.2.1 shows the x-ray diffraction pattern (XRD) of samples A (spherical; aspect ratio:1) and D (spindle shaped; aspect ratio:6). No additional peak is observed related to other possible phase of

iron oxide, thus confirming pure hematite phase in these crystalline nanoparticles. Also, the given XRD result is similar to reported XRD pattern of pure hematite nanoparticles<sup>107-110</sup>.

,

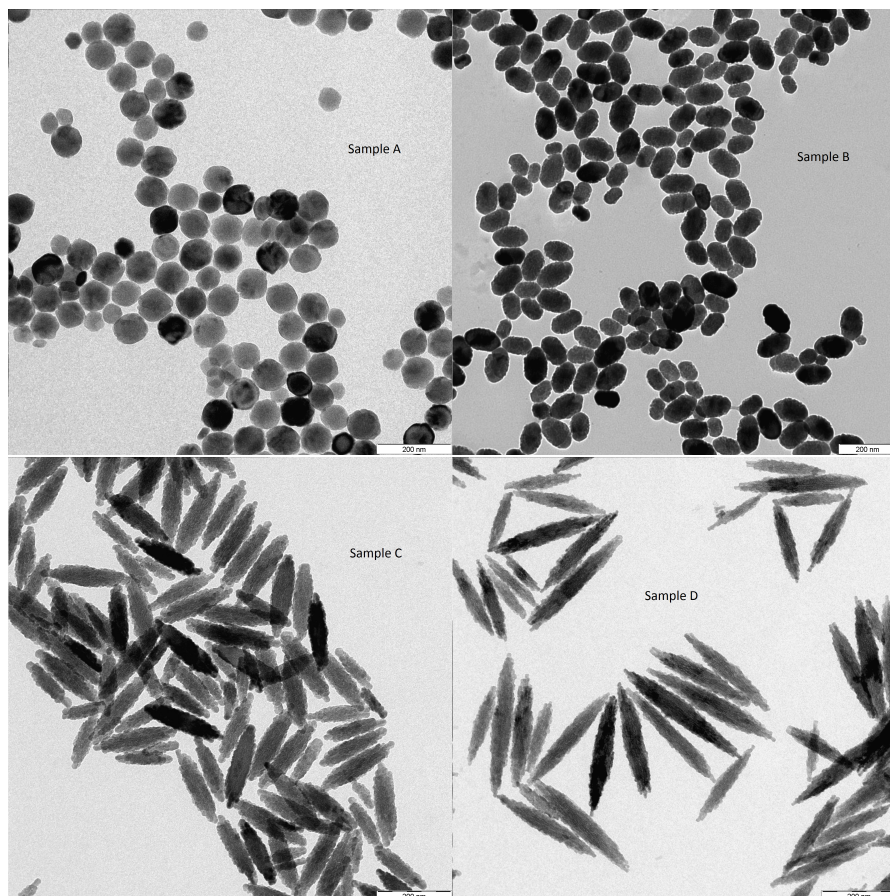


Figure 5.2.2: TEM images of hematite nanoparticles of sample A, sample B, sample C and sample D

The transmission electron microscopy (TEM) was measured on Zeiss Libra TM 120. The electron beam accelerating voltage was set at 120 kV. The TEM images of given samples of hematite nanoparticles are shown in Fig. 5.2.2, which confirm the spherical shaped nanoparticles in sample A, ellipsoidal in sample B and spindle like in samples C and D. The uniformity in the shape of the nanoparticles of the given sample, is also conformed from the TEM image. The length of major and minor axes of the nanoparticles were measured through TEM measurements (shown in Table. 5.1). The sizes of hematite nanoparticles which are studied in this chapter, are in the range of single domain (SD). The grain size limit of SD hematite nanoparticles

is usually large and nanoparticles below 450 nm are SD<sup>111;112</sup>.

### 5.3 Magnetic characterization of hematite nanoparticles

I have studied the magnetic characterizations of these hematite nanoparticles using SQUID magnetometer (MPMS XL-7) at II. Physikalisches Institut A, RWTH Aachen University. The powder form of these hematite nanoparticles were encapsulated in small teflon capsule for the magnetic measurements. The magnetic moment of teflon capsule is very small as compared to these hematite nanoparticles, so its contribution is negligible.

#### 5.3.1 Study of exchange bias

To study exchange bias (EB) phenomenon in these hematite nanoparticles, the samples were field cooled from 350 K to 5 K in different cooling fields applied along positive direction. The measurements of magnetization versus field loops (MH-loops) were started from 5 K and then to higher temperatures, subsequently. Prior to these measurements, an additional hysteresis loop was measured at 5 K, in order to reduce the training effect. The exchange bias field ( $H_{EB}$ ) and coercive field ( $H_C$ ) were determined from left and right coercive fields ( $H_C^{Left}$ ,  $H_C^{Right}$ ) of hysteresis loop, where  $H_{EB}=(H_C^{Left}+H_C^{Right})/2$  and  $H_C=-(H_C^{Left}-H_C^{Right})/2$ .

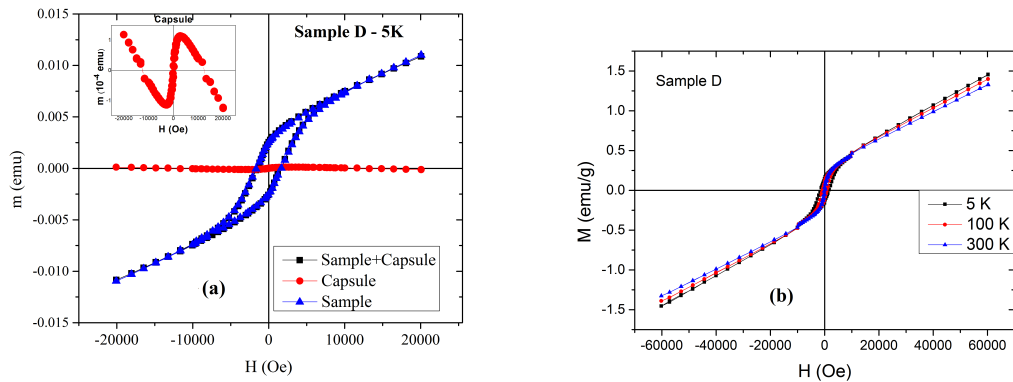


Figure 5.3.1: (a)  $M(H)$  loops show the magnetic moment ( $m$ ) of empty capsule and sample D, inset shows magnetic response of empty capsule; (b) Magnetization versus field,  $M(H)$  loops of sample D at different temperatures after field cooling in 60 kOe;

The four samples of hematite nanoparticles with different aspect ratios were studied. In this section, the magnetic properties of samples B (aspect ratio 1.5), C (aspect ratio 4.4) and D (aspect ratio 6) having aspect ratio greater than 1 are discussed. While sample A (aspect ratio 1) will be discussed in the next section. Fig. 5.3.1(a) shows the magnetic moment ( $m$ ) of empty teflon capsule and sample D at 5 K at 2T filed, the background signal is subtracted, in order to get magnetic response of hematite nanoparticles. It is found that there is negligible effect of background signal of empty capsule. Fig. 5.3.1(b) indicates the field cooled hysteresis loops of sample D at different temperatures, which present clearly the ferromagnetic behaviour over all temperature values.

It is found that 60 kOe field is not sufficient to saturate the nanoparticles, as shown in the hysteresis loops in Fig. 5.3.1(b). The increase in the magnetization with external field is related to the presence of weak ferromagnetic phase. As the magnitude of the external magnetic field is increased, the randomness of ferromagnetic spins decreases and the alignment along the field direction is enhanced that contributes to the magnetization<sup>113</sup>. The MH-loops of samples B and C also show similar hysteresis behaviour indicating the presence of ferromagnetic phase in these nanoparticles over the whole temperature range. There is no clear indication of Morin transition in these nanoparticles till 5 K.

The behaviour of  $H_{EB}$  as a function of temperature of the samples B, C and D is shown in Fig. 5.3.2(a). The presented results are taken from the hysteresis loops where the cooling and measuring field is 20 kOe. At lower temperatures,  $H_{EB}$  is positive, i.e., hysteresis loop shifts towards right in the direction of cooling field. With increase in temperature, magnitude of  $H_{EB}$  decreases and becomes to zero at higher temperatures. Altough, there are small variations at temperature higher than 150 K but the error bars show that values are in the range of zero field.

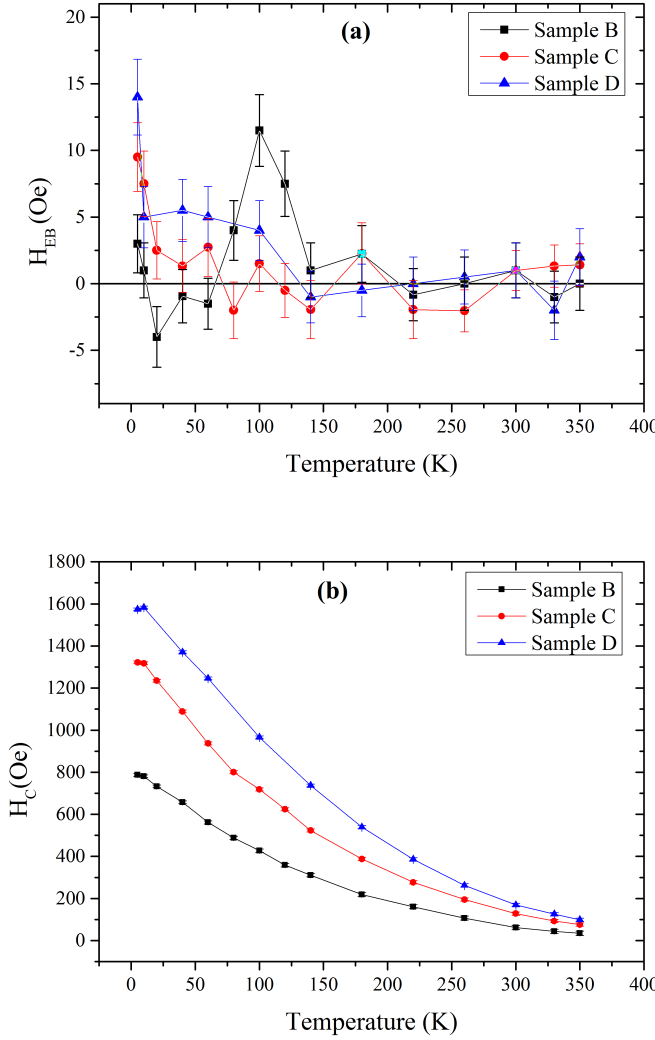


Figure 5.3.2: Temperature dependence of (a) an exchange bias field ( $H_{EB}$ ) and (b) coercive field ( $H_C$ ) of samples B, C and D in the cooling field of 20 kOe.

From the EB behaviour of these three samples, the magnitude of  $H_{EB}$  is larger for the sample D. This indicates the dependence of EB phenomenon on the size and shape of Hematite nanoparticles. Where,  $H_{EB}$  is well established in the sample D, i.e., spindle shaped nanoparticles (with maximum aspect ratio). The  $H_{EB}$  of sample D decreases sharply from 5 K to 10 K and then there is slow decrease till 132 K, and after that it nearly vanishes.

The EB behaviour of sample B, that has ellipsoidal shape, is deviated from samples C and D at temperatures lower than 140 K. Instead of having maximum  $H_{EB}$  at 5 K, the  $H_{EB}$  has small positive and negative values at low temperatures and

has maximum positive value at 100 K, afterward it has similar behaviour as of samples C and D. This anomaly in the  $H_{EB}$  of sample B around 100 K is related to Morin transition and will be discussed later. From the temperature dependence of  $H_C$  (shown in Fig. 5.3.2(b)), it is clear that sample D (having maximum size) has largest  $H_C$  and it decreases with decrease in the size of nanoparticles. This increase in the  $H_C$  with increasing size of nanoparticles also verifies that these hematite nanoparticles are SD, because in multi-domains nanoparticles,  $H_C$  decreases with increasing size of nanoparticles<sup>114</sup>.

### 5.3.2 Study of spin dynamics and spin glass behaviour

Usually, the effect of EB is observed in the nanoparticles having conventional core/shell structure, where the core is ferromagnet (FM) and the shell is antiferromagnet (AFM). In this core/shell structure, shell is not always typical AFM but can be spin glass (SG) in order to produce EB<sup>115,116</sup>. The hematite nanoparticles which are studied here, do not have any specific core/shell structure. The presence of EB in these nanoparticles indicates the presence of another magnetic phase which causes the pinning of the spins of hematite weak ferromagnetic part. In the nanoparticles without clear core/shell structure, exchange bias is generated due to the SG behaviour of surface spins, where the surface disorders produce frustration in the surface spins<sup>117-120</sup>.

In the SD magnetic nanoparticles (superspin: magnetic moment of a SD nanoparticle), there are two possible origins of slow dynamics, depending upon the interaction between nanoparticles. In the weak interacting magnetic nanoparticles, the only source of slow dynamics is the broad distribution of relaxation times originating solely from that of anisotropy energy barriers of each nanoparticle moment. This system of nanoparticles is superparamagnet (SPM). In strong interacting magnetic nanoparticles, there is another possible slow dynamics called cooperative SG dynamics. The reason is the frustration caused by randomness in the particle positions and anisotropy axis orientations with strong dipolar interactions among the particles. Such dense system of nanoparticles exhibit SG behaviour called superspin glass (SSG)<sup>121</sup>. SSG is also the reason of originating EB phenomenon in SD nanoparticles of different systems like  $Fe/\gamma-Fe_2O_3$  nanoparticles<sup>122</sup> and  $BiFeO_3-Bi_2Fe_4O_9$  nanocomposite<sup>123</sup>. The surface contributions are also important in SD nanoparticles, since the number of surface atoms can be comparable to the inner atoms with

decrease in the size of nanoparticle. Therefore, in the single domain nanoparticles, surface SG and SSG both can occur.

According to the literature survey, the EB phenomenon is reported in hematite hollow spheres due to surface paramagnetic and ferrimagnetic attributes<sup>124</sup>. Moreover, in  $\alpha\text{-Fe}_2\text{O}_3$  nanoleaves, the reason is  $\text{Fe}_3\text{O}_4$  phase<sup>125</sup> and in  $[(\text{n-FeO}_x)/\text{C}]_{10}$  multi-layers ( $\alpha\text{-Fe}_2\text{O}_3$  phase), it is due to the interactions between different spin sublattice configurations<sup>126</sup>. In all these three different systems of hematite, Morin transition is absent and negative  $H_{EB}$  is observed which is different from the present case where positive  $H_{EB}$  is observed. In order to investigate the reason of the EB effect in the present  $\alpha\text{-Fe}_2\text{O}_3$  nanoparticles, different magnetic measurements were done. Here, these measurements of sample D are reported as it has more pronounced EB as compared to samples B and C.

#### 5.3.2.1 Magnetization versus temperature measurements and AT-line

The magnetization versus temperature  $M(T)$  measurements were done under different conditions. Zero field cooled (ZFC) curves were obtained after cooling the sample from 350 K to 5 K in zero field and then were measured in the respective field during heating. For field cooled (FC)  $M(T)$  curves, the sample was cooled from 350 K to 5 K in the presence of respective field and the measurement was taken in the same field.

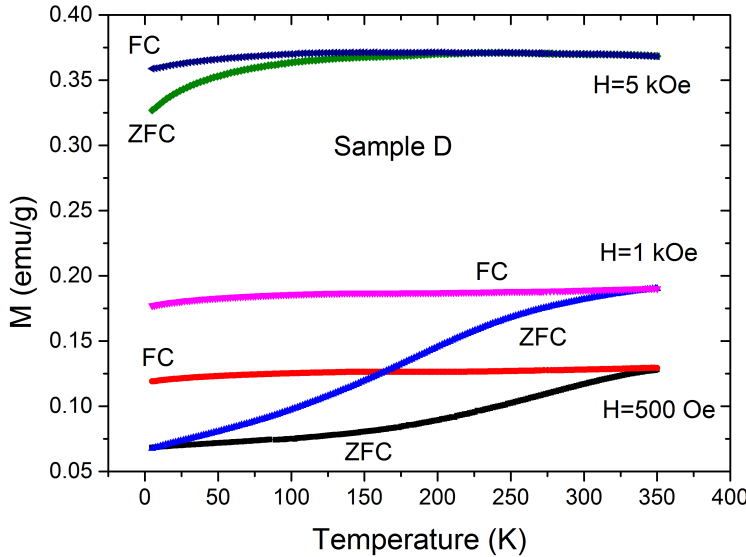


Figure 5.3.3: Zero-field cooled (ZFC) and field cooled (FC) magnetization versus temperature,  $M(T)$  measurements of sample D in 500 Oe, 1 kOe and 5 kOe fields.

Fig. 5.3.3 presents the  $M(T)$  measurements in different magnetic fields. The ZFC magnetization curves of 500 Oe and 1 kOe fields increase with temperature without showing any peak related to blocking temperature ( $T_B$ ). This indicates that the magnetic moments of these nanoparticles are still blocked till 350 K. The FC magnetization curves of 500 Oe and 1 kOe are also shown in Fig. 5.3.4(a), where the magnetization decreases with decrease in temperature, instead of increasing due to the presence of magnetic field. It is observed that the FC magnetization curve of 500 Oe has two peaks, the first peak ( $T_{F1}$ ) is at 348 K and the second peak ( $T_{F2}$ ) at 149 K. This decrease in the FC magnetization clearly indicates the presence of SG phase. As for SPMs, the FC magnetization always increases with decrease in temperature. The reason is the blocking of spins in the direction of applied field<sup>121</sup>. While for the SG phase, the FC magnetization curve does not increase with temperature, either it saturates to a constant value or even decreases with decreasing temperature. In the SG phase, the frustrated spins start freezing and do not align along the external magnetic field, cause decrease in the magnetization. This constant or decreasing behaviour of FC magnetization curve is observed in many SSGs and surface SGs<sup>116;121;127</sup>. The two peaks related to sudden decrease of FC magnetization curve of 500 Oe field, indicate two phases of SG in the hematite nanoparticles of sample D. The sharp decrease in the magnetization below 149 K, indicates that

the SG phase becomes more stronger as more spins freeze.

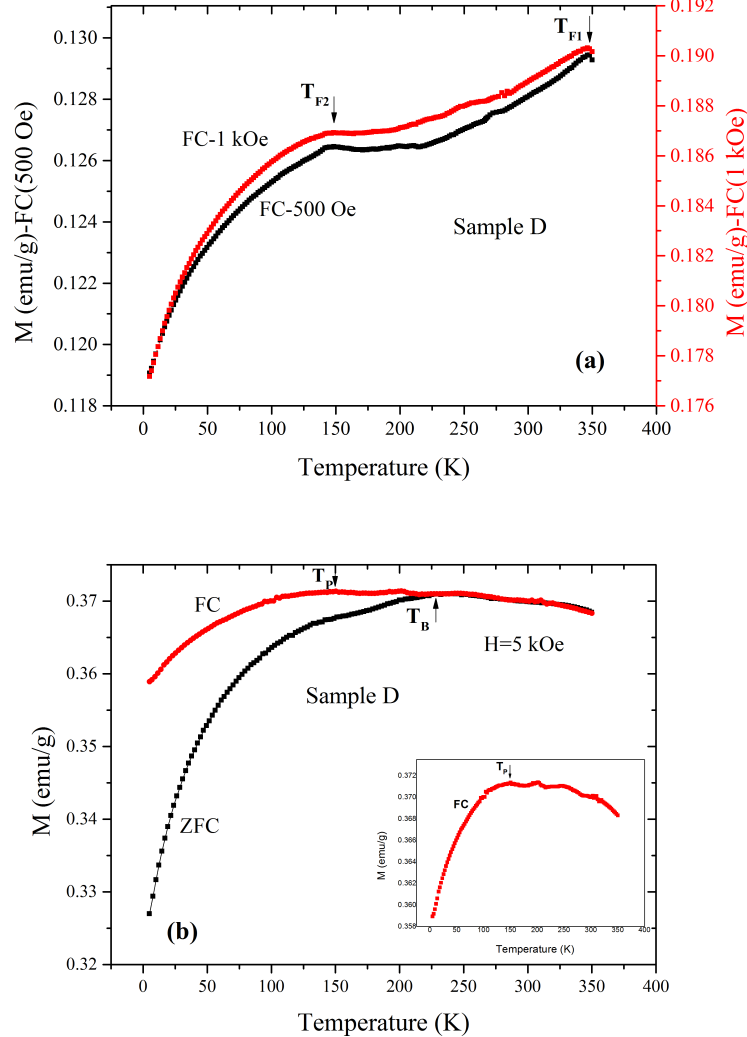


Figure 5.3.4: (a) FC  $M(T)$  measurements of sample D in the fields of 500 Oe (black curve and left scale) and 5 kOe (red curve and right scale); (b) FC and ZFC measurements of sample D in 5 kOe field, inset shows the FC  $M(T)$  curve of sample D in 5 kOe .

The FC magnetization curve in 1 kOe field resembles the  $M(T)$  curve of 500 Oe, having both peaks at the same temperatures (i.e., 348 K and 149 K), approximately. This indicates that the small increase in the magnetic field does not affect the SG phases strongly. However, the FC magnetization curve in 5 kOe field has only single peak around 149 K (see inset in Fig. 5.3.4(b)), indicating the sensitivity of first peak to high fields. In the FC magnetization curves of 500 Oe, 1 kOe and 5 kOe

field, the observed peak at 149 K presents the strong freezing of spins around this temperature. The peak in the ZFC magnetization curve of 5 kOe at 239 K shows the mean  $T_B$  of the nanoparticles (see Fig. 5.3.4(b)). The broadness of the peak is related to the size distribution of nanoparticles.

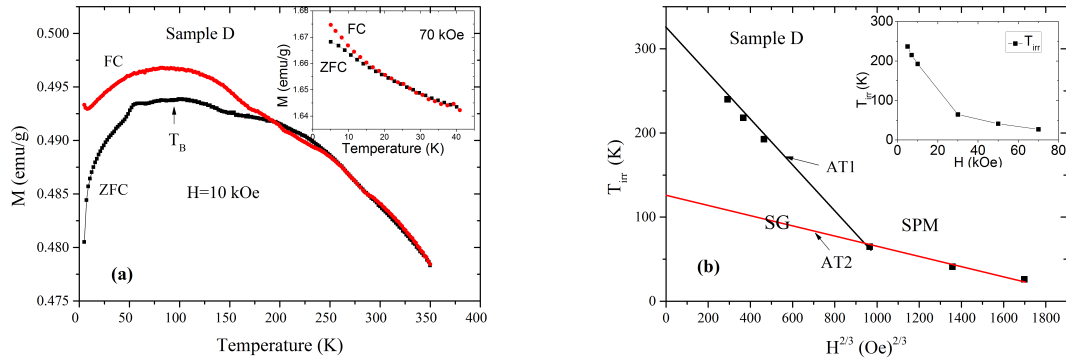


Figure 5.3.5: (a) ZFC and FC  $M(T)$  measurements of sample D in the field of 10 kOe, inset shows the irreversibility in ZFC and FC  $M(T)$  curves in 70 kOe ; (b)  $T_{irr}$  as function of  $H^{2/3}$  exhibits two Almeida-Thouless (AT) lines as shown by black (AT1), and red (AT2) lines. Inset shows the  $T_{irr}$  behaviour versus field.

Fig. 5.3.5(a) presents the FC and ZFC magnetization curves in 10 kOe field. The  $T_B$  decreases from 239 K to 102 K as the field increases from 5 kOe to 10 kOe. In general, the applied magnetic field can decrease the crystal field anisotropy. At high fields, less thermal energy is needed to overcome the barrier between two orientations. Therefore, with increasing the external field,  $T_B$  decreases and eventually disappears at the critical field. Irreversibility is observed in the FC and ZFC magnetization curves below temperature ( $T_{irr}$ ), where the FC and ZFC curves split from each other and corresponds to  $T_B$  of the largest nanoparticles in the system. In general, a few kOe field is enough to wipe out irreversibility related to the blocking process of nanoparticles, when external field surpasses the anisotropy field and particles are saturated. However, irreversibility strongly depends upon anisotropy, dipole-dipole interaction and disordered spins. It has been suggested that irreversibility at high fields is due to the existence of SG phase in the system at the surface of nanoparticles<sup>116;120</sup>. The irreversibility is clearly observed in the FC and ZFC magnetization curves up to 70 kOe field (inset of Fig. 5.3.5(a)) which verifies the presence of disordered spins at the surface in the present system of hematite nanoparticles. The field dependence of  $T_{irr}$  can be used to characterize the SG system. The behaviour of  $T_{irr}$  as a function of the applied field is exhibited in inset

of Fig. 5.3.5(b). According to the mean-field theory, the glassy behaviour of the system will be destroyed above the critical field for a fixed temperature, described by Almeida-Thouless (AT) line in H-T phase diagram. The experimental and theoretical studies show that the AT-line corresponds to the phase boundary between superparamagnetic and SG phase<sup>122;128;129</sup> and is given by,

$$1-T_{irr}/T_f(0) \propto (H/H_a)^{2/3}$$

where  $T_f$  is the freezing temperature at  $H=0$ ;  $H_a=2K_{eff}/\rho M_s$  is the critical field below which SG phase can survive when temperature was supposed to be 0 K.  $K_{eff}$  is the effective anisotropy constant,  $M_s$  is the saturation magnetization and  $\rho$  is the density. The measured dependence of  $T_{irr}$  on  $H^{2/3}$  in both low and high fields regimes is presented in Fig. 5.3.5(b), where instead of one, two AT-lines AT1 and AT2 are obtained depending on the field strength. The AT-line differentiates the SG phase from the superparamagnetic phase, the nanoparticles behave like SG on the left of AT-line and SPM on the right. The presence of two AT-lines indicate two different SG phases in the given hematite nanoparticles. As the y intercept of AT-line indicates the freezing temperature at  $H=0$ , therefore, two different freezing temperatures are observed. For low field regime, y intercept of AT-line AT1 is related to freezing temperature ( $T_{f1}$ ) of 326 K and for high field regime, y intercept of AT2 is  $T_{f2}=127$  K. The AT-line corresponds to  $H^{2/3}$  dependence of temperature and is observed in both surface SG and SSG systems<sup>120;128;130</sup>.

It is important to distinguish the SG phase which corresponds to the low and high field regimes. In the SSG system, the low temperature SG phase is very sensitive to the magnetic field and disappears at high fields, while the surface SG phase can survive at very high fields due to the large effective anisotropy induced by surface anisotropy<sup>128</sup>. Therefore, in the low field regime,  $T_{f1}$  (326 K) relates to the freezing of SSG, while the SG phase in the high fields regime is surface SG whose freezing temperature is 127 K ( $T_{f2}$ ). Thus AT-line infers the coexistence of superparamagnetic, SSG and surface SG phases in the given system.

From the previous study of the FC magnetization, the FC M(T) curves of 500 Oe and 1 kOe have two peaks (see Fig. 5.3.4(a)), first one at 348 K ( $T_{F1}$ ) and second at 149 K ( $T_{F2}$ ). The strong decrease in the FC magnetization indicates the presence of the SG phase. These two peaks correspond to two different SG phases related to freezing of SSG and surface SG at 348 K and 149 K, respectively, which is also confirmed by AT-line. Due to the high field sensitivity, the SSG phase is not clearly indicated by the FC M(T) curve of 5 kOe, having only one prominent peak at 149 K

related to surface SG phase (see Fig. 5.3.4(b)). The freezing temperatures deduced from AT-lines are 326 K and 127 K which are relatively smaller than 348 K and 149 K as indicated from FC M(T) curve for SSG and surface SG, respectively. This difference in the freezing temperature exhibited by AT-line and FC curves, is related to the use of different methods, where curve fitting is used for AT-line. The FC M(T) curve depicts direct indication of SG phases, therefore, 348 K and 149 K are more precise freezing temperatures for the SSG and surface SG phases, respectively.

The presence of the SSG and surface SG phases is also exhibited by the study of the  $H_{EB}$  of the sample D. The  $H_{EB}$  is larger at 5 K and decreases with temperature where it becomes zero at 132 K and then oscillates with small magnitude (see Fig. 5.3.2(a)). As 149 K is the freezing temperature of the surface SG, therefore, below 132 K, the presence of strong  $H_{EB}$  presents the onset of stronger surface SG phase. The presence of weak EB field at higher temperatures is related to the SSG phase. From this study, it is concluded that both SSG and surface SG phases exist in the present hematite nanoparticles, along with superparamagnetic phase at higher temperatures and at large fields. These nanoparticles can be considered as core-shell structure, where the core of nanoparticles is weak FM with SSG behaviour, while the shell comprises the surface SG part. The existence of the broken bounds and the translational symmetry breaking of the lattice at the surface, causes randomness in the exchange interactions between the spins, which extends to some atomic layers from the surface. These competing interactions cause frustration among the spins generating surface SG. The presence of enhanced  $H_{EB}$ , a sharp decrease in the magnetization of FC curves below 149 K and irreversibility in the FC and ZFC M(T) curves at 70 kOe verify the presence of strong surface SG phase in these hematite nanoparticles. The coexistence of superparamagnetic, SSG and surface SG phases are observed in  $\text{La}_{0.8}\text{Ca}_{0.2}\text{MnO}_3$  nanoparticles but it lacks the study of EB phenomenon<sup>128</sup>.

### 5.3.2.2 Aging and memory effects

The study of slow dynamics such as aging and memory effects in the nanoparticles and the other systems (e.g., thin films, supercooled liquids) is important, especially in the deep understanding of SGs<sup>121</sup>. The memory and aging effects are observed in the different phases of SGs like SSG<sup>121;131</sup>, re-entrant SG<sup>132;133</sup>, Ising SG<sup>134;135</sup> and surface SG<sup>136;137</sup>. Sasaki et al.<sup>121</sup> has studied aging and memory effects in the SSG and superparamagnetic systems. The SPMs and SSGs show similar FC aging and

memory effects. The SSG differs from SPM through the FC  $M(T)$  measurements, where the FC magnetization of SSG does not increase, either it decreases or stays constant with decrease in the temperature. The second important difference between them is the presence of memory effect in the ZFC measurements of SSG. The aging and memory effects in SSGs are well understood by droplet theory<sup>121</sup>. In general, the random energy model consists of states having random and independent energy barriers but the link between each state and actual spin configuration is not clear. In droplet model, at each temperature, the equilibrium state consists of a ground state plus thermally activated droplet excitations of various sizes forming with respect to time after the quenching of SG below critical temperature. A droplet is low energy compact clusters of spins with volume  $V$ , or linear size  $L$ . Each droplet can be flipped by a thermal activation process which governs the response of clusters to the applied field<sup>121</sup>. This is similar to two states description of superparamagnet but with time dependent distribution.

In addition to the memory effect, the aging in ZFC measurements is reported through stop and wait protocol during the heating of ZFC magnetization curve and is related to the SG phase<sup>138</sup>. For these measurements, the stop and wait protocol is used during heating (SWH). The sample was cooled in zero field from 350 K to 5 K at the rate of 10 K/min, the magnetization ( $M_{ZFC}^{SWH}$ ) was measured during heating in 500 Oe at the rate of 2 K/min. During this, the measurement was stopped at three different temperatures (50 K, 270 K and 315 K) and at these temperatures, the sample was aged for 2 hrs in the presence of field. The reference magnetization curve ( $M_{ZFC}^{ref}$ ), was obtained in a similar way but without any stop during heating.

The temperature dependence behaviour of  $M_{ZFC}^{SWH}$  and  $M_{ZFC}^{ref}$  curves are shown in Fig. 5.3.6(a).  $M_{ZFC}^{ref}$  is increased monotonically showing a normal behaviour with increasing temperature. In  $M_{ZFC}^{SWH}$  curve, as the measurement is restarted after the wait of 2 hrs at the intermittent stops (i.e., at 50 K, 270 K and 315 K), the magnetization jumps to a higher value and it continues to increase but with much slower rate than  $M_{ZFC}^{ref}$  curve. This increase in the magnetization of  $M_{ZFC}^{SWH}$  curve, as the temperature increased just after the 'stopping' temperature, depicts the presence of SG. After this slow increase in the  $M_{ZFC}^{SWH}$  curve at the intermittent stops, the magnetization follows the  $M_{ZFC}^{ref}$  curve. This aging behaviour was observed in Ising spin glass  $Fe_{0.5}Mn_{0.5}TiO_3$ <sup>138</sup> and re-entrant spin glass  $Cu_{0.2}Co_{0.8}Cl_2-FeCl_3$  systems too, where the explanation is based on the droplet picture for the SG phase<sup>132</sup>.

Fig. 5.3.6(a<sub>1</sub>), (a<sub>2</sub>)and (a<sub>3</sub>) represent the behaviour of magnetization at the intermittent stops, clearly showing that the  $M_{ZFC}^{SWH}$  increases after re-heating at these three stopping temperatures. This increasing trend of the magnetization clearly indicates the presence of SG phase at 315 K, because the decrease in the magnetization after the stopping temperature is reported for ferromagnetic phase. The jump in the  $M_{ZFC}^{SWH}$  values is different for different temperatures, having a small change at 50 K. The reason of this small increase in magnetization at 50 K is related to the frozen spins at the surface which do not easily align along the field during aging.

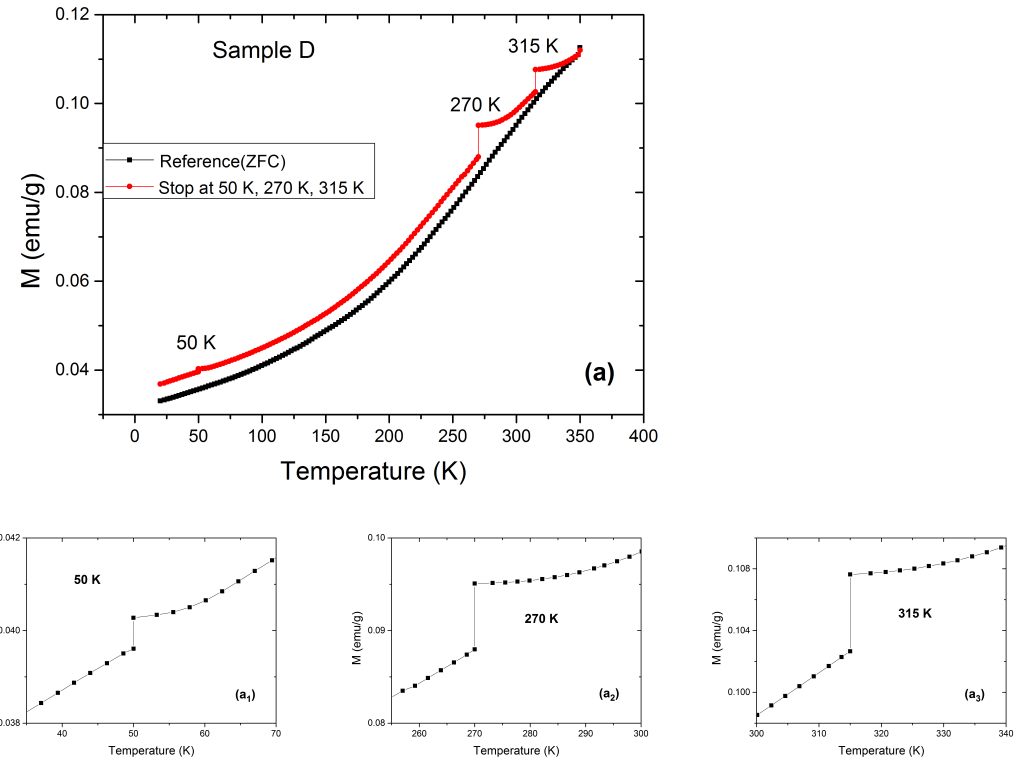


Figure 5.3.6:  $M_{ZFC}^{ref}$  and  $M_{ZFC}^{SWH}$  measurements as the function of temperature (a);  $M_{ZFC}^{SWH}$  versus temperature measurements after aging at 50 K (a<sub>1</sub>), at 270 K (a<sub>2</sub>) and 315 K (a<sub>3</sub>).

Recently, the presence of SSG is confirmed in  $\text{BiFeO}_3\text{-Bi}_2\text{Fe}_4\text{O}_9$  nanocomposite through the memory effect with same procedure, i.e., the difference between the  $M_{ZFC}^{ref}$  and  $M_{ZFC}^{SWH}$  curves<sup>123</sup>. Although this memory effect is not with genuine ZFC protocol where stop and wait protocol is used during cooling as described later in Fig. 5.4.8. This memory effect is the result of stop and wait during heating. The difference between the  $M_{ZFC}^{ref}$  and  $M_{ZFC}^{SWH}$  curves of the sample D is shown in

Fig. 5.3.7, depicting the memory effect at 50 K, 270 K and 315 K. The presence of SG phase in these nanoparticles is also indicated by the dips in  $\Delta M$  at 50 K, 270 K and 315 K. The dip at 50 K is smaller due to the small change in the  $M_{ZFC}^{SWH}$  during aging because of frozen surface spins. The inset of Fig. 5.3.7 clearly shows the dip at 50 K. Here it is important to note that from my analysis, the memory effect which is indicated through the dip in the difference of  $M_{ZFC}^{ref}$  and  $M_{ZFC}^{SWH}$  curves (this is not genuine ZFC memory effect), is not an authentic tool for the indication of SG phase contrary to Maity et al.<sup>123</sup>. This analysis will be discussed during the same measurements (memory effect through SWH protocol) of sample A in section 4.5.1.

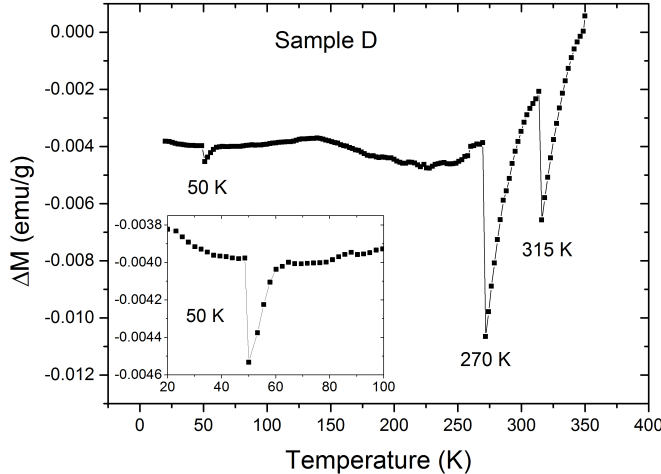


Figure 5.3.7: Memory effect in sample D after “stop and wait” protocol during heating (SWH) at 50 K, 270 K and 315 K.

The various studies of aging and memory effects in these nanoparticles are done till 315 K, confirming the presence of SSG in these nanoparticles up to this temperature. From the previous study of sample D (spindle shaped), both surface SG (low temperatures and high fields) and SSG (high temperatures and low field) phases are observed due to freezing of surface spins and core spins, respectively. For a system to generate EB, there must be two exchange coupled phases, a fixed phase and a reversible phase. In the under study system of hematite nanoparticles, the core part is reversible phase, while the surface spins (can be considered as shell) act as a fixed phase. At the temperatures above 149 K, the presence of weak  $H_{EB}$  in sample D is due to the SSG phase of core spins and small pinning centers at the surface due to surface disorders, where the “frozen” core can be reversed under an application of

field<sup>122</sup>. Below the freezing temperature of surface SG (149 K), a rapid increase in the  $H_{EB}$  occurs (see Fig. 5.3.2(a)) due to increase in the number of frozen spins at the interface. These observations also rule out the coexistence of antiferromagnetic and weak ferromagnetic phases of hematite at the same temperature.

### 5.3.3 Cooling field dependence of exchange bias

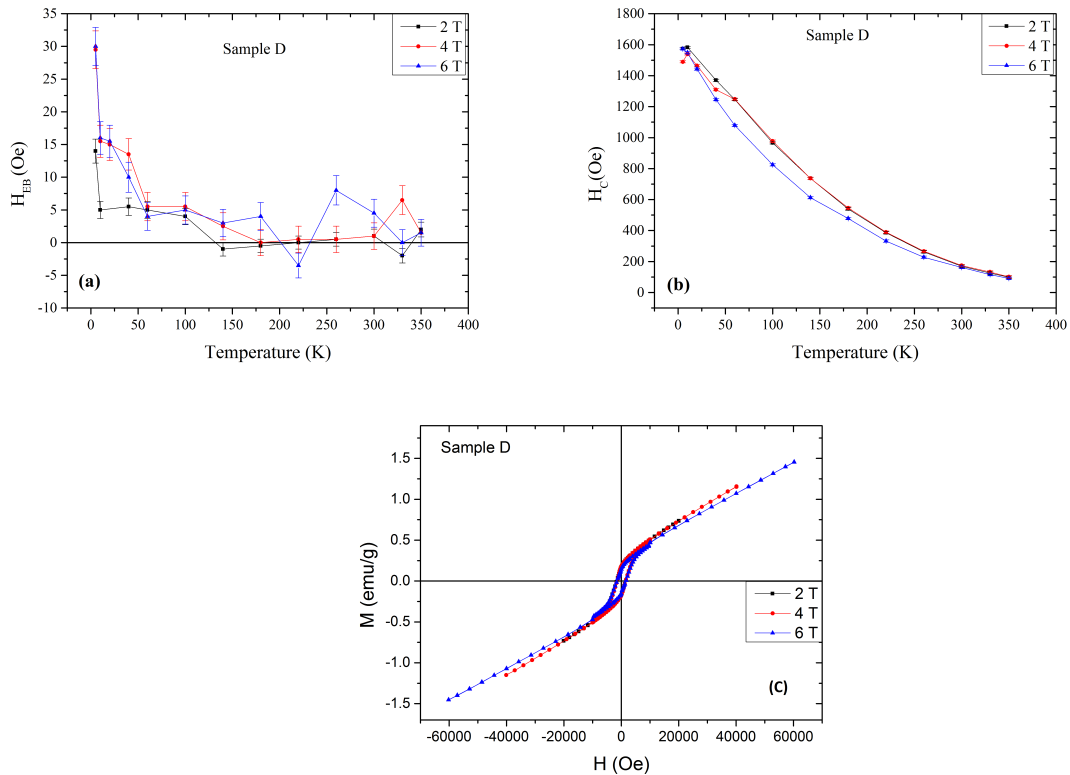


Figure 5.3.8: The temperature dependence of (a)  $H_{EB}$  and (b)  $H_C$  in sample D; (c) the FC M(H) loops of sample D at in different cooling fields ( It is noted that in this Fig. Telsa, T is used where 1 T=10 kOe).

The effect of external magnetic field on EB is studied in the sample D where the cooling and measuring fields were 20 kOe, 40 kOe and 60 kOe. Fig 5.3.8(a) and (b) depicts the behaviour of  $H_{EB}$  and  $H_C$  as functions of temperature in different magnetic fields, respectively. The  $H_{EB}$  increases with increasing the external magnetic field, especially at lower temperatures. From the hysteresis loops of sample D at 5 K in the different magnetic fields (as shown in Fig. 5.3.8(c)), the magnetization increases with field and 60 kOe is not enough to saturate these nanoparticles.

The increase in the magnetization with field indicates that the alignment degree of the ferromagnetic moments along the preferential direction is enhanced, which reduces the effect of averaging of anisotropy due to randomness<sup>113</sup>. Therefore, with increasing the cooling field, the  $H_{EB}$  and the magnetization increases, but  $H_C$  is not strongly affected. The increase in the magnetization at higher fields because of antiferromagnetic (in this case it is surface disordered spins) contribution can not be considered due to increase in  $H_{EB}$  with field. As the alignment of surface disordered moments along the field can cause decrease in the  $H_{EB}$ .

## 5.4 Morin transition

Morin transition (spin-flip transition) the magnetic phase transition of hematite, is clearly observed in the sample A, containing the spherical shaped nanoparticles having diameter 73 nm (aspect ratio : 1). The FC hysteresis loops were taken at different temperatures where 20 kOe was cooling and measuring field, as shown in Fig. 5.4.1. Below 180 K, the hysteresis loops are straight lines indicating the antiferromagnetic behaviour of hematite below Morin transition. At 180 K, the MH-loop shows strong hysteresis behaviour indicating the start of ferromagnetic phase. Above 180 K, the weak ferromagnetic phase is exhibited through hysteresis in the MH-loops.

In order to investigate Morin transition in this sample, the M(T) measurements were done. The sample was ZFC from 350 K to 5 K and the measurements were taken during heating in the presence of different magnetic fields. Fig. 5.4.2 exhibits the ZFC M(T) curves which show abrupt jump in the magnetization at certain temperatures related to Morin temperature ( $T_M$ ). These M(T) curves clearly indicate the presence of FM at higher temperatures. It is also observed that Morin transition is field dependent; with increasing external magnetic field, it moves to lower temperatures, similar behaviour is also reported in pure hematite nanoparticles of size 57 nm<sup>107</sup>. Morin transition occurs due to the competition of two kinds of anisotropies, i.e., the single-ion anisotropy caused by spin-orbit coupling that tries to align the spins along [111] axis, and the long-range magnetic dipolar anisotropy which tries to align the spins along (111) plane. The antisymmetric exchange interaction (Dzyaloshinskii-Moriya interaction) is the reason of small canting of moments above  $T_M$  which causes weak ferromagnetic moment<sup>108;109;139</sup>.

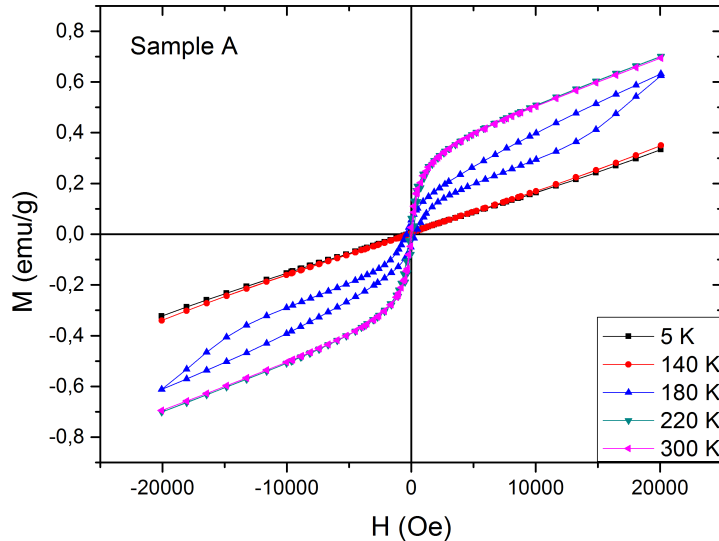


Figure 5.4.1: Hysteresis loops of sample A (aspect ratio : 1) at different temperatures after field cooling in 20 kOe.

From ZFC  $M(T)$  curves, it is observed that below  $T_M$ , magnetization is not zero and increases with external magnetic field. Even in zero field (see Fig. 5.4.4(a)), the presence of very small magnetization indicates that the system below  $T_M$  is not ideally an AFM, the reasons are the crystal defects and the surface disorders. Below  $T_M$ , the magnetization remains nearly constant till 30 kOe but in the  $M(T)$  curves of 40 kOe and 50 kOe, magnetization increases with increasing temperature and transition occurs with sloppy increase in the magnetization (see also inset of Fig. 5.4.2(b)). The decrease in the magnetization of  $M(T)$  curve of 50 kOe above Morin transition might be related to the blocking phenomena of nanoparticles where they are in superparamagnetic regime at higher temperatures. The  $M(T)$  curves of 60 kOe and 70 kOe exhibit Morin transition but the magnetization decreases with increasing temperature. The low temperature increase in magnetization might be related to the contribution of uncompensated spins present on the surface of nanoparticles of sample A. This indicates the core-shell structure in these nanoparticles where the core is hematite and shell consists of disordered surface spins<sup>140</sup>.

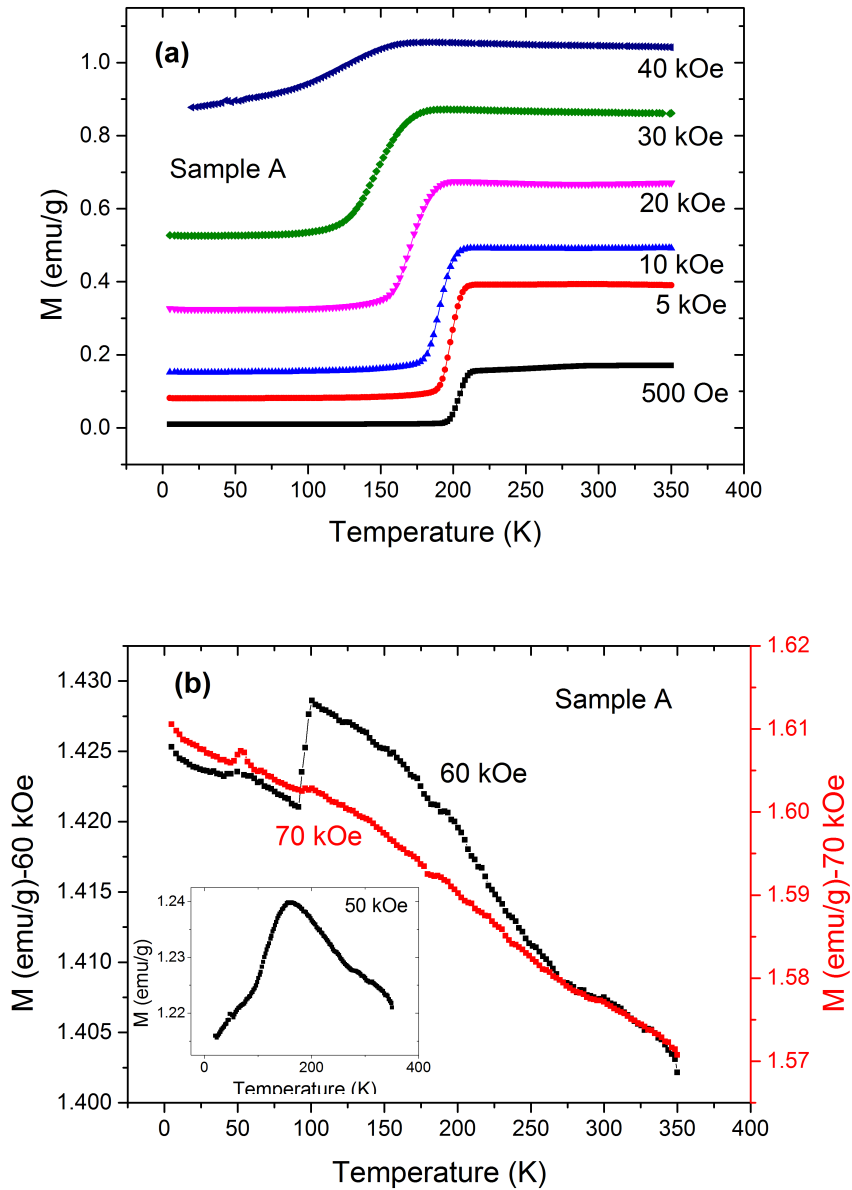


Figure 5.4.2: The  $M(T)$  curves of sample A in different external fields after zero field cooling: (a) 500 Oe to 40 kOe fields, (b) 60 kOe and 70 kOe fields, (inset:  $M(T)$  curve of 50 kOe).

The effect of an external magnetic field on Morin transition is clearly observed from the ZFC  $M(T)$  measurements, higher fields reduce the antiferromagnetic regime and can induce weak ferromagnetic phase at temperature where antiferromagnetic phase is present at low field (e.g., compare  $M(T)$  curves of 500 Oe and 30 kOe).  $T_M$ , which is determined from the temperature at maximum  $dM/dT$ , is shown in

Fig 5.4.3(a) as a function of applied field. The linear behaviour is observed from 0 Oe to 60 kOe, conforming to literature<sup>107</sup>, except the value for 70 kOe which is very small. The reason of this diminishing antiferromagnetic behaviour in hematite nanoparticles is the strong external field which is also observed from  $M(T)$  curve of 70 kOe. This also indicates that the magnetic field stabilizes the high temperatures (ferromagnetic) phase as compared to low temperatures (antiferromagnetic phase).

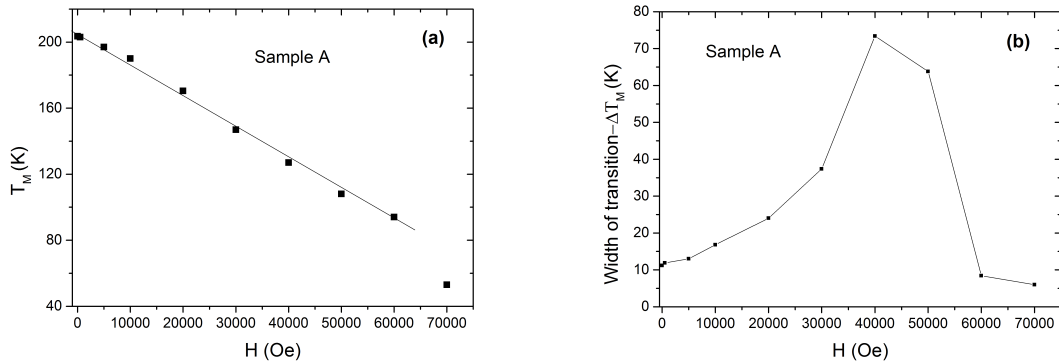


Figure 5.4.3: (a) Morin transition temperature ( $T_M$ ) versus external magnetic field in sample A; (b) the width of Morin transition ( $\Delta T_M$ ) versus magnetic field in sample A.

The width of the transition ( $\Delta T_M$ ), determined from full width at half maximum (FWHM) of ZFC  $dM/dT$  curve, is field dependent, which is quite surprising because it is found as field independent in literature<sup>108;141</sup>. This depicts that the temperature range of spin transition increases with external field, the reason is strong Zeeman energy which competes with magnetocrystalline anisotropy. The external field strengthens the magnetic dipolar interactions which move the aligned spins along [111] axis to (111) plane, thus reduces the antiferromagnetic regime. The fields above 50 kOe are strong enough to align the spins in antiferromagnetic phase along the field direction and suppress the Morin transition. The  $M(T)$  measurements were also done under cooling and heating in the presence of field, i.e., under FC conditions as shown in Fig. 5.4.4.  $T_M$  is different during cooling ( $T_M(C)$ ) and heating ( $T_M(H)$ ), even in the absence of magnetic field  $T_M$  is 176 K and 203 K during cooling and heating, respectively. The presence of thermal hysteresis indicates the Morin transition as first-order transition and also relates to the presence of defects, crystal imperfections and impurities etc. which could act as nucleation centers for magnetic phase. The thermal hysteresis, difference between  $T_M(H)$  and

$T_M(C)$  is decreasing with increasing magnetic field<sup>107,108</sup>.

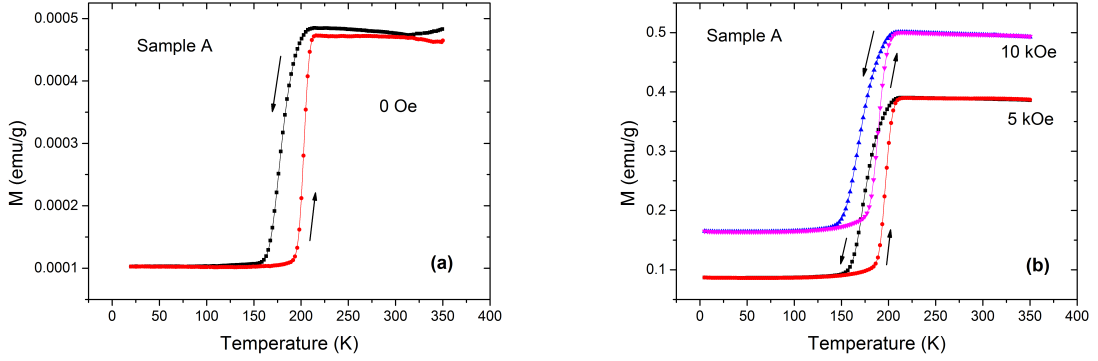


Figure 5.4.4: FC  $M(T)$  during cooling and heating in sample A in (a) 0 Oe field, (b) 5 kOe and 10 kOe fields .

#### 5.4.1 Presence of exchange bias below Morin transition

The study of Morin transition in hematite nanoparticles is also reported in literature<sup>107,108,139,140</sup>, but the remarkable part in the present work is the presence of EB along with the Morin transition in the same system which has not yet been reported. The FC hysteresis curve in 20 kOe of sample A at 5 K clearly shows an antiferromagnetic behaviour, where the MH-loop is not centered and shifted towards negative direction as shown in inset of Fig. 5.4.5(a). At 5 K,  $H_{EB}=-249$  Oe,  $H_C=49$  Oe and the remanent magnetization,  $M_r=0.001$  emu/g. The MH-loop at 5 K also shows vertical shift along upward direction with the value  $\Delta M_r=0.0049$  emu/g.

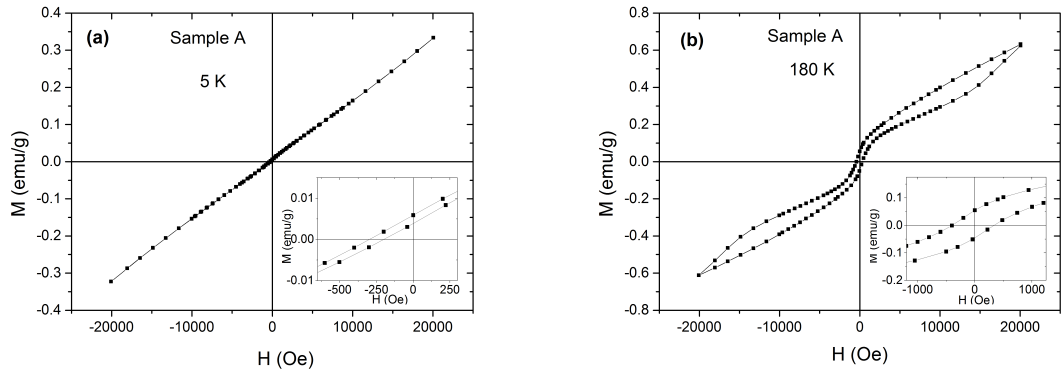


Figure 5.4.5: FC MH-loops of sample A at (a) 5 K; (b) 180 K. Insets show the respective MH-loops around zero field.

The sample A was field cooled from 350 K to 5 K in 20 kOe field, measurements were done under same conditions as for previous samples.  $H_{EB}$  and  $H_C$  are calculated from the FC hysteresis loops at different temperatures during subsequent heating from 5 K to 350 K. The temperature dependent  $H_{EB}$  and  $H_C$  of sample A is shown in Fig. 5.4.6. It is observed that  $H_{EB}$  is negative with large magnitude at low temperatures and decreases slowly from 5 K (-249 Oe) to 160 K (-202 Oe), then jumps to smaller value of -30 Oe at 180 K after that  $H_{EB}$  becomes constant having very small positive values (around 0.5 Oe to 3 Oe). While  $H_C$  remains nearly constant or decreases slowly from 5 K (49 Oe) to 140 K (44 Oe), becomes maximum to the value of 367 Oe at 180 K and then decreases with increase in the temperature. The sudden change in the behaviour of  $H_{EB}$  and  $H_C$  is observed at 180 K.

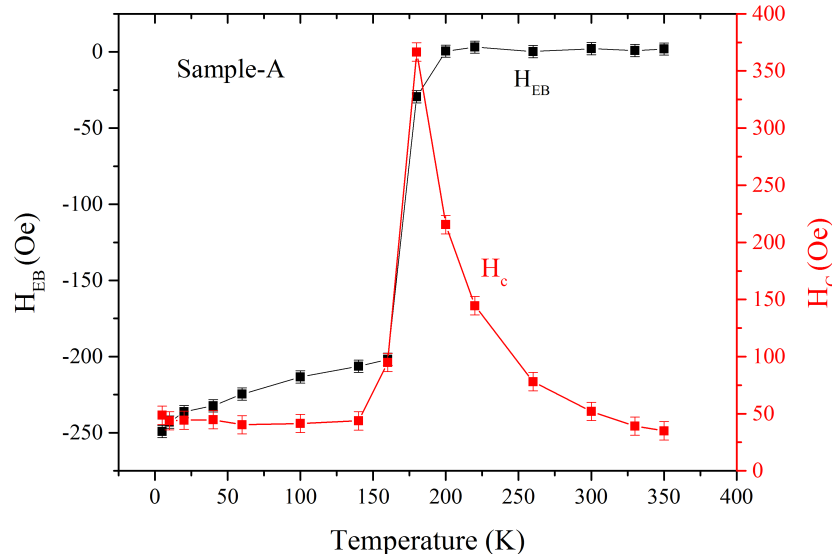


Figure 5.4.6: Temperature dependence of  $H_{EB}$  (represents through black curve and left scale) and  $H_C$  (represents through red curve and right scale) of sample A, after field cooling of 20 kOe.

The MH-loop at 180 K in 20 kOe magnetic field also shows clear hysteresis, indicating the start of weak ferromagnetic phase in hematite nanoparticles of sample A (also see Fig. 5.3.12). Therefore, 180 K is the temperature where Morin transition occurs in these nanoparticles in the presence of 20 kOe field. From  $T_M$  versus magnetic field curve (shown in Fig. 5.4.3(a)),  $T_M$  obtained at 20 kOe field is 171 K, which is in good agreement with 180 K as observed by the MH-loops, because the hysteresis loop was not taken at 170 K but measured at 160 K and then 180 K.

The presence of exchange bias in the antiferromagnetic regime is due to the antiferromagnetic core and the surface SG phase. It is also important to check the presence of AFM and FM phases at the same time, which could be the reason of EB and can easily observe from the hysteresis loops. Fig. 5.4.7 presents the ZFC MH-loop of sample A at 5 K, where  $H_C=18$  Oe,  $M_r=3.8 \times 10^{-4}$  emu/g and  $M_S=0.327$  emu/g. The small value of coercivity and negligible remanence at 5 K can easily rule out this hypothesis. The shape of MH-loop is a straight line clearly indicating antiferromagnetic behaviour. From the  $M(T)$  behaviour at 0 Oe (see Fig. 5.4.5(a)), the presence of antiferromagnetic phase and absence of ferromagnetic phase in low temperature regime, are also verified. Therefore, there is no clear evidence of coexistence of both phases which could be the origin of EB. In the previous section, the magnetic study of sample D (spindle shaped with aspect ratio 6) also revealed the role of surface SG in the EB phenomenon.

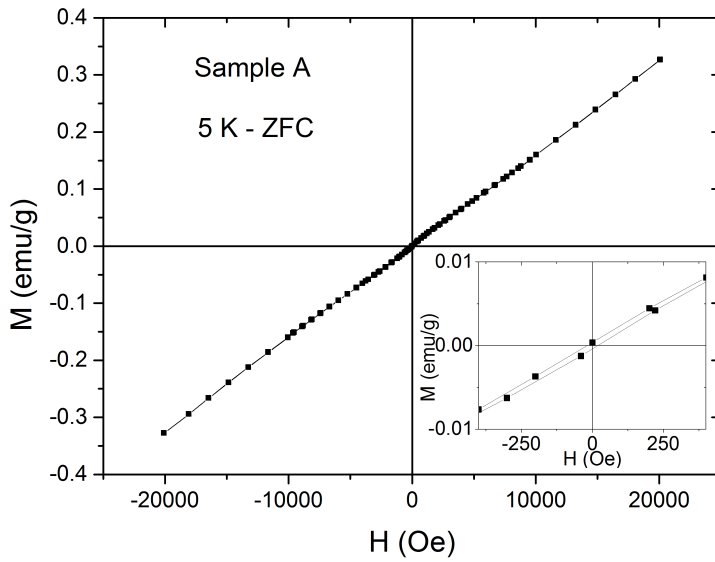


Figure 5.4.7: ZFC MH-loop of sample A at 5 K, (inset: magnify  $M(H)$  loop near  $H=0$ ).

In order to study the memory effect in the genuine ZFC magnetization curve, the “stop and wait” protocol is used during the cooling (SWC) process<sup>121</sup>. The sample A (spherical shaped with aspect ratio 1) was cooled in zero field from 350 K to 100 K, then stopped and kept to wait for  $2 \times 10^5$  s, after that the cooling was continued to 5 K. The magnetization was measured during heating ( $M_{ZFC}^{SWC}$ ) from 5 K in the external field of 500 Oe. The reference ZFC magnetization curve ( $M_{ZFC}^{ref}$ ) was

measured during heating after the sample was ZFC from 350 K to 5 K without any stop and wait during cooling. The difference between both magnetization curves ( $M_{ZFC}^{SWC} - M_{ZFC}^{ref}$ ) is plotted in Fig. 5.4.8, which shows the dip at 100 K depicting the memory effect in ZFC magnetization.

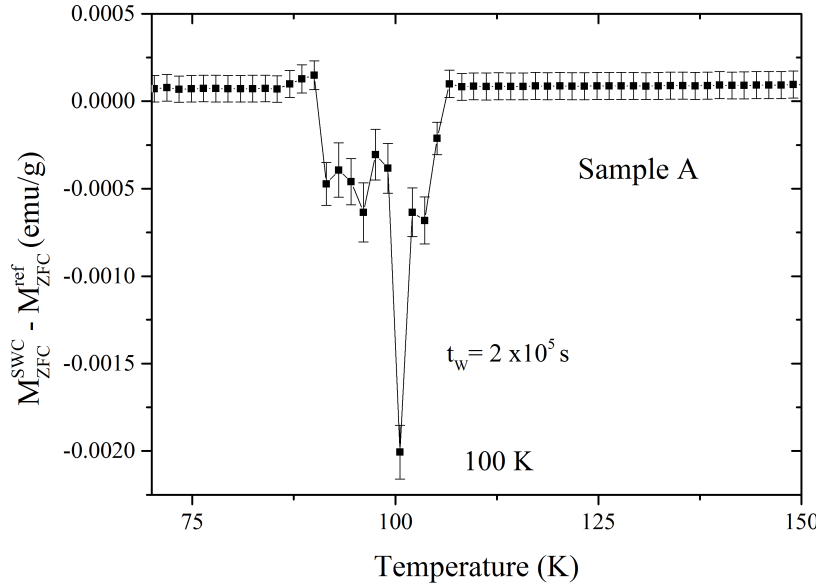


Figure 5.4.8: Memory effect ( $M_{ZFC}^{SWC} - M_{ZFC}^{ref}$ ) in SWC protocol of sample A at 100 K at different wait-time ( $t_W$ ), of  $2 \times 10^5$  s.

The aging effect during SWH protocol is also measured and is shown in Fig. 5.4.9(a). The  $M_{ZFC}^{ref}$  curve was obtained during heating from 5 K to 350 K in 500 Oe field after zero field cooling. The  $M_{ZFC}^{SWH}$  curve was obtained under the same procedure but measurement is stopped during heating at the temperatures of 100 K, 200 K, 270 K and 315 K for 2 h. The measurement at 200 K was taken to observe the aging and memory effect during Morin transition. There is an evident change in the magnetization in  $M_{ZFC}^{SWH}$  curve at 200 K and 270 K.

Fig. 5.4.9 (a<sub>1</sub>), (a<sub>2</sub>) and (a<sub>3</sub>) present the change in  $M_{ZFC}^{SWH}$  curve after  $t_W$  of 2 h at the temperatures of 100 K, 270 K and 315 K, respectively, this measurement is related to the aging of ZFC measurements of sample A. At 100 K, the jump in  $M_{ZFC}^{SWH}$  is very small because of the antiferromagnetic phase of core (less moments to respond the external magnetic field) and freezing of the large number of surface spins which do not align along the applied external field. As the measurement is started again, there is a remarkable increase in the magnetization, this sharp

increase in the magnetization clearly indicates the presence of strong SG phase in these nanoparticles. At 270 K (see Fig. 5.4.9 (a<sub>2</sub>)), there is a small decreasing trend in the magnetization, as  $M_{ZFC}^{SWH}$  were started after the stop. This decrease in the magnetization is strongly visible after the stop at 315 K and indicates the absence of SG phase<sup>132;138</sup>. The presence of very small values of  $H_{EB}$  (around 0.5 Oe to 3 Oe) after 220 K also verify the presence of a weak SG phase at higher temperatures.

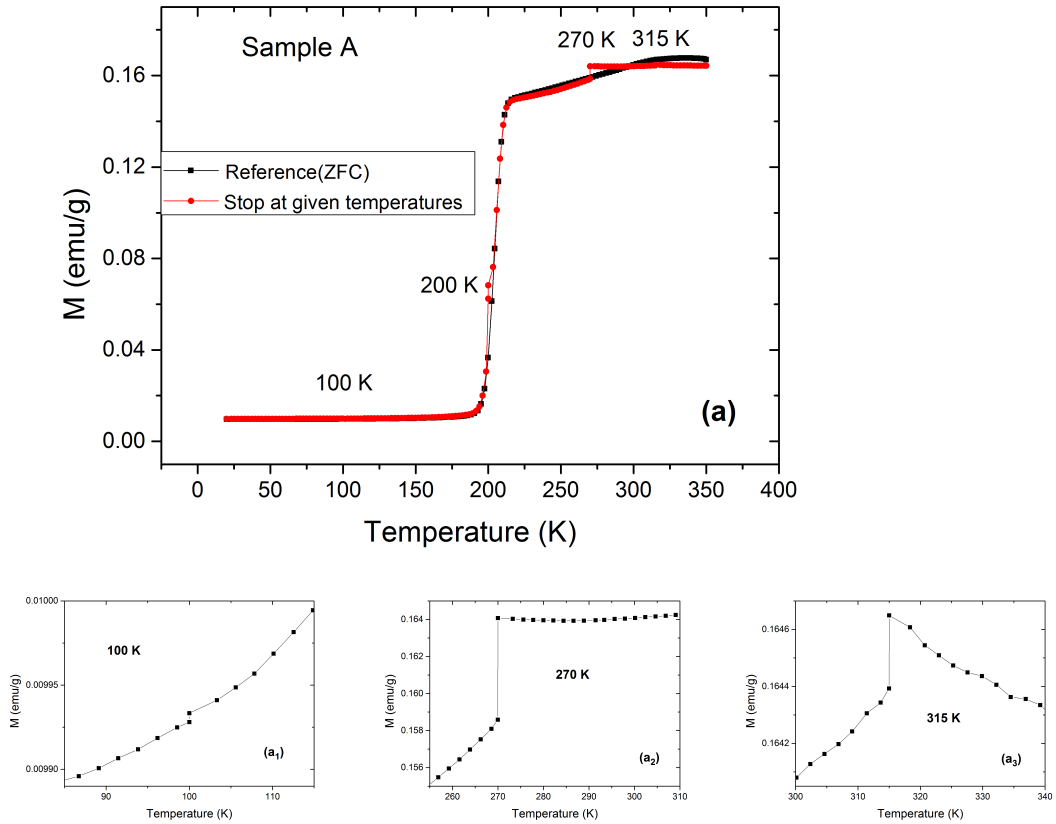


Figure 5.4.9: (a)  $M_{ZFC}^{SWH}$  and  $M_{ZFC}^{Ref}$  as function of temperature,  $M_{ZFC}^{SWH}$  after aging of 2 h at 100 K (a<sub>1</sub>), at 270 K (a<sub>2</sub>) and at 315 K (a<sub>3</sub>), in sample A

The memory effect is obtained from the difference between  $M_{ZFC}^{ref}$  and  $M_{ZFC}^{SWH}$  curves, indicating from the presence of dips at the intermittent stops, as shown in Fig. 5.4.10. There is a need to investigate this memory effect obtained through SWH protocol as described by Maity et al.<sup>123</sup>. There is a larger dip at 200 K, the temperature where the transition to ferromagnetic phase occurs. This large difference at 200 K is due to the reason that the moments can align easily along the field because of ferromagnetic phase. There is very small dip at 100 K (see inset

of Fig. 5.4.10) but the presence of strong memory effect in SWC protocol (genuine memory effect),  $H_{EB}$  and sharp increase in  $M_{ZFC}^{SWH}$  at 100 K after stop, clearly verify the presence of surface SG at this temperature. The reason of this small dip at 100 K is due to the fact that the shell (outer part) of nanoparticles of sample A is frozen because of surface SG phase and only the small moments from antiferromagnetic core can align along the field, causing small increase in the magnetization, thus generating the small difference ( $\Delta M$ ).

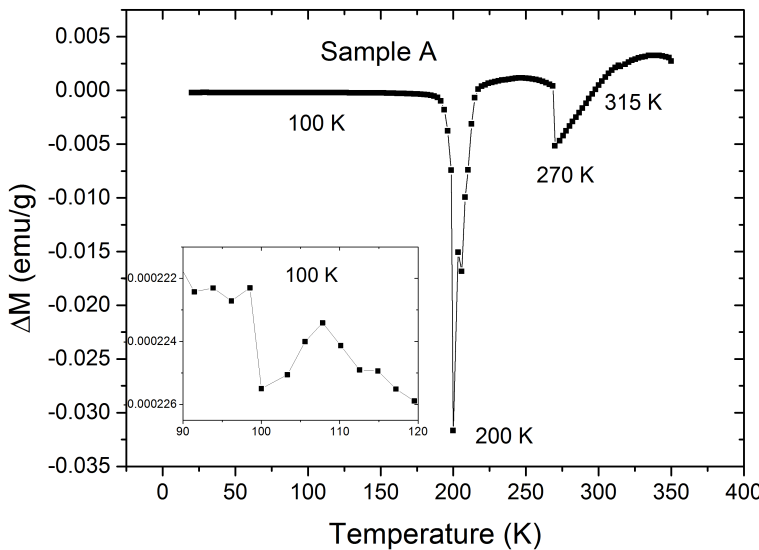


Figure 5.4.10: Memory effect ( $M_{ZFC}^{Ref} - M_{ZFC}^{SWH}$ ) in SWH protocol in sample A.

The small dips are also present at 270 K and 315 K which should relate to the SG phase but they do not correspond to the SG phase because of the decreasing trend in  $M_{ZFC}^{SWH}$  after the stop and the presence of very weak  $H_{EB}$  at these temperatures. The reason of this weak  $H_{EB}$  is small number of pinning centers due to surface disorders but not a clear SG phase. From the analysis of the memory effect which is obtained from the difference of  $M_{ZFC}^{ref}$  and  $M_{ZFC}^{SWH}$  curves due to SWH protocol, reveals that the strength of the dip at a stopping temperature may not relate to the surface SG phase. Instead of this, the presence of memory effect in SWC protocol (Fig. 5.4.8) and the sharp increasing trend of  $M_{ZFC}^{SWH}$  at stopping temperature after waiting time (Fig. 5.4.9 (a<sub>1</sub>)) are the strong tools to prove the presence of SG phase.

The interesting behavior in the EB effect of sample A is the sign change in  $H_{EB}$  from negative to positive along with the peak in  $H_C$  at Morin transition, which has not

yet been reported after careful literature survey. This indicates the effect of rotation of spins in the core of hematite nanoparticles above  $T_M$  on interfacial exchange coupling. The present nanoparticles are pure hematite, the crystal structure at the surface is disordered due to surface effects and dislocations, which generates surface SG phase. Therefore, the ordered crystal structure is present inside the core of nanoparticles. During Morin transition, above  $T_M$ , Fe ions in hematite core rotate from [111] axis to (111) plane and magnetocrystalline anisotropy changes its sign from positive to negative. With the rotation of Fe ions, the moments of hematite core change direction with SG shell's moments at interface. Consequently, the interfacial coupling between both moments changes its alignment and now favours antiparallel coupling to generate positive EB. This is the possible explanation of the sign change in  $H_{EB}$  at Morin transition which is related to the movement of the spins of hematite core. Thus, the negative  $H_{EB}$  becomes positive as the hematite core changes from antiferromagnetic phase to ferromagnetic phase. The positive EB is also reported in sample D and sample C due to surface SG and ferromagnetic core, as described in the section 5.3.1.

#### 5.4.2 Shape dependence Morin transition

In the above study Morin transition is clearly observed and discussed in spherical shaped hematite nanoparticles (sample A-aspect ratio:1). In order to investigate the effect of shape anisotropy on Morin transition, FC M(T) curves of sample B (ellipsoidal shape - aspect ratio:1.5) are shown in Fig. 5.4.11(a).

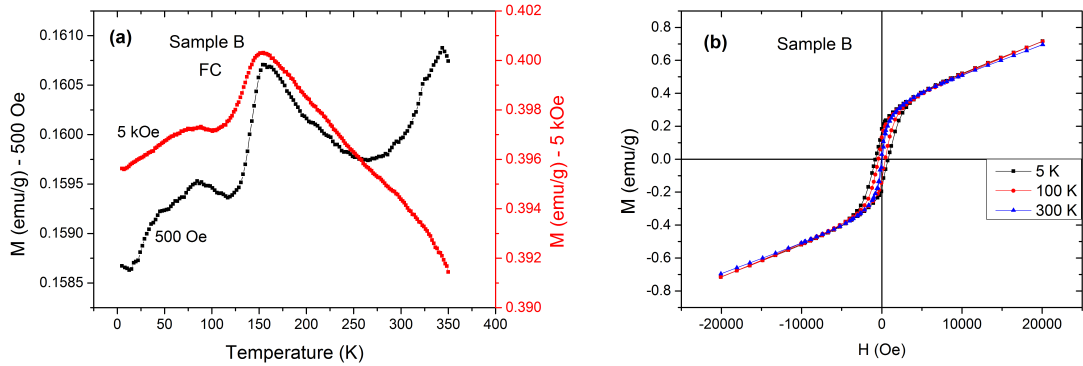


Figure 5.4.11: (a) FC M(T) curves of sample B at 500 Oe (black curve and left scale) and 5 kOe (red curve and right scale); (b) FC hysteresis loops of sample B at different temperatures .

The FC magnetization curves in 500 Oe field, shows a clear jump in the magnetization in the temperature range of 156 K to 118 K which relates to Morin transition in the sample. There is a peak in the magnetization at 344 K, which is also observed in sample D at 348 K relating to the onset of SSG phase. The M(T) curve of 5 kOe also shows jump in magnetization.  $T_M$  is determined from temperature at maximum  $dM/dT$  and is 142 K for 500 Oe and 135 K for 5 kOe field. Here the decrease in  $T_M$  with field is also observed. After Morin transition, the magnetization still decreases and does not reach to minimum value, indicating the absence of pure AFM phase. This is also clear from hysteresis loops (see Fig. 5.4.11(b)), where MH-loops at 5 K and 100 K show hysteresis indicating the presence of ferromagnetic phase. It means that with increasing the aspect ratio, the shape anisotropy reduces Morin transition effect in the nanoparticles. The  $H_{EB}$  behaviour of the sample B (see Fig. 5.3.2(a)) is different from the samples C and D and is more similar to sample A. Instead of 5 K,  $H_{EB}$  has peak at 100 K in positive direction due to ferromagnetic phase while at low temperatures,  $H_{EB}$  is either positive or negative. The negative  $H_{EB}$  at low temperatures relates to antiferromagnetic phase which is similar to sample A, where  $H_{EB}$  is negative below Morin transition due to antiferromagnetic core and surface SG. The magnetic behaviour related to Morin transition of sample B is found similar to hematite nanocubes, negative ZFC  $H_{EB}$  is observed below Morin transition but there is no sign change in  $H_{EB}$  after Morin transition<sup>110</sup>.

Morin transition is affected by the shape, size, surface and crystallinity of nanoparticles,  $T_M$  decreases sharply with decreasing size and vanishes below diameter of 8 nm for spherical hematite nanoparticles<sup>111;139;140;142;143</sup>. The shape dependent Morin transition is not well clear, it is observed in spherical shaped<sup>144</sup>, in SD and MD nanoparticles of different shapes<sup>111</sup>, in SD ellipsoidal nanoparticles<sup>112</sup>, in spindle, ellipsoidal and rhombohedral shaped nanoparticles<sup>108;139;143</sup>. In spindle shaped hematite nanoparticles, Morin transition is not observed but unless annealed<sup>145</sup>. In the present study of hematite nanoparticles, Morin transition is well defined in spherical shaped nanoparticles decreases with increasing aspect ratio and totally absent in spindle shaped nanoparticles. The reason of this behaviour is related to shape anisotropy, lattice strains, crystal defects and surface effects which are enhanced as the shape of nanoparticles when becomes elliptical results in diminished Morin transition.

### 5.4.3 Summary of study of the un-coated hematite nanoparticles

In the previous sections, hematite nanoparticles with different aspect ratios are studied. The SSG behaviour is clearly observed along with the surface SG. The SSG phase is sensitive to high magnetic fields and present at high temperatures even at room temperature (this is a unique characteristic as in general SG phase occurs at low temperatures), while the surface SG exists at low temperature and can survive in high fields. In the spindle shaped hematite nanoparticles, positive  $H_{EB}$  is present at low temperatures due to exchange interaction between the ferromagnetic core and the surface SG phase. The surface SG is more prominent and dominates over SSG in the  $H_{EB}$  behaviour. In the spherical shaped hematite nanoparticles, Morin transition is clearly observed which is diminished with increasing aspect ratio and vanishes in the spindle shaped nanoparticles due to the shape anisotropy, lattice strain and lattice distortion. The study of EB phenomenon in hematite nanoparticles reveals that  $H_{EB}$  is positive when the core is ferromagnetic and the shell consists of surface SG, while negative  $H_{EB}$  occurs due to the exchange interaction between the antiferromagnetic core and the surface SG. This concludes that the sign of  $H_{EB}$  depends on the magnetic order in the hematite nanoparticles. The most interesting part is the study of  $H_{EB}$  during Morin transition, which is not yet reported in the literature. During Morin transition,  $H_{EB}$  changes its sign from negative to positive with a peak in  $H_C$  at Morin transition. For positive  $H_{EB}$ , antiparallel interfacial coupling between the surface SG and the ferromagnetic hematite core moments at the interface is generated due to the rotation of Fe ions from [111] axis to (111) plane, i.e., changing from antiferromagnetic phase to ferromagnetic phase during Morin transition.

## 5.5 Silica coated hematite nanoparticles

The silica shell is used as the stabilizer. Unlike polymers, it is not subject to microbial attack (good for biocompatibility) and does not change porosity in response to the environmental pH values. Silica is chemically inert, and therefore does not affect the redox reaction at the core surface. Silica coating also suppress the particle-particle magnetic bipolar interaction and prevents them from aggregating and agglomerating. Because of nontoxic nature, thermal stability, optical transparency and easy surface modification, silica coated nanoparticles are widely used in biolabeling, drug delivery and biosensors<sup>146;147</sup>.

### 5.5.1 Silica coating on hematite nanoparticles

To coat hematite particles with silica<sup>105</sup>, the procedure described by Graf et al. was followed<sup>148</sup>, using the amphiphilic Polyvinylpyrrolidone (PVP) as adhesion promoter to enhance affinity between hematite surface and silica. After stabilizing hematite particles with PVP transfer to ethanol can be performed. The silica-shell growth can be carried out by addition of Tetraethyl orthosilicate (TEOS) and Tetramethyl ammoniumhydroxide (TMAH) to the nanoparticles dispersion. In a typical reaction, 7.9 g of PVP was dissolved by mechanical stirring in 120 mL of demineralized water. To this viscous solution, 67.5 mg hematite nanoparticles were added and the mixture was kept under stirring for 24 h. To remove unabsorbed PVP molecules, the dispersion was centrifuged for 3 hrs at 2000 rpm (Eppendorf® Centrifuge 5810) and sediments were re-dispersed in 12 mL of ethanol. For the synthesis of the first silica shell, 12 mL dispersion of PVP-stabilized hematite particle were diluted to a total volume of 92 mL with ethanol. 7 mL de-ionized water and 1 mL of TMAH (1%v/v aqueous solution) were added. Under stirring a mixture of TEOS and Ethanol (ratio 2:1) was added under the surface of the reaction mixture in portions of 0.2 mL every 20 min. The addition of TEOS was continued until a total volume of 1.2 mL TEOS was added. Centrifuged with a rotation speed of 10,000 rpm for 10 min was performed after stirring the sample over night. The nanoparticles were redispersed in ethanol. To increase the shell thickness even further the procedure described above was repeated up to four times.

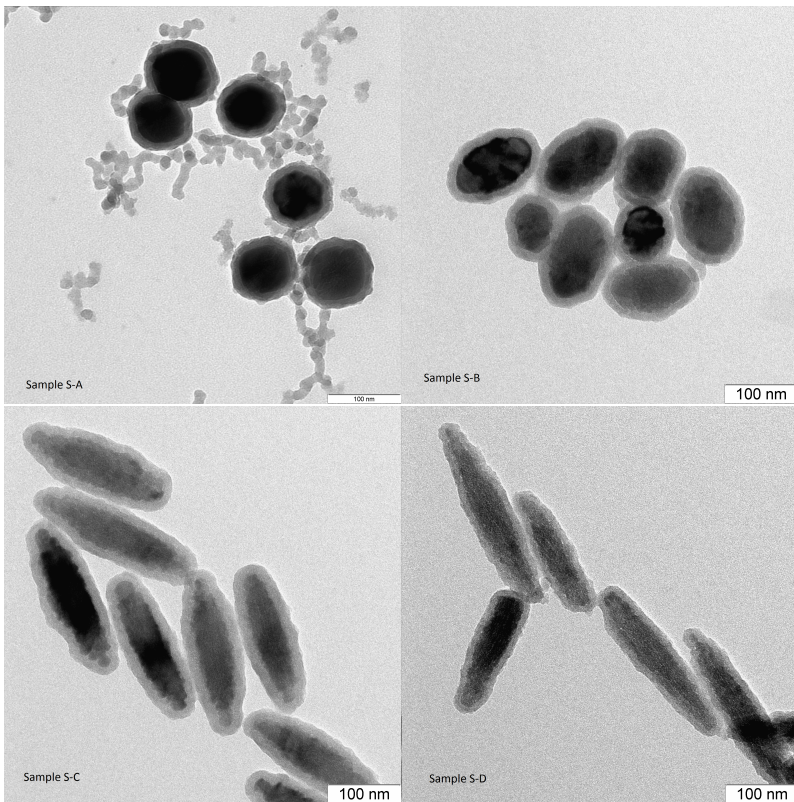


Figure 5.5.1: TEM images of sample sc-A (a), sample sc-B (b), sample sc-C (c) and sample sc-D (d)

The hematite nanoparticles samples A, B, C and D which are studied in previous sections 5.2, 5.3 and 5.4 (see Table. 5.1 for their sizes), are now silica coated and named as sc-A, sc-B, sc-C and sc-D, respectively. The TEM images of these silica coated samples are shown in Fig. 5.5.1.

## 5.5.2 Study of exchange bias in silica coated hematite nanoparticles

The hysteresis measurements were done in the field cooling of 20 kOe field from 350 K to 5 K, the MH-loops are shown in Fig. 5.5.2 at the different temperatures during subsequent heating. It should be noted that the magnetization of silica coated nanoparticles is normalized by the mass of hematite nanoparticles, it does not include the coated silica part. It is found that 20 kOe field is enough to saturate samples sc-D, sc-B and sc-C, where as the MH-loops of samples sc-B and sc-C are not shown here. While for the sample sc-A, 20 kOe field is not enough for the

saturation but the loops are closed. The increase in magnetization is related to the alignment of disordered spins along the applied field.

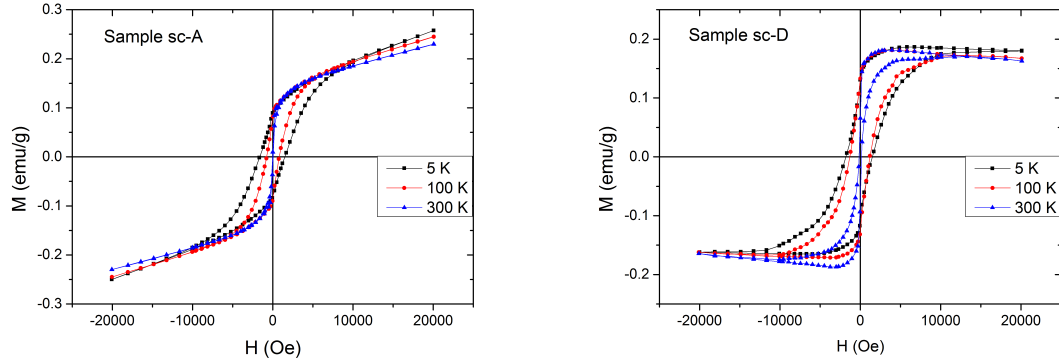


Figure 5.5.2: FC hysteresis loops at different temperatures, (a) sample sc-A , (b) sample sc-D .

The effect of EB is observed in these silica coated hematite nanoparticles, the behaviour of  $H_{EB}$  and  $H_C$  as function of temperature is shown in Fig. 5.5.3(a) and Fig 5.5.3(b), respectively. In general, the  $H_{EB}$  is negative (MH-loop is shifted opposite to the field cooling direction) at low temperatures. With increase in temperature, its magnitude decreases and the  $H_{EB}$  changes sign at temperature ( $T_0$ ) above which it becomes positive. This change in sign of  $H_{EB}$  as function of temperature strongly depends on the aspect ratio of silica coated hematite nanoparticles.

In the sample sc-A (spherical; aspect ratio:1), the  $H_{EB}$  decreases with increasing temperature, changes the sign at 30 K and becomes positive.  $H_{EB}$  has a peak at 60 K and then it decreases with temperature but remains positive til 350 K. In samples sc-B, sc-C and sc-D, with increase in the temperature, the magnitude of negative  $H_{EB}$  decreases and changing the sign at 171 K, 210 K and 289 K, respectively. The nanoparticles with spherical shape (sample sc-A) show sign change at low temperature with clear peak in positive  $H_{EB}$ . The peak is diminished and the sign change in  $H_{EB}$  moves to higher temperatures as the aspect ratio of the nanoparticles increases, which causes elongation in the shape of nanoparticles.

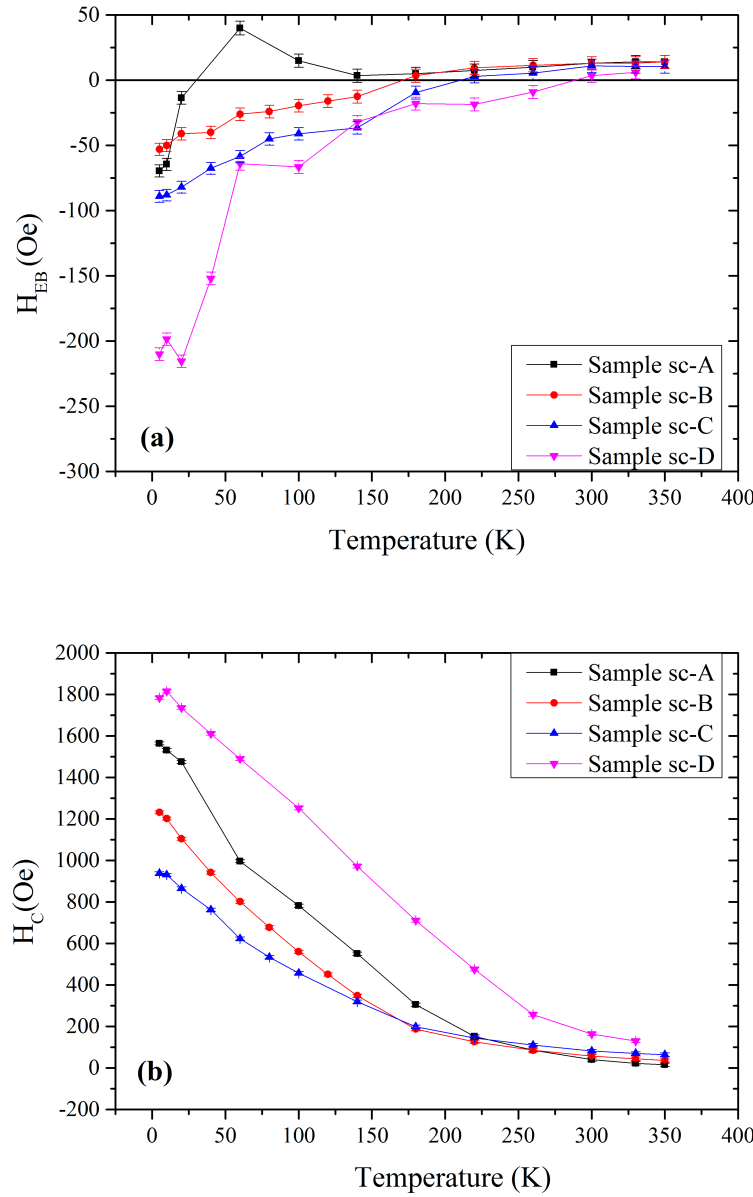


Figure 5.5.3: Temperature dependence of (a)  $H_{EB}$  and (b)  $H_C$  of silica coated Hematite nanoparticles, after field cooling of 20 kOe.

The change in  $H_{EB}$  behaviour due to difference in the aspect ratios, relates the role of shape anisotropy to  $H_{EB}$  in these silica coated hematite nanoparticles. From the  $H_{EB}$  behaviour of these nanoparticles as shown in Fig. 5.5.3(a), the magnitude of negative  $H_{EB}$  is larger for the nanoparticles having larger aspect ratios, where the  $H_{EB}$  at 5 K is -70 Oe and -177 Oe of samples sc-A and sc-D, respectively. On the other hand, the positive  $H_{EB}$  is getting smaller for the samples having larger

aspect ratios, where maximum positive  $H_{EB}$  of 40 Oe is observed in the sample sc-A. This indicates that the negative  $H_{EB}$  is stronger in spindle shaped silica coated hematite nanoparticles while positive exchange bias is dominant in spherical shaped nanoparticles. All these observations indicate the effect of shape anisotropy on the phenomenon of EB, where stronger shape anisotropy weakens the positive  $H_{EB}$  and strengthens negative  $H_{EB}$ .

For the silica coated nanoparticles systems, EB is reported in the silica coated  $\text{NiFe}_2\text{O}_4$  nanoparticles<sup>149</sup> and in the silica coated Fe nanoparticles<sup>150</sup>. The EB effect is also studied in non-interacting hematite nanoparticles of size 5 nm embedded in porous silica matrix<sup>151</sup> and polymer matrix<sup>152</sup>, where the  $H_{EB}$  is negative and becomes zero till 30 K and 20 K, respectively without any sign change. The reason of EB is related to uncompensated surface spins without any clear indication of freezing of surface spins or SG phase. From the literature survey, it seems that phenomenon of EB is not well reported in silica coated nanoparticles, especially in hematite. Therefore the present study of EB in silica coated hematite nanoparticles is important to reveal the effect of silica coating on the exchange interactions at the surface of nanoparticles. In order to investigate the reasoning of EB phenomenon, different magnetic measurements such as ac-susceptibility,  $M(T)$  and memory effect were done.

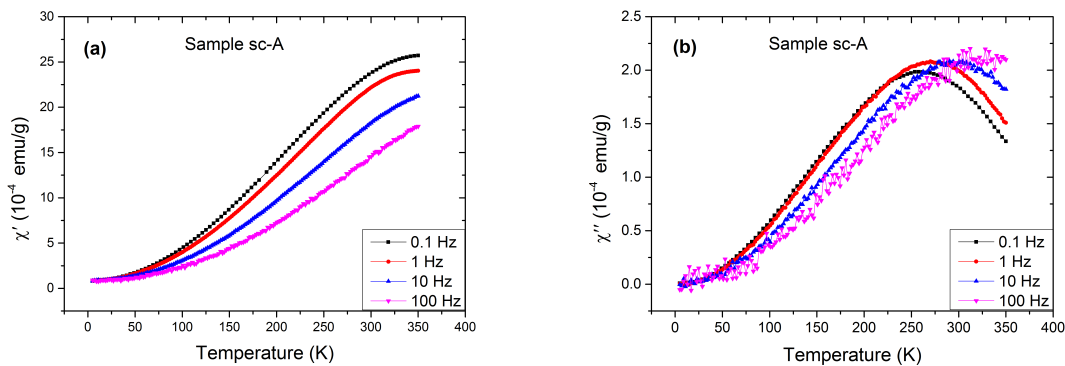


Figure 5.5.4: The ac-susceptibility measurements of sample sc-A at different frequencies in the range of 0.1 Hz to 100 Hz, (a) in-phase part,  $\chi'$  versus temperature and (b) out-of-phase part  $\chi''$  versus temperature.

In this section, the EB effect is reported in the different samples of silica coated hematite nanoparticles depending on aspect ratio. However, the magnetic measurements are discussed in two samples sc-A (spherical; aspect ratio:1) and sc-D (spindle

shaped; aspect ratio:6), therefore, covering the whole regime from minimum to maximum aspect ratio. In the uncoated hematite particles, the magnetic measurements are also discussed in detail in samples A and D, so its good to study samples sc-A and sc-D for the comparison in order to reveal the effect of silica coating. Firstly, the magnetic measurements will be discussed in sample sc-A (silica coated spherical shaped nanoparticles), the ac-susceptibility measurements were done under 5 Oe ac field at different frequencies (0.1 Hz to 100 Hz), as shown in Fig. 5.5.4. The in-phase part,  $\chi'$  of ac-susceptibility measurements, increases with temperature without showing any peak, while the out-of-phase part ( $\chi''$ ) has a peak which shifts toward the higher temperatures with increase in the frequency. The shift in the peak of ac-susceptibility to higher temperature as a function of frequency is observed in many systems and indicates the presence of SG phase in the system<sup>116;127;153;154</sup>.

In these nanoparticles, the peak of ac-susceptibility curve is related to the SG freezing at the surface. The similar shift in the peak of ac-susceptibility curve at higher frequencies is observed in Fe<sub>50</sub>Ni<sub>50</sub> nanoparticles with average size 8.9 nm without any clear indication of SG phase<sup>155</sup>. In order to further investigate the presence of SG phase in these silica coated nanoparticles, other magnetization measurements were also done.

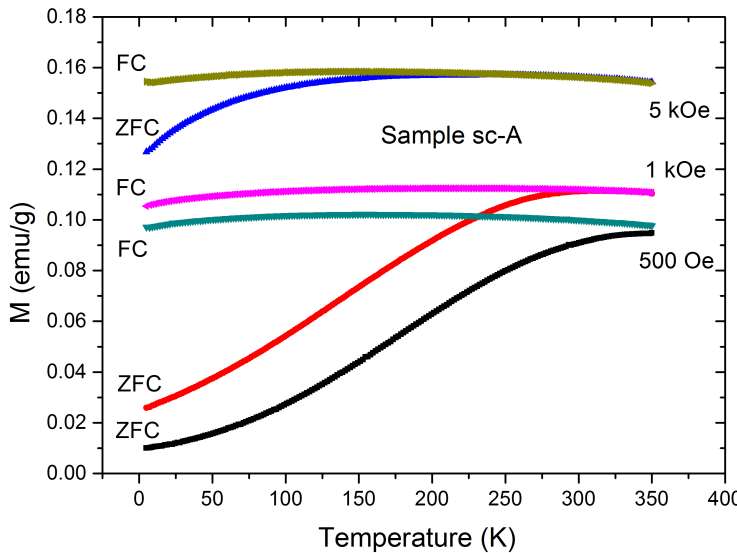


Figure 5.5.5: ZFC and FC M(T) measurements of sample sc-A in 500 Oe, 1 kOe and 5 kOe fields.

The FC and ZFC M(T) measurements of sample sc-A were done in 500 Oe, 1 kOe

and 5 kOe magnetic fields as shown in Fig 5.5.5. The ZFC curves at 1 kOe and 5 kOe show peak at 318 K and 244 K, respectively, while ZFC curve of 500 Oe field does not show any peak related to  $T_B$  of nanoparticles. The irreversibility is also observed from the FC and ZFC curves at 338 K (for 1 kOe) and 275 K (for 5 kOe), above which the nanoparticles are SPMs. Fig. 5.5.6(a), clearly shows the magnetization behaviour of FC and ZFC curves in 5 kOe field. According to the FC curves of 500 Oe and 5 kOe, instead of increase in magnetization with decreasing temperature, there is a significant decrease as shown in the Fig 5.5.6(b). The freezing of the frustrated spins, causes the decrease in the magnetization of FC curve and peak is related to the onset of the strong surface SG phase (as it is discussed earlier in the section 5.3.2.1). From the FC M(T) curves, surface's spins freezing temperature is 156 K in 500 Oe field which is slightly shifted to lower value (149 K) at the higher field of 5 kOe. It is noted that only one peak is observed in FC M(T) curve of 500 Oe which is related to the surface SG, because nearly same peak is observed at higher field of 5 kOe, therefore, the peak in the FC curve is not related to SSG phase as SSG phase is suppressed at high fields.

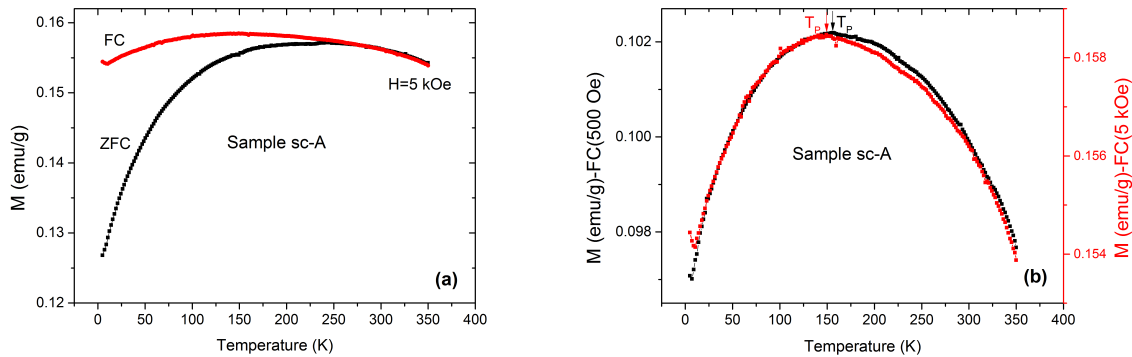


Figure 5.5.6: (a) ZFC and FC M(T) measurements in the field of 5 kOe of sample sc-A; (b) Temperature dependence FC curves in the fields of 500 Oe (black curve and left scale) and 5 kOe (red curve and right scale) of sample sc-A.

The indication of strong freezing of surface spins around 150 K through M(T) measurements is also verified through the EB behaviour, where below 140 K the magnitude of  $H_{EB}$  is enhanced and prominent at low temperatures (see  $H_{EB}$  curve of sc-A in Fig. 5.5.3(a)). Above 140 K, the presence of  $H_{EB}$  till 350 K with small magnitude indicates the presence of weak SG phase. The ac-susceptibility measurements of this sample, where in-phase part has no maximum till 350 K and out-of-phase part has

maximum at 257 K, reveal the presence of SG phase at higher temperatures. As ac-susceptibility measurements are more sensitive measurements so they can even exhibit the presence of weak SG phase in the system, while dc  $M(T)$  measurements indicate strong SG phase.

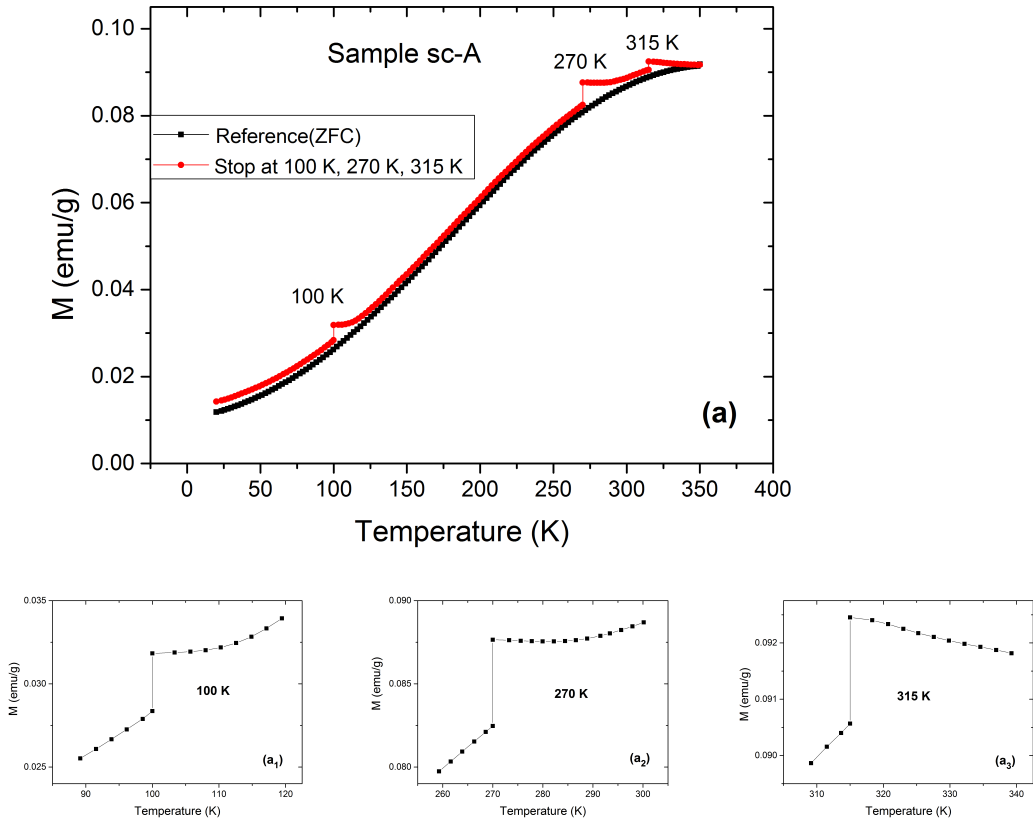


Figure 5.5.7:  $M_{ZFC}^{SWH}$  and  $M_{ZFC}^{Ref}$  measurements as a function of temperature (a),  $M_{ZFC}^{SWH}$  after aging of 2 h at 100 K ( $a_1$ ), at 270 K ( $a_2$ ) and at 315 K ( $a_3$ ), in sample sc-A.

In order to further investigate the SG phase in this system, aging measurements were done. The sample sc-A was cooled in zero field from 350 K to 5 K at the rate of 10 K/min, the magnetization ( $M_{ZFC}^{SWH}$ ) was measured during heating in 500 Oe at the rate of 2 K/min. During this, measurement was stopped at three different temperatures (100 K, 270 K and 315 K) and sample was aged for 2 hrs. Both  $M_{ZFC}^{SWH}$  and  $M_{ZFC}^{ref}$  curves are shown in Fig. 5.5.7(a).  $M_{ZFC}^{ref}$  is increased monotonically showing a normal behaviour as function of temperature. At intermittent stops (i.e., at 100 K, 270 K and 315 K)  $M_{ZFC}^{SWH}$  jumps to higher value and when heating is

restarted it continues to increase but much slower than  $M_{ZFC}^{ref}$  curve. As it is indicated earlier that the increase in the magnetization of  $M_{ZFC}^{SWH}$  curve as the temperature is increased after the stopping temperature, depicts the presence of SG<sup>138</sup>. The prominent increases in  $M_{ZFC}^{SWH}$  after stop at 100 K, indicates clearly SG phase (Fig. 5.5.7(a<sub>1</sub>)). The decreasing trend in  $M_{ZFC}^{SWH}$  at 270 K and clear decrease at 315 K shows weak and absence of SG phase, respectively (Fig. 5.5.7(a<sub>2</sub>) and (a<sub>3</sub>)). The presence of strong SG phase at 100 K is in accordance to FC M(T) measurements which indicates peak at 156 K. The low temperature strong SG phase is due to the freezing of surface spins, while weak SG phase at higher temperature may relate to weak SSG behaviour of these nanoparticles.

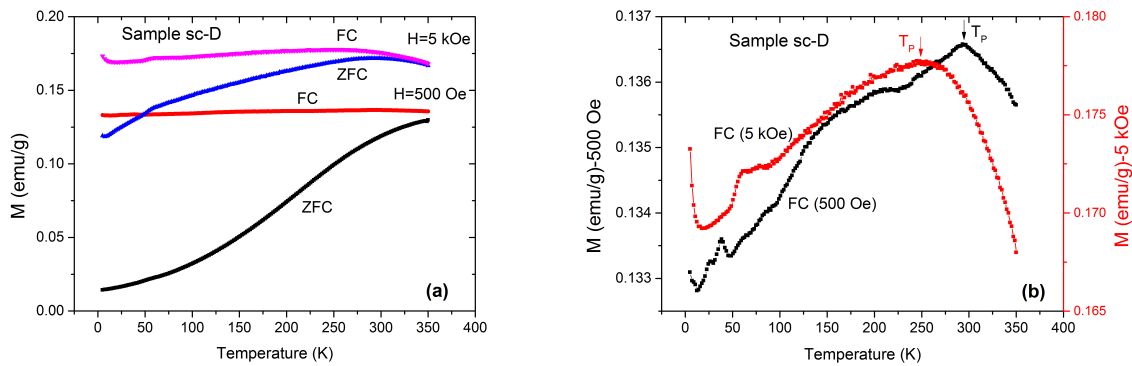


Figure 5.5.8: (a) Temperature dependence of ZFC and FC measurements in 500 Oe and 5 kOe, (b) temperature dependence of FC curves in 500 Oe (black curve and left scale) and 5 kOe (red curve and right scale), of sample sc-D.

To investigate the presence of SG phase in sample sc-D (spindle shaped; aspect ratio:6), the M(T) and ac-susceptibility measurements were done under the same procedure as described for other samples. No irreversibility between the FC and ZFC curves, is observed in the FC ZFC M(T) curves till 350 K, only the ZFC curve in 5 kOe field has maximum at 293 K related to  $T_B$  (see Fig. 5.5.8(a)). In the sample sc-D, the nanoparticles are blocked and  $T_B$  is higher than sample sc-A, the reasons are larger size and shape anisotropy. The peak in the FC M(T) curves at 294 K (500 Oe) and 250 K (5 kOe) indicates the surface SG phase, where the spins freezing at the surface causes decrease in the magnetization (see Fig. 5.5.8(b)). There is no clear indication of SSG phase from the M(T) curve in 500 Oe field, contrary to this the similar M(T) curve of un-coated sample D also indicates the presence of SSG phase along with surface SG (as discussed above in section 5.3.2). Being sensitive to

high fields, the indication of SSG phase at 5 kOe is difficult, so the single prominent peak in both FC  $M(T)$  curves in 500 Oe and 5 kOe fields, corresponds to surface SG.

The aging measurements were done under the same “stop and wait” protocol during heating in sample sc-D. The  $M_{ZFC}^{SWH}$  and  $M_{ZFC}^{ref}$  curves are shown in Fig. 5.5.9(a). It is observed that  $M_{ZFC}^{SWH}$  increases as the measurements were again started after 2 hr aging at 100 K and 270 K, which is clearly shown in Fig. 5.5.9(a<sub>1</sub>), (a<sub>2</sub>). The presence of SG phase is also verified by this increasing behaviour of  $M_{ZFC}^{SWH}$  at 100 K and 270 K. The decreasing trend of  $M_{ZFC}^{SWH}$  at 315 K relates to the absence of strong SG phase (Fig. 5.5.9(a<sub>3</sub>)).

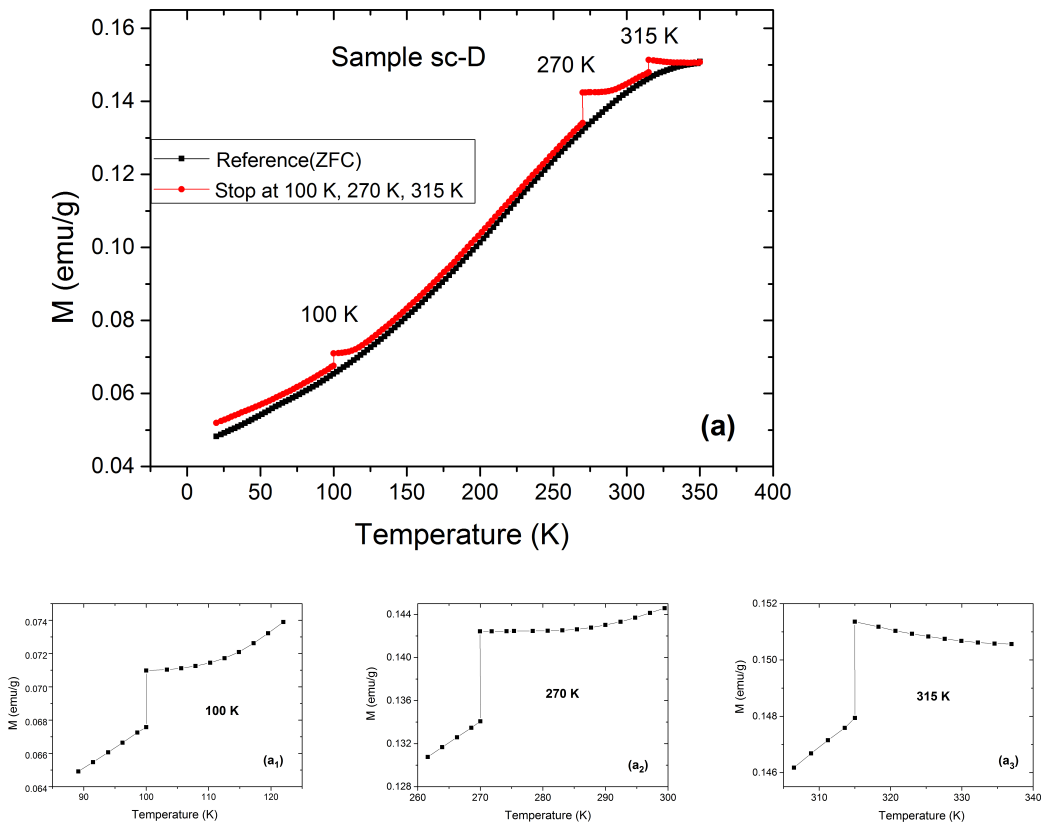


Figure 5.5.9:  $M_{ZFC}^{SWH}$  and  $M_{ZFC}^{Ref}$  as function of temperature (a),  $M_{ZFC}^{SWH}$  after aging of 2 h at 100 K (a<sub>1</sub>), at 270 K (a<sub>2</sub>) and at 315 K (a<sub>3</sub>), in sample sc-D.

From the above  $M(T)$  measurements of sample sc-D, it is clear that the surface SG phase is present, where strong surface spin freezing is observed at 294 K (peak in the FC  $M(T)$  curve in 500 Oe) is also manifested by large  $H_{EB}$  below 290 K. There

is a sign change in  $H_{EB}$  at 290 K, then it becomes positive with small magnitude till 350 K (see  $H_{EB}$  curve of sc-D in Fig. 5.5.3(a)). The non zero  $H_{EB}$  above 294 K relates to the presence of weak SG phase. From the previous study, it is clear that M(T) measurements indicate the presence of strong SG phase due to the freezing of surface spins, while ac-susceptibility measurements are needed to reveal weak SG phase.

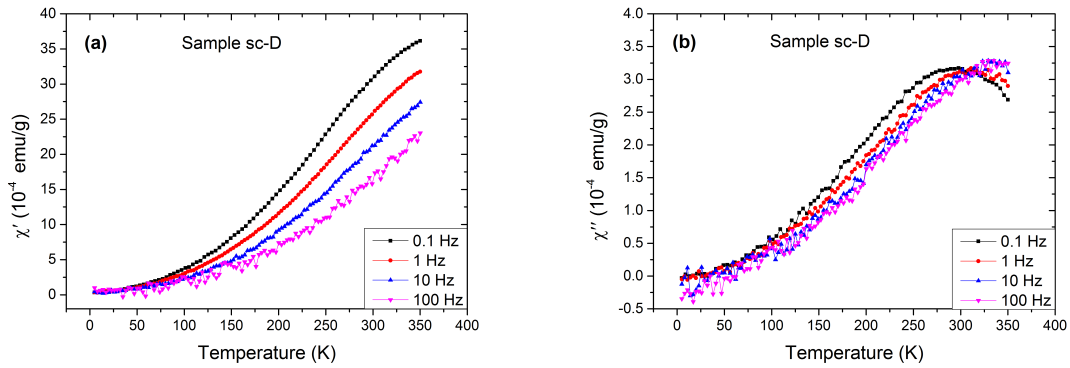


Figure 5.5.10: Temperature dependence of ac-susceptibility measurements of sample sc-D, in-phase part ( $\chi'$ ) (a), out-of-phase part ( $\chi''$ ) (b) at different frequencies from 0.1 Hz to 100 Hz.

The ac-susceptibility measurements are shown in Fig. 5.5.10, where  $\chi'$  monotonically increases but frequency dependent.  $\chi''$  has a peak at 298 K which shifts to higher temperatures with increase in frequency, indicating SG phase above room temperature. The  $H_{EB}$  at higher temperatures is justified by the presence of SG phase through ac-susceptibility measurements.

## 5.6 Effect of silica coating

In the previous sections of 5.3, 5.4 and 5.5, the magnetic characteristics of hematite and silica coated hematite nanoparticles of different aspect ratios are discussed separately in detail, here some results are again presented for the ease in the comparison. Fig. 5.6.1 shows M(T) measurements at 5 kOe in the samples A (spherical shaped; aspect ratio:1) and D (spindle shaped; aspect ratio:6) with comparison to their silica coated ones i.e., samples sc-A and sc-D, respectively. The first important effect of silica coating is observed in sample A where Morin transition vanishes after silica

coating (Fig. 5.6.1(a)). The second effect which is observed, is decrease in the magnetic moment after silica coating. The magnetization decreases from 0.395 emu/g to 0.159 emu/g and 0.371 emu/g to 0.176 emu/g in samples A and D, respectively after silica coating. It should be noted that magnetization of silica coated nanoparticles is normalized by the mass of hematite part only, excluding silica contributions. Therefore, the magnetization of uncoated and silica coated nanoparticles can be compared. The decrease in the magnetization is also observed from MH-loops of samples A and D when compared to samples sc-A and sc-D, respectively (see Fig. 5.3.10, Fig. 5.4.1 and Fig. 5.5.2). The increase in the number of spins that contributes to the distortion at the surface of these nanoparticles can be considered as the reason of decrease in the magnetization due to silica coating<sup>149</sup>. The absence of Morin transition in the sample sc-A is also related to the change due to frustration, where the silica coating causes increase in the distortion at the surface and lattice strain<sup>156</sup>. It is noted that interparticle interaction in the agglomerated hematite nanoparticles may support Morin transition. In  $\alpha\text{-Fe}_2\text{O}_3@\text{SiO}_2$  nanocomposites, Morin transition is observed, which is different from the present case due to cubic shape of nanoparticles of these nanocomposites<sup>147</sup>.

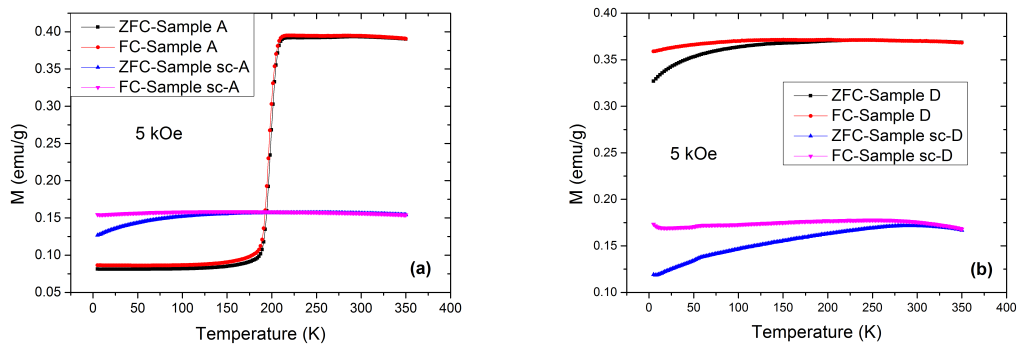


Figure 5.6.1:  $M(T)$  measurements at 5 kOe of uncoated and silica coated hematite nanoparticles, sample A (a), sample D (b).

Usually, superparamagnetism is enhanced in silica coated nanoparticles due to decrease in dipolar interactions between the nanoparticles, the effect of superparamagnetism is reported in coated  $\alpha\text{-Fe}_2\text{O}_3$  nanoparticles and superparamagnetic relaxation is suppressed in uncoated ones<sup>156-158</sup>. This implies that  $T_B$  should reduce in silica coated nanoparticles, which is contrary to the present study, where  $T_B$  of sample sc-D (293 K) is higher than sample D (239 K). Fig. 5.6.1(b) clearly indicates the decrease in magnetization and increase in  $T_B$  of silica coated sample D (sc-D)

as compared to uncoated one. The enhanced surface distortion due to silica coating, strengthens the role of surface anisotropy which reduces the superparamagnetic behaviour of the bulk part of nanoparticles. In the present hematite nanoparticles, inter-particle interactions are decreased due to silica coating but strong surface effects cause the anomalous increase of  $T_B$ .

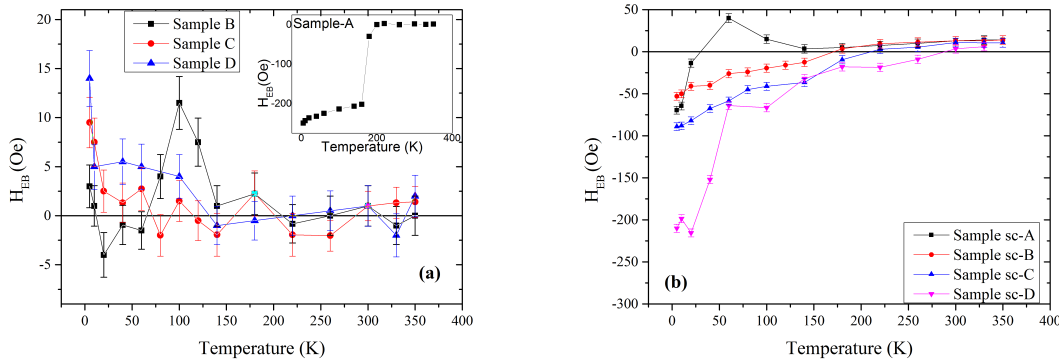


Figure 5.6.2: Temperature dependence of  $H_{EB}$  after field cooling of 20 kOe, (a) uncoated hematite nanoparticles (inset shows  $H_{EB}$  of sample A), (b) silica coated Hematite nanoparticles.

In the comparison of EB behaviour of hematite with silica coated hematite nanoparticles (shown in Fig. 5.6.2), two important points are observed. First is the change of sign at low temperatures and second one is enhanced magnitude of  $H_{EB}$  after silica coating. From the study of uncoated hematite nanoparticles, it is clear that the exchange interaction between antiferromagnetic core and surface SG generates negative  $H_{EB}$ , while positive  $H_{EB}$  is due to exchange interaction between weak ferromagnetic core and surface SG phase. The  $H_{EB}$  in the silica coated hematite nanoparticles is negative although having similar interaction i.e., between weak ferromagnetic core and surface SG which is contrary to uncoated ones (in uncoated hematite nanoparticles having weak ferromagnetic core and surface SG,  $H_{EB}$  is positive; in silica coated nanoparticles having weak ferromagnetic core and interface as well as surface SG,  $H_{EB}$  is negative). The enhancement in the magnitude of  $H_{EB}$  from 14 Oe to -177 Oe at 5 K of sample D and sc-D, respectively can easily be explained due to increase in the surface distortion. As silica coating results into large number of spins contribute to surface disorders which makes surface SG phase more strong and weakens SSG phase. The enhanced surface SG phase is also observed from FC M(T) curve in 500 Oe of sample sc-D having prominent peak at 294 K related to freezing of surface SG (see Fig. 5.5.8(b)). While in the respective

uncoated sample, i.e., sample D, two peaks are present, 348 K due to SSG and 149 K corresponds to the surface SG (see Fig. 5.3.4(a)). This implies that silica coating changes exchange interaction at the interface between core and surface spins (shell). In sample A (uncoated hematite nanoparticles depicting Morin transition), the abrupt sign change in  $H_{EB}$  from negative to positive is related to the rotation of Fe ions during Morin transition. On the other hand, in the silica coated nanoparticles, Morin transition is not evident which indicates that sign change is not related to the magnetic order of core part of hematite nanoparticles, rather to the interface, as interfacial spins are now more important due to silica coating.

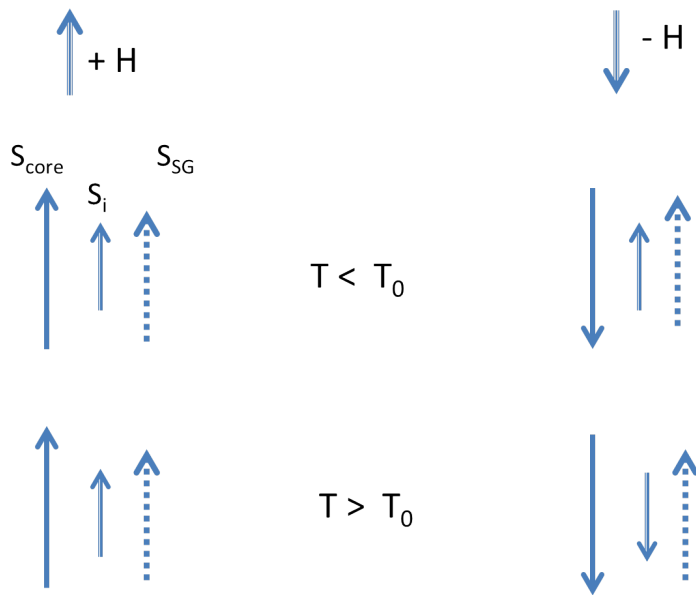


Figure 5.6.3: Schematic presentation of spins at different temperatures regime in core  $S_{core}$ , at interface  $S_i$  and in SG  $S_{SG}$  of silica coated hematite nanoparticles.

In order to explain the inverse EB in silica coated nanoparticles as compared to respective uncoated hematite nanoparticles, a model is proposed as illustrated in Fig. 5.6.3<sup>159</sup>. Here, three different spins are described, the spins present in surface SG ( $S_{SG}$ ), the interfacial spins ( $S_i$ ) and the spins present in the core of the nanoparticles ( $S_{core}$ ). During field cooling, the  $S_{SG}$  freeze along with the magnetic moments of core and  $S_i$  in the direction of cooling field. As the external field reverses, only the core magnetic moments rotate along the field, while the fixed spins at the interface apply pinning force which results into normal negative EB. Above  $T_0$ , the temperature where the  $H_{EB}$  changes sign, the thermal fluctuation weakens the stability of  $S_i$ , now rotating interfacial moments along with the magnetic moments of core

hematite during magnetization reversal. Where as, for the spins deep inside the SG phase, moments retain in the field cooling direction because they are still in frozen state. The rotation of  $S_i$  may results into antiparallel coupling between core and SG moments, which generates positive EB field.

The silica coating causes symmetry breaking, interstitial spaces, which results in more disorder, increased effective SG region and decrease in the magnetization. Morin transition also vanishes due to strain effect. This also affects exchange interaction between the interfacial and core moments, which results into different sign reversal of EB behaviour as compared to the uncoated ones.

## 5.7 Summary of chapter

The phenomena of memory effect, aging, Morin transition and EB are studied in the agglomerated hematite nanoparticles of different shapes from spherical to spindle shaped. The SSG and surface SG behaviours are observed that generate  $H_{EB}$ . The unusual presence of SSG phase above 300 K makes the system hematite nanoparticles interesting for the studies of SG. The new and remarkable behaviour of EB which has not been reported yet after careful literature survey, is the sign change in  $H_{EB}$  along with Morin transition, where the rotation of Fe ions in the core changes the exchange coupling at the interface and results in positive  $H_{EB}$  above  $T_M$ . However, below  $T_M$ , the  $H_{EB}$  due to the antiferromagnetic core and surface SG is negative. It is observed that Morin transition is diminished by shape anisotropy, present in spherical while absent in spindle shaped nanoparticles. The reasons are the enhanced lattice strain and surface defects with increasing the aspect ratio.

In order to eliminate agglomeration, the silica coating is used around the nanoparticles. The silica coating enhances the surface disorder, decreases magnetization and depletes Morin transition. In the silica coated nanoparticles, the surface SG phase is enhanced as compared to SSG behaviour, which strongly affects the EB behaviour. In the uncoated hematite nanoparticles,  $H_{EB}$  between weak ferromagnetic core and surface SG is positive while it is negative after silica coating. . The sign change and enhanced  $H_{EB}$  (change in the direction of loop shift) due to the silica coating in these hematite nanoparticles is an interesting phenomenon which is not yet studied. This change in the direction of loop shift is not related to Morin transition, but occurs due to the rotation of interfacial spins along with the core moments.

# Chapter 6

## Study of zero-field cooled exchange bias in $Co_{1-x}Mg_xFe_2O_4$ nanoparticles

### 6.1 Introduction

The spinel ferrites are the magnetic materials having general formula  $MFe_2O_4$ , where M is the divalent metal ion such as  $Mg^{2+}$ ,  $Mn^{2+}$ ,  $Co^{2+}$ ,  $Ni^{2+}$  etc. In the spinel structure, the oxygen ions in the lattice touch each other and form a close-packed face-centered cubic lattice. In this oxygen lattice, the metal ions take interstitial positions which can be classified into two groups; one group of lattice sites called tetrahedral sites or 8a sites (also denoted as A sites), each site is surrounded by four oxygen atoms. The other group is called octahedral or 16d sites (also denoted as B sites), each of which is surrounded by six oxygen atoms. The numbers of oxygen ions which surround tetrahedral and octahedral sites are in the ratio 2:3 (see Fig. 6.1.1).

In normal spinel structure,  $M^{2+}$  ions occupy the tetrahedral sites, while all  $Fe^{3+}$  ions occupy octahedral sites. The other structure is inverse spinel, where  $M^{2+}$  ions lie on the octahedral sites and  $Fe^{3+}$  ions equally distributed in octahedral and tetrahedral sites. The magnetic properties of spinel ferrites are strongly dependent on the type and distribution of metal ions amongst two interstitial sites. The cation distribution is influenced by radii of metal ions, electronic configuration and electrostatic energy of lattice. Other factors, such as composition, magnetocrystalline anisotropy and composition of metal ions also effect the distribution. Because of superparamagnetic nature and high surface to volume ratio, the ferrites have many

technological applications such as drug delivery, recording media, ferrofluids, sensors, medical diagnostic and magnetic resonance imaging<sup>160-162</sup>.

Cobalt ferrite ( $CoFe_2O_4$ ) is chemically stable and has large magnetocrystalline anisotropy (of the order of  $5 \times 10^6$  erg/cm<sup>3</sup>) with inverse spinel crystal structure,  $(Fe)[CoFe]O_4$  is the structural formula, where () and [] present tetrahedral and octahedral sites, respectively<sup>160-162</sup>. As the number of  $Fe^{3+}$  ions on both sites are same and their spins are antiparallel, so their moments are canceled, the net magnetic moment is due to the Co ions present at octahedral sites in the ideal system. Magnesium ferrite ( $MgFe_2O_4$ ) has mixed spinel structure, where  $Mg^{2+}$  and  $Fe^{3+}$  cations are unequally distributed among tetrahedral and octahedral lattice sites, the distribution is also temperature dependent. The structural formula is  $(Fe_{1-x}Mg_x)[Mg_{1-x}Fe_{1+x}]O_4$ .  $MgFe_2O_4$  has strong application in microwave devices because of their low magnetic and dielectric losses and high resistivity<sup>163</sup>.

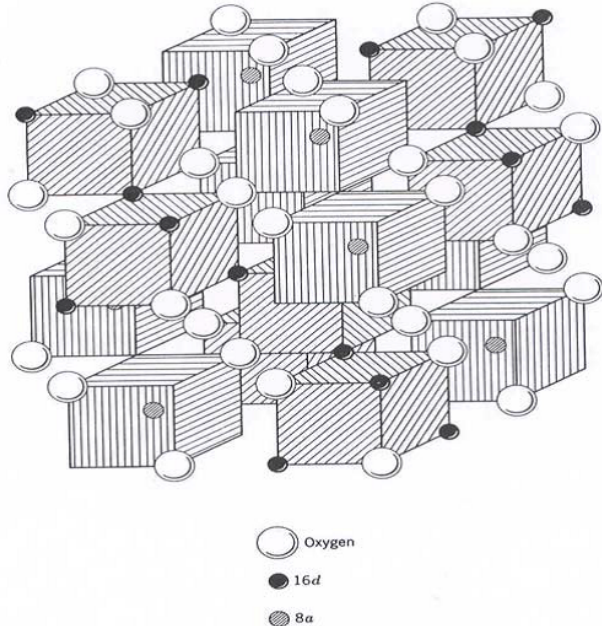


Figure 6.1.1: Arrangement of 8a, 16d sites and oxygen ions in the spinel structure

## 6.2 Synthesis

In order to study the dilution of strong cobalt ferrite by non magnetic atoms and to investigate the interaction mechanism, the structural and magnetic changes, Mg substituted Cobalt ferrite particles ( $Co_{1-x}Mg_xFe_2O_4$ ) with different compositions

were synthesized by sol-gel auto combustion. The ferric nitrate ( $\text{Fe}(\text{NO}_3)_3 \cdot 9\text{H}_2\text{O}$ ), magnesium nitrate ( $\text{Mg}(\text{NO}_3)_2 \cdot 6\text{H}_2\text{O}$ ), glycine ( $\text{C}_2\text{H}_5\text{NO}_2$ ) and cobalt nitrate ( $\text{Co}(\text{NO}_3)_2 \cdot 6\text{H}_2\text{O}$ ) with analytical grade were used as raw materials. The equal molar ratio of metal nitrates to glycine was dissolved in 75 mL of deionized water. The aqueous solution containing all raw materials was heated with continuous stirring until a clear sol has transformed into gel. The sol was dried into gel at 100 °C and then xerogel at 180 °C. The increase in temperature up to 220 °C led to self propagating combustion process to form as burnt loose powder. At the final stage, the burnt fluffy powder was annealed in furnace at 700 °C for 6 hrs with heating rate of 10 °C /min in order to get a desired spinel structure. These nanoparticles were prepared in collaboration with School of Science and Engineering, Lahore University of Management Sciences (LUMS), Pakistan. I am thankful to Dr. Shahid Ramay and Dr Tahir Farid for their cooperation. The discussed magnetic study was done by me at RWTH Aachen University.

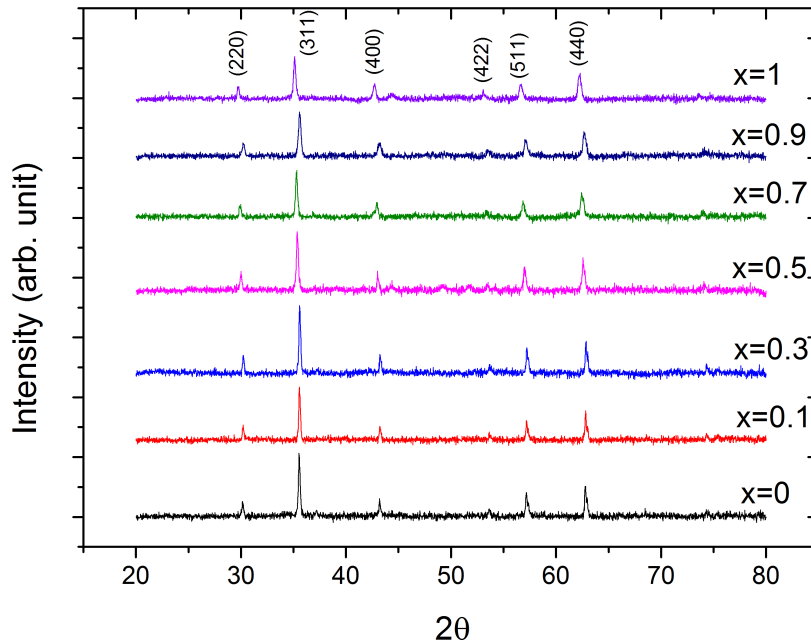


Figure 6.2.1: X-ray diffraction of  $\text{Co}_{1-x}\text{Mg}_x\text{Fe}_2\text{O}_4$  nanoparticles containing different values of Mg substitution.

The x-ray diffraction patterns of  $\text{Co}_{1-x}\text{Mg}_x\text{Fe}_2\text{O}_4$  nanopowder, where  $x = 0, 0.1, 0.3, 0.5, 0.7, 0.9$  and 1 are shown in Fig. 6.2.1. The data shows single phase spinel structure with cubic symmetry and no other extra peak is found related to secondary

phase. The average particle size is calculated by Scherrer formula  $D = 0.9\lambda/\beta\cos\theta$ , where  $\lambda$  is the wavelength (0.15406 nm),  $\beta$  is full-width at half maximum of (311) peak and  $\theta$  is diffraction angle of (311) peak<sup>164</sup>. The average size and lattice parameter (a) of  $Co_{1-x}Mg_xFe_2O_4$  nanoparticles for different Mg substitution are given in the graph (see Fig. 6.2.2). In the graph, the black colour curve and left scale denotes the size of these nanoparticles, while red colour curve and right scale corresponds to lattice parameter. The size of the nanoparticles with different Mg ions substitution, ranges from 30 nm to 45 nm which is not a big difference to be noticed. The lattice parameter of  $Co_{1-x}Mg_xFe_2O_4$  ( $x = 0$ ) is 8.37 Å which is in good agreement to the literature<sup>165</sup>. For  $Co_{1-x}Mg_xFe_2O_4$  ( $x = 1$ ) sample, the value of lattice parameter is 8.41 Å which is slightly larger than reported value of 8.38 Å<sup>166</sup>, the increased lattice parameter is also related to large strain effect in the sample due to Mg ions substitution. It seems that lattice parameter is nearly same due to high uncertainty (because of more calculations including systematic and random errors) but still there should be slightly change in the lattice parameter with substitution of Mg ions in  $Co_{1-x}Mg_xFe_2O_4$  which is not visible here. The distribution of data points shows small relative large value around  $x = 0.5$ .

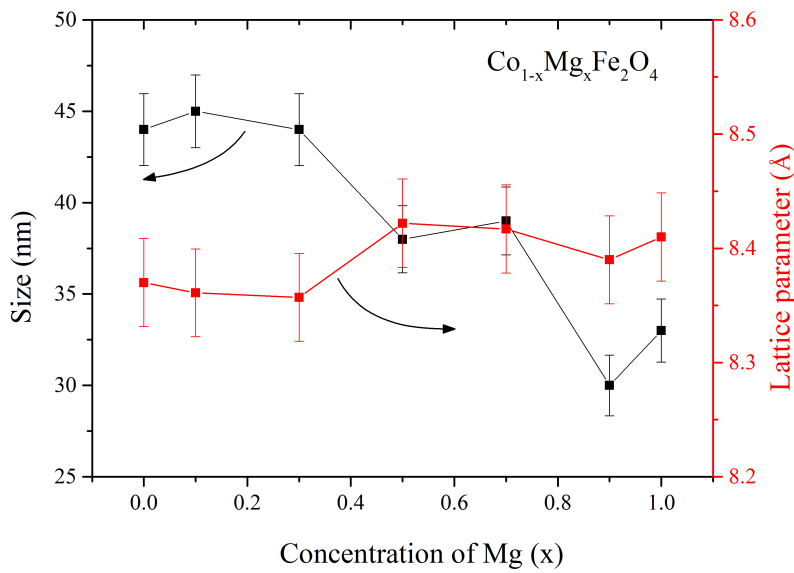


Figure 6.2.2: Size and lattice parameter as function of Mg substitution ( $x$ ) in  $Co_{1-x}Mg_xFe_2O_4$  nanoparticles. Left scale corresponds to size (black curve), while right scale denotes the lattice parameter (red curve).

Fig. 6.2.3 presents the TEM images of samples  $Co_{1-x}Mg_xFe_2O_4$  ( $x = 0.5, 0.7$ )

nanoparticles, the particles are spherical in shape and with uniform size distribution. Most of the particles are agglomerated, but by keen observation one can figure out that the size of nanoparticles is inconsistent with XRD measurements.

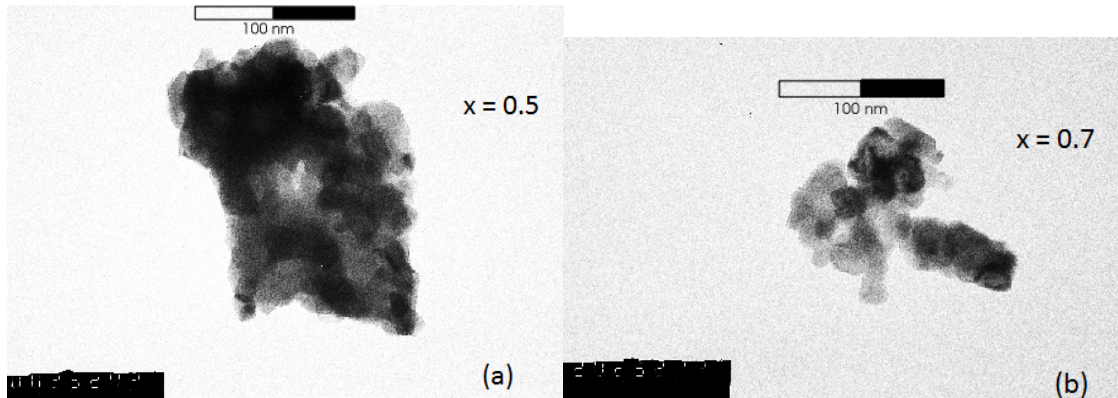


Figure 6.2.3: TEM images of  $\text{Co}_{1-x}\text{Mg}_x\text{Fe}_2\text{O}_4$  samples showing two different substitutions of Mg ions, (a)  $x = 0.5$  , (b)  $x = 0.7$  .

### 6.3 Magnetic characterization of nanoparticles in quasi-free state

The magnetic characterization of  $\text{Co}_{1-x}\text{Mg}_x\text{Fe}_2\text{O}_4$  nanopowder were done by MPMS XL-7 SQUID-magnetometer. The powdered nanoparticles were put in the small tube and just slightly pressed in order to avoid empty space in the tube, thus the particles were in quasi-free state. In the present section, all the magnetic measurements are for the  $\text{Co}_{1-x}\text{Mg}_x\text{Fe}_2\text{O}_4$  nanoparticles in quasi-free state and are not mentioned on the graphs. If the nanopowder was measured in other form, then it would be mentioned.

#### 6.3.1 Spontaneous exchange bias

In nanoparticles, the exchange bias (EB) is well known phenomenon and also observed in  $\text{CoFe}_2\text{O}_4$ <sup>167;168</sup>,  $\text{MgFe}_2\text{O}_4$  and  $\text{Co}_{1-x}\text{Mn}_x\text{Fe}_2\text{O}_4$  nanoparticles<sup>9;169</sup>, however not much data related to EB effect is reported in  $\text{CoFe}_2\text{O}_4$  and the substituted systems. Generally, the EB phenomenon is manifested by the shift in the hysteresis loop of the sample after cooling from  $T \geq T_N$  to low temperature in the presence of magnetic field, which is also called conventional EB (CEB). Recently,

the EB effect is observed after zero field cooling in  $Ni_{0.5}Mn_{0.5-x}In_x$  bulk alloy<sup>170</sup>,  $NiMnSn$  alloy<sup>171</sup>,  $BiFeO_3$ - $Bi_2Fe_4O_9$ nanocomposite<sup>123</sup>,  $Mn_2PtGa$  bulk alloy<sup>14</sup> and  $BiFeO_3$  –  $NiFe_2O_4$  core-shell nanoparticles<sup>172</sup>. The unconventional EB due to shift in hysteresis loop after zero field cooling is called ZFC EB or spontaneous EB (SEB).

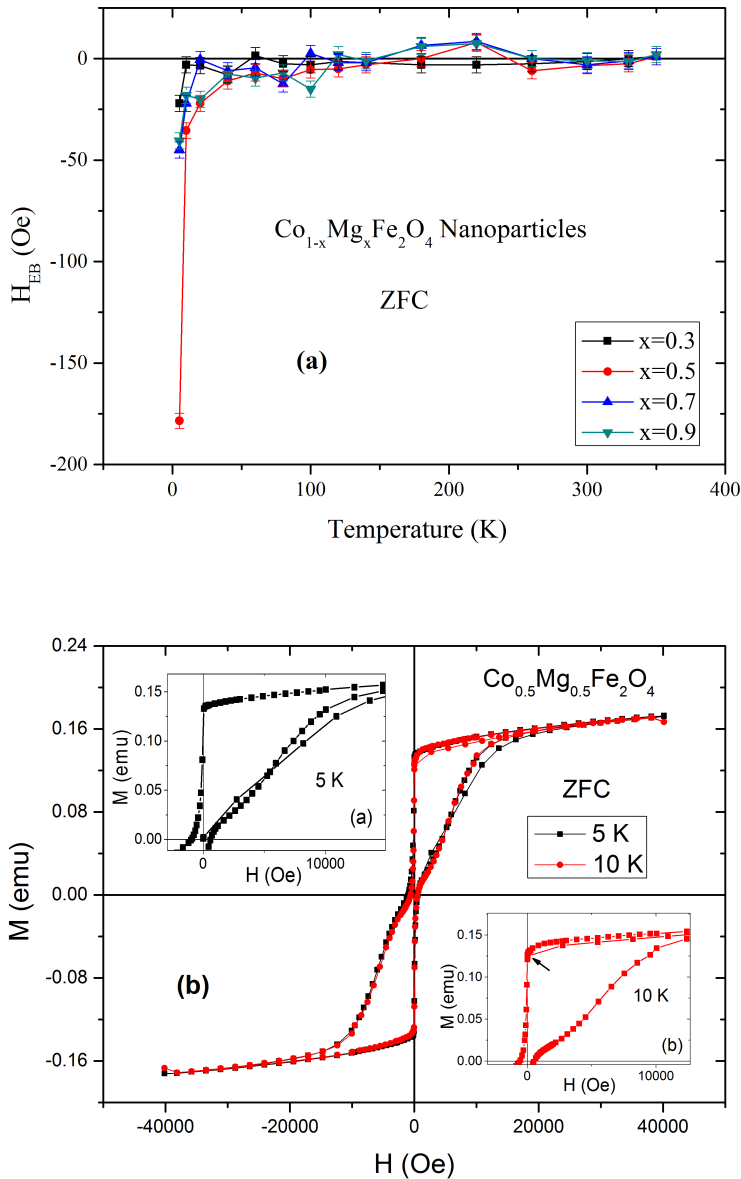


Figure 6.3.1: (a) Spontaneous exchange bias, SEB (exchange bias field,  $H_{EB}$  after ZFC) in  $Co_{1-x}Mg_xFe_2O_4$  nanoparticles with different concentrations of Mg; (b) Hysteresis loops at 5 K and 10 K of sample  $Co_{0.5}Mg_{0.5}Fe_2O_4$  after zero field cooling to 5 K .

The under studied  $Co_{1-x}Mg_xFe_2O_4$  nanoparticles show both CEB and SEB effects, the detailed magnetic study of these nanoparticles in this chapter helps to understand the SEB phenomenon. The samples of nanoparticles were measured by SQUID magnetometer after cooling from 300 K to 5 K in the absence of magnetic field, exhibit SEB. The hysteresis loops were started from 5 K, then the temperature was increased in steps to the required temperature subsequently, the sweeping field was 40 kOe. For CEB, the samples were FC under the same measuring field of 40 kOe from 350 K to 5 K and then temperature was increased from 5 K to 350 K to measure at different temperatures. Before starting the measurement, an additional loop at 5 K was measured in order to reduce training effect. The exchange bias field ( $H_{EB}$ ) and coercive field ( $H_C$ ) were determined from the left and right coercive fields ( $H_C^{Left}$ ,  $H_C^{Right}$ ) of the hysteresis loop.

The SEB in  $Co_{1-x}Mg_xFe_2O_4$  nanoparticles ( $x = 0.3, 0.5, 0.7, 0.9$ ) is reported in Fig. 6.3.1(a), where the maximum SEB  $H_{EB}$  ( $H_{SEB}$ ) is observed in  $Co_{0.5}Mg_{0.5}Fe_2O_4$  sample at 5 K. The behaviour of SEB as function of temperature is nonmonotonic,  $H_{SEB}$  is negative at low temperatures, it decreases with temperature and becomes positive with a peak at 220 K in positive direction. This behaviour of SEB with a sign change having peak in positive direction has not been reported yet, although it is observed in CEB<sup>173</sup>. The presence of maximum SEB in  $Co_{1-x}Mg_xFe_2O_4$  nanoparticles with  $x = 0.5$ , considers the sample for the detailed study. The ZFC hysteresis loops of  $Co_{0.5}Mg_{0.5}Fe_2O_4$  sample at 5 K and 10 K are shown in Fig. 6.3.1(b), the sample is ZFC from 300 K to 5 K and measurement is started from  $H = 0$ . Although, the sample is cooled from magnetized state because at 300 K, hysteresis is still present, but the magnetic moment at the starting point of initial curve ( $H = 0$ ) is nearly zero (i.e. 0.001 emu; see inset (a) of Fig 6.3.1(b)). After measurement of hysteresis loop at 5 K, temperature is increased to 10 K in zero field and measurement is again started from  $H = 0$ , now the initial curve is started from 0.126 emu (see inset (b) of Fig 6.3.(b)), as a result  $H_{SEB}$  decreases sharply from -179 Oe to -36 Oe at 5 K and 10 K, respectively. The increase in the magnetic moment of initial curve of hysteresis loop at 10 K is due to the remanent magnetic moment because of the application of high field of 40 kOe at 5 K. This indicates the importance of initial magnetic state of the sample before measurement on SEB effect.

In order to investigate the effect of initial magnetic state on SEB, the ZFC hysteresis loops of  $Co_{0.5}Mg_{0.5}Fe_2O_4$  sample were again measured, but in this case sample was ZFC from 300 K to the each measuring temperature, individually. The behaviour

of SEB in this case is shown in Fig. 6.3.2(a), where  $H_{SEB}$  changes from -179 Oe to -151 Oe for 5 K to 10 K, respectively. The change in SEB from 5 K to 10 K in this measurement (ZFC-each) is small as compared to the previous measurement (ZFC-Fig. 6.3.1), which is because of the presence of small initial magnetic moment at the start of the hysteresis loop of 10 K. This difference is also clear from hysteresis loops of 5 K and 10 K, presented in Fig. 6.3.2(b).

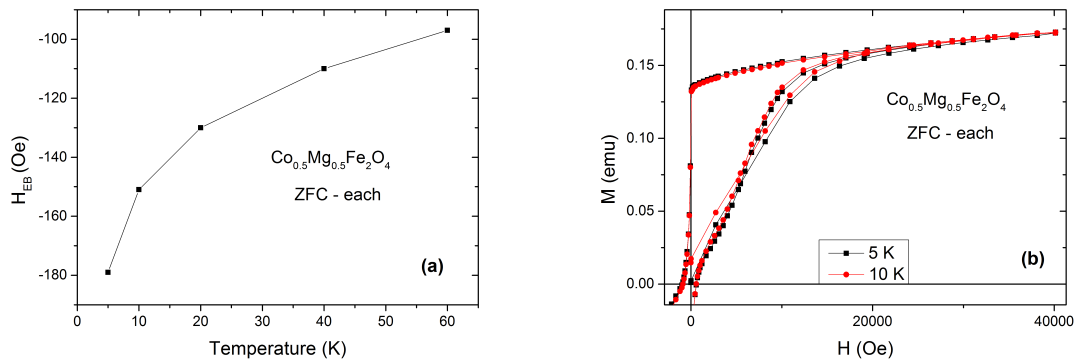


Figure 6.3.2: (a) Temperature dependence of  $H_{EB}$  after zero-field cooling to the respective measuring temperature of  $Co_{0.5}Mg_{0.5}Fe_2O_4$  sample. (b) Hysteresis loops of  $Co_{0.5}Mg_{0.5}Fe_2O_4$  sample after zero-field cooling to 5 K and 10 K, individually.

For the measurement of hysteresis loop at 10 K, the sample was ZFC from 300 K to 10 K, the initial magnetic moment is 0.014 emu and  $H_{SEB}$  is -151 Oe (here is a difference from previous case, where sample was heated from 5 K to 10 K in zero field and initial magnetic moment at 10 K is 0.126 emu with  $H_{SEB} = -36$  Oe). The increase in  $H_{SEB}$  after zero-field cooling to each temperature individually, is also observed at 20 K, 40 K and 60 K as compared to the  $H_{SEB}$  after cooling to 5 K and then subsequent heating to these temperatures. These measurements indicate the strong dependence of SEB on the initial magnetic moment, where depression in initial magnetic moment results in enhanced SEB.

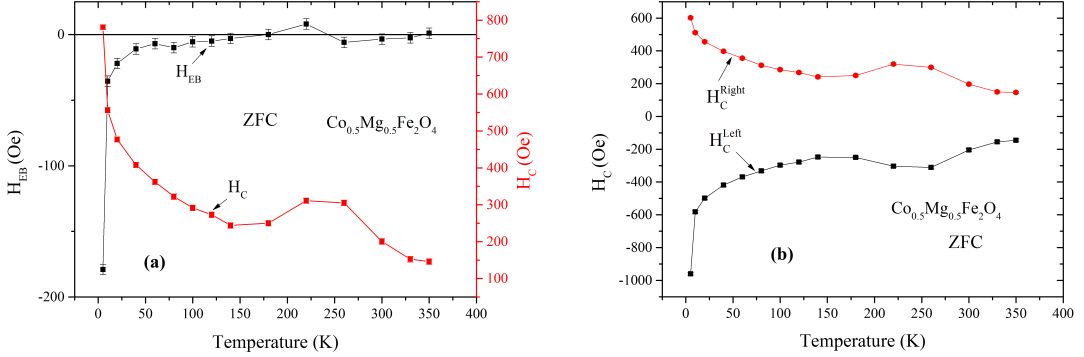


Figure 6.3.3: (a) Temperature dependence of  $H_{EB}$  (black curve, left scale) and coercive field,  $H_C$  (red curve, right scale), (b) temperature dependence of  $H_C^{Left}$  and  $H_C^{Right}$  of  $Co_{0.5}Mg_{0.5}Fe_2O_4$  sample after zero field cooling.

Fig. 6.3.3(a) presents the temperature dependence of  $H_{SEB}$  (black curve, left scale) and  $H_C$  (red curve, right scale) after zero-field cooling to 5 K and then heating to respective temperatures in  $Co_{0.5}Mg_{0.5}Fe_2O_4$  sample. The SEB field shows a sign change with peak in positive direction at 220 K, the behaviour of  $H_C$  is also unusual with a peak at 220 K. The peak in SEB at 220 K is also observed in other samples of  $Co_{1-x}Mg_xFe_2O_4$  nanoparticles having concentration of Mg ions, where  $x = 0.7, 0.9$  (see Fig. 6.3.1(a)).

In  $Ni_{50}Mn_{50-x}Sn_x$  alloy<sup>171</sup>,  $BiFeO_3$ - $Bi_2Fe_4O_9$  nanocomposite<sup>123</sup> and  $Mn_2PtGa$  bulk alloy<sup>14</sup>, the temperature dependence of SEB is reported but without any sign change. The temperature driven sign change in SEB is a unique behaviour which is only yet obtained by Monte Carlo simulation in nanoparticles with antiferromagnetic core and ferromagnetic shell<sup>174</sup>, which is contrary to the present  $Co_{0.5}Mg_{0.5}Fe_2O_4$  sample where the core is ferrimagnetic and shell is SG (as discussed later). In CEB, the sign change is observed through variation either in field or temperature, where temperature induced sign change has different explanations in different systems<sup>8;159;173;175;176</sup>. In the field driven sign change in CEB, positive  $H_{EB}$  is due to the antiferromagnetic coupling of interfacial FM-AFM spins where Zeeman energy induced the magnetic ordering of AFM spins<sup>177</sup>.

The sign change in  $Co_{1-x}Mg_xFe_2O_4$  nanoparticles is thermally activated without any field cooling, therefore, it is different to the mechanism where the large cooling fields are responsible for the positive EB. In the present system, the observed peak in  $H_C$  which is coincided with the peak in SEB at 220 K, is different from other systems

where peak in  $H_C$  is observed at the sign change temperature of  $H_{EB}$ <sup>178</sup> or near the Blocking temperature (where  $H_{EB}$  becomes zero)<sup>179</sup>.  $H_C^{Left}$  and  $H_C^{Right}$  are plotted as function of temperature in Fig. 6.3.3(b), where both are non-monotonic, having a peak at 220 K related to the positive peak in SEB.

According to the literature survey, the sign change with positive peak in CEB (EB after field cooling) is reported in Co/CoO bilayers<sup>175;176</sup>, due to reversible change in AFM's grains causing disordered interface and unidirectional enhancement of  $H_C$  along field cooling direction<sup>176</sup>. In other report, the magnetization reversal is the reason of sign change in CEB in Co/CoO bilayers, where it is more pronounced along the hard axis<sup>175</sup>. These two cases are different from the present case, because in these systems only  $H_C^{Right}$  has a peak while  $H_C^{Left}$  decreases monotonically. The reported behaviour of  $H_C$  is similar to Co/CuMn system, where the sign reversal of CEB is due to long-ranged Ruderman-Kittel-Kasuya-Yosida (RKKY) interactions<sup>8</sup>. Fe/Cr bilayers<sup>173</sup> also exhibits temperature driven sign change with non-monotonic behaviour of  $H_C^{Left}$  and  $H_C^{Right}$ , the presence of re-entrant SG due to interface alloying is the reason of the sign change in CEB (The study of EB in Fe/Cr bilayer is discussed in next chapter). Although the behaviours of EB and coercivity in these two systems are similar to the given  $Co_{1-x}Mg_xFe_2O_4$  nanoparticles, but in these two systems the sign change is observed in CEB and there are well defined FM and SG phases. In present case, the results are also obtained after zero field cooling which makes the system different. Therefore, new interpretations are required to understand the sign change in SEB.

In order to observe the effect of field cooling on EB and coercivity,  $Co_{0.5}Mg_{0.5}Fe_2O_4$  sample was measured after cooling from 350 K to 5 K in the presence of 40 kOe field, results are shown in Fig. 6.3.4(a). The  $H_{EB}$  is presented by black curve and corresponds to left scale, it is observed that it drastically decreased from -179 Oe to -14 Oe because of field cooling. The  $H_C$  (red curve, right scale) is nearly constant from 5 K to 350 K without any large quantitative change (magnitude remains between 112 Oe and 101 Oe with uncertainty, see Fig. 6.3.4(a)). After field cooling, it is clear that both  $H_{EB}$  and  $H_C$  are reduced in magnitude in comparison to ZFC measurements, this indicates the difference in mechanism for CEB and SEB.

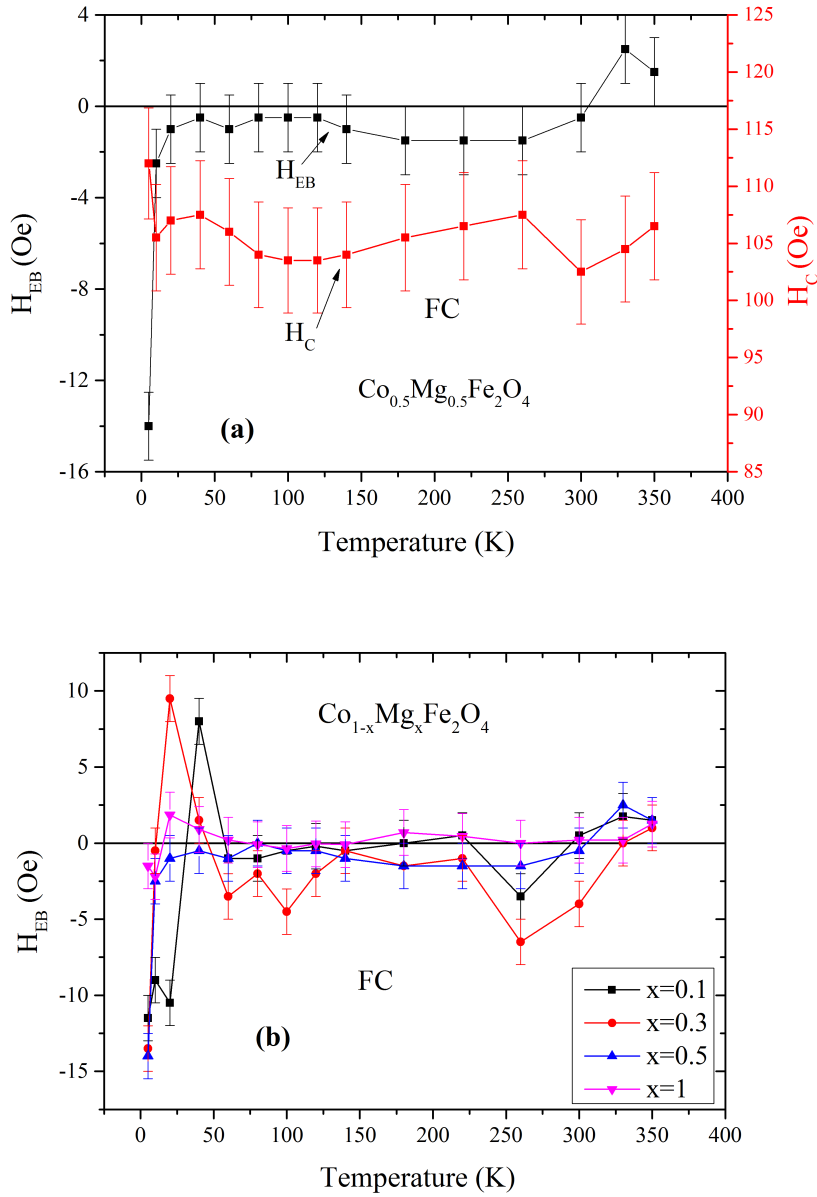


Figure 6.3.4: (a) Temperature dependence of  $H_{EB}$  (black curve, left scale) and  $H_C$  (red curve, right scale) of  $\text{Co}_{0.5}\text{Mg}_{0.5}\text{Fe}_2\text{O}_4$  sample after field cooling, (b) Temperature dependence of  $H_{EB}$  after field cooling in  $\text{Co}_{1-x}\text{Mg}_x\text{Fe}_2\text{O}_4$  nanoparticles with different concentration of Mg ions.

FC EB phenomenon (CEB) as function of temperature in the different samples of  $\text{Co}_{1-x}\text{Mg}_x\text{Fe}_2\text{O}_4$  nanoparticles, where  $x = 0.1, 0.3, 0.5$  and  $1$  are shown in Fig. 6.3.4(b). It is observed that CEB depicts non-monotonic behaviour with small magnitude as compared to SEB.

### 6.3.2 Spin dynamics

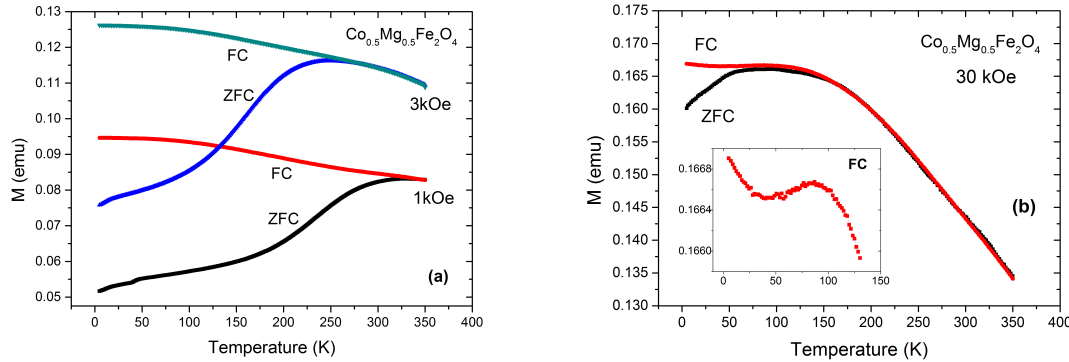


Figure 6.3.5: Zero-field cooled (ZFC) and field cooled (FC) magnetic moment versus temperature,  $M(T)$ , measurements in  $Co_{0.5}Mg_{0.5}Fe_2O_4$  sample in (a) 1 kOe and 3 kOe fields, (b) in the field of 30 kOe (inset: FC  $M(T)$  curve of 30 kOe).

The ZFC and FC magnetic moment versus temperature,  $M(T)$ , measurements of  $Co_{0.5}Mg_{0.5}Fe_2O_4$  sample were done under different fields in the temperature range of 5 K to 350 K. It is important to note that in this chapter, the term “magnetization” is not used because the magnetic moment of the measured nanoparticles is neither normalized by mass nor volume, however, “ $M$ ” presents the magnetic moment in the figures and descriptions in only this chapter. Fig. 6.3.5(a) shows the ZFC and FC curves of magnetic moment versus temperature under an applied field of 1 kOe and 3 kOe. The peak in ZFC curve is related to blocking temperature ( $T_B$ ) of non-interacting nanoparticles, above  $T_B$  the thermal energy overcomes to magnetic anisotropy energy barrier of single domain nanoparticles as a result spins are randomly oriented causes superparamagnetism.

The ZFC and FC curves show an irreversible magnetic behaviour below the temperature called irreversibility temperature ( $T_{irr}$ ), this temperature relates to the blocking of largest nanoparticles under small applied fields. The irreversible behaviour due to blocking of nanoparticles is vanished when the field of few kOe is applied, and reversibility under high fields relates with freezing of surface spins of nanoparticles<sup>9;117;120</sup>. The presence of enhanced irreversibility in the ZFC and FC curves of  $Co_{0.5}Mg_{0.5}Fe_2O_4$  sample up to the high field of 30 kOe (see Fig. 6.3.5(b)), discards its relation to blocking, and indicates the freezing of surface spin glass. The disorder is produced in the surface spins due to broken exchange bonds between the spins, change of coordination of surface atoms and translational symmetry breaking

of the lattice, the freezing of these disordered surface spins results into spin glass (SG) phase<sup>120</sup>.

From the present measurements,  $T_{irr}$  in 1 kOe field is 345 K and decreased to 164 K under 30 kOe field depicts strong irreversibility at high field of 30 kOe. It has been reported that the decrease or the saturation in the FC curve with decreasing temperature is related to the SG phase, while it monotonically increases with decreasing temperature for superparamagnets (SPMs)<sup>127</sup>. The presence of SG phase through decrease in FC magnetization curve with increasing temperature is vividly observed in hematite nanoparticles (see chapter 5). Here in  $Co_{0.5}Mg_{0.5}Fe_2O_4$  nanoparticles, the FC curves of 1 kOe and 3 kOe are tending towards saturation at low temperatures (see Fig. 6.3.5(a)), also the magnetic moment of FC curve in 30 kOe slightly decreases below 90 K as shown in the inset of Fig. 6.3.5(b). These features of FC curves manifest the presence of SG phase in these nanoparticles. After decrease in magnetic moment, FC curve of 30 kOe tends to saturate due to complete freezing of surface spins but it does not happen due to high applied field. The increase in magnetic moment at higher temperatures corresponds to alignment of spins along the external field.

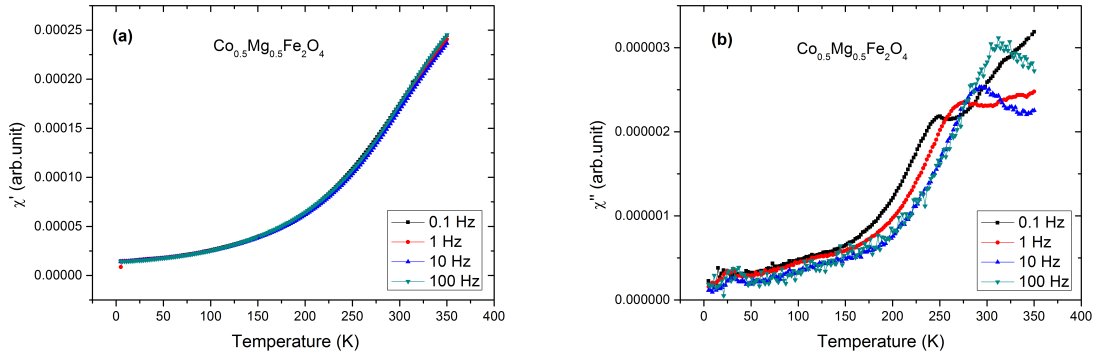


Figure 6.3.6: The ac- susceptibility measurements of  $Co_{0.5}Mg_{0.5}Fe_2O_4$  sample at different frequencies of 0.1 Hz, 1 Hz, 10 Hz and 100 Hz, (a) in-phase part ( $\chi'$ ), (b) out-of-phase part ( $\chi''$ ).

The ac-susceptibility measurements are helpful to understand the dynamics of the spins in the system, the peak in the ac-susceptibility measurement indicates either  $T_B$  or freezing temperature for SPMs or SG systems, respectively. In order to manifest the SG phase in these nanoparticles, the ac-susceptibility measurements were done during heating from 5 K to 350 K under 5 Oe oscillating field after zero

field cooling at frequency ranges from 0.1 Hz to 100 Hz. The temperature dependence of in-phase part ( $\chi'$ ) is increased monotonically over the whole temperature range at all given frequencies. The out-of-phase part ( $\chi''$ ) increases and indicates a transition through a peak at 250 K for 0.1 Hz. The peak in  $\chi''$  shifts to higher temperatures with increase in frequency, where transition occurs at 313 K for 100 Hz. As it is already cleared from dc measurements that the irreversibility in ZFC and FC curves of these nanoparticles is related to surface SG phase instead of superparamagnetism. In order to prove that the given frequency dependent ac-susceptibility measurements indicates SG phase, the quantitative measure of frequency shift is calculated by,

$$\Gamma = \Delta T_P / T_P \Delta (\log_{10} \omega)$$

where  $T_P$  is peak temperature,  $\omega$  is the frequency and  $\Delta$  refers to the difference. For SGs,  $\Gamma$  ranges from 0.0045 to 0.08 while for SPMs  $\Gamma \approx 0.3^{34;127}$ . The calculated value of  $Co_{0.5}Mg_{0.5}Fe_2O_4$  sample is approximately 0.06, which indicates that the given system is SG and the ac-susceptibility measurements are not related to SPMs. The above M(T) and ac-susceptibility measurements have verified the presence of surface SG due to frustration of surface spins in these nanoparticles.

## 6.4 Exchange bias in semi-compressed form

Now, the powder  $Co_{1-x}Mg_xFe_2O_4$  nanoparticles were pressed physically in small teflon capsule. The magnetic characterization of the nanoparticles were done by MPMS XL-7 SQUID-magnetometer under same conditions. The magnetic moment of teflon capsule is very small as compared to nanoparticles, so its contribution is negligible.

The semi-compressed (Comp)  $Co_{0.5}Mg_{0.5}Fe_2O_4$  nanoparticles were measured under zero field from 350 K to 5 K, the hysteresis measurement was taken at 5 K and then the temperature was increased in steps to the required temperature subsequently, similar to previous measurements. The ZFC measurements result the SEB which is shown in Fig. 6.4.1(a). CEB measurement were done under the same conditions as for quasi-free particles and presented in Fig. 6.4.1(b). The magnitude of CEB is larger than SEB in semi-compressed form of nanoparticles which is opposite to quasi-free state. Both, SEB and CEB show sign change with peak in positive direction at 220 K. It is also observed that coercive field in SEB and CEB is nearly same and much higher than quasi-free state. The strong interparticle attraction and restricted

movement of nanoparticles do not differentiate vigorously, under both conditions of cooling.

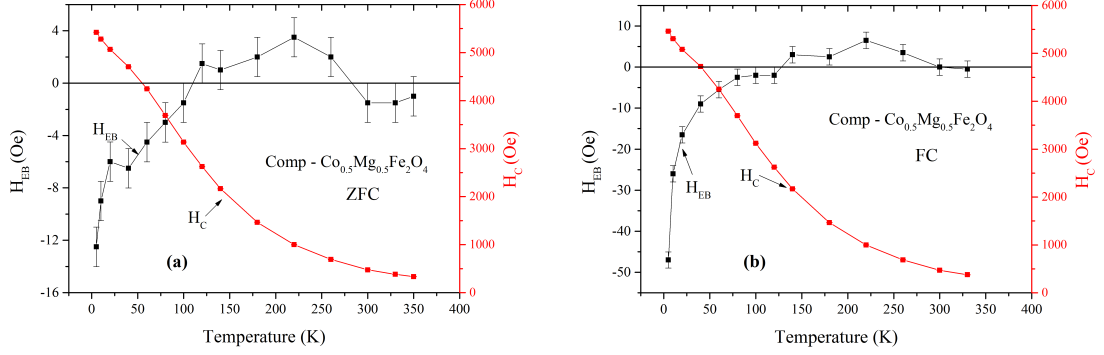


Figure 6.4.1: Temperature dependence of  $H_{EB}$  (black curve, left scale) and  $H_C$  (red curve, right scale) of semi compressed  $Co_{0.5}Mg_{0.5}Fe_2O_4$  sample, (a) after zero field cooling, (b) after field cooling.

Here it is important to mention that after careful literature survey, the sign change in SEB is only observed through Monte Carlo method in single nanoparticle having antiferromagnetic core and ferromagnetic shell<sup>174</sup>. Although the sign change is temperature driven and depends on exchange interaction at interface which relates EB to interfacial effect, only. This system is quite different from the present system of  $Co_{1-x}Mg_xFe_2O_4$  nanoparticles, where interparticle interactions and dilution also play major roles and exhibit surface and bulk contributions to SEB (ZFC-EB) besides interface.

## 6.5 Explanation

In the present system of  $Co_{1-x}Mg_xFe_2O_4$  nanoparticles, a new behaviour of SEB is occurred as not reported experimentally, where ZFC EB changes the sign from negative to positive  $H_{EB}$  with a peak at 220 K. In CEB, the magnitude of  $H_{EB}$  and  $H_C$  is small as compared to SEB with sign change in  $H_{EB}$ , which is not periodic. In order to understand these new results of SEB in comparison with CEB, new mechanism is required depends upon the interaction of SG to the external field. Instead of having two distinct materials as core/shell structure, these nanoparticles consist of ferrimagnetic core and surface SG as shell with irregular interface and the disorder in spins from inner core to surface is not abrupt. After zero field cooling

to 5 K, nearly zero magnetic moment indicates the randomness in the system. This strong randomness among the spins, increases the volume fraction of SG phase which interact to the ferrimagnetic grains in the nanoparticles. In ZFC, the exchange interactions at the interface are randomly oriented, so EB should be zero collectively. Upon applying field during initial magnetization process, ferrimagnetic grains try to align along the field direction, where spins from SG phase do not align in few kOe fields. As the field increases to 40 kOe, the magnetic moment of ferrimagnetic core is along the field while moments of SG phase also try to align in the field direction. This disturbs the unidirectional exchange interaction between ferrimagnetic core and SG phase at the shell. The increase in magnetic moment at very low temperature of FC curve at 30 kOe verifies the response of spins of SG phase at high field (see Fig. 6.3.5(b)).

In quasi-free powder form, EB is much stronger in ZFC as compared to FC condition, the reason is related to the large volume fraction of SG phase in ZFC. During field cooling from high temperature, large number of spins of ferrimagnetic phase align along the field. This enhances the ferrimagnetic core and reduces the SG phase to the surface, thus decreasing the pinning centers. On the other hand, during zero field cooling, the spins at and near the surface of nanoparticles are not aligned to the preferred direction causing frustration and freeze in random direction, which contribute to the surface SG phase. The saturation magnetic moment of ZFC loop is also less than FC due to large SG phase and decrease in the ferrimagnetic core part. From ZFC hysteresis loops, it is also clear that reduced initial magnetic moment increases SEB (see Fig. 6.3.1(b) and Fig. 6.3.2(b)), reason is large pinning centers due to increase in volume of SG phase. The enhanced frustration, large pinning sites and decreased ferrimagnetic region are also responsible for increased coercivity in SEB as compared to CEB<sup>180,181</sup>.

The strong relation of SEB to the disordered spins is also verified by the presence of maximum SEB in quasi-free powder of  $Co_{1-x}Mg_xFe_2O_4$  nanoparticles with  $x = 0.5$  (see Fig. 6.3.1(a)). As the structural formula is  $(Fe_{1-\delta}Mg_{\delta})[Co_{1-x}Mg_{x-\delta}Fe_{1+\delta}]O_4$ , where Mg ions are unequally distributed among both tetrahedral and octahedral lattice sites. The substitution of Mg ions causes frustration in the system due to competition between Co and Mg ions at octahedral sites<sup>182</sup>. It appears that frustration is maximum at  $x = 0.5$ , which strengthens the SG phase and manifests the largest SEB in these nanoparticles.

The reduction in SEB and enhancement in CEB in semi-compressed nanoparticles

as compared to quasi-free powder, are related to the interparticle attraction and the movement of particles. In quasi-free powder, the interparticle attraction is weak and particles can rotate themselves easily along the field direction. This helps the nanoparticles to adjust such that moments in SG phase align along the field with ferrimagnetic spins, decreasing the angle between them and enhances the SEB. In FC, the convenient movement of particles and core spins along the field direction with large thermal energy at high temperature in presence of field, strengthens spin order and reduces SG phase which weakens CEB in quasi-free state.

Besides the presence of SEB, the other interesting feature is the sign change in EB field with peak in positive direction at 220 K. In quasi-free powder form, it is found that sign change occurs in all samples irrespective of concentration of Mg ions and FC or ZFC measurements. In SEB, a visible peak is observed at 220 K in  $Co_{1-x}Mg_xFe_2O_4$  samples with  $x>0.3$ , while in CEB sign change occurs with non periodic peaks (see Fig. 6.3.1(a) and Fig. 6.3.4(b)). In semi-compressed  $Co_{0.5}Mg_{0.5}Fe_2O_4$  sample, peak at 220 K is also observed both in SEB and CEB (see Fig. 6.4.1). The presence of Peak at 220 K in most cases, seems intrinsic to the system and relates to structural characteristic. Mg substitution may change the lattice parameter, although for the present system, the visible change in the lattice parameter is not reported due to high uncertainty (see Fig. 6.2.2).

The strain is exerted due to high frustration caused by competition of Co and Mg ions (it may also cause due to change in the lattice parameter). The exerted strain induces the metastable domains in the system, as the domains are energetically favourable structure because they allow the system to release elastic stress<sup>183;184</sup>. The non-magnetic dilution in the system also facilitate the metastable domain formations which is also applicable in the present system<sup>30</sup>. These metastable domains are formed during cooling, thus they are thermally activated and can deplete when enough thermal energy is available to switch them. The sign change in EB field is related to the formation and depletion of these metastable domains, especially at interface.

The temperature driven sign change in EB field in the present nanoparticles can be interpreted as follows. During cooling, the metastable domains are formed mainly in the ferrimagnetic core part, which makes the interface interaction frustrated and antiferromagnetically coupled<sup>179</sup>. This generates negative EB at low temperatures. This explanation is also evident from maximum SEB in  $Co_{0.5}Mg_{0.5}Fe_2O_4$  sample, where the metastable domains due to strain and high frustration, cause strong anti-

ferromagnetic coupling. With increase in the temperature, most of these metastable domains at the interface disappear as enough thermal energy is available to switch them along with core ferrimagnetic moments. This changes the exchange coupling at the interface and yields effective coupling to generate positive EB. The magnetic moments in SG phase away from interface, mostly retain in the frozen state. The peak in positive EB is accompanied with local peak in both  $H_C^{Left}$  and  $H_C^{Right}$  (see Fig. 6.3.3). The change in coercivity in the temperature range of inverse bias is related to decrease in the number of metastable domains, as domain walls move easily within the magnet and have a low coercivity. The FC, ZFC conditions, dilution and frustration are the important factors which influence the formation of metastable domains in the present system. Therefore, the metastable domains also control the magnitude of SEB and CEB along with sign reversal.

## 6.6 Summary

In this chapter,  $Co_{1-x}Mg_xFe_2O_4$  nanoparticles ( $x = 0, 0.1, 0.3, 0.5, 0.7, 0.9, 1$ ) are studied in quasi-free state and semi-compressed form. In these nanoparticles, the core is ferrimagnetic with surface spin glass phase at shell, having irregular and frustrated interface. SEB is observed along with CEB in both states of nanoparticles. In quasi-free state of nanoparticles, SEB is larger than CEB, along with increased coercivity in ZFC as compared to FC conditions. While in semi-compressed form, CEB is stronger as compared to SEB with similar coercive field. The initial magnetic state has strong influence on SEB, where strong randomness contributes to the volume fraction of SG phase. The frustration and smooth movement of nanoparticles enhance SEB in quasi-free state of nanoparticles. The unidirectional anisotropy is established between ferrimagnetic domains and SG moments during initial magnetization process up to high fields. Maximum SEB in  $Co_{0.5}Mg_{0.5}Fe_2O_4$  sample is related to large frustration in sample due to competition between Co and Mg ions on octahedral sites.

The sign change in SEB is reported experimentally here for the first time in a system having SG shell after careful literature survey. The temperature driven sign change is observed in SEB and CEB, with the peak in  $H_{EB}$  occurs at 220 K (in most cases) in the direction of cooling field. The metastable domain states are developed in the system due to strain and dilution. With increase in temperature, the metastable domains at the interface have enough thermal energy to move when perturbed by

rotation of ferrimagnetic core moments. Some metastable domains disappear due to switching with core ferrimagnetic moment and generates positive EB field. It is also important to mention that sign change in EB after ZFC condition has been observed first time experimentally, along with effect of interparticle interactions. The present system is different to single nanoparticle with antiferromagnetic core and ferromagnetic shell<sup>174</sup>, where sign change in ZFC  $H_{EB}$  is observed through simulation and EB is only related to the interface.

.



# Chapter 7

## Effect of interface alloying on exchange bias in Fe/Cr bilayers

In this chapter, the systematic study of low temperature enhancement and sign reversal in the exchange bias (EB) is done in Fe/Cr bilayers. The competing interactions at the interface between the Fe and FeCr interdiffused alloy, is responsible for the present behaviour of EB. The re-entrant spin glass (RSG) phase is observed due to intermixing of Fe and Cr at interface. Samples with different interfaces, Fe/Cr, Cr/Fe and  $Fe/Cr_{1-x}Fe_x$ , are investigated to explain these effects. This work has already been published<sup>173</sup>

### 7.1 Introduction

Cr and its alloys exhibit various interesting magnetic phases like spin-density-wave (SDW), SG, ferromagnetic and paramagnetic characteristics<sup>185;186</sup>. Giant magnetoresistance (GMR) effect in Fe/Cr multilayers<sup>187</sup> and study of antiferromagnetic coupling between two Fe layers in Fe/Cr/Fe trilayers<sup>188</sup>, give remarkable importance to Cr as an antiferromagnet (AFM). The interface alloying is an important effect during device fabrication, it has been observed that GMR in Fe/Cr is sensitive to interface alloying<sup>189</sup>.

## 7.2 Study of exchange bias in Fe/Cr samples

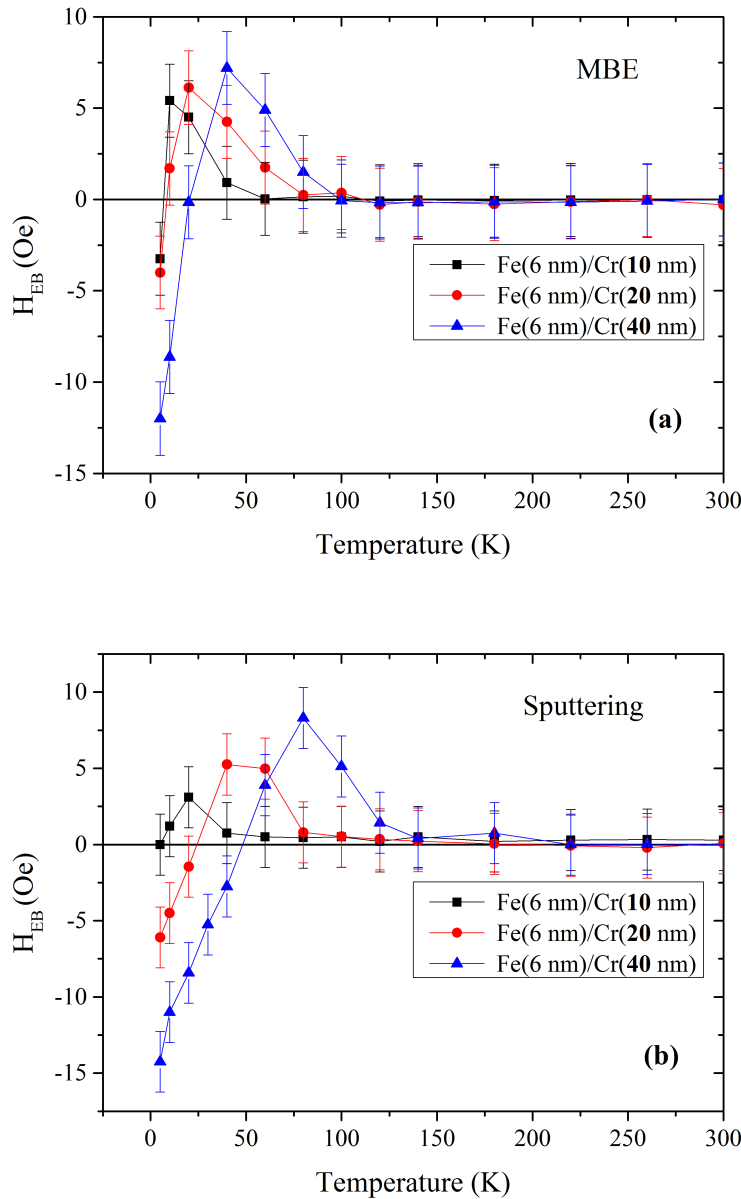


Figure 7.2.1: Temperature dependence of exchange bias field,  $H_{EB}$  in  $\text{Fe}(6 \text{ nm})/\text{Cr}(t_{Cr} \text{ nm})$  samples where  $t_{Cr}=10, 20, 40 \text{ nm}$ , grown by (a) molecular-beam epitaxy (MBE), (b) sputtering techniques.

To investigate EB in Cr, the series of samples having layer sequence of  $\text{Si}/\text{SiO}_2/\text{Cu}(10 \text{ nm})/\text{Fe}(6 \text{ nm})/\text{Cr}(t_{Cr} \text{ nm})$  containing different thicknesses of Cr layer,  $t_{Cr}=10, 20, 40 \text{ nm}$ , were deposited by

molecular-beam epitaxy (MBE) and sputtering techniques. The magnetic measurements were done by SQUID magnetometry under different conditions. In order to study EB phenomenon, the samples were field cooled from 370 K to 5 K ( $T_N$  of bulk Cr is 311 K) in the field of 1 kOe. The temperature was increased in steps from 5 K to 330 K, for the measurement of hysteresis loop at the required temperature. The exchange bias field ( $H_{EB}$ ) and coercive field ( $H_C$ ) were determined from the left and right coercive fields ( $H_C^{Left}$ ,  $H_C^{Right}$ ) of hysteresis loop, where  $H_{EB}=(H_C^{Left}+H_C^{Right})/2$  and  $H_C=-(H_C^{Left}-H_C^{Right})/2$ .

The behaviour of  $H_{EB}$  as a function of temperature in Fe(6 nm)/Cr( $t_{Cr}$  nm) samples ( $t_{Cr}=10, 20, 40$  nm) is shown in Fig. 7.2.1(a) and (b), which are deposited through MBE and sputtered techniques, respectively. The important feature is the sign reversal in  $H_{EB}$  at low temperatures. In both types of samples,  $H_{EB}$  is negative at low temperature and decreases with temperature up to temperature  $T_0$  at which it changes its sign and passes through a positive maximum before vanishing at blocking temperature,  $T_B$ . The sign reversal temperature,  $T_0$  and the magnitude of  $H_{EB}$  strongly depend on  $t_{Cr}$ , where thicker Cr sample enhances  $H_{EB}$  and shifts  $T_0$  to higher temperatures.  $T_0$  increases from 7 K to 20 K as  $t_{Cr}$  increases from 10 nm to 40 nm in MBE grown samples. The Fe(6 nm)/Cr(40 nm) sample would be discussed in detail, as magnitude and sign reversal in  $H_{EB}$  are more pronounced in this sample.

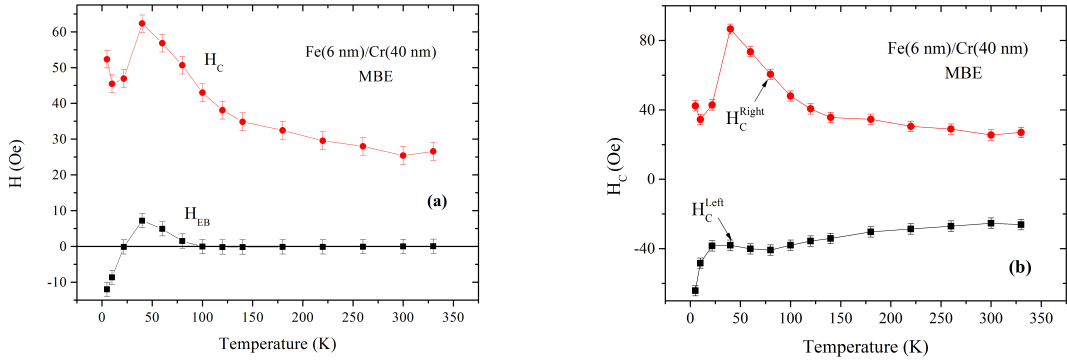


Figure 7.2.2: (a) Temperature dependence of  $H_{EB}$  and coercive field,  $H_C$ , (b) temperature dependence of  $H_C^{Left}$  and  $H_C^{Right}$  of MBE grown Fe(6 nm)/Cr(40 nm) sample.

The temperature dependence of  $H_{EB}$  and  $H_C$  in Fe(6)/Cr(40 nm) sample grown by MBE and sputtering, are presented in Fig. 7.2.2(a) and Fig. 7.2.3(a), respectively.

The  $H_C$  shows nonmonotonic behaviour, varies in a close relation with  $H_{EB}$ .  $H_C$  is enhanced at a maximum negative  $H_{EB}$ , it decreases with decrease in  $H_{EB}$ , having local minimum when  $H_{EB}$  passes through  $T_0$ . Above  $T_0$ ,  $H_C$  has maximum nearly at the same temperature where  $H_{EB}$  has peak in positive direction. This close correlation between  $H_C$  and  $H_{EB}$  is not commonly observed. In order to get an insight into the underlying mechanism of sign reversal of EB,  $H_C^{Left}$  and  $H_C^{Right}$  of the hysteresis loops should be considered as the function of temperature. Fig. 7.2.2(b) and Fig. 7.2.3(b) present the temperature dependence of  $H_C^{Left}$  and  $H_C^{Right}$  of Fe(6)/Cr(40 nm) sample, deposited through MBE and sputtered techniques, respectively.  $H_C^{Left}$  and  $H_C^{Right}$  show nonmonotonic behaviour in accordance with  $H_C$ .  $H_C^{Right}$  has peak nearly at  $T_0$  along with dip in  $H_C^{Left}$ , while  $H_C^{Left}$  has maximum at same temperature where there is dip in  $H_C^{Right}$ , corresponds to maximum in  $H_{EB}$ . Similar behaviour of  $H_C$  with  $H_{EB}$  is observed in canonical SG (CuMn) with Co layer and is explained through Ruderman-Kittel-Kasuya-Yosida (RKKY) interactions<sup>8</sup>.

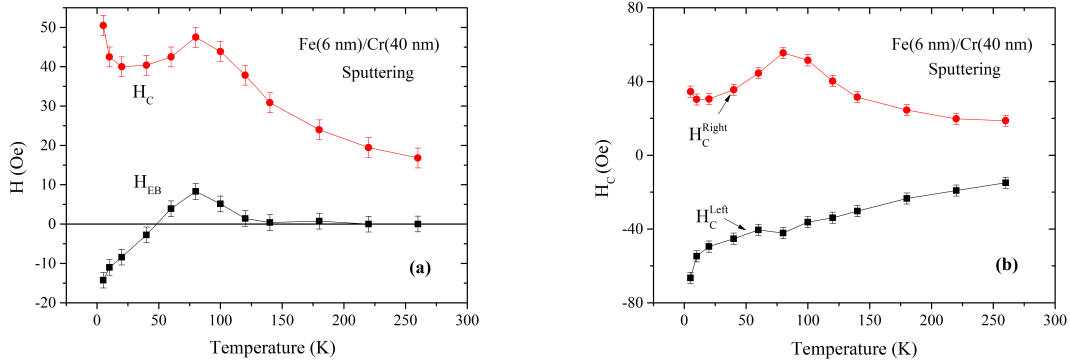


Figure 7.2.3: (a) Temperature dependence of  $H_{EB}$  and  $H_C$ , (b) temperature dependence of  $H_C^{Left}$  and  $H_C^{Right}$  of sputtered grown Fe(6 nm)/Cr(40 nm) sample

### 7.3 Effect of reversed interface: Cr/Fe interface

In order to study the role of interface on EB phenomenon in detail, the sample with reversed order was prepared, where Fe was deposited on the top of Cr. The sequence of sample is Si/Si<sub>3</sub>N<sub>4</sub>/Cu(10 nm)/Cr(40 nm)/Fe(6 nm)/Au(5 nm), simply denoted as Cr/Fe, deposited by MBE technique. The temperature dependence of  $H_{EB}$  and  $H_C$  are shown in Fig. 7.3.1(a), where there is no sign reversal in  $H_{EB}$  is found along with monotonic behaviour of  $H_C$ . The two main results can be inferred from this

measurement, first one is the importance of the order of overlayer and underlayer and secondly, the verification of correlation of nonmonotonic behaviour of  $H_C$  with  $H_{EB}$ . It is observed that  $H_C^{Left}$  and  $H_C^{Right}$  also show monotonic behaviour in accordance with  $H_C$ .

The reverse order of under and over layers strongly affects the EB mechanism, this is related to the interdiffusion at the interface. The melting point of Fe is 1808 K which is lower than that of Cr (2130 K). In Fe/Cr sample, where Cr was deposited at the top of Fe, interface alloying can occur which may cause the sign reversal in  $H_{EB}$ . In Cr/Fe sample, due to low melting point of overlayer, the formation of alloy is exempt, which is consistent with the absence of sign reversal in temperature dependence of  $H_{EB}$ . In polycrystalline samples, interfacial defects and roughness can act as nucleation centers to enhance the interface diffusion<sup>190</sup>.

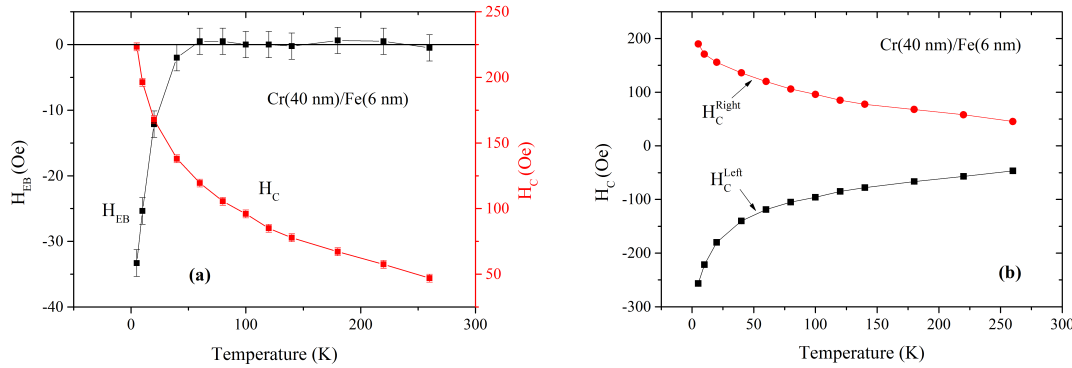


Figure 7.3.1: a) Temperature dependence of  $H_{EB}$  and  $H_C$ , (b) temperature dependence of  $H_C^{Left}$  and  $H_C^{Right}$  of MBE grown Cr(40 nm)/Fe(6 nm) sample.

## 7.4 Oxide barrier: Verification of interdiffusion

The previous results indicate the presence of interface alloying in Fe/Cr bilayers, in order to verify this assumption, oxide layer was used as a diffusion barrier between Fe and Cr bilayers. During the deposition, oxygen was introduced into the deposition chamber at different growth stages, for the intentional oxidation in two different samples. In the first sample, oxidation was carried out after the formation of Fe/Cr interface i.e. after the deposition of 5 nm Cr on the top of Fe (sample 1). The remaining 35 nm Cr and Au cap layers were deposited after recovering the vacuum. In this sample, interface comprises Fe/Cr but without any effect of bulk Cr. The  $H_{EB}$

behaviour of sample 1, exhibits sign change in positive direction, similar to Fe/Cr result (see Fig. 7.4.1(a)). In second sample (sample 2), the oxidation was carried out after the Fe underlayer, that results into Fe-Fe oxide-Cr interfaces. This method of oxidation exempts the formation of Fe/Cr interface. The  $H_{EB}$  behaviour of sample 2 is shown in Fig. 7.4.1(b), where sign reversal is absent, similar to Cr/Fe sample. In the sample 2, the exchange interaction between Fe and Fe-oxide (either  $\alpha$ - $Fe_2O_3$  or FeO) is responsible for the presence of negative  $H_{EB}$  at low temperatures.

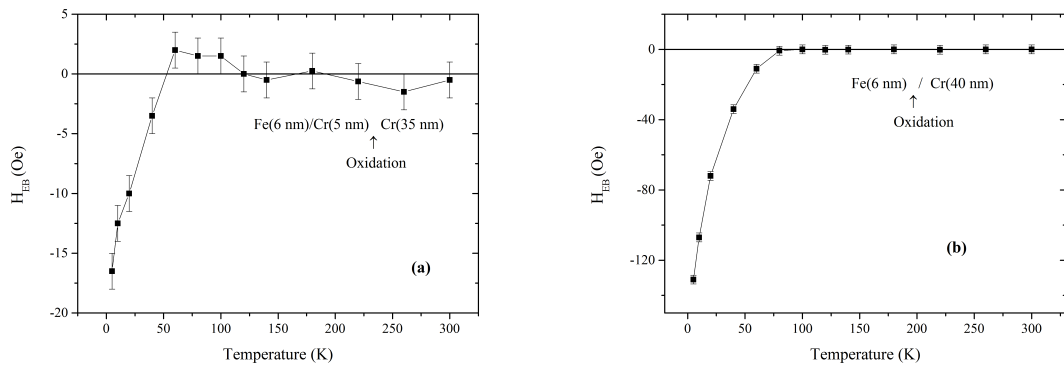


Figure 7.4.1: Temperature dependence of  $H_{EB}$  in (a) sample where oxidation occurred after 5 nm Cr, (b) in sample where oxidation occurred after Fe.

The difference in  $H_{EB}$  due to oxide barrier at different growth stages, verifies the reason of sign reversal of  $H_{EB}$  and nonmonotonic behaviour of  $H_C$ , i.e., the interface alloying. The oxide layer at the top of Fe layer, prohibits the intermixing of Fe with Cr. This indicates that the sign reversal EB with temperature in Fe/Cr sample is due to the exchange interaction between Fe and FeCr alloy, rather than the exchange interaction between Fe and Cr. In Fe/Cr bilayer, the interface is not abrupt, it is diffused due to intermixing of Fe and Cr layers.

## 7.5 Effect of Fe dilution in Cr on exchange bias

From the previous studies, it is clear that interface alloying is responsible for sign reversal in  $H_{EB}$ , where the exchange interaction is developed between Fe and Fe-Cr alloy. In order to give direct proof, the series of samples containing  $Cr_{1-x}Fe_x$  alloy underneath the Fe top layer, are deposited. This results into a interface between Fe-Cr alloy and Fe, similar to Fe/Cr, but without any direct interdiffusion of Fe and Cr at

interface, because Fe was deposited at top of  $Cr_{1-x}Fe_x$  layer. The layer sequence is Si/Si $O_2$ /Cu(10 nm)/ $Cr_{1-x}Fe_x$ (40 nm)/Fe(6 nm)/Au(5 nm), where  $0.15 \leq x \leq 0.20$ .

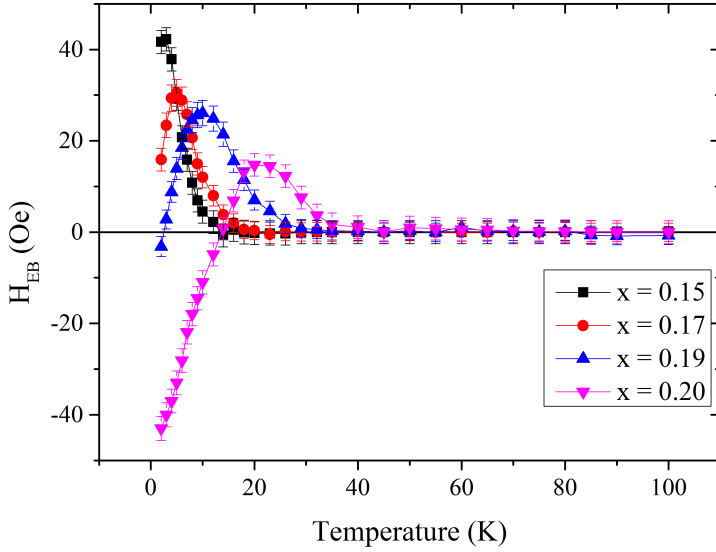


Figure 7.5.1: Temperature dependence of  $H_{EB}$  in  $Cr_{1-x}Fe_x$ (40 nm)/Fe(6 nm), with different values of Fe concentration (x).

The temperature dependence of  $H_{EB}$  in  $Cr_{1-x}Fe_x$ (40 nm)/Fe(6 nm) samples, where Fe concentration is,  $x = 0.15, 0.17, 0.19$  and  $0.20$  is shown in Fig. 7.5.1. For the low concentrations of Fe in  $Cr_{1-x}Fe_x$ (40 nm)/Fe(6 nm) samples ( $x = 0.15, 0.17$ ), the  $H_{EB}$  is positive with a peak but without any sign reversal. In the  $Cr_{1-x}Fe_x$ (40 nm)/Fe(6 nm) sample containing  $x = 0.19$ ,  $H_{EB}$  is negative at low temperature, changes the sign at  $T_0$  and goes through a positive peak before vanishing at  $T_B$ . The negative  $H_{EB}$  enhances with increasing Fe dilution in Cr and  $T_0$  shifts to higher temperatures. The results obtained in  $Cr_{1-x}Fe_x$ /Fe samples are similar to Fe/Cr samples, this proves the formation of FeCr alloy at interface in Fe/Cr samples. In Fe/Cr bilayers, the alloy formation is not uniform, because it forms unintentionally. While, in  $Cr_{1-x}Fe_x$ /Fe samples, the controlled intentional alloying yields a uniform  $Cr_{1-x}Fe_x$ alloy.

## 7.6 Explanation

For better understanding of the origin of sign reversal in  $H_{EB}$ , magnetic characterization of FeCr alloy is needed. Sole  $Cr_{1-x}Fe_x$  layer with  $x = 0.19$  was deposited under same conditions. The low field magnetization versus temperature,  $M(T)$  and ac-susceptibility measurements were done by SQUID magnetometer. Fig. 7.6.1(a), presents the zero-field cooled (ZFC) and field cooled (FC)  $M(T)$  measurements in the field of 35 Oe. The FC  $M(T)$  curve increases with temperature but becomes constant at low temperatures with slightly decreasing trend. The decrease in FC  $M(T)$  curve is nearly at 25 K, which indicates the strong freezing of SG phase<sup>127</sup>. The presence of strong SG phase in sole  $Cr_{1-x}Fe_x$  layer with  $x = 0.19$  is also verified by rapid increase in the magnitude of  $H_{EB}$  below 25 K in the  $Cr_{1-x}Fe_x$  (40 nm)/Fe(6 nm), where  $x = 0.19$  (see Fig. 7.5.1).

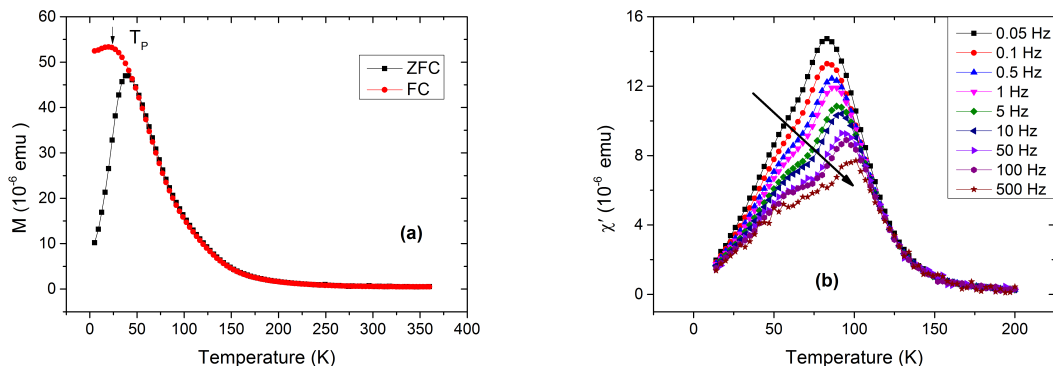


Figure 7.6.1: (a) Zero-field cooled (ZFC) and field cooled (FC) magnetization versus temperature,  $M(T)$  measurements in 35 Oe field, (b) in-phase part ( $\chi'$ ) of ac-susceptibility measurements of  $Cr_{1-x}Fe_x$ (40 nm) sample, where  $x= 0.19$ .

Fig. 7.6.1(b), presents the temperature dependence of in-phase part ( $\chi'$ ) of ac-susceptibility in  $Cr_{1-x}Fe_x$  layer for  $x = 0.19$ , from 0.05 Hz to 500 Hz. The peak in  $\chi'$ , is moved to higher temperatures with increasing frequencies. The single peak at 0.05 Hz, changes to plateau with increase in frequencies, exhibits double peak structure. The high temperature peak is related to transition of ordered antiferromagnetic or ferromagnetic phases into disordered paramagnetic phase. The low temperature peak is related to transition into re-entrant SG (RSG) phase from ordered antiferromagnetic or ferromagnetic phase, with decrease in temperature, consider as  $T_{RSG}$ <sup>173</sup>.

According to the magnetic phase diagram of bulk  $Cr_{1-x}Fe_x$  alloy<sup>191</sup>, SG phase exists between ferromagnetic and antiferromagnetic phase for  $0.16 < x < 0.19$ . It also exhibits RSG phase transition for SG composition lying near the boundaries to antiferromagnetic and ferromagnetic phases. Different studies show temperature driven RSG phase into ferromagnetic and antiferromagnetic phases, generally for  $0.18 < x < 0.25$ <sup>173</sup>. It is observed that RSG transition is not sharp on the microscopic scale, i.e., the system can neither be described by a single Curie temperature or Néel temperature nor by single value of  $T_{RSG}$ <sup>192</sup>. The magnetic properties of  $Cr_{1-x}Fe_x$  alloy, are sensitive to local concentration of Fe atoms or clusters in Cr matrix. The clustering in  $Cr_{1-x}Fe_x$  alloy causes nonuniform distribution of Fe atoms, which could support RSG to ferromagnetic phase transition. Similarly in Fe deficient regions, the alloy composition would be closer to that near the RSG-AFM boundary, in this case temperature driven transition favours RSG to antiferromagnetic phase. The RSG transitions is originated due to competing exchange interactions in  $Cr_{1-x}Fe_x$  alloy, where Fe-Fe interactions are ferromagnetic, while Cr-Fe and Cr-Cr interactions are antiferromagnetic.

Sign reversal in  $H_{EB}$  can be explained on these competing exchange interactions in  $Cr_{1-x}Fe_x$  alloy. During field cooling, the  $Cr_{1-x}Fe_x$  alloy undergoes into RSG transition, Fe clusters in RSG are frozen and give ferromagnetic coupling to adjacent Fe (ferromagnetic) layer at the interface. The Fe clusters also couple to other moments in SG, the strength of coupling depends upon size, shape and local magnetic anisotropy of clusters. The strong coupled clusters will remain pinned during the reversal of Fe layer, which results into negative EB. During heating, as the temperature approaches to  $T_{RSG}$ , the effective ferromagnetic coupling between Fe clusters and ferromagnetic layer decreases as the  $Cr_{1-x}Fe_x$  alloy undergoes a transition from RSG to either antiferromagnetic or ferromagnetic phase. Due to Cr rich alloy composition, local regions favour RSG to antiferromagnetic phase transition. Above this transition, the uncompensated moments of Cr prefer antiparallel alignment with Fe layer at interface. This antiparallel coupling at interface generates temperature driven sign reversal in  $H_{EB}$  from negative to positive. The increase in the magnitude of positive  $H_{EB}$  is related to inhomogeneous composition of alloy and gradual disappearance of FM clusters. Near  $T_B$ ,  $H_{EB}$  decreases because of disappearance of antiferromagnetic order<sup>173</sup>. In thin films,  $T_B$  is generally small as compared to bulk, due to finite size effects.

The sign reversal in Fe/Cr system is related to the exchange interaction between

Fe and FeCr alloy, where competing exchange interactions not only control the magnitude but also cause sign change with increase in temperature.

## 7.7 Summary

The temperature driven sign reversal in Fe/Cr system is studied and explained by the formation of interface alloying. The FeCr alloy at the interface transforms into SG phase during cooling. At the low temperatures, the ferromagnetic interactions between frozen Fe clusters in alloy and adjacent Fe layer, results into enhanced negative  $H_{EB}$ . The Cr rich alloy favours RSG to antiferromagnetic phase transition in alloy with increase in the temperature. This phase transition changes the ferromagnetic coupling to antiferromagnetic between uncompensated Cr moments and Fe layer at interface, resulting into positive EB.

# Chapter 8

## Summary and future work

This thesis presents the various studies on the phenomena of exchange bias ( EB ), spin dynamics, perpendicular magnetic anisotropy ( PMA ), spin glass ( SG ) in different magnetic systems of thin films and nanoparticles. In addition to the conventional EB (EB after field cooling), spontaneous EB (SEB) is observed which is a unique behaviour according to the reported studies in different magnetic materials. The different SG phases, including super spin glass (SSG), surface SG and re-entrant SG (RSG) and their contributions to the EB effect are studied in both magnetic thin films and nanoparticles. The investigation of EB and different SG phases in nanoparticles are also important for the deep understanding of these phenomena and their technological applications in various systems. Moreover, this thesis includes some new magnetic behaviours which have not been reported yet after the careful literature survey. This comprises the study of EB in CoPd alloy, effect of 2Q-3Q spin structure transition of IrMn on EB, the sign reversal in EB along with Morin transition in hematite nanoparticles and sign change in SEB which is observed in  $Co_{1-x}Mg_xFe_2O_4$  nanoparticles.

The perpendicular anisotropy of sole  $Co_{27}Pd_{73}$  alloy, the perpendicular exchange bias ( PEB ) in  $Co_{27}Pd_{73}/Ir_{23}Mn_{77}$  along with spin structure and spin re-orientation transitions ( SRT ), are discussed with various thicknesses of CoPd layer, in chapter 4. It is found that the spins of CoPd alloy are not exactly directed along perpendicular direction, rather they are tilted at a certain angle depending upon the thickness of the CoPd alloy. In sole CoPd samples, with increasing the thickness of sole CoPd film, the effective magnetic anisotropy,  $K_{eff}$  increases and PMA becomes stronger. It is found that in sole CoPd samples containing thin CoPd layer, the tilted spins can easily follow the external field because of the weak  $K_{eff}$ , which results in large

saturation magnetization,  $M_S$ . Thus in sole CoPd samples,  $M_S$  increases with decreasing the thickness of the CoPd alloy. IrMn is used as an antiferromagnet to the study of PEB in  $\text{Co}_{27}\text{Pd}_{73}/\text{Ir}_{23}\text{Mn}_{77}$  system. The EB field is strongly affected by the 2Q and 3Q spin structure of  $\gamma$ -phase disordered IrMn alloy. The 2Q spin structure is present at low temperatures and favours in-plane ( IP ) while the spin structure at higher temperature, 3Q favours out-of-plane ( OP ) direction. The effect of spin structure transition of IrMn from 2Q to 3Q is observed in EB and magnetization versus temperature  $M(T)$  measurements, where it is more pronounced in CoPd/IrMn samples containing thin CoPd layer. The direct proof of 2Q-3Q spin structure transition is verified through the  $M(T)$  measurement in sole IrMn sample along IP and OP directions. The SRT is observed in the exchange biased samples due to CoPd layer and has no effect on the EB. The interesting part of the magnetic study in  $\text{Co}_{27}\text{Pd}_{73}/\text{Ir}_{23}\text{Mn}_{77}$  samples is the inverse behaviour of PMA as compared to the sole CoPd samples, where the PMA decreases with increasing the thickness of CoPd layer in the exchange biased samples. This anomalous behaviour of  $K_{eff}$  as a function of thickness of CoPd layer in exchange biased samples, is related to the difference in the angle between the magnetic moments of CoPd and IrMn at the interface. The effect of bulk 3Q spin structure of IrMn is dominant in CoPd(8 nm)/IrMn(15 nm) sample due to small angle difference between CoPd and IrMn spins at the interface and 3Q spin structure enhances the perpendicular anisotropy. In CoPd(16 nm)/IrMn(15 nm) and CoPd(30 nm)/IrMn(15 nm) samples, the increased  $K_{eff}$  of the CoPd under layer with increasing the thickness and the large angle difference between the CoPd and IrMn spins at the interface weakens the effective control of bulk spin structure of IrMn on CoPd spins. This results in the weak exchange interaction between the spins of IrMn and CoPd, disturbing the 3Q spin structure of IrMn at the interface and causing spin frustration. The interfacial frustration and roughness induce an additional anisotropy which causes the movement of antiferromagnetic spins from OP to IP direction. The magnetic study in CoPd/IrMn system gives the direction of controlling the perpendicular anisotropy of the system through the interface and the spin structure of IrMn. In this chapter, the effect of thickness of CoPd layer is studied, therefore, it is important to investigate the thickness dependence of IrMn layer on the perpendicular anisotropy as a future work.

Chapter 5 describes the spin dynamics, the role of shape anisotropy and silica coating in the magnetic study of hematite nanoparticles. The phenomena of memory effect, aging, Morin transition and EB are studied in the agglomerated hematite

---

nanoparticles of different shapes from spherical to spindle. The SG and surface SG behaviours are observed that generate  $H_{EB}$ . The interesting behaviour of EB is the sign change in  $H_{EB}$  along with Morin transition, where the rotation of Fe ions in the core changes the exchange coupling at the interface and results in positive EB field ( $H_{EB}$ ) above  $T_M$ . However, below  $T_M$ , the antiferromagnetic core and surface SG generates negative  $H_{EB}$ . It is observed that Morin transition is diminished due to shape anisotropy, where it is present in spherical while absent in spindle shaped nanoparticles. The enhanced lattice strain and surface defects are the reasons of the depleting Morin transition with increasing the aspect ratio. The silica coating is used around the nanoparticles in order to eliminate agglomeration. The silica coating enhances the surface disorder, decreases magnetization and vanishes Morin transition, it also strengthens the surface SG phase as compared to SSG behaviour. In the uncoated hematite nanoparticles,  $H_{EB}$  between weak ferromagnetic core and surface SG is positive while it becomes negative after silica coating. The sign change in  $H_{EB}$  in the silica coated nanoparticles is also observed, which is not related to Morin transition, but occurs due to the rotation of interfacial spins along with the core moments. These studies help to understand the effect of shape anisotropy and agglomeration on EB, spin dynamics and SG phases which are useful for the technological applications.

In the chapter 6, SEB is observed and studied in  $Co_{1-x}Mg_xFe_2O_4$  nanoparticles ( $x = 0, 0.1, 0.3, 0.5, 0.7, 0.9, 1$ ) in the quasi-free state and semi-compressed form. In these nanoparticles, the core is ferrimagnetic having surface SG phase at shell containing irregular and frustrated interface. The SEB is also observed along with CEB in both states of nanoparticles. In quasi-free state of nanoparticles, SEB is larger than CEB, along with increased coercivity in ZFC as compared to FC conditions. On the other hand, CEB is stronger as compared to SEB with similar coercive field in semi-compressed form. The interesting part of the study is the strong influence of the initial magnetic state on SEB, where increased randomness contributes to the volume fraction of surface SG phase. The frustration and smooth movement of nanoparticles enhance SEB in quasi-free state of nanoparticles. The unidirectional anisotropy is established between ferrimagnetic domains and surface SG moments during initial magnetization process up to high fields. Maximum SEB in  $Co_{0.5}Mg_{0.5}Fe_2O_4$  sample is related to large frustration in the sample due to competition between Co and Mg ions on octahedral sites. The temperature driven sign change is observed in SEB and CEB, with the peak in  $H_{EB}$  in the direction of cooling field. The metastable domain states are developed in the system due to

the strain and dilution. With increase in temperature, the metastable domains at the interface have enough thermal energy to move when perturbed by rotation of ferrimagnetic core moments. Some metastable domains disappear due to switching with core ferrimagnetic moment and generates positive  $H_{EB}$ . The magnetic studies in  $Co_{1-x}Mg_xFe_2O_4$  nanoparticles relates the initial magnetic state and interparticle interactions to SEB, where negligible initial remanence and weak interactions enhances SEB. It is helpful to study SEB in  $Co_{1-x}Mg_xFe_2O_4$  nanoparticles in pellet form to observe the effect of strong interparticle interactions.

The temperature driven sign reversal in Fe/Cr system is studied and explained by the formation of interface alloying in the chapter 7. The FeCr alloy is formed at the interface due to high melting temperature of Cr top layer and it transforms into SG phase during cooling. At the low temperatures, the ferromagnetic interactions between frozen Fe clusters in alloy and adjacent Fe layer, results into enhanced negative  $H_{EB}$ . The Cr rich alloy favours RSG to antiferromagnetic phase transition in alloy with increase in the temperature. This phase transition changes the ferromagnetic coupling to antiferromagnetic between uncompensated Cr moments and Fe layer at interface, resulting into positive EB. This system emphasizes the role of interface alloying on the magnetic behaviour.

# Bibliography

- [1] G. Binasch, P. Grünberg, F. Saurenbach, and W. Zinn. Enhanced magnetoresistance in layered magnetic structures with antiferromagnetic interlayer exchange. *Phys. Rev. B*, 39:4828–4830, Mar 1989.
- [2] Claude Chappert, Albert Fert, and Frederic Nguyen Van Dau. The emergence of spin electronics in data storage. *Nat Mater*, 6(11):813–823, November 2007.
- [3] W. H. Meiklejohn and C. P. Bean. New magnetic anisotropy. *Phys. Rev.*, 102:1413–1414, Jun 1956.
- [4] An-Hui Lu, E. L. Salabas, and Ferdi Schüth. Magnetic nanoparticles: Synthesis, protection, functionalization, and application. *Angewandte Chemie International Edition*, 46(8):1222–1244, 2007.
- [5] J Nogués and Ivan K Schuller. Exchange bias. *Journal of Magnetism and Magnetic Materials*, 192(2):203 – 232, 1999.
- [6] M. Ali, C. H. Marrows, M. Al-Jawad, B. J. Hickey, A. Misra, U. Nowak, and K. D. Usadel. Antiferromagnetic layer thickness dependence of the IrMn/Co exchange-bias system. *Phys. Rev. B*, 68:214420, Dec 2003.
- [7] P.J. van der Zaag, R.M. Wolf, A.R. Ball, C. Bordel, L.F. Feiner, and R. Jungblut. A study of the magnitude of exchange biasing in [111]  $\text{Fe}_3\text{O}_4/\text{CoO}$  bilayers. *Journal of Magnetism and Magnetic Materials*, 148(1 - 2):346 – 348, 1995.
- [8] Mannan Ali, Patrick Adie, Christopher H. Marrows, Denis Greig, Bryan J. Hickey, and Robert L. Stamps. Exchange bias using a spin glass. *Nat Mater*, 6(1):70–75, January 2007.

- [9] R. Topkaya, Ö. Akman, S. Kazan, B. Aktas, Z. Durmus, and A. Baykal. Surface spin disorder and spin-glass-like behaviour in manganese-substituted cobalt ferrite nanoparticles. *Journal of Nanoparticle Research*, 14(10), 2012.
- [10] William C. Cain and Mark H. Kryder. Investigation of the exchange mechanism in NiFe-TbCo bilayers. *Journal of Applied Physics*, 67(9):5722–5724, 1990.
- [11] Oscar Iglesias, Xavier Batlle, and Amílcar Labarta. Microscopic origin of exchange bias in core/shell nanoparticles. *Phys. Rev. B*, 72:212401, Dec 2005.
- [12] Florin Radu and Hartmut Zabel. Exchange bias effect of ferro-/antiferromagnetic heterostructures. In Hartmut Zabel and SamuelD. Bader, editors, *Magnetic Heterostructures*, volume 227 of *Springer Tracts in Modern Physics*, pages 97–184. Springer Berlin Heidelberg, 2008.
- [13] J. Nogués, J. Sort, V. Langlais, V. Skumryev, S. Suriñach, J.S. Muñoz, and M.D. Baró. Exchange bias in nanostructures. *Physics Reports*, 422(3):65 – 117, 2005.
- [14] A. K. Nayak, M. Nicklas, S. Chadov, C. Shekhar, Y. Skourski, J. Winterlik, and C. Felser. Large zero-field cooled exchange-bias in bulk Mn<sub>2</sub>PtGa. *Phys. Rev. Lett.*, 110:127204, Mar 2013.
- [15] Arjun K. Pathak, I. Dubenko, S. Stadler, and N. Ali. Exchange bias in bulk Ni<sub>50</sub>Mn<sub>35</sub>In<sub>15-x</sub>Si<sub>x</sub> Heusler alloys. *Magnetics, IEEE Transactions on*, 45(10):3855–3857, Oct 2009.
- [16] W. H. Meiklejohn and C. P. Bean. New magnetic anisotropy. *Phys. Rev.*, 105:904–913, Feb 1957.
- [17] J.M. Daughton and Y.J. Chen. GMR materials for low field applications. *Magnetics, IEEE Transactions on*, 29(6):2705–2710, Nov 1993.
- [18] M. Avrarn, A. Angelescu, I. Kleps, M. Simion, and M. Miu. Spin-valve structures for giant magnetoresistive sensor applications. In *Semiconductor Conference, 2001. CAS 2001 Proceedings. International*, volume 2, pages 371–374 vol.2, Oct 2001.

- [19] S.E Russek, J.O Oti, and Young K Kim. Switching characteristics of spin valve devices designed for MRAM applications. *Journal of Magnetism and Magnetic Materials*, 198 - 199(0):6 – 8, 1999.
- [20] W. H. Meiklejohn. Exchange anisotropy - a review. *Journal of Applied Physics*, 33(3):1328–1335, 1962.
- [21] R L Stamps. Mechanisms for exchange bias. *Journal of Physics D: Applied Physics*, 33(23):R247, 2000.
- [22] N. Kurti. *Selected Works of Louis Neel*. Taylor & Francis, 1988.
- [23] A. P. Malozemoff. Random-field model of exchange anisotropy at rough ferromagnetic-antiferromagnetic interfaces. *Phys. Rev. B*, 35:3679–3682, Mar 1987.
- [24] Yoseph Imry and Shang-keng Ma. Random-field instability of the ordered state of continuous symmetry. *Phys. Rev. Lett.*, 35:1399–1401, Nov 1975.
- [25] D. Mauri, H. C. Siegmann, P. S. Bagus, and E. Kay. Simple model for thin ferromagnetic films exchange coupled to an antiferromagnetic substrate. *Journal of Applied Physics*, 62(7):3047–3049, 1987.
- [26] N. C. Koon. Calculations of exchange bias in thin films with ferromagnetic/antiferromagnetic interfaces. *Phys. Rev. Lett.*, 78:4865–4868, Jun 1997.
- [27] T. C. Schulthess and W. H. Butler. Consequences of spin-flop coupling in exchange biased films. *Phys. Rev. Lett.*, 81:4516, Mar 1998.
- [28] Miguel Kiwi. Exchange bias theory. *Journal of Magnetism and Magnetic Materials*, 234(3):584 – 595, 2001.
- [29] P. Miltényi, M. Gierlings, J. Keller, B. Beschoten, G. Güntherodt, U. Nowak, and K. D. Usadel. Diluted antiferromagnets in exchange bias: Proof of the domain state model. *Phys. Rev. Lett.*, 84:4224–4227, May 2000.
- [30] U. Nowak, K. D. Usadel, J. Keller, P. Miltényi, B. Beschoten, and G. Güntherodt. Domain state model for exchange bias. I. Theory. *Phys. Rev. B*, 66:014430, Jul 2002.

## Bibliography

---

- [31] J. Keller, P. Miltényi, B. Beschoten, G. Güntherodt, U. Nowak, and K. D. Usadel. Domain state model for exchange bias. II. experiments. *Phys. Rev. B*, 66:014431, Jul 2002.
- [32] U. Nowak and K. D. Usadel. Diluted antiferromagnets in a magnetic field: A fractal-domain state with spin-glass behavior. *Phys. Rev. B*, 44:7426–7432, Oct 1991.
- [33] Marian Fecioru-Morariu, Syed Rizwan Ali, Cristian Papusoi, Martin Sperlich, and Gernot Güntherodt. Effects of Cu dilution in IrMn on the exchange bias of CoFe/IrMn bilayers. *Phys. Rev. Lett.*, 99:097206, Aug 2007.
- [34] J.A. Mydosh. *Spin Glasses: An Experimental Introduction*. Taylor & Francis, 1993.
- [35] K. Binder and A. P. Young. Spin glasses: Experimental facts, theoretical concepts, and open questions. *Rev. Mod. Phys.*, 58:801–976, Oct 1986.
- [36] S F Edwards and P W Anderson. Theory of spin glasses. *Journal of Physics F: Metal Physics*, 5(5):965, 1975.
- [37] R. H. Kodama, A. E. Berkowitz, E. J. McNiff, and S. Foner. Surface spin disorder in ferrite nanoparticles (invited). *Journal of Applied Physics*, 81(8):5552–5557, 1997.
- [38] John R. Arthur. Molecular beam epitaxy. *Surface Science*, 500(1 - 3):189 – 217, 2002.
- [39] Paul Finnie and Yoshikazu Homma. Epitaxy: the motion picture. *Surface Science*, 500(1-3):437 – 457, 2002.
- [40] Shunichi Hashimoto, Yoshitaka Ochiai, and Koichi Aso. Perpendicular magnetic anisotropy in sputtered CoPd alloy films. *Japanese Journal of Applied Physics*, 28(Part 1, No. 9):1596–1599, 1989.
- [41] Takashi Yamaoka. Antiferromagnetism in  $\gamma$ -phase Mn-Ir alloys. *Journal of the Physical Society of Japan*, 36(2):445–450, 1974.
- [42] L. Szunyogh, B. Lazarovits, L. Udvardi, J. Jackson, and U. Nowak. Giant magnetic anisotropy of the bulk antiferromagnets IrMn and IrMn<sub>3</sub> from first principles. *Phys. Rev. B*, 79:020403, Jan 2009.

- [43] J. R. Childress, J. L. Duvail, S. Jasmin, A. Barthélémy, A. Fert, A. Schuhl, O. Durand, and P. Galtier. Perpendicular magnetic anisotropy in CoPd alloy films grown by molecular beam epitaxy. *Journal of Applied Physics*, 75(10):6412–6414, 1994.
- [44] Sebastiaan van Dijken, Magali Besnier, Jerome Moritz, and J. M. D. Coey. IrMn as exchange-biasing material in systems with perpendicular magnetic anisotropy. *Journal of Applied Physics*, 97(10):10k114, 2005.
- [45] S. Hashimoto, Y. Ochiai, and K. Aso. Perpendicular magnetic anisotropy and magnetostriction of sputtered Co/Pd and Co/Pt multilayered films. *Journal of Applied Physics*, 66(10):4909–4916, 1989.
- [46] D Weller, H Brändle, and C Chappert. Relationship between kerr effect and perpendicular magnetic anisotropy in  $\text{Co}_{1-x}\text{Pt}_x$  and  $\text{Co}_{1-x}\text{Pd}_x$  alloys. *Journal of magnetism and magnetic materials*, 121(1):461–470, 1993.
- [47] H. Takahashi, S. Tsunashima, S. Iwata, and S. Uchiyama. Measurement of magnetostriction constants in polycrystalline alloy and multilayer films of PdCo and PtCo. *Journal of magnetism and magnetic materials*, 126(1):282–284, 1993.
- [48] D. Weller, H. Brandle, G. Gorman, C.-J. Lin, and H. Notarys. Magnetic and magneto-optical properties of cobalt-platinum alloys with perpendicular magnetic anisotropy. *Applied Physics Letters*, 61(22):2726–2728, 1992.
- [49] Sang-Koog Kim, V. A. Chernov, J. B. Kortright, and Y. M. Koo. Anisotropic short-range structure of  $\text{Co}_{0.16}\text{Pd}_{0.84}$  alloy films having perpendicular magnetic anisotropy. *Applied Physics Letters*, 71(1):66–68, 1997.
- [50] J.I. Hong, S. Sankar, A.E. Berkowitz, and W.F. Egelhoff Jr. On the perpendicular anisotropy of Co/Pd multilayers. *Journal of Magnetism and Magnetic Materials*, 285(3):359 – 366, 2005.
- [51] Hendrik Ohldag, Hongtao Shi, Elke Arenholz, Joachim Stöhr, and David Lederman. Parallel versus antiparallel interfacial coupling in exchange biased Co/FeF<sub>2</sub>. *Phys. Rev. Lett.*, 96:027203, Jan 2006.
- [52] C.-J. Lin and G. L. Gorman. Evaporated copt alloy films with strong perpendicular magnetic anisotropy. *Applied Physics Letters*, 61(13):1600–1602, 1992.

- [53] Y. Matsuo. Ordered alloys in the cobalt-palladium system. *Journal of the Physical Society of Japan*, 32(4):972–978, 1972.
- [54] Brad N. Engel, Craig D. England, Robert A. Van Leeuwen, Michael H. Wiedmann, and Charles M. Falco. Interface magnetic anisotropy in epitaxial superlattices. *Phys. Rev. Lett.*, 67:1910–1913, Sep 1991.
- [55] C. Scott Brown, J. W. Harrell, and S. Matsunuma. Time and temperature dependences of the magnetization reversal in a Co/Pd multilayer film. *Journal of Applied Physics*, 100(5):053910, 2006.
- [56] Hiroshi Takahashi, Shigeru Tsunashima, Satoshi Iwata, and Susumu Uchiyama. Measurement of magnetostriction constants in (111)-oriented polycrystalline PdCo alloy and multilayered films. *Japanese Journal of Applied Physics*, 32(Part 2, No. 9B):L1328–L1331, 1993.
- [57] Y. Wu, J. Stöhr, B. D. Hermsmeier, M. G. Samant, and D. Weller. Enhanced orbital magnetic moment on Co atoms in Co/Pd multilayers: A magnetic circular x-ray dichroism study. *Phys. Rev. Lett.*, 69:2307–2310, Oct 1992.
- [58] C. Boeglin, E. Beaurepaire, V. Halté, V. López-Flores, C. Stamm, N. Pontius, H.A. Dürr, and J.Y. Bigot. Distinguishing the ultrafast dynamics of spin and orbital moments in solids. *Nature*, 465(7297):458–461, 2010.
- [59] N. Deo, M.F. Bain, J.H. Montgomery, and H.S. Gamble. Study of magnetic properties of thin cobalt films deposited by chemical vapour deposition. *Journal of Materials Science: Materials in Electronics*, 16:387–392, 2005.
- [60] R. M. Bozorth, P. A. Wolff, D. D. Davis, V. B. Compton, and J. H. Wernick. Ferromagnetism in dilute solutions of cobalt in palladium. *Phys. Rev.*, 122:1157–1160, May 1961.
- [61] Kaoru Miura, Hitoshi Kimura, Syunji Imanaga, and Yoshinori Hayafuji. Magnetic interaction between Co layers and Pd layers in Co/Pd multilayers. *Journal of Applied Physics*, 72(10):4826–4829, 1992.
- [62] M T Johnson, P J H Bloemen, F J A den Broeder, and J J de Vries. Magnetic anisotropy in metallic multilayers. *Reports on Progress in Physics*, 59(11):1409, 1996.

- [63] M.V. Mansilla, J. Gomez, and Alejandro Butera. Ferromagnetic resonance of disordered FePt thin films. *Magnetics, IEEE Transactions on*, 44(11):2883–2886, 2008.
- [64] S. M. Zhou, L. Sun, P. C. Searson, and C. L. Chien. Perpendicular exchange bias and magnetic anisotropy in CoO/permalloy multilayers. *Phys. Rev. B*, 69:024408, Jan 2004.
- [65] Ju-Hyun Kim, Kwang-Su Ryu, Jae-Woo Jeong, and Sung-Chul Shin. Large converse magnetoelectric coupling effect at room temperature in CoPd/PMN-PT (001) heterostructure. *Applied Physics Letters*, 97(25):252508, 2010.
- [66] S. U. Jen and C. M. Chung. Intrinsic stress of Co<sub>35</sub>Pd<sub>65</sub> alloy films. *Journal of Vacuum Science & Technology A: Vacuum, Surfaces, and Films*, 19(1):223–227, 2001.
- [67] Kun Xun and Defang Shen. Grain growth in Co<sub>27</sub>Pt<sub>73</sub> alloy films with perpendicular magnetic anisotropy. *Journal of Applied Physics*, 89(12):8054–8056, 2001.
- [68] M.V. Mansilla, J. Gomez, and Alejandro Butera. Ferromagnetic resonance of disordered FePt thin films. *Magnetics, IEEE Transactions on*, 44(11):2883–2886, 2008.
- [69] J. Sort, V. Baltz, F. Garcia, B. Rodmacq, and B. Dieny. Tailoring perpendicular exchange bias in [Pt/Co]-IrMn multilayers. *Phys. Rev. B*, 71:054411, Feb 2005.
- [70] Kousuke Tobari, Mitsuru Ohtake, Katsumasa Nagano, and Masaaki Futamoto. Influence of layer thickness on the structure and the magnetic properties of Co/Pd epitaxial multilayer films. *Journal of Magnetism and Magnetic Materials*, 324(6):1059 – 1062, 2012.
- [71] A. Sakuma, K. Fukamichi, K. Sasao, and R. Y. Umetsu. First-principles study of the magnetic structures of ordered and disordered Mn-Ir alloys. *Phys. Rev. B*, 67:024420, Jan 2003.
- [72] R. S. Fishman and S. H. Liu. Magnetic susceptibility of  $\gamma$ -Mn alloys. *Phys. Rev. B*, 59:8672–8680, Apr 1999.

## Bibliography

---

- [73] R. S. Fishman, W.-T. Lee, S. H. Liu, D. Mandrus, J. L. Robertson, K. J. Song, and J. R. Thompson. Structural and magnetic phase transitions in Mn-Ni alloys. *Phys. Rev. B*, 61:12159–12168, May 2000.
- [74] Akimasa Sakuma. First-principles study on the non-collinear magnetic structures of disordered alloys. *Journal of the Physical Society of Japan*, 69(9):3072–3083, 2000.
- [75] C. H. Marrows. Three-dimensional exchange bias in  $(\text{Co}/\text{Pd})_N/\text{FeMn}$ . *Phys. Rev. B*, 68:012405, Jul 2003.
- [76] Lin Lin, Naganivetha Thiagarajah, Ho Wan Joo, Jang Heo, Ky Am Lee, and Seongtae Bae. A physical model of exchange bias in  $(\text{Pd}/\text{Co})_5/\text{FeMn}$  thin films with perpendicular anisotropy. *Journal of Applied Physics*, 108(6):063924, 2010.
- [77] C. Mitsumata, A. Sakuma, and K. Fukamichi. Mechanism of the exchange-bias field in ferromagnetic and antiferromagnetic bilayers. *Phys. Rev. B*, 68:014437, Jul 2003.
- [78] C. Mitsumata, A. Sakuma, and K. Fukamichi. Influence of the spin structure on the exchange bias of antiferromagnetic and ferromagnetic bilayer. *Magnetics, IEEE Transactions on*, 39(5):2738 – 2740, sept. 2003.
- [79] C. Mitsumata, A. Sakuma, and K. Fukamichi. Exchange bias model in ferromagnetic/antiferromagnetic bilayer with  $\text{L}1_2$ -type ordered antiferromagnet. *Magnetics, IEEE Transactions on*, 41(10):2700 – 2702, oct. 2005.
- [80] C. Mitsumata, A. Sakuma, K. Fukamichi, and M. Tsunoda. Uncompensated spin elements in ferromagnetic and antiferromagnetic bilayer with non-collinear spin structure. *Materials transactions*, 47(1):11, 2006.
- [81] M. Tsunoda, S. Yoshitaki, Y. Ashizawa, C. Mitsumata, T. Nakamura, H. Ochiai, T. Hirono, DY Kim, and M. Takahashi. Uncompensated antiferromagnetic spins at the interface in mn-ir based exchange biased bilayers. *Journal of applied physics*, 101(9):09E510–09E510, 2007.
- [82] M. Tsunoda, H. Takahashi, T. Nakamura, C. Mitsumata, S. Isogami, and M. Takahashi. Linear correlation between uncompensated antiferromagnetic spins and exchange bias in Mn-Ir/Co $_{100-x}$ Fe $_x$  bilayers. *Applied Physics Letters*, 97(7):072501–072501, 2010.

[83] H. Takahashi, Y. Kota, M. Tsunoda, T. Nakamura, K. Kodama, A. Sakuma, and M. Takahashi. Uncompensated antiferromagnetic moments in Mn-Ir/FM (FM= Ni-Co, Co-Fe, Fe-Ni) bilayers: Compositional dependence and its origin. *Journal of Applied Physics*, 110(12):123920–123920, 2011.

[84] L. Sun, S. M. Zhou, P. C. Searson, and C. L. Chien. Longitudinal and perpendicular exchange bias in FeMn/(FeNi/FeMn)<sub>n</sub> multilayers. *Journal of Applied Physics*, 93(10):6841–6843, 2003.

[85] H. Xing, K. Keshoju, S. M. Zhou, and L. Sun. Field cooling induced perpendicular exchange bias in FeMn/(FeNi/FeMn)<sub>n</sub> multilayers. *Journal of Applied Physics*, 101(9):09E509, 2007.

[86] N.N. Phuoc and T. Suzuki. Hybrid exchange bias in (FePt-FeMn)<sub>N</sub> multilayers. *Magnetics, IEEE Transactions on*, 41(10):2715 – 2717, oct. 2005.

[87] N.N. Phuoc and T. Suzuki. Perpendicular exchange bias and magnetic anisotropy in FePt/FeMn multilayers. *Magnetics, IEEE Transactions on*, 42(10):2996 –2998, oct. 2006.

[88] Nguyen N. Phuoc and Takao Suzuki. Study of parallel and perpendicular exchange biases in FePt-FeMn multilayers. *Journal of Applied Physics*, 99(8):08C107, 2006.

[89] Nguyen N. Phuoc and Takao Suzuki. Mechanism of blocking temperature difference for parallel and perpendicular exchange biases in FePt/FeMn multilayers. *Magnetics, IEEE Transactions on*, 43(2):897 –899, feb. 2007.

[90] Nguyen N. Phuoc and Takao Suzuki. Perpendicular exchange bias mechanism in FePt/FeMn multilayers. *Journal of Applied Physics*, 101(9):09E501, 2007.

[91] K. Chesnel, EE Fullerton, MJ Carey, JB Kortright, and SD Kevan. Magnetic memory in ferromagnetic thin films via exchange coupling. *Physical Review B*, 78(13):132409, 2008.

[92] S. Maat, K. Takano, S. S. P. Parkin, and Eric E. Fullerton. Perpendicular exchange bias of Co/Pt multilayers. *Phys. Rev. Lett.*, 87:087202, Aug 2001.

[93] TC Schulthess, WH Butler, GM Stocks, S. Maat, and GJ Mankey. Non-collinear magnetism in substitutionally disordered face-centered-cubic FeMn. *Journal of applied physics*, 85(8):4842–4844, 1999.

- [94] Parmanand Sharma, Hisamichi Kimura, Akihisa Inoue, Elke Arenholz, and J.-H. Guo. Temperature and thickness driven spin-reorientation transition in amorphous Co-Fe-Ta-B thin films. *Phys. Rev. B*, 73:052401, Feb 2006.
- [95] J. Sort, F. Garcia, S. Auffret, B. Rodmacq, B. Dieny, V. Langlais, S. Surinach, J. S. Munoz, M. D. Baro, and J. Nogués. Using exchange bias to extend the temperature range of square loop behavior in [Pt/Co] multilayers with perpendicular anisotropy. *Applied Physics Letters*, 87(24):242504, 2005.
- [96] R. Morales, Zhi-Pan Li, J. Olamit, Kai Liu, J. M. Alameda, and Ivan K. Schuller. Role of the antiferromagnetic bulk spin structure on exchange bias. *Phys. Rev. Lett.*, 102:097201, Mar 2009.
- [97] M. Finazzi, A. Brambilla, P. Biagioni, J. Graf, G.-H. Gweon, A. Scholl, A Lanzara, and L. Duò. Interface coupling transition in a thin epitaxial antiferromagnetic film interacting with a ferromagnetic substrate. *Phys. Rev. Lett.*, 97:097202, Aug 2006.
- [98] Marco Finazzi. Interface coupling in a ferromagnet/antiferromagnet bilayer. *Phys. Rev. B*, 69:064405, Feb 2004.
- [99] J. Wu, J. Choi, A. Scholl, A. Doran, E. Arenholz, Chanyong Hwang, and Z. Q. Qiu. Ni spin switching induced by magnetic frustration in FeMn/Ni/Cu(001). *Phys. Rev. B*, 79:212411, Jun 2009.
- [100] H. M. Lu and X. K. Meng. Morin temperature and Neel temperature of hematite nanocrystals. *The Journal of Physical Chemistry C*, 114(49):21291–21295, 2010.
- [101] A.H. Morrish. *Canted Antiferromagnetism: Hematite*. World Scientific, 1994.
- [102] C. G. Shull, W. A. Strauser, and E. O. Wollan. Neutron diffraction by paramagnetic and antiferromagnetic substances. *Phys. Rev.*, 83:333–345, Jul 1951.
- [103] Franz Bødker, Mikkel F. Hansen, Christian Bender Koch, Kim Lefmann, and Steen Mørup. Magnetic properties of hematite nanoparticles. *Phys. Rev. B*, 61:6826–6838, Mar 2000.
- [104] G. Rollmann, A. Rohrbach, P. Entel, and J. Hafner. First-principles calculation of the structure and magnetic phases of hematite. *Phys. Rev. B*, 69:165107, Apr 2004.

[105] Karla Doermbach, Garima Agrawal, Mark Servos, Susanne Schipmann, Sabrina Thies, Uwe Klemradt, and Andrij Pich. Silica-coating of hematite nanoparticles using reactive water-soluble polyalkoxysiloxanes. *Particle & Particle Systems Characterization*, 31(3):365–373, 2014.

[106] Masataka Ozaki, Stanka Kratohvil, and Egon Matijevic. Formation of monodispersed spindle-type hematite particles. *Journal of Colloid and Interface Science*, 102(1):146 – 151, 1984.

[107] J. M. Pastor, J. I. Perez-Landazabal, C. Gomez-Polo, V. Recarte, S. Larumbe, R. Santamarta, M. Fernandes Silva, E. A. Gomez Pineda, A. A. Winkler Hechenleitner, and M. K. Lima. Entropy change linked to the magnetic field induced Morin transition in Hematite nanoparticles. *Applied Physics Letters*, 100(6):063102, 2012.

[108] L. Suber, P. Imperatori, A. Mari, G. Marchegiani, M. Vasquez Mansilla, D. Fiorani, W. R. Plunkett, D. Rinaldi, C. Cannas, G. Ennas, and D. Peddis. Thermal hysteresis of morin transition in hematite particles. *Phys. Chem. Chem. Phys.*, 12:6984–6989, 2010.

[109] R.K. Gupta, K. Ghosh, L. Dong, and P.K. Kahol. Green synthesis of hematite ( $\text{Fe}_2\text{O}_3$ ) submicron particles. *Materials Letters*, 64(19):2132 – 2134, 2010.

[110] Ji Ma and Kezheng Chen. Magnetic dead layer is not magnetically dead in hematite nanocubes. *Physics Letters A*, 377(34):2216 – 2220, 2013.

[111] Özden Özdemir, David J. Dunlop, and Thelma S. Berquo'. Morin transition in hematite: Size dependence and thermal hysteresis. *Geochemistry, Geophysics, Geosystems*, 9(10):1–12, 2008.

[112] Yimin Zhao, Charles W. Dunnill, Yanqiu Zhu, Duncan H. Gregory, Walter Kockenberger, Yanhui Li, Weibing Hu, Iftikhar Ahmad, and David G. McCartney. Low-temperature magnetic properties of hematite nanorods. *Chemistry of Materials*, 19(4):916–921, 2007.

[113] Yan-kun Tang, Young Sun, and Zhao-hua Cheng. Cooling field dependence of exchange bias in phase-separated  $\text{La}_{0.88}\text{Sr}_{0.12}\text{CoO}_3$ . *Journal of Applied Physics*, 100(2):023914, 2006.

## Bibliography

---

- [114] Suvankar Chakraverty and Malay Bandyopadhyay. Coercivity of magnetic nanoparticles: A stochastic model. *Journal of Physics: Condensed Matter*, 19(21):216201, 2007.
- [115] Lucia Del Bianco, Dino Fiorani, Alberto M. Testa, Ennio Bonetti, and Luca Signorini. Field-cooling dependence of exchange bias in a granular system of Fe nanoparticles embedded in an Fe oxide matrix. *Phys. Rev. B*, 70:052401, Aug 2004.
- [116] G. Hassnain Jaffari, S. Rizwan Ali, S. K. Hasanain, Gernot Güntherodt, and S. Ismat Shah. Stabilization of surface spin glass behavior in core-shell  $\text{Fe}_{67}\text{Co}_{33}/\text{CoFe}_2\text{O}_4$  nanoparticles. *Journal of Applied Physics*, 108(6):063921–063925, 2010.
- [117] R. H. Kodama, A. E. Berkowitz, E. J. McNiff, Jr., and S. Foner. Surface spin disorder in  $\text{NiFe}_2\text{O}_4$  nanoparticles. *Phys. Rev. Lett.*, 77:394–397, Jul 1996.
- [118] S. K. Giri, A. Poddar, and T. K. Nath. Evidence of exchange bias effect and surface spin glass ordering in electron doped  $\text{Sm}_{0.09}\text{Ca}_{0.91}\text{MnO}_3$  nanomanganites. *Journal of Applied Physics*, 112(11):113903, 2012.
- [119] Srimanta Middey, Somnath Jana, and Sugata Ray. Surface spin-glass and exchange bias in  $\text{Sr}_2\text{FeMoO}_6$  nanoparticle. *Journal of Applied Physics*, 108(4):043918, 2010.
- [120] B. Martínez, X. Obradors, Ll. Balcells, A. Rouanet, and C. Monty. Low temperature surface spin-glass transition in  $\text{Fe}_2\text{O}_3$  nanoparticles. *Phys. Rev. Lett.*, 80:181–184, Jan 1998.
- [121] M. Sasaki, P. E. Jönsson, H. Takayama, and H. Mamiya. Aging and memory effects in superparamagnets and superspin glasses. *Phys. Rev. B*, 71:104405, Mar 2005.
- [122] Sayan Chandra, H. Khurshid, Wanfeng Li, G. C. Hadjipanayis, M. H. Phan, and H. Srikanth. Spin dynamics and criteria for onset of exchange bias in superspin glass  $\text{Fe}/\gamma\text{-Fe}_2\text{O}_3$  core-shell nanoparticles. *Phys. Rev. B*, 86:014426, Jul 2012.
- [123] Tuhin Maity, Sudipta Goswami, Dipten Bhattacharya, and Saibal Roy. Superspin glass mediated giant spontaneous exchange bias in a nanocomposite of  $\text{BiFeO}_3\text{-Bi}_2\text{Fe}_4\text{O}_9$ . *Phys. Rev. Lett.*, 110:107201, Mar 2013.

[124] Ji Ma and Kezheng Chen. New magnetic regime in hematite hollow spheres. *physica status solidi (RRL) Rapid Research Letters*, 6(7):324–326, 2012.

[125] Y.Y. Xu, D. Zhao, X.J. Zhang, W.T. Jin, P. Kashkarov, and H. Zhang. Synthesis and characterization of single-crystalline  $\alpha$ -Fe<sub>2</sub>O<sub>3</sub> nanoleaves. *Physica E: Low-dimensional Systems and Nanostructures*, 41(5):806 – 811, 2009.

[126] Jorge Sanchez-Marcos, M Angeles Laguna-Marco, Rocio Martinez-Morillas, Eva Cespedes, Felix Jimenez-Villacorta, Nieves Menendez, and Carlos Prieto. Exchange bias in iron oxide nanoclusters. *Journal of Physics: Condensed Matter*, 23(47):476003, 2011.

[127] Masatsugu Suzuki, Sharbani I. Fullem, Itsuko S. Suzuki, Lingyan Wang, and Chuan-Jian Zhong. Observation of superspin-glass behavior in Fe<sub>3</sub>O<sub>4</sub> nanoparticles. *Phys. Rev. B*, 79:024418, Jan 2009.

[128] Shaobo Xi, Wenjian Lu, and Yuping Sun. Magnetic properties and magnetocaloric effect of La<sub>0.8</sub>Ca<sub>0.2</sub>MnO<sub>3</sub> nanoparticles tuned by particle size. *Journal of Applied Physics*, 111(6):063922, 2012.

[129] L. E. Wenger and J. A. Mydosh. Nonuniqueness of H<sup>2/3</sup> and H<sup>2</sup> field-temperature transition lines in spin-glasses. *Phys. Rev. B*, 29:4156–4158, Apr 1984.

[130] Vojislav Spasojevic, Ana Mrakovic, Marija Perovic, Vladan Kusigerski, and Jovan Blanusa. Superspin-glass like behavior of nanoparticle La<sub>0.7</sub>Ca<sub>0.3</sub>MnO<sub>3</sub> obtained by mechanochemical milling. *Journal of Nanoparticle Research*, 13(2):763–771, 2011.

[131] S Thomas, M Uhlig, U Wiedwald, L Han, P Ziemann, and M Albrecht. Super spin-glass state and exchange bias in Fe/CoO hybrid nanostructures. *Nanotechnology*, 24(15):155703, 2013.

[132] Masatsugu Suzuki and Itsuko S. Suzuki. Aging dynamics in a reentrant ferromagnet: Cu<sub>0.2</sub>Co<sub>0.8</sub>Cl<sub>2</sub>-FeCl<sub>3</sub> graphite bi-intercalation compound. *Phys. Rev. B*, 71:174437, May 2005.

[133] V. Dupuis, E. Vincent, M. Alba, and J. Hammann. Aging, rejuvenation and memory effects in re-entrant ferromagnets. *The European Physical Journal B - Condensed Matter and Complex Systems*, 29(1):19–26, 2002.

## Bibliography

---

- [134] R. Mathieu, P. E. Jönsson, P. Nordblad, H. Aruga Katori, and A. Ito. Memory and chaos in an Ising spin glass. *Phys. Rev. B*, 65:012411, Nov 2001.
- [135] M. Suzuki and I.S. Suzuki. Aging, rejuvenation, and memory effects in short-range ising spin glass:  $\text{Cu}_{0.5}\text{Co}_{0.5}\text{Cl}_2\text{-FeCl}_3$  graphite bi-intercalation compound. *The European Physical Journal B - Condensed Matter and Complex Systems*, 41(4):457–470, 2004.
- [136] Vijay Bisht and K P Rajeev. Memory and aging effects in NiO nanoparticles. *Journal of Physics: Condensed Matter*, 22(1):016003, 2010.
- [137] K. Nadeem, H. Krenn, T. Traussing, and I. Letofsky-Papst. Distinguishing magnetic blocking and surface spin-glass freezing in nickel ferrite nanoparticles. *Journal of Applied Physics*, 109(1):013912, 2011.
- [138] Lorenzo W. Bernardi, Hajime Yoshino, Koji Hukushima, Hajime Takayama, Aya Tobe, and Atsuko Ito. Aging of the zero-field-cooled magnetization in Ising spin glasses: Experiment and numerical simulation. *Phys. Rev. Lett.*, 86:720–723, Jan 2001.
- [139] Subarna Mitra, Soumen Das, Soumen Basu, Puspendu Sahu, and Kalyan Mandal. Shape- and field-dependent morin transitions in structured -  $\text{Fe}_2\text{O}_3$ . *Journal of Magnetism and Magnetic Materials*, 321(18):2925 – 2931, 2009.
- [140] R. N. Bhowmik and A. Saravanan. Surface magnetism, morin transition, and magnetic dynamics in antiferromagnetic  $\alpha\text{-Fe}_2\text{O}_3$  (hematite) nanograins. *Journal of Applied Physics*, 107(5):053916, 2010.
- [141] G.F. Goya, M. Veith, R. Rapalavuite, H. Shen, and S. Mathur. Thermal hysteresis of spin reorientation at Morin transition in alkoxide derived hematite nanoparticles. *Applied Physics A*, 80(7):1523–1526, 2005.
- [142] A.R.B de Castro, R.D Zysler, M Vasquez Mansilla, C Arciprete, and M Dimitrijewits. Magnetic circular dichroism in nanostructured hematite. *Journal of Magnetism and Magnetic Materials*, 231(2 - 3):287 – 290, 2001.
- [143] R. D. Zysler, D. Fiorani, A. M. Testa, L. Suber, E. Agostinelli, and M. Godinho. Size dependence of the spin-flop transition in hematite nanoparticles. *Phys. Rev. B*, 68:212408, Dec 2003.

[144] S-H Gee, Y-K Hong, J.C. Sur, D.W. Erickson, M.H. Park, and F. Jeffers. Spin orientation of hematite ( $\alpha$ -Fe<sub>2</sub>O<sub>3</sub>) nanoparticles during the morin transition. *Magnetics, IEEE Transactions on*, 40(4):2691–2693, July 2004.

[145] Lorenza Suber, Antoni Garcia Santiago, Dino Fiorani, Patrizia Imperatori, Alberto Maria Testa, Massimo Angiolini, Amelia Montone, and Jean L. Dормann. Structural and magnetic properties of  $\alpha$ -Fe<sub>2</sub>O<sub>3</sub> nanoparticles. *Applied Organometallic Chemistry*, 12(5):347–351, 1998.

[146] Y P He, S Q Wang, C R Li, Y M Miao, Z Y Wu, and B S Zou. Synthesis and characterization of functionalized silica-coated Fe<sub>3</sub>O<sub>4</sub> superparamagnetic nanocrystals for biological applications. *Journal of Physics D: Applied Physics*, 38(9):1342, 2005.

[147] Chun-Liu Fang, Kun Qian, Jianhua-Zhu, Shangbin Wang, Xiaoxuan Lv, and Shu-Hong Yu. Monodisperse Fe<sub>2</sub>O<sub>3</sub>@SiO<sub>2</sub>@Au core/shell nanocomposite spheres: synthesis, characterization and properties. *Nanotechnology*, 19(12):125601, 2008.

[148] Christina Graf, Dirk LJ Vossen, Arnout Imhof, and Alfons van Blaaderen. A general method to coat colloidal particles with silica. *Langmuir*, 19(17):6693–6700, 2003.

[149] S Larumbe, J I Pérez-Landazábal, J M Pastor, and C Gómez-Polo. Sol-gel NiFe<sub>2</sub>O<sub>4</sub> nanoparticles: Effect of the silica coating. *Journal of Applied Physics*, 111(10):103911, 2012.

[150] Mingzhong Wu, Y. D. Zhang, S. Hui, T. D. Xiao, Shihui Ge, W. A. Hines, J. I. Budnick, and M. J. Yacaman. Magnetic properties of SiO<sub>2</sub>-coated Fe nanoparticles. *Journal of Applied Physics*, 92(11):6809–6812, 2002.

[151] Vladimir Zelenak, Adriana Zelenakova, Jozef Kovac, Ulla Vainio, and Nataliya Murafa. Influence of surface effects on magnetic behavior of hematite nanoparticles embedded in porous silica matrix. *The Journal of Physical Chemistry C*, 113(30):13045–13050, 2009.

[152] R.D. Zysler, M. Vasquez Mansilla, and D. Fiorani. Surface effects in  $\alpha$ -Fe<sub>2</sub>O<sub>3</sub> nanoparticles. *The European Physical Journal B - Condensed Matter and Complex Systems*, 41(2):171–175, 2004.

## Bibliography

---

- [153] Masatsugu Suzuki and Itsuko S. Suzuki. Nonlinear magnetic susceptibility and aging phenomena in a reentrant ferromagnet:  $\text{Cu}_{0.2}\text{Co}_{0.8}\text{Cl}_2\text{-FeCl}_3$  graphite bi-intercalation compound. *Phys. Rev. B*, 69:144424, Apr 2004.
- [154] D. Parker, V. Dupuis, F. Ladieu, J.-P. Bouchaud, E. Dubois, R. Perzynski, and E. Vincent. Spin-glass behavior in an interacting  $\gamma\text{-Fe}_2\text{O}_3$  nanoparticle system. *Phys. Rev. B*, 77:104428, Mar 2008.
- [155] D. De, A. Karmakar, M. K. Bhunia, A. Bhaumik, S. Majumdar, and S. Giri. Memory effects in superparamagnetic and nanocrystalline  $\text{Fe}_{50}\text{Ni}_{50}$  alloy. *Journal of Applied Physics*, 111(3):033919, 2012.
- [156] M Reufer, H Dietsch, U Gasser, B Grobety, A M Hirt, V K Malik, and P Schurtenberger. Magnetic properties of silica coated spindle-type hematite particles. *Journal of Physics: Condensed Matter*, 23(6):065102, 2011.
- [157] Cathrine Frandsen and Steen Mørup. Spin rotation in  $\alpha\text{Fe}_2\text{O}_3$  nanoparticles by interparticle interactions. *Phys. Rev. Lett.*, 94:027202, Jan 2005.
- [158] A Zeleňáková, J Kováč, and V Zeleňák. Magnetic properties of  $\text{Fe}_2\text{O}_3$  nanoparticles embedded in hollows of periodic nanoporous silica. *Journal of Applied Physics*, 108(3):034323, 2010.
- [159] Fu-Te Yuan, Jeng-Kai Lin, Y. D. Yao, and Shang-Fan Lee. Exchange bias in spin glass (FeAu)/NiFe thin films. *Applied Physics Letters*, 96(16):162502, 2010.
- [160] S. Chikazumi. *Physics of Magnetism*. Wiley series on the science and technology of materials. New York, Wiley, 1964.
- [161] Y. Ying, T. W. Eom, Y. P. Lee, L. S. Ling, and V. L. Mathe. Detailed magnetic structure of  $\text{Zn}_{1-x}\text{Ni}_x\text{Fe}_2\text{O}_4$  nanoparticles. *Journal of Applied Physics*, 108(2):023911, 2010.
- [162] Kavita Verma, Ashwini Kumar, and Dinesh Varshney. Dielectric relaxation behavior of  $\text{A}_x\text{Co}_{1-x}\text{Fe}_2\text{O}_4$  ( $\text{A} = \text{Zn, Mg}$ ) mixed ferrites. *Journal of Alloys and Compounds*, 526(0):91 – 97, 2012.
- [163] M. Hamedoun, A. Benyoussef, and M. Bousmina. Magnetic properties of magnetic  $\text{Co}_{1-x}\text{Mg}_x\text{Fe}_2\text{O}_4$  spinel by HTSE method. *Physica B: Condensed Matter*, 406(9):1633 – 1638, 2011.

[164] M.A. Ahmed and A.A. EL-Khawlan. Enhancement of the crystal size and magnetic properties of Mg-substituted Co ferrite. *Journal of Magnetism and Magnetic Materials*, 321(13):1959 – 1963, 2009.

[165] R.C. Kambale, P.A. Shaikh, N.S. Harale, V.A. Bilur, Y.D. Kolekar, C.H. Bhosale, and K.Y. Rajpure. Structural and magnetic properties of  $\text{Co}_{1-x}\text{Mn}_x\text{Fe}_2\text{O}_4$  spinel ferrites synthesized by combustion route. *Journal of Alloys and Compounds*, 490(1):568–571, 2010.

[166] R.A. Candeia, M.A.F. Souza, M.I.B. Bernardi, S.C. Maestrelli, I.M.G. Santos, A.G. Souza, and E. Longo.  $\text{MgFe}_2\text{O}_4$  pigment obtained at low temperature. *Materials Research Bulletin*, 41(1):183 – 190, 2006.

[167] K. Maaz, M. Usman, S. Karim, A. Mumtaz, S. K. Hasanain, and M. F. Bertino. Magnetic response of core-shell cobalt ferrite nanoparticles at low temperature. *Journal of Applied Physics*, 105(11):113917, 2009.

[168] D Peddis, C Cannas, G Piccaluga, E Agostinelli, and D Fiorani. Spin-glass-like freezing and enhanced magnetization in ultra-small  $\text{CoFe}_2\text{O}_4$  nanoparticles. *Nanotechnology*, 21(12):125705, 2010.

[169] Roberto Köferstein, Till Walther, Dietrich Hesse, and StefanG. Ebbinghaus. Preparation and characterization of nanosized magnesium ferrite powders by a starch-gel process and corresponding ceramics. *Journal of Materials Science*, 48(19):6509–6518, 2013.

[170] B. M. Wang, Y. Liu, P. Ren, B. Xia, K. B. Ruan, J. B. Yi, J. Ding, X. G. Li, and L. Wang. Large exchange bias after zero-field cooling from an unmagnetized state. *Phys. Rev. Lett.*, 106:077203, Feb 2011.

[171] B. M. Wang, Y. Liu, B. Xia, P. Ren, and L. Wang. Large exchange bias obtainable through zero-field cooling from an unmagnetized state in Ni-Mn-Sn alloys. *Journal of Applied Physics*, 111(4):043912, 2012.

[172] S. M. Yusuf, P. K. Manna, Mandar M. Shirolkar, S. K. Kulkarni, R. Tewari, and G. K. Dey. A study of exchange bias in  $\text{BiFeO}_3$  core/ $\text{NiFe}_2\text{O}_4$  shell nanoparticles. *Journal of Applied Physics*, 113(17):–, 2013.

[173] S. Rizwan Ali, M. Bilal Janjua, M. Fecioru-Morariu, D. Lott, C. J. P. Smits, and G. Güntherodt. Role of interface alloying in the exchange bias of Fe/Cr bilayers. *Phys. Rev. B*, 82:020402, Jul 2010.

## Bibliography

---

- [174] Yong Hu and An Du. Anomalous temperature and interfacial-coupling dependence of exchange bias in antiferromagnetic (core)/ferromagnetic (shell) nanoparticles. *physica status solidi (b)*, 248(8):1967–1974, 2011.
- [175] A. K. Suszka, O. Idigoras, E. Nikulina, A. Chuvalin, and A. Berger. Crystallography-driven positive exchange bias in Co/CoO bilayers. *Phys. Rev. Lett.*, 109:177205, Oct 2012.
- [176] T. Gredig, I. N. Krivorotov, P. Eames, and E. D. Dahlberg. Unidirectional coercivity enhancement in exchange-biased Co/CoO. *Applied Physics Letters*, 81(7):1270–1272, 2002.
- [177] J Nogu  s, D Lederman, TJ Moran, and Ivan K Schuller. Positive exchange bias in FeF<sub>2</sub>-Fe bilayers. *Phys. Rev. Lett.*, 76:4624–4627, Jun 1996.
- [178] Wenhong Wang, Fumiyoshi Takano, Masato Takenaka, Hiro Akinaga, and Hironori Ofuchi. Anomalous temperature-dependent exchange bias in Fe films deposited on Si substrates with the native oxide layer. *Journal of Applied Physics*, 103(9):093914, 2008.
- [179] Hongtao Shi, D. Lederman, N. R. Dilley, R. C. Black, J. Diedrichs, K. Jensen, and M. B. Simmonds. Temperature-induced sign change of the exchange bias in Fe<sub>0.82</sub>Zn<sub>0.18</sub>F<sub>2</sub>/Co bilayers. *Journal of Applied Physics*, 93(10):8600–8602, 2003.
- [180] Yang Zhao and H. Neal Bertram. Disorder and coercivity in magnetic particle systems. *Journal of Magnetism and Magnetic Materials*, 114(3):329 – 335, 1992.
- [181] Y. F. Tian, J. F. Ding, W. N. Lin, Z. H. Chen, A. David, M. He, W. J. Hu, L. Chen, and T. Wu. Anomalous exchange bias at collinear/noncollinear spin interface. *Sci. Rep.*, 3, January 2013.
- [182] Li qin Yan, Ferran Macia, Zhong wei Jiang, Jun Shen, Lun hua He, and Fang wei Wang. Glassy magnetic behavior induced by Cu 2+ substitution in the frustrated antiferromagnet ZnCr<sub>2</sub>O<sub>4</sub>. *Journal of Physics: Condensed Matter*, 20(25):255203, 2008.
- [183] B. S. Kwak, A. Erbil, J. D. Budai, M. F. Chisholm, L. A. Boatner, and B. J. Wilkens. Domain formation and strain relaxation in epitaxial ferroelectric heterostructures. *Phys. Rev. B*, 49:14865–14879, Jun 1994.

[184] S. Bleil, H. H. von Gruenberg, J. Dobnikar, R. Castaneda-Priego, and C. Bechinger. Strain-induced domain formation in two-dimensional colloidal systems. *EPL (Europhysics Letters)*, 73(3):450, 2006.

[185] E. Fawcett, H. L. Alberts, V. Yu. Galkin, D. R. Noakes, and J. V. Yakhmi. Spin-density-wave antiferromagnetism in chromium alloys. *Rev. Mod. Phys.*, 66:25–127, Jan 1994.

[186] S K Burke and B D Rainford. Determination of the antiferromagnetic phase boundary in Cr-Fe alloys. *Journal of Physics F: Metal Physics*, 8(10):L239, 1978.

[187] M. N. Baibich, J. M. Broto, A. Fert, F. Nguyen Van Dau, F. Petroff, P. Etienne, G. Creuzet, A. Friederich, and J. Chazelas. Giant magnetoresistance of (001)Fe/(001)Cr magnetic superlattices. *Phys. Rev. Lett.*, 61:2472–2475, Nov 1988.

[188] P. Grünberg, R. Schreiber, Y. Pang, M. B. Brodsky, and H. Sowers. Layered magnetic structures: Evidence for antiferromagnetic coupling of Fe layers across Cr interlayers. *Phys. Rev. Lett.*, 57:2442–2445, Nov 1986.

[189] M. C. Cyrille, S. Kim, M. E. Gomez, J. Santamaria, Kannan M. Krishnan, and Ivan K. Schuller. Enhancement of perpendicular and parallel giant magnetoresistance with the number of bilayers in Fe/Cr superlattices. *Phys. Rev. B*, 62:3361–3367, Aug 2000.

[190] B. Heinrich, J. F. Cochran, T. Monchesky, and R. Urban. Exchange coupling through spin-density waves in Cr(001) structures:Fe-whisker/Cr/Fe(001) studies. *Phys. Rev. B*, 59:14520–14532, Jun 1999.

[191] S K Burke, R Cywinski, J R Davis, and B D Rainford. The evolution of magnetic order in CrFe alloys. II. onset of ferromagnetism. *Journal of Physics F: Metal Physics*, 13(2):451, 1983.

[192] S. M. Dubiel, Ch. Sauer, and W. Zinn. Mössbauer-effect investigation of a Cr-13.5 at.% Fe alloy doped with 0.7 at. %<sup>119</sup>Sn. *Phys. Rev. B*, 32:2745–2751, Sep 1985.

*Bibliography*

---

# Appendix A

## Appendices

### A.1 Appendix 1

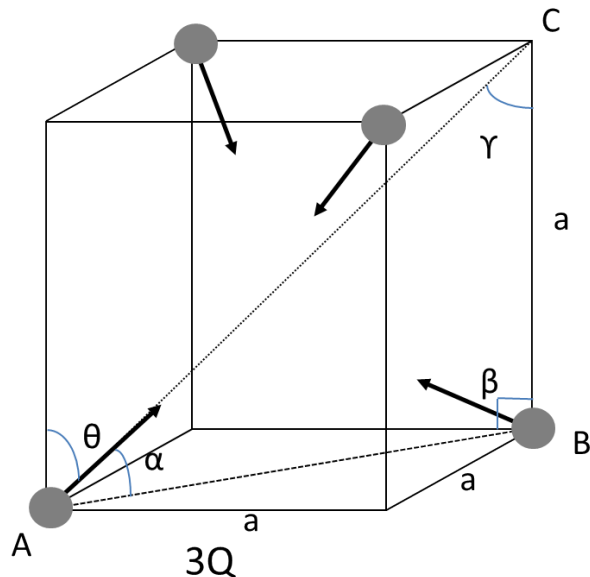


Figure A.1.1: The schematic presentation of the unit cell of 3Q spin structure of  $\gamma$ -phase disordered IrMn alloy.

The schematic presentation of 3Q spin structure (with  $c/a=1$ ) of  $\text{IrMn}^{71}$ , where the spins are directed to the center of tetrahedron is shown in Fig. A1.1. The spins are making an angle  $\theta$  along the c axis. The diagonal  $AB=\sqrt{2}a$ , where "a" is the length

of the side of the cube. In right angled triangle ABC,  $\alpha = \tan^{-1}(a/\sqrt{2}a) = 35.3^\circ$ . The value of  $\theta = 90^\circ - \alpha = 54.7^\circ$ .

## A.2 Appendix 2

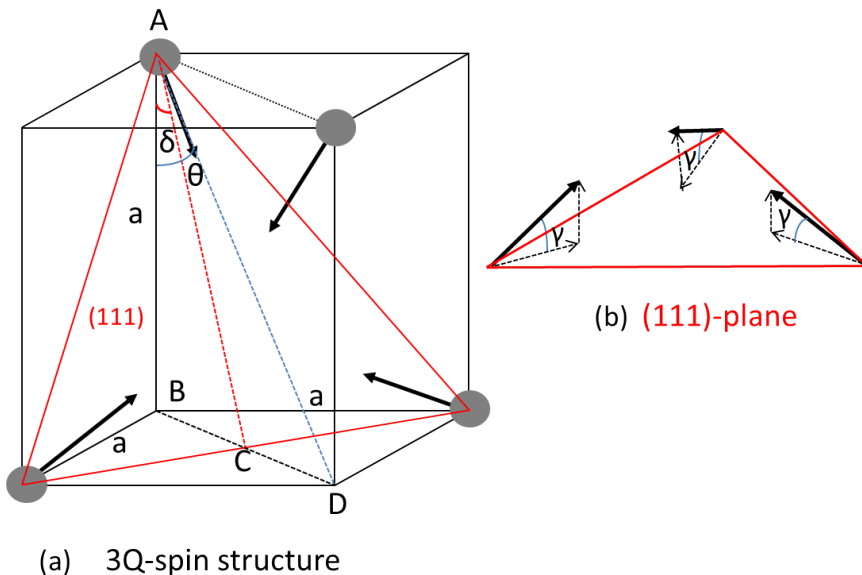


Figure A.2.1: The schematic presentation of unit cell of 3Q spin structure of  $\gamma$ -phase disordered IrMn alloy, where (111) plane is represented by the red triangle passing through three corners of unit cell (a); the three spins at an angle of  $\gamma$  w.r.t. (111) plane (b).

Fig. A.2.1(a) presents the 3Q structure of IrMn. The spin at position A is directed toward the center of tetrahedron, making an angle  $\theta$  along c axis (vertical side of tetrahedron). In the right angled triangle ABD,  $\theta = \tan^{-1}(\sqrt{2}a/a) = 54.73^\circ$ , where AB = a and BD =  $\sqrt{2}a$ . The (111) plane is presented through the red lines (passing through three corners of unit cell) and at an angle of  $\delta$  w.r.t. the c axis of the tetrahedron. In right angled triangle ABC, AB = a and BC =  $\sqrt{2}a/2$  which gives  $\delta = \tan^{-1}(\sqrt{2}a/2a) = 35.27^\circ$ . The angle between the spin and the (111) plane is  $\gamma$  which is equal to  $(\theta - \delta) 19.5^\circ$ .

# List of publications

- "Role of interface alloying in the exchange bias of Fe/Cr bilayer" S. Rizwan Ali, M. Bilal Janjua, M. Fecioru-Morariu, D. Lott, C.J.P Smits, G. Güntherodt. Physical Review B Rapid Communications 82, 020402 (2010).
- "Exchange bias and vertical shift in CoFe<sub>2</sub>O<sub>4</sub> nanoparticles" A. Mumtaz, K. Maaz, B. Janjua, S. K. Hasanain, M. F. Bertino. Journal of Magnetism and Magnetic Materials 313, 266 (2007).
- "Effect of spin-structure of IrMn and anomalous magnetic anisotropy in CoPd/IrMn perpendicular exchange biased system" M. B. Janjua and G. Güntherodt (to be submitted).
- "Study of spin dynamics, Morin transition, exchange bias and shape anisotropy in hematite nanoparticles" M. B. Janjua, K. Dörmbach, A. Pich and G. Güntherodt (to be submitted).

## Talks and Posters

- "Spin-structure and spin-reorientation transitions in the CoPd/IrMn exchange bias system" Muhammad Bilal Janjua and Gernot Güntherodt. Talk in 76th DPG (Deutsche Physikalische Gesellschaft) Conference, Berlin, Germany 2012.
- "Effect of spin structure transition in IrMn on the CoP/IrMn perpendicular exchange biased system" Muhammad Bilal Janjua and Gernot Güntherodt. Poster in 75th DPG Conference, Dresden, Germany 2011.
- "Role of interface alloying on the exchange bias in Fe/Cr bilayers" S. Rizwan Ali, M. Bilal Janjua, M. Fecioru-Morariu, D. Lott, C. J. P Smits, G. Güntherodt. Presentation in DPG Spring Meeting, Dresden, Germany 2009.



# Acknowledgments

I am really thankful to ALLAH Almighty, most Gracious, for giving me strength, for all His blessings, favours and mercy He showered me. As I write the acknowledgment of my dissertation, I can't help recollecting how much this journey taught me as a person and as a physicist. I have learnt to deal with academics and organizations and also to work alone, I also learnt how to bridge theory and practice, critical analysis and literature review.

I would like to express my sincere gratitude to my advisor Prof. Gernot Güntherodt for his valuable suggestions and technical guidance during my Ph.D. research. He has been a great inspiration for me because of his immense knowledge and hard working. I also thank him for providing me an opportunity to join his team and to use laboratory and research facilities.

I would like to thank Prof. Markus Morgenstern and Prof. Wolfgang Kuch (Freie Universität Berlin) for their kind acceptance as my co-supervisors, reviewing my research and for their support. I would also like to thank Prof. Christoph Stampfer and Prof. Stefan Wessel for their valuable time and being members of the doctorate committee. I thank again my doctorate committee who read over my thesis draft. Their insightful comments and encouragement incensed me to widen and improve my research from various perspectives.

I am thankful to Prof. Uwe Klemradt for the use of x-ray diffractometer and Dr. Bernd Beschoten for providing his support in various scientific and organizational matters. I would like to thank all my colleagues especially Rizwan, Marian, Nicolas, Klaus, Stefan, Coen, Lars, Frank, Marc, Sammy, Ivan and Sebastian. I am thankful to all my administrative and technical staff including workshop team for providing their support and helping me in various matters during.

I am highly indebted to my parents, my khala, my wife, my brothers, my sisters and my friends for their never-ending support and prayers. I would like to thank

*Appendix A. Appendices*

---

my wife for her patience during my Ph.D. I dedicate my Ph.D. dissertation to my parents and my khala.

# Curriculum Vitae

## Personal Data

Name: Muhammad Bilal Janjua

Nationality: Pakistani

Email: bilal.janjua@physik.rwth-aachen.de

## Academic Qualification

2006 – 2014	Ph.D. Dissertation in the field of Nanomagnetism II. Physikalisches Institut A, RWTH Aachen University, Germany
2005 – 2006	Research Assistant at Department of Physics in Quaid-i-Azam University, Islamabad, Pakistan
2003 – 2005	M.Phil. in Physics (Condensed matter physics), from Quaid-i-Azam University, Islamabad, Pakistan
2001 – 2003	M.Sc. in Physics from Quaid-i-Azam University, Islamabad, Pakistan
1998 – 2000	B.Sc. from Punjab University, Pakistan
1995 – 1997	Higher Secondary School Certificate, Rawalpindi Board, Pakistan
1992 – 1994	Secondary School Certificate from Saint Pauls Cambridge School, Pakistan